Modeling and understanding dynamics of charged particles in the Earth's inner magnetosphere

Nikita Alexandrovich Aseev

Kumulative Dissertation
zur Erlangung des akademischen Grades
"doctor rerum naturalium"
(Dr. rer. nat.)
in der Wissenschaftsdisziplin "Computational Physics"

eingereicht an der
Mathematisch-Naturwissenschaftlichen Fakultät
der Universität Potsdam

Institut für Physik und Astronomie

September 2020

BETREUER:
Hauptbetreuer: Prof. Dr. Yuri Shprits
Zweitbetreuer: Prof. Dr. Richard Horne

GUTACHTER:
Prof. Dr. Claudia Stolle
Prof. Dr. Allison Jaynes
Prof. Dr. Arkady Pikovsky
Prof. Dr. Stephan Sobolev
Prof. Dr. Michael Rosenblum

Published online on the
Publication Server of the University of Potsdam:
https://doi.org/10.25932/publishup-47921
https://nbn-resolving.org/urn:nbn:de:kobv:517-opus4-479211

Declaration

I, Nikita Alexandrovich Aseev, hereby declare that this thesis entitled "Modeling and understanding dynamics of charged particles in the Earth's inner magnetosphere" has been composed entirely by myself. The work contained herein is my own, except where explicitly stated otherwise. I confirm that:

- I have fully acknowledged and referenced the ideas and work of others, whether published or unpublished.
- This dissertation has not been submitted for any other degree or professional qualification.

Nikita Alexandrovich Aseev

Contents

Contents v
Acknowledgments ix
List of Abbreviations x
List of Figures xiii
List of Tables xv
Publications xvi
Abstract xviii
Zusammenfassung xx

1 Introduction **1**
1.1 Charged Particle Populations in the Inner Magnetosphere 1
1.2 Dynamics of Charged Particles 4
1.2.1 Gyro, Bounce, and Drift Motion 4
1.2.2 Adiabatic Invariants 9
1.2.3 Violation of Adiabatic Invariants and Main Loss and Acceleration Mechanisms in the Inner Magnetosphere 11
1.2.4 Phase Space Density and Fokker-Planck Equation 15
1.2.5 Modified Fokker-Planck Equation with Advection Terms 16
1.3 Objectives and Structure of the Dissertation 18

2 Numerical Applications of the Advective-Diffusive Codes for the Inner Magnetosphere **21**
Abstract 21
2.1 Introduction 22
2.2 Approach of the VERB-4D Code 26
2.3 Theoretical Framework for Testing of Inner Magnetospheric Models . . . 28
2.3.1 One-Dimensional Convection 29
2.3.2 Two-Dimensional Convection 32
2.3.3 One-Dimensional Diffusion and Two-Dimensional Diffusion with Mixed Terms 33
2.4 Numerical Scheme Influence on Magnetospheric Convection Modeling . 37

2.5 Summary and Conclusions . . . 41
2.A Courant-Friedrichs-Lewy Condition . . . 42
2.B Elimination of Unphysical Oscillations Using the Universal Limiter . . . 42
Acknowledgments . . . 45

3 Transport and Loss of Ring Current Electrons Inside Geosynchronous Orbit during the 17 March 2013 Storm 47
Abstract . . . 47
3.1 Introduction . . . 48
3.2 Observations of the 17 March 2013 Storm . . . 51
3.3 Model Description . . . 55
3.4 Results . . . 57
3.4.1 Model-Data Comparison along Van Allen Probes Orbits . . . 57
3.4.2 Sensitivity to the Outer Boundary Conditions . . . 60
3.4.3 Role of the Electric Field Model . . . 61
3.4.4 Sensitivity to the Electron Lifetime Model . . . 66
3.4.5 Effects of Radial Diffusion . . . 66
3.4.6 Effects of SAPS . . . 67
3.5 Discussion . . . 68
3.6 Summary . . . 71
Acknowledgments . . . 72

4 Reanalysis of Ring Current Electron Phase Space Densities using Van Allen Probe Observations, Convection Model, and Log-Normal Kalman Filter 73
Abstract . . . 73
4.1 Introduction . . . 74
4.2 Data and Methods . . . 76
4.2.1 Data . . . 76
4.2.2 Convection Model . . . 77
4.2.3 Log-Transformed Convection Model . . . 79
4.2.4 Kalman Filter . . . 79
4.3 Experiments with Synthetic Data . . . 82
4.3.1 Metrics . . . 83
4.3.2 Errors in Electron Lifetimes . . . 85
4.3.3 Errors in Boundary Conditions . . . 86
4.3.4 Errors in Convection Electric Field . . . 89
4.4 Reanalysis of Ring Current Electrons using Van Allen Probes Data . . . 92
4.4.1 Long-Term Reanalysis from 1 February 2013 to 16 June 2013 . . . 92

4.4.2 Reanalysis during the 1 June 2013 Storm 95
4.4.3 Reanalysis for Different Values of μ 97
4.5 Discussion 99
4.6 Summary and Conclusions 101
Acknowledgments 102

5 Signatures of Ultrarelativistic Electron Loss in the Heart of the Outer Radiation Belt Measured by Van Allen Probes 105
Abstract 105
5.1 Introduction 106
5.2 Van Allen Probes Measurements from 9 October to 29 November 2012 . 108
5.3 Data and Methods 110
5.4 Signatures of EMIC Wave-Driven Ultrarelativistic Electron Loss 110
5.5 Discussion 114
Acknowledgments 118

6 Summary and Future Work 119
6.1 Summary 119
6.2 Key scientific findings and developed tools 121
6.3 Future Work 122

Bibliography 125

Acknowledgments

First and foremost, I would like to express my deepest gratitude to my advisor, Yuri Shprits, for the continuous support throughout my years at GFZ and University of Potsdam. The atmosphere that he created in his research group encouraged me to generate and put into practice my own ideas, at the same time heading in the right direction under his supervision. I sincerely appreciate his willingness to share his broad expertise in space physics and readiness to answer any question at any time. The completion of this research project would not be possible without his patient guidance.

I wish to pay my special regards to Richard Horne, with whom I have been lucky to have interesting discussions that have laid foundations for the ideas and results presented in this dissertation. I would like to thank Alexander Drozdov for the introduction into the exciting field of space physics and for advising me during my first days at UCLA. I am grateful to Adam Kellerman for sharing with me his fundamental knowledge of radiation belt physics, as well as his expertise in a variety of numerical tools.

I would like to thank my colleagues at GFZ, who helped me with the work that has become part of this dissertation: Dedong Wang, Irina Zhelavskaya, Ingo Michaelis, Frederic Effenberger, and Dominika Sörgel. I wish to show my gratitude to Geoff Reeves, John Wygant, Daniel Weimer, Maria Usanova, Natalia Ganushkina, Reiner Friedel, Michael Schulz, Michael Henderson, Drew Turner, Sharon Uy, Sandra Paulin, Alexander Jordan, Martina Krüger, Antje Timmermann, Hayley Allison, Juan Cervantes-Villa, Angelica Castillo, Stefano Bianco, Ruggero Vasile, Melanie Burns, Artem Smirnov, and Matyas Szabo-Roberts for their valuable feedback and assistance during my research project. Pursuing my scientific path at GFZ was a pleasurable journey together with Tarique Siddiqui, Juan Rodriguez-Zuluaga, Robin Senftleben, Leonie Pick, and Foteini Vervelidou.

I wish to express my sincere gratitude to my former supervisor at MIPT, Valery Agoshkov, who nurtured my interest in scientific research, and colleagues at INM RAS and MIPT, Victor Shutyaev, Evgeny Parmuzin, Ivan Novikov, Maxim Rakhuba, Natalia Zakharova, and Tatiana Sheloput, for the countless hours that we spent together in numerous conversations.

Finally, I would like to thank my parents, who were the ones to actually start my project, and my beloved little sister.

List of Abbreviations

BAS code British Antarctic Survey radiation belt model (Glauert et al., 2014)

BBF Bursty Bulk Flow (Angelopoulos et al., 1992)

CARISMA Canadian Array for Real-time Investigations of Magnetic Activity (Mann et al., 2008)

CIMI code Comprehensive Inner-Magnetosphere Ionosphere model (Fok et al., 1999)

CRRES Combined Release and Radiation Effects Satellite (Johnson and Kierein, 1992)

DREAM3D code three-dimensional Dynamic Radiation Environment Assimilation Model (Tu et al., 2013)

Dst Disturbance storm-time (used as Dst index or Dst effect)

ECT Energetic Particle, Composition, and Thermal Plasma suite on board Van Allen Probes (Spence et al., 2013)

EFW Electric Field and Waves instrument on board Van Allen Probes (Wygant et al., 2013)

EMFISIS Electric and Magnetic Field Instrument Suite and Integrated Science instrument on board Van Allen Probes (Kletzing et al., 2013)

EMIC Electromagnetic Ion-Cyclotron (waves)

ERG Exploration of energization and Radiation in Geospace satellite (Miyoshi et al., 2018)

EnKF Ensemble Kalman Filter

GEO Geostationary Orbit

GOES Geostationary Operational Environmental Satellite mission

GSE Geocentric Solar Ecliptic coordinate system

HEIDI code Hot Electron and Ion Drift Integrator (Liemohn et al., 2001)

HOPE Helium, Oxygen, Proton, and Electron mass spectrometer on board Van Allen Probes (Funsten et al., 2013)

IGRF	International Geomagnetic Reference Field (Thébault et al., 2015)
IMPTAM code	Inner Magnetosphere Particle Transport and Acceleration Model (Ganushkina et al., 2012)
IRBEM library	International Radiation Belt Environment Modeling library (Boscher et al., 2012)
LANL GEO	Los Alamos National Laboratory geosynchronous satellite mission
LAPACK	Linear Algebra PACKage (Anderson et al., 1999)
LFM	Lyon-Fedder-Mobarry global magnetospheric model (Lyon et al., 2004)
MagEIS	Magnetic Electron Ion Spectrometer on board Van Allen Probes (Blake et al., 2013)
MdSA	Median Symmetric Accuracy metric (Morley, 2016)
MFSE	Mean Fractional Symmetric Error metric (see equation (4.22))
MetOp	Meteorological Operational Satellite Program of Europe
MGSE	Modified GSE coordinate system
MLT	Magnetic Local Time
ND	Normalized Difference (see equation (2.28))
POES	Polar Operational Environmental Satellites
PSD	Phase Space Density
RAM code	Ring current Atmosphere interactions Model (Jordanova et al., 1996)
REPT	Relativistic Electron-Proton Telescope on board Van Allen Probes (Baker et al., 2013a)
RBE code	Radiation Belt Environment model (Fok et al., 2008)
RBSP	Radiation Belt Storm Probes (former name of Van Allen Probes)
RCM code	Rice Convection Model (Toffoletto et al., 2003)
RCM-E code	Rice Convection Model with self-consistently computed magnetic field (Lemon et al., 2004)
SAPS	Subauroral Polarization Streams (Foster and Burke, 2002)

SI units	International System of Units
STEERB code	Storm-Time Evolution of Electron Radiation Belt (three-dimensional diffusion code (Zhang et al., 2014))
T01S	(Tsyganenko, 2002) magnetic field model
T04S	(Tsyganenko and Sitnov, 2005) magnetic field model
T89	(Tsyganenko, 1989) magnetic field model
T96	(Tsyganenko, 1995) magnetic field model
THEMIS	Time History of Events and Macroscale Interactions during Substorms satellite mission
TS07D	(Tsyganenko and Sitnov, 2007) magnetic field model
ULF	Ultra-Low Frequency (waves)
VERB code	Versatile Electron Radiation Belt code (Shprits et al., 2009)
VERB-4D code	four-dimensional Versatile Electron Radiation Belt code (Shprits et al., 2015)
VERB-CS code	simplified version of the VERB-4D code that accounts for convection and parameterized loss (see Chapter 4)
VLF	Very Low Frequency (waves)
VSMC	(Volland, 1973; Stern, 1975) convection electric field model
W05	(Weimer, 2005) polar cap potential model

List of Figures

1.1 The Earth's magnetosphere, adapted from Walt (1994). 2
1.2 Lines of constant electrostatic potential, adapted from Baumjohann and Treumann (2012). 7
1.3 Electron drift trajectories, adapted from Lyons and Williams (1984). . . 8
1.4 Contours of constant adiabatic gyration, bounce, and drift frequency, adapted from Schulz and Lanzerotti (1974). 12
1.5 Loss and acceleration processes in the Earth's inner magnetosphere, adapted from Shprits et al. (2008b). 13

2.1 Comparison of the analytical and VERB-4D code solutions of 1D convection equation. 31
2.2 Comparison of the analytical and VERB-4D code solutions of 2D convection equation. 33
2.3 Same as Figure 2.2 but for longer end time. 34
2.4 Comparison of the analytical and VERB-4D code solutions of 2D diffusion equation with mixed terms. 37
2.5 Electron fluxes obtained by using the third- and ninth-order schemes. . 39
2.6 Dependence of numerically calculated profiles of electron fluxes on the scheme order. 40

3.1 Combined HOPE and MagEIS spectrum. 51
3.2 Electron PSD derived from Van Allen Probes observations. 52
3.3 Energies and pitch angles corresponding to different values of μ and constant K. 53
3.4 Profiles of electron PSD for $K = 0.3$ $G^{1/2}R_E$ and different values of μ calculated, using different magnetic field models. 54
3.5 Comparison of Van Allen Probes PSD and VERB-4D code results for different values of μ and constant K. 58
3.6 Comparison of Van Allen Probe radial PSD profiles and VERB-4D code results for different values of μ and constant K (including confidence intervals). 60

3.7 Comparison between measured electric fields and W05 and VSMC empirical models. 62
3.8 Comparison of Van Allen Probe radial PSD profiles and VERB-4D code results for different values of μ and constant K. Different electric field models are used. 64
3.9 Global PSD distribution of μ = 2.3 MeV/G and K = 0.3 $G^{1/2}R_E$ electrons obtained with the VERB-4D code if the W05 electric field model is used. $R \equiv R_0$. 65
3.10 Global PSD distribution of μ = 2.3 MeV/G and K = 0.3 $G^{1/2}R_E$ electrons obtained with the VERB-4D code if the VSMC electric field model is used. $R \equiv R_0$. 65
3.11 Comparison of Van Allen Probe radial PSD profiles and VERB-4D code results for different values of μ and constant K (sensitivity to lifetimes). 67
3.12 Comparison of Van Allen Probe radial PSD profiles and VERB-4D code results for K = 0.3 $G^{1/2}R_E$ and μ = 9.9 MeV/G electrons (sensitivity to radial diffusion coefficient). 68
3.13 Comparison of Van Allen Probe radial PSD profiles and VERB-4D code results for different values of μ and constant K (sensitivity to SAPS electric field). 69

4.1 Illustration of Van Allen Probes orbits. 77
4.2 Energies and pitch angles corresponding to different values of μ and constant K. 78
4.3 Fraternal twin experiment: errors in electron lifetimes. 86
4.4 Fraternal twin experiment: errors in boundary conditions. 88
4.5 Fraternal twin experiment: errors in convection electric fields (overestimation). 90
4.6 Fraternal twin experiment: errors in convection electric fields (underestimation). 91
4.7 Long-term reanalysis, using Van Allen Probes data, μ = 2.3 MeV/G and K = 0.3 $G^{1/2}R_E$. 93
4.8 Innovation vector. 95
4.9 The Kp and Dst indices on 1 June 2013. 96
4.10 Global comparison between reanalysis and the model. 96
4.11 Long-term reanalysis, using Van Allen Probes data, μ = 0.1 MeV/G and K = 0.3 $G^{1/2}R_E$. 98
4.12 Long-term reanalysis, using Van Allen Probes data, μ = 9.9 MeV/G and K = 0.3 $G^{1/2}R_E$. 99

5.1 Signatures of the electron loss from the outer radiation belt, adapted from Shprits et al. (2017). 108
5.2 Differential fluxes of ultrarelativistic electrons measured by REPT on board Van Allen Probes. 109
5.3 Evolution of PSD profiles derived from RBSP-A flux measurements. . . 111
5.4 Evolution of ultrarelativistic electron PSD profiles during periods when the most pronounced minimums were detected. 112
5.5 Presence of EMIC waves measured by CARISMA, formation of new local minimums in ultrarelativistic electron PSD profiles, and pitch-angle distributions of directional differential fluxes. 113
5.6 Local minimums observed on 12 November. 116
5.7 Local minimums observed on 1 November. 116
5.8 Last closed drift shell. 117
5.9 Evolution of electron fluxes at $L^* = 5 \pm 0.25$ measured by MagEIS and REPT instruments. 118

List of Tables

2.1 Coefficients for calculation $2 \cdot D^{k,(N)}_{i+1/2}$. 44
2.2 Coefficients for calculation $\delta^{k,(M)}_{i+1/2}$. 45

Publications

Aseev, N. A., Shprits, Y. Y., Drozdov, A. Y., and Kellerman, A. C., 2016. Numerical Applications of the Advective-Diffusive Codes for the Inner Magnetosphere. *Space Weather*, 14(11):993–1010. doi:10.1002/2016SW001484

Aseev, N. A., Shprits, Y. Y., Drozdov, A. Y., Kellerman, A. C., Usanova, M. E., Wang, D., and Zhelavskaya, I. S., 2017. Signatures of Ultrarelativistic Electron Loss in the Heart of the Outer Radiation Belt Measured by Van Allen Probes. *Journal of Geophysical Research: Space Physics*, 122(10):10,102–10,111. doi:10.1002/2017JA024485

Aseev, N. A., Shprits, Y. Y., Wang, D., Wygant, J., Drozdov, A. Y., Kellerman, A. C., and Reeves, G. D., 2019. Transport and Loss of Ring Current Electrons Inside Geosynchronous Orbit during the 17 March 2013 Storm. *Journal of Geophysical Research: Space Physics*, 124(2):915–933. doi:10.1029/2018JA026031

Aseev, N. A. and Shprits, Y. Y., 2019. Reanalysis of Ring Current Electron Phase Space Densities Using Van Allen Probe Observations, Convection Model, and Log-Normal Kalman Filter. *Space Weather*, 17(4):619–638. doi:10.1029/2018SW002110

Shprits, Y. Y., Drozdov, A. Y., Spasojevic, M., Kellerman, A. C., Usanova, M. E., Engebretson, M. J., Agapitov, O. V., Zhelavskaya, I. S., Raita, T. J., Spence, H. E., Baker, D. N., Zhu, H., and Aseev, N. A., 2016. Wave-Induced Loss of Ultra-Relativistic Electrons in the Van Allen Radiation Belts. *Nature Communications*, 7: 12883. doi:10.1038/ncomms12883

Shprits, Y. Y., Kellerman, A., Aseev, N., Drozdov, A. Y., and Michaelis, I., 2017. Multi-MeV Electron Loss in the Heart of the Radiation Belts. *Geophysical Research Letters*, 44(3):1204–1209. doi:10.1002/2016GL072258

Drozdov, A. Y., Shprits, Y. Y., Aseev, N. A., Kellerman, A. C., and Reeves, G. D., 2017a. Dependence of Radiation Belt Simulations to Assumed Radial Diffusion Rates Tested for Two Empirical Models of Radial Transport. *Space Weather*, 15(1):150–162. doi:10.1002/2016SW001426

Drozdov, A. Y., Shprits, Y. Y., Usanova, M. E., Aseev, N. A., Kellerman, A. C., and Zhu, H., 2017b. EMIC Wave Parameterization in the Long-Term VERB Code Simulation. *Journal of Geophysical Research: Space Physics*, 122(8):8488–8501. doi:10.1002/2017JA024389

Smirnov, A. G., Kronberg, E. A., Latallerie, F., Daly, P. W., Aseev, N., Shprits, Y. Y., Kellerman, A., Kasahara, S., Turner, D., and Taylor, M. G. G. T., 2019. Electron In-

tensity Measurements by the Cluster/RAPID/IES Instrument in Earth's Radiation Belts and Ring Current. *Space Weather*, 17(4):553–566. doi:10.1029/2018SW001989

Wang, D., Shprits, Y. Y., Zhelavskaya, I. S., Agapitov, O. V., Drozdov, A. Y., and Aseev, N. A., 2019. Analytical Chorus Wave Model Derived from Van Allen Probe Observations. *Journal of Geophysical Research: Space Physics*, 124(2):1063–1084. doi:10.1029/2018JA026183

Castillo, A. M., Shprits, Y. Y., Ganushkina, N., Drozdov, A., Aseev, N., Wang, D., and Dubyagin, S., 2019. Simulations of the Inner Magnetospheric Energetic Electrons Using the IMPTAM-VERB Coupled Model. *Journal of Atmospheric and Solar-Terrestrial Physics*, 191. doi:10.1016/j.jastp.2019.05.014

Drozdov, A. Y., Aseev, N., Effenberger, F., Turner, D. L., Saikin, A., and Shprits, Y. Y., 2019. Storm-Time Depletions of Multi-MeV Radiation Belt Electrons Observed at Different Pitch Angles. *Journal of Geophysical Research: Space Physics*, 124(11):8943–8953. doi:10.1029/2019JA027332

Cervantes, S., Shprits, Y. Y., Aseev, N. A., Drozdov, A. Y., Castillo, A., and Stolle, C., 2019. Identifying Radiation Belt Electron Source and Loss Processes by Assimilating Spacecraft Data in a Three-Dimensional Diffusion Model. *Journal of Geophysical Research: Space Physics*. doi:10.1029/2019JA027514

Abstract

The Earth's inner magnetosphere is a very dynamic system, mostly driven by the external solar wind forcing exerted upon the magnetic field of our planet. Disturbances in the solar wind, such as coronal mass ejections and co-rotating interaction regions, cause geomagnetic storms, which lead to prominent changes in charged particle populations of the inner magnetosphere – the plasmasphere, ring current, and radiation belts. Satellites operating in the regions of elevated energetic and relativistic electron fluxes can be damaged by deep dielectric or surface charging during severe space weather events. Predicting the dynamics of the charged particles and mitigating their effects on the infrastructure is of particular importance, due to our increasing reliance on space technologies.

The dynamics of particles in the plasmasphere, ring current, and radiation belts are strongly coupled by means of collisions and collisionless interactions with electromagnetic fields induced by the motion of charged particles. Multidimensional numerical models simplify the treatment of transport, acceleration, and loss processes of these particles, and allow us to predict how the near-Earth space environment responds to solar storms. The models inevitably rely on a number of simplifications and assumptions that affect model accuracy and complicate the interpretation of the results. In this dissertation, we quantify the processes that control electron dynamics in the inner magnetosphere, paying particular attention to the uncertainties of the employed numerical codes and tools.

We use a set of convenient analytical solutions for advection and diffusion equations to test the accuracy and stability of the four-dimensional Versatile Electron Radiation Belt code (VERB-4D code). We show that numerical schemes implemented in the code converge to the analytical solutions and that the VERB-4D code demonstrates stable behavior independent of the assumed time step. The order of the numerical scheme for the convection equation is demonstrated to affect results of ring current and radiation belt simulations, and it is crucially important to use high-order numerical schemes to decrease numerical errors in the model.

Using the thoroughly tested VERB-4D code, we model the dynamics of the ring current electrons during the 17 March 2013 storm. The discrepancies between the model and observations above 4.5 R_E, where R_E denotes the Earth's radius, can be explained by uncertainties in the outer boundary conditions. Simulation results indicate that the electrons were transported from Geostationary Orbit (GEO) towards the Earth by the global-scale electric and magnetic fields. We investigate how simulation results depend on the input models and parameters. The model is shown to be particularly

sensitive to the global electric field and electron lifetimes below 4.5 R_E. The effects of radial diffusion and subauroral polarization streams are also quantified.

We developed a data-assimilative code that blends together a convection model of energetic electron transport and loss and Van Allen Probes satellite data by means of the Kalman filter. We show that the Kalman filter can correct model uncertainties in the convection electric field, electron lifetimes, and boundary conditions. It is also demonstrated how the innovation vector – the difference between observations and model prediction – can be used to identify physical processes missing in the model of energetic electron dynamics.

We computed radial profiles of phase space density of ultrarelativistic electrons, using Van Allen Probes measurements. We analyze the shape of the profiles during geomagnetically quiet and disturbed times and show that the formation of new local minimums in the radial profiles coincides with the ground observations of Electromagnetic Ion-Cyclotron (EMIC) waves. This correlation indicates that EMIC waves are responsible for the loss of ultrarelativistic electrons from the heart of the outer radiation belt into the Earth's atmosphere.

Zusammenfassung

Die innere Magnetosphäre der Erde ist ein sehr dynamisches System, das hauptsächlich vom äußeren Sonnenwind beeinflusst wird, der auf das Magnetfeld unseres Planeten einwirkt. Störungen im Sonnenwind, wie z.B. koronale Massenauswürfe und sogenannte Korotierende Wechselwirkungsbereiche, verursachen geomagnetische Stürme, die zu deutlichen Veränderungen der Populationen geladener Teilchen in der inneren Magnetosphäre führen - Plasmasphäre, Ringstrom und Strahlungsgürtel. Satelliten, die in Regionen mit erhöhten energetischen und relativistischen Elektronenflüssen betrieben werden, können durch tiefe dielektrische Ladung oder Oberflächenladungen bei schweren Weltraumwetterereignissen beschädigt werden. Die Vorhersage der Dynamik der geladenen Teilchen und die Abschwächung ihrer Auswirkungen auf die Infrastruktur sind heutzutage von besonderer Bedeutung, insbesondere aufgrund unserer zunehmenden Abhängigkeit von Weltraumtechnologien.

Die Dynamik von Teilchen in der Plasmasphäre, des Ringstrom und in den Strahlungsgürteln sind durch Kollisionen und kollisionsfreie Wechselwirkungen mit elektromagnetischen Feldern, die durch die Bewegung geladener Teilchen induziert werden, stark gekoppelt. Mehrdimensionale numerische Modelle vereinfachen die Betrachtung von Transport-, Beschleunigungs- und Verlustprozessen dieser Partikel und ermöglichen es uns, vorherzusagen, wie die erdnahe Weltraumumgebung auf Sonnenstürme reagiert. Die Modelle beruhen zwangsläufig auf einer Reihe von Vereinfachungen und Voraussetzungen, die sich auf die Modellgenauigkeit auswirken und die Interpretation der Ergebnisse erschweren. In dieser Dissertation quantifizieren wir die Prozesse, die die Dynamik der Elektronen in der inneren Magnetosphäre steuern. Dabei richten wir den Fokus insbesondere auch auf die Unsicherheiten der verwendeten numerischen Codes.

Wir verwenden eine Reihe praktischer analytischer Lösungen für Advektions- und Diffusionsgleichungen, um die Genauigkeit und Stabilität des 4-dimensionalen "Versatile Electron Radiation Belt" Codes (VERB-4D Code) zu testen. Wir zeigen, dass die im Code implementierten numerischen Schemata zu den analytischen Lösungen konvergieren und der Code sich unabhängig vom angenommenen Zeitschritt stabil verhält. Wir demonstrieren, wie die Genauigkeit des numerischen Schemas für die Konvektionsgleichung die Ergebnisse von Ringstrom- und Strahlungsgürtelsimulationen beeinflussen kann, und dass es von entscheidender Beteutung ist, numerische Schemata höherer Ordnung zu verwenden, um numerische Fehler im Modell zu reduzieren.

Mit dem ausführlich getesteten VERB-4D Code modellieren wir die Dynamik der

Ringstromelektronen während des Sturms vom 17. März 2013. Wir zeigen, dass die Diskrepanzen zwischen dem Modell und Beobachtungen oberhalb von 4.5 R_E durch Unsicherheiten in den äußeren Randbedingungen erklärt werden können und dass die Elektronen durch die globalen elektrischen und magnetischen Felder von der geostationäre Umlaufbahn zur Erde transportiert wurden. Wir untersuchen weiterhin, wie die Simulationsergebnisse von den Eingabemodellen und Parametern abhängen. Wir zeigen, dass das Modell besonders empfindlich für das globale elektrische Feld und die Lebensdauer der Elektronen unterhalb von 4.5 R_E ist. Außerdem quantifizieren wir auch die Auswirkungen von radialer Diffusion und subauroralen Polarisationsströmen.

Wir haben einen datenassimilativen Code entwickelt, der mithilfe des Kalman-Filters ein Konvektionsmodell für den Transport und den Verlust energetischer Elektronen mit den Satellitendaten der Van Allen Probes kombiniert. Wir zeigen, dass die Verwendung eines Kalman-Filters Modellunsicherheiten im elektrischen Konvektionsfeld, in der Lebensdauer der Elektronen und in den Randbedingungen korrigieren kann. Weiterhin zeigen wir, wie der Innovationsvektor - die Differenz zwischen Beobachtungen und Modellvorhersagen - verwendet werden kann, um physikalische Prozesse zu identifizieren, die im Modell der Dynamik der energetischen Elektronen fehlen.

Außerdem berechnen wir radiale Profile der Phasenraumdichte ultrarelativistischer Elektronen mithilfe von Van Allen Probes-Messungen. Wir analysieren die Form der Profile und zeigen, dass die Entstehung neuer lokaler Minima in den radialen Profilen mit den Bodenbeobachtungen von EMIC-Wellen übereinstimmt. Diese Korrelation legt nahe, dass EMIC-Wellen für den Verlust ultrarelativistischer Elektronen vom Herzen des äußeren Strahlungsgürtels in die Erdatmosphäre verantwortlich sind.

Chapter 1

Introduction

1.1 Charged Particle Populations in the Inner Magnetosphere

Charged particles that populate the Earth's inner magnetosphere (see Figure 1.1) have been studied for over 60 years. The first discovery of the space age was the existence of the radiation belts (Van Allen and Frank, 1959) – two torus-shaped regions filled with electrons and protons surrounding the Earth. The following years led to the discovery of the plasmasphere – the region of the cold dense plasma (Gringauz, 1961; Carpenter, 1963; Dungey, 1967) and in-situ particle measurements of the ring current – the westward toroidal current flowing around the Earth (Frank, 1967a,b).

The Earth's radiation belts exhibit a two-zone structure. The inner belt is located at radial distances between 120 km above the Earth's surface and 2 R_E, where R_E denotes Earth's radius, and consists mainly of energetic electrons (energies from several 100 keV to ~800 keV) (Fennell et al., 2015) and protons with energies exceeding 10-100 MeV (e.g., Selesnick and Albert, 2019). The inner radiation belt is relatively stable and can undergo rapid profound changes only during the most severe geomagnetic storms (Baker et al., 2004; Shprits et al., 2011). The outer radiation belt contains electrons with energies from 100 keV to several MeV and resides at approximately 4 to 8 R_E. The outer belt shows very dynamic behavior, being intermittently depleted and replenished (e.g., Reeves et al., 2003) during geomagnetic storms. The region of low electron fluxes between the inner and outer belts is referred to as the slot region. The slot region is most pronounced during quiet times at energies above several 100 keV and can be refilled during disturbed geomagnetic conditions (Thorne et al., 2007).

The ring current consists primarily of H^+, He^+, and O^+ ions and electrons of energies from about 1 to several 100 keV (Kronberg et al., 2014; Ganushkina et al., 2017). The largest energy contribution to the ring current comes from positively charged ions, while electrons may provide up to 25% of the total energy (Frank, 1967a; Liu et al., 2005; Zhao et al., 2016). Observations and modeling studies reported large local

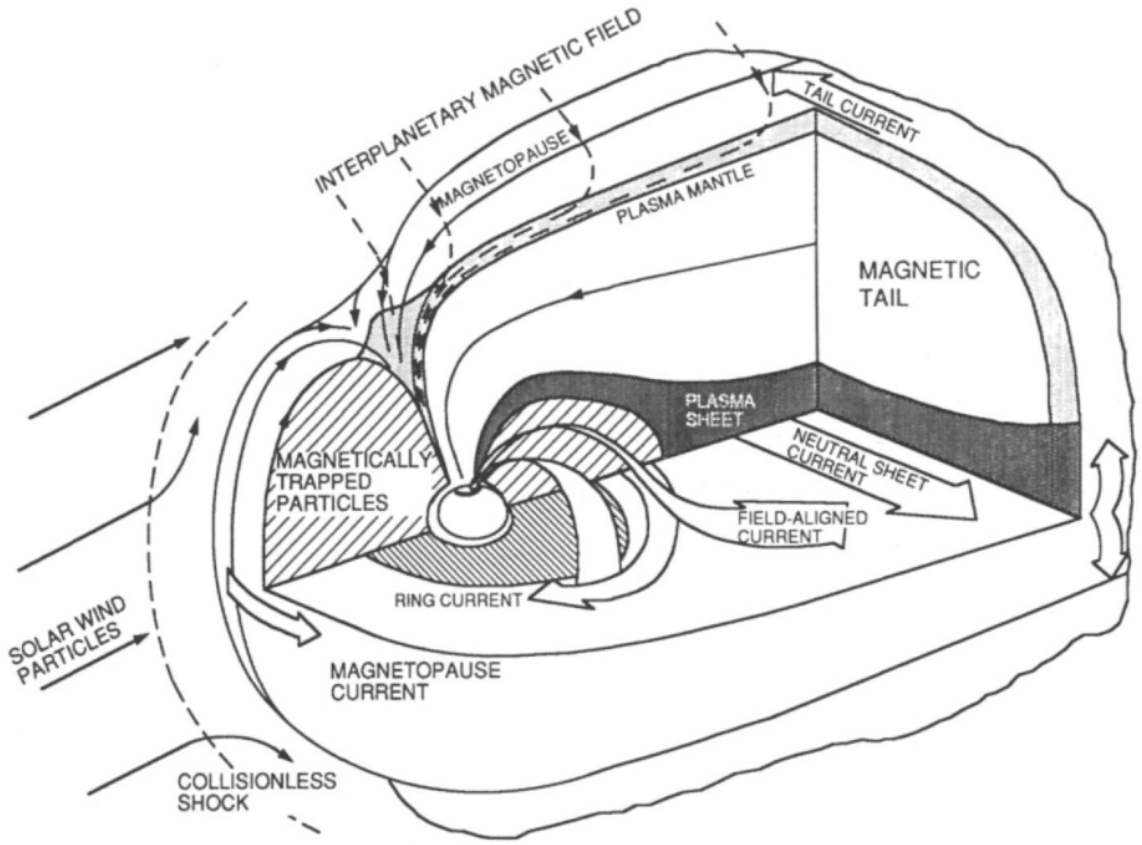

Figure 1.1: The Earth's magnetosphere, adapted from Walt (1994).

time asymmetry in the ring current during the storm main phase (e.g., Liemohn et al., 2001, and references therein). The ring current distorts the Earth's magnetic field and is coupled to the dynamics of the radiation belts, plasmasphere, and ionosphere. The ring current significantly contributes to the Disturbance storm-time (Dst) index that is based on the average value of the horizontal component of the Earth's magnetic field, measured hourly near the geomagnetic equator and used in many space weather studies as a proxy of geomagnetic storms.

The plasmasphere contains electrons and ions of ionospheric origin. Typical plasma temperature and density inside the plasmasphere are 1 eV and 10^2–10^4 cm^{-3}, respectively (e.g., Lemaire and Gringauz, 2005, and references therein). The plasmasphere extends to 4–6 R_E, with a large density gradient at the boundary that is referred to as the plasmapause. During geomagnetic storms, the plasmasphere shrinks, and the plasmapause can be observed at radial distances below 2 R_E (Baker et al., 2004). Geomagnetic disturbances lead to the formation of dayside drainage plumes – narrow regions of sunward flowing plasma (e.g., Goldstein et al., 2004, and references therein). During the storm recovery phase, the eroded plasmasphere is refilled with the ionospheric plasma, gradually restoring its quiet-time state. The plasmasphere plays an

important role in the evolution of the radiation belts (Shprits et al., 2008b; Thorne, 2010) and the ring current (Ganushkina et al., 2017).

Although plasmasphere, ring current, and radiation belts are usually considered as different particle populations, they spatially overlap and their dynamics is closely coupled. Plasma waves inside the plasmasphere are an important driver of ring current and radiation belt electron loss. Hiss waves confined within the plasmasphere (Thorne et al., 1973) and plasmaspheric plumes (Summers et al., 2008) are responsible for the formation of the slot region that separates the inner and the outer radiation belts (Lyons and Thorne, 1973). Electron lifetimes due to scattering by hiss waves depend strongly on kinetic energy and radial distance, and can be less than a day for electron energies from tens of keV up to MeV (Orlova et al., 2016). Energetic electrons from the plasma sheet provide a seed population for the radiation belts (Jaynes et al., 2015). Injections of energetic electrons outside of the plasmasphere excite chorus waves (Hwang et al., 2007; Thorne, 2010) which may lead to the pitch-angle scattering of previously trapped radiation belt and ring current electrons into the Earth's atmosphere. Injections of the ring current ions may cause rapid loss of ultrarelativistic electrons (multi-MeV energies) by means of resonant interactions with Electromagnetic Ion-Cyclotron (EMIC) waves, which are generated in the overlapping region of the ring current and plasmasphere and drainage plumes (e.g., Thorne, 2010, and references therein). The disturbance of the Earth's magnetic field by the ring current may also lead to reversible changes of electron fluxes in the outer radiation belt via the so-called Dst effect (Kim and Chan, 1997).

Satellites operating in the inner magnetosphere are subject to failures related to the ambient space environment. MeV and multi-MeV radiation belt electrons can penetrate into spacecraft components, charging internal dielectric materials of the spacecraft (Reagan et al., 1983; Baker, 2000). This type of charging can result in the electric field that reaches breakdown levels, and the subsequent discharge can damage satellite electronics. Satellite anomalies coinciding with high levels of relativistic and ultrarelativistic electron fluxes have been reported, for example, by Baker et al. (1987, 1994) and Baker (2000). Injected during substorms and storms, 1–10 keV electrons can be responsible for charging the insulated surfaces of a satellite (Choi et al., 2011; Thomsen et al., 2013). The resulting electrostatic discharge can lead to satellite failures (e.g., Ganushkina et al., 2017, and references therein). For this reason, quantifying and modeling the dynamics of the charged particles in the inner magnetosphere is important not only for better understanding fundamental physical processes in the near-Earth space environment, but also for mitigating the negative impact of space weather on human infrastructure in space.

1.2 Dynamics of Charged Particles

1.2.1 Gyro, Bounce, and Drift Motion

Charged particles in the inner magnetosphere undergo three types of periodic motion: gyration about a geomagnetic field line, bounce motion along the field line between mirror points, and drift around the Earth. In this section, we briefly describe these types of periodic motion and consider them in the context of magnetic and electric fields in the inner magnetosphere, following, in general Northrop (1963); Lyons and Williams (1984); Baumjohann and Treumann (2012); Gurnett and Bhattacharjee (2017). For simplicity, we consider a case of non-relativistic charged particle motion in static electric and magnetic fields and simple geometry that can be extended to the case of relativistic particles and more sophisticated field configurations.

Gyro Motion

Motion of a non-relativistic charged particle in the static uniform magnetic and electric fields $\boldsymbol{B}$ and $\boldsymbol{E}$ can be described by the following equation in SI units:

$$m\frac{d\dot{\boldsymbol{r}}}{dt} = q(\dot{\boldsymbol{r}} \times \boldsymbol{B} + \boldsymbol{E}), \tag{1.1}$$

where $\boldsymbol{r}$ is the vector from some origin to the location of the particle of mass m and charge q, t is time, bold variables represent vectors in three-dimensional space, and the right-hand side is the Lorentz force. It can be shown that the magnetic field does not do work on a charged particle.

It is convenient to split equation (1.1) into two equations corresponding to the motion perpendicular and parallel to the magnetic field and denote variables parallel to the magnetic field with subscript $\parallel$ and perpendicular with subscript $\perp$. Under an assumption of $E = 0$ and zero velocity parallel to the magnetic field line, the solution of equation (1.1) represents gyro motion about the magnetic field line with the radius of gyration (also referred to as cyclotron radius)

$$\rho_c = \frac{mv_\perp}{|q|B}, \tag{1.2}$$

where $v_\perp$ is the velocity perpendicular to the field line. In the case of non-zero velocity parallel to $\boldsymbol{B}$, the trajectory of the particle is a helix.

Bounce Motion

Let us consider a case of inhomogeneous magnetic field converging to some axis of symmetry z. From the parallel component of equation (1.1), it can be shown that there

is a force F_z exerted upon a particle along z-axis:

$$F_z = -\frac{mv_\perp^2}{2B}\frac{\partial B_z}{\partial z}. \tag{1.3}$$

If the particle moves into the region of stronger magnetic field, force F_z acts in the direction opposite to particle motion, decreases its parallel velocity (simultaneously increasing perpendicular velocity so that the total kinetic energy is conserved), and tends to repel the particle from the region of the stronger magnetic field. When the parallel velocity reaches zero (this point is referred to as the mirror point) the particle changes its direction of travel and moves back until it again encounters the region of the converging field lines (if it exists). As a result, the particle becomes trapped in the magnetic field geometry between the mirror points.

Drift Motion

The helical motion of a charged particle can be approximated as gyration about the center (also referred to as the guiding center) that may move along or across a magnetic field line. This approximation is referred to as the guiding-center approximation. The trajectory of the guiding center can be obtained by averaging equation (1.1) over a period of gyration. The guiding center approximation is convenient for describing particle motion in the presence of the electric field and spatial and temporal variations of the magnetic field. It is also useful for practical purposes since gyro motion is typically so fast that it is impossible to measure particle gyro phase. The guiding center approximation can be used to derive equations for charged particle drifts (a type of motion where the particle changes its line of force during the motion) in electric and magnetic fields, among which the $\boldsymbol{E}\times\boldsymbol{B}$, gradient, and curvature drifts are most important for describing the dynamics of the plasma in the inner magnetosphere.

$\boldsymbol{E}\times\boldsymbol{B}$ drift Let us first consider the static uniform electric field with the only component perpendicular to the static uniform magnetic field $\boldsymbol{B}$: $E_\perp \neq 0$ and $E_\parallel = 0$. We also assume $v_\parallel = 0$. In this case, the guiding center will move in the direction perpendicular to $\boldsymbol{E}\times\boldsymbol{B}$ with velocity

$$\boldsymbol{v}_{E\times B} = \frac{\boldsymbol{E}\times\boldsymbol{B}}{B^2}. \tag{1.4}$$

Velocity $\boldsymbol{v}_{E\times B}$ is referred to as the $\boldsymbol{E}\times\boldsymbol{B}$ drift velocity. The $\boldsymbol{E}\times\boldsymbol{B}$ drift velocity does not depend on particle charge, mass, or energy. Thus, positively and negatively charged particles move in the same direction, and the $\boldsymbol{E}\times\boldsymbol{B}$ drift produces no net current.

Gradient drift Let us assume that there is no external electric field $\boldsymbol{E}$ and that the magnetic field is static and spatially non-uniform with a gradient in some direction.

As a particle moves in a region of stronger magnetic field, its gyro radius decreases, and the guiding center will move perpendicular to ∇B and $\boldsymbol{B}$, due to the differences in the gyro radii in the weaker and stronger magnetic fields. It can be shown that the velocity $\boldsymbol{v}_{\nabla B}$ of the gradient drift is expressed as follows:

$$\boldsymbol{v}_{\nabla B} = \frac{m v_{\perp}^2}{2qB^3} \boldsymbol{B} \times \nabla B. \tag{1.5}$$

Unlike the $\boldsymbol{E} \times \boldsymbol{B}$ drift, the gradient drift depends on particle energy and charge. The gradient drift produces a net current since positively and negatively charged particles move in opposite directions.

Curvature drift In the presence of the magnetic field line curvature, the particle experiences the centrifugal force $F_c = m v_{\parallel}^2 / R_c$, where R_c is the radius of curvature. The centrifugal force results in the motion of gyro center across the field lines with the velocity $\boldsymbol{v}_c$ referred to as curvature drift velocity:

$$\boldsymbol{v}_c = \frac{m v_{\parallel}^2}{q R_c^2 B^2} \boldsymbol{R}_c \times \boldsymbol{B}. \tag{1.6}$$

In a cylindrically symmetric field, $\nabla B = -(B/R_c^2)\boldsymbol{R}_c$, and the curvature drift velocity can be expressed as

$$\boldsymbol{v}_c = \frac{m v_{\parallel}^2}{qB^3} \boldsymbol{B} \times \nabla B. \tag{1.7}$$

The curvature drift depends on particle energy and charge, leading to the net current.

Drifts in the Inner Magnetosphere

$\boldsymbol{E} \times \boldsymbol{B}$, gradient, and curvature drifts play an important role in the dynamics of plasmasphere, ring current, and radiation belts. Dependence of gradient and curvature drift velocities on charge and energy leads to the generation of currents and to different drift orbits at different energies.

Electrons and ions in the plasmasphere experience only $\boldsymbol{E} \times \boldsymbol{B}$ drift, since their energy is so small that gradient and curvature drifts are negligible. A typical trajectory of a plasmaspheric particle is shown in Figure 1.2. The particle follows the lines of constant electrostatic potential. Near the Earth, the co-rotation electric field that points earthward is much stronger than the convection electric field, and the particle stays trapped on the closed equipotential lines. At higher radial distances, the dawn-to-dusk convection field takes over, and the particle moves earthward from the magnetotail. Such a particle resides on the open equipotential line and escapes the magnetosphere through the dayside magnetopause.

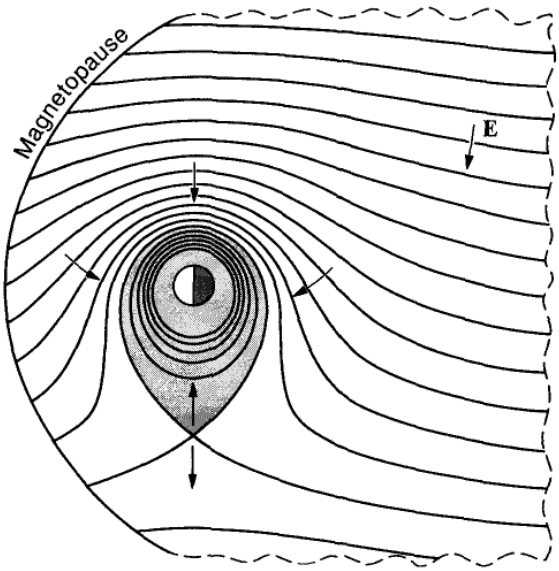

Figure 1.2: Lines of constant electrostatic potential, adapted from Baumjohann and Treumann (2012).

Energetic ring current electrons and ions undergo all three types of drift motion since gradient, curvature, and $\boldsymbol{E} \times \boldsymbol{B}$ drift velocities are comparable for a typical energy range of ring current particles. Figure 1.3 illustrates trajectories of an electron for energies 0.1, 1, 10, and 100 keV at 10 R_E. Similar to the trajectories of plasmaspheric particles, energetic electrons may reside on open or closed trajectories. The boundary that separates open and closed drift trajectories is referred to as the Alfvén boundary. As Figure 1.3 shows, the Alfvén boundary extends to higher radial distances for higher energy, so that the region of trapped particles widens with increasing energy. Note that the shape of the Alfvén boundary for 0.1, 1, and 10 keV electrons resembles that of the plasmaspheric particles. Subject to gradient and curvature drifts, ring current ions drift in the direction opposite to the electrons, resulting in the westward flowing electric current. Gradient and curvature drifts take over the $\boldsymbol{E} \times \boldsymbol{B}$ drift for radiation belt electrons, and their drift trajectories become more symmetric in local time (e.g., see Figure 1.3 for 100 keV electrons).

Figures 1.2 and 1.3 show electron trajectories for electric and magnetic fields that do not change in time. In practice, electric and magnetic fields in the magnetosphere are variable, and the most prominent changes occur during substorm and storm times. As a result, the Alfvén boundary expands and contracts, leading, respectively, to trapping of the particles residing on the open field lines or loss of the trapped particles into the magnetopause.

The bounce and drift motion require averaging over particle gyration and bounce, respectively. The averages, in turn, require separation of time scales of the correspond-

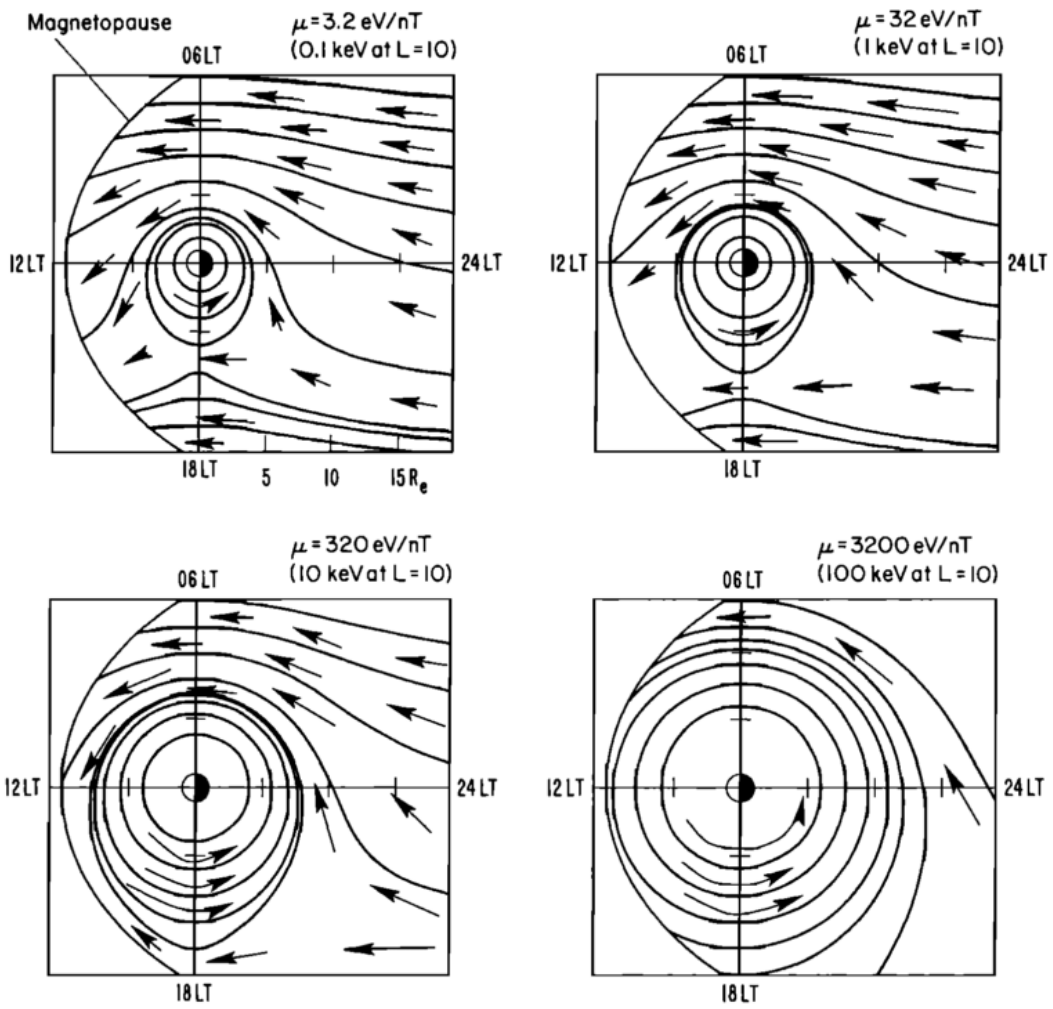

Figure 1.3: Electron drift trajectories for 0.1, 1, 10, and 100 keV at 10 R_E, adapted from Lyons and Williams (1984).

ing types of motion. For radiation belt particles, gyration, bounce, and drift are separated by a factor

$$|\varepsilon| = \left| \left\langle \frac{v}{\omega_c S} \right\rangle \right| \ll 1, \tag{1.8}$$

where ω_c is the cyclotron frequency, S is the arc length of a field line, and $\langle \cdot \rangle$ denotes the average over the entire particle orbit (Schulz and Lanzerotti, 1974). The condition (1.8) holds true if the particle gyroradius is much smaller compared to the length of the guiding field line. If $|\varepsilon| \gg 1$, the averaging over gyration and bounce cannot be performed, and particle motion must be described by applying numerical methods for tracing each particle individually.

1.2.2 Adiabatic Invariants

Each type of periodic motion of a charged particle in the inner magnetosphere – gyration about a magnetic field line, bounce motion between mirror points, and drift around the Earth – is associated with an adiabatic invariant. An adiabatic invariant stays approximately constant under slow variations of parameters of the system, compared to the period of the corresponding motion. A general expression of adiabatic invariant I is given by the following integral:

$$I = \oint p dq, \tag{1.9}$$

where p and q are conjugate momentum and position coordinates, and the integral is taken over a period of the corresponding periodic trajectory (Goldstein et al., 2002).

The first adiabatic invariant μ, which corresponds to the cyclotron motion of a particle, can be expressed as follows (Roederer, 2012):

$$\mu = \frac{p_\perp^2}{2m_0 B}, \tag{1.10}$$

where $p_\perp$ is the component of the momentum of the particle perpendicular to the magnetic field line, m_0 is the rest mass of the particle, and B is the magnitude of the magnetic field. It is convenient to consider $p_\perp$ as a function of pitch angle α – an angle between momentum and magnetic field:

$$p_\perp = p \sin\alpha, \tag{1.11}$$

where p is the total momentum of the particle. At the mirror point with magnetic field magnitude B_m, $p_\perp$ is equal to p, and the first adiabatic invariant (1.10) can be written as

$$\mu = \frac{p^2}{2m_0 B_m}. \tag{1.12}$$

If there is no electric field parallel to the magnetic field line at which the particle resides, p is conserved, and B_m is also conserved, as follows from the conservation of μ.

The second adiabatic invariant J is associated with particle bounce motion between the mirror points. It can be written as (Roederer, 2012):

$$J = 2 \int_{s'}^{s''} p_\parallel \, ds, \tag{1.13}$$

where $p_\parallel$ is parallel to the magnetic field line component of the particle momentum, and the integral is taken along the magnetic field line between mirror points s' and s''.

Expressing $p_{\|}$ in terms of p and α and using equations (1.10) and (1.12), the second adiabatic invariant J can be rewritten as

$$J = 2\frac{p}{\sqrt{B_m}} \int_{s'}^{s''} \sqrt{B_m - B(s)}\, ds, \tag{1.14}$$

where we assumed that p is conserved along the bounce path between the mirror points.

It is often convenient in practice to use modified second adiabatic invariant K instead of J:

$$K = \frac{J}{\sqrt{8m_0\mu}} = \int_{s'}^{s''} \sqrt{B_m - B(s)}\, ds. \tag{1.15}$$

Unlike adiabatic invariant J, K does not depend on particle energy and can be considered as a purely field-geometric quantity.

Subbotin and Shprits (2012) suggested a new adiabatic invariant V that is convenient for radiation belt modeling:

$$V = \mu \cdot (K + 0.5)^2. \tag{1.16}$$

A grid in V and K coordinates facilitates implementation of numerical schemes and improves accuracy, stability, and performance of radiation belt codes.

The third adiabatic invariant Φ is the magnetic flux enclosed by the drift path of a charged particle. A more intuitive form of the third adiabatic invariant is the L^* parameter (Roederer, 2012):

$$L^* = \frac{2\pi B_E R_E^2}{\Phi}, \tag{1.17}$$

where R_E is the Earth's radius, and B_E is the magnitude of the magnetic field at the Earth's surface at the geomagnetic equator. In a dipole field approximation

$$\Phi = \frac{2\pi B_E R_E^3}{R_0}, \tag{1.18}$$

where R_0 is the radial distance to a given point at the geomagnetic equator, and (1.17) becomes

$$L^* = \frac{R_0}{R_E} \equiv L, \tag{1.19}$$

where L is referred to as the L-shell. In the case of a non-dipole magnetospheric field, L^* can be considered as an L-shell in the field that is obtained by turning off external magnetic field sources and internal Earth's multipoles, leaving just the field of a pure dipole so slowly that Φ is conserved (Roederer, 2012).

1.2.3 Violation of Adiabatic Invariants and Main Loss and Acceleration Mechanisms in the Inner Magnetosphere

The presence of forces that act on the timescales comparable to gyro, bounce, or drift motion can lead to violation of adiabatic invariants. The timescales of the electron and proton motion are shown in Figure 1.4. For example, a 1 MeV electron at $L = 4$ completes one gyration in $\sim 10^{-4}$ seconds, one bounce in $\sim 10^{-1}$ seconds, and one drift in ~ 15 minutes. Mechanisms that are responsible for violation of the invariants and loss or acceleration of the particles are schematically illustrated in Figure 1.5. In this section, we briefly describe most important of these mechanisms.

ULF Waves

Ultra-Low Frequency (ULF) waves (1-10 mHz) play an important role in the energization and loss of radiation belt particles. ULF waves are strongly driven by interaction of the solar wind with the Earth's magnetosphere (e.g., McPherron, 2005). The waves are excited in response to velocity shear or solar wind pressure fluctuations (Ukhorskiy et al., 2006; Claudepierre et al., 2008, 2009). Strong correlation between the increase in the wave power and enhancement of relativistic electron flux has been reported by Baker et al. (1998) and Rostoker et al. (1998). Elkington et al. (1999, 2003) showed that magnetospheric electrons can be adiabatically transported and accelerated via drift-resonant interaction with ULF waves.

Drift resonance with global-scale ULF waves can violate the third adiabatic invariant while conserving the first and second invariants (e.g., Schulz and Lanzerotti, 1974). The drift resonance results in the stochastic radial displacement of trapped electrons that can be described by radial diffusion (Kellogg, 1959; Fälthammar, 1965; Schulz and Eviatar, 1969; Shprits et al., 2008a). In the case of net inward motion, particles move in the region of stronger magnetic field, and energy of the particles increases due to the conservation of the first adiabatic invariant. The outward radial motion leads, in contrast, to the decrease in energy. Shprits et al. (2006) and Turner et al. (2012) demonstrated that the outward radial diffusion can also lead to the loss of the electrons to the interplanetary medium during geomagnetically disturbed times when the magnetosphere is significantly compressed.

Chorus Waves

Chorus waves are coherent whistler-mode Very Low Frequency (VLF) electromagnetic emissions that are typically observed outside of the plasmasphere in two distinct bands below and above one half electron gyrofrequency, separated by a gap (Tsurutani and Smith, 1974). Often, an incoherent part of the spectrum in this frequency range out-

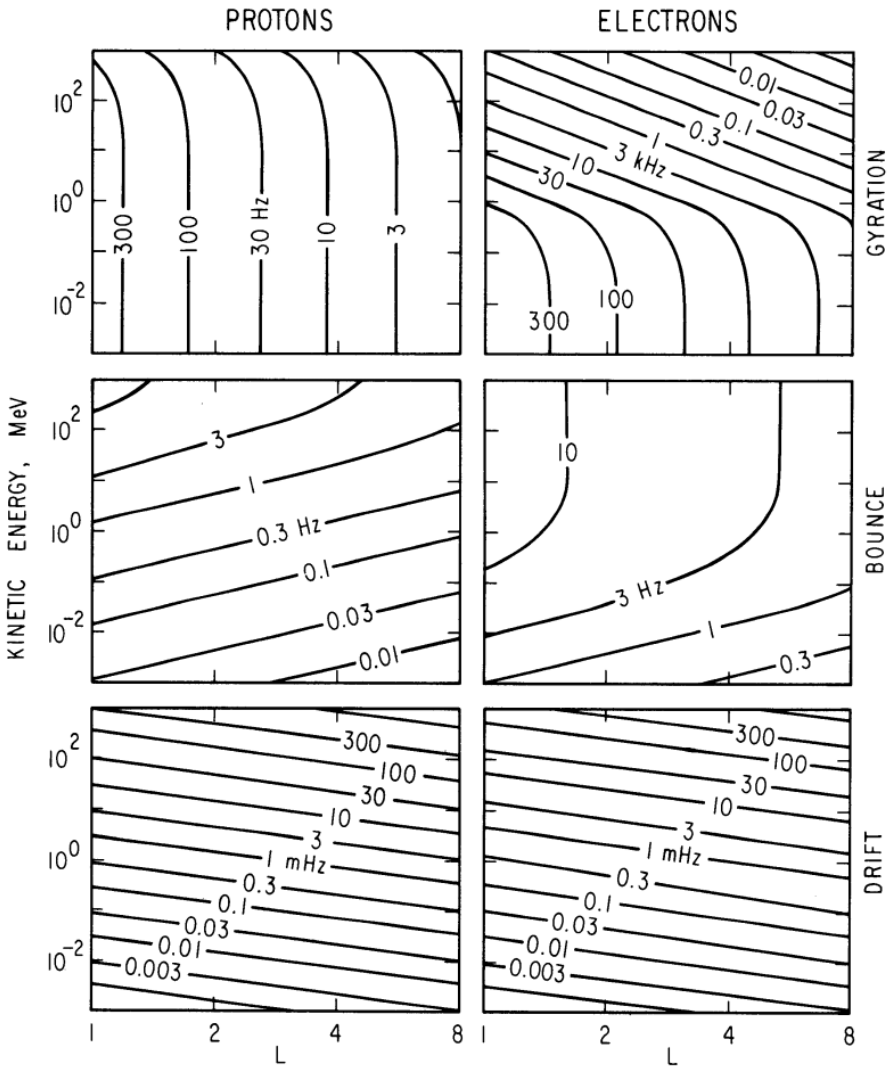

Figure 1.4: Contours of constant adiabatic gyration, bounce, and drift frequency for equatorially mirroring particles in the Earth's inner magnetosphere, adapted from Schulz and Lanzerotti (1974).

side of the plasmasphere is also referred to as chorus. The waves are excited by injections of energetic electrons from the plasma sheet into the inner magnetosphere (Hwang et al., 2007). The distribution of the wave power shows pronounced day-night asymmetry and dependence on L-shell and geomagnetic conditions (e.g., Wang et al., 2019, and references therein). The nightside chorus is confined within 15° geomagnetic latitude (Bortnik et al., 2007), while the dayside chorus can extend to 30° and beyond (Agapitov et al., 2015, 2018). The chorus waves below and above one half electron gyrofrequency are also referred to as lower- and upper-band chorus, respectively. Li et al. (2019) recently suggested that the initially excited single-band chorus wave suppresses electron anisotropy at medium energies and divides the anisotropy in two parts that excite lower- and upper-band emissions.

Resonant cyclotron interaction with chorus waves is an important mechanism of

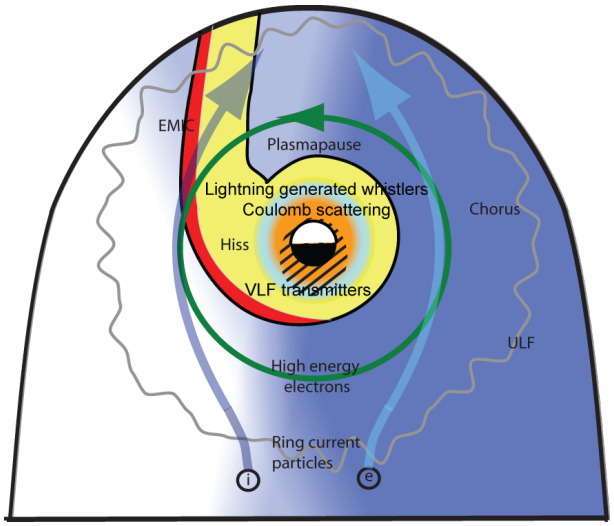

Figure 1.5: Illustration of dominant loss and acceleration processes in the Earth's inner magnetosphere during disturbed geomagnetic times. Yellow color denotes plasmasphere region. Gray and light blue lines correspond to ring current ion and electron drift trajectories. Green circular line denotes radiation belt electron trajectory. The curved gray line illustrates ULF waves that drive radial diffusion. Red color indicates the region where EMIC waves are present. In orange and blue circles, Coulomb collision and lightening-generated whistlers play important roles. Adapted from Shprits et al. (2008b).

electron pitch-angle scattering as well as local acceleration. The upper-band chorus can interact with ring current electrons, leading to diffuse auroral precipitation (Ma et al., 2016; Thorne et al., 2010; Ni et al., 2008, 2011, 2016). The lower-band chorus is responsible for the diffusion of radiation belt electrons in pitch angle that can ultimately remove trapped electrons from the belts (Albert, 2005; Horne and Thorne, 2003; Thorne et al., 2005), and the energy diffusion can lead to local electron acceleration to MeV energies (Summers et al., 1998; Horne and Thorne, 1998; Horne et al., 2005; Reeves et al., 2013; Shprits et al., 2008a).

Hiss Waves

Plasmaspheric hiss waves are incoherent whistler-mode emissions in the frequency range between hundreds of Hz and several kHz, which are predominantly present within the plasmasphere and dayside plasmaspheric plumes (Russell et al., 1969; Thorne et al., 1973). The waves are observed over a broad range of Magnetic Local Time (MLT) and are more intense on the dayside (e.g., Li et al., 2015). Typical hiss wave amplitudes depend on L-shell, magnetic latitude and geomagnetic activity (e.g., Spasojevic et al., 2015). Bortnik et al. (2008) showed that hiss can originate from chorus waves that propagate into the plasmasphere and form incoherent hiss emissions, avoiding Landau damping due to high cold electron density and low electron fluxes.

Chen et al. (2012) suggested that hiss waves can be amplified inside the plasmasphere since observed hiss wave power is higher than the wave power obtained from simulation of hiss wave formation from chorus emissions.

Hiss waves are a dominant mechanism of the radiation belt electron loss inside the plasmasphere. Lyons and Thorne (1973) showed that the quiet-time two-zone radiation belt structure can be explained by the balance between electron inward motion due to radial diffusion and hiss wave-induced loss into the atmosphere due to violation of the first adiabatic invariant via gyro-resonant interaction. Drozdov et al. (2015) demonstrated that the results of the long-term numerical simulation of the dynamics of relativistic electrons that included the parameterization of the hiss waves by Orlova et al. (2014) agree well with Van Allen Probes satellite observations. Pitch-angle scattering by plasmaspheric hiss is also responsible for the loss of ring current electrons (see electron lifetimes computed by Orlova et al. (2016)) and is incorporated in modern ring current models (e.g., Chen et al., 2015a,b; Yu et al., 2016).

EMIC Waves

EMIC (Electromagnetic Ion-Cyclotron) waves are left-hand polarized electromagnetic waves that occur in distinct bands separated by ion cyclotron frequencies. EMIC waves are observed in space and on the ground in the frequency range between 0.1 and 5 Hz (e.g., Bossen et al., 1976). EMIC wave generation mechanisms include excitation by anisotropic ring current protons in the overlapping region between the plasmasphere and ring current (Mauk and McPherron, 1980; Engebretson et al., 2007; Pickett et al., 2010) and fluctuations of the solar wind dynamic pressure (Usanova et al., 2008; McCollough et al., 2009). Due to the left-hand polarization, EMIC waves can interact only with electrons above some energy threshold when the electron overtakes the wave and senses the wave as right-hand polarized in the electron reference frame. Such energy threshold is also referred to as minimum resonant energy and is typically larger than 2 MeV (Cao et al., 2017).

EMIC waves are responsible for pitch-angle scattering of ultrarelativistic radiation belt electrons via cyclotron resonance (Thorne and Kennel, 1971; Horne and Thorne, 1998; Shprits et al., 2016). The waves can efficiently resonate with $<\sim 50^\circ$ electrons, leading to a narrowing of pitch-angle distribution of electron flux (Usanova et al., 2014). EMIC waves contribute significantly to the net loss of the ultrarelativistic electrons (Engebretson et al., 2015; Shprits et al., 2017; Drozdov et al., 2017b, 2019; Cervantes et al., 2019). EMIC waves played a leading role in the formation of the unusual three-zone radiation belt structure on 2 September 2012 (Baker et al., 2013b; Shprits et al., 2013b).

1.2.4 Phase Space Density and Fokker-Planck Equation

The large number of charged particles in the inner magnetosphere renders it impossible to trace a trajectory of each particle. Instead of considering each particle individually, it is more convenient to deal with particle distribution functions. One of such functions is Phase Space Density (PSD) – the number of particles per unit volume of the six-dimensional space that consists of three coordinates and three conjugate momenta (Walt, 1994).

Under an assumption of uniform distribution of particles in gyro, drift, and bounce phases (which is often true for radiation belt particles) and the existence of a phase mixing mechanism that sustains the uniform distribution after any small perturbation, we can reduce dimensionality of PSD and consider it as a function of three adiabatic invariants μ, J, and Φ. In this coordinate system, the evolution of PSD f due to the violation of adiabatic invariants can be described by the Fokker-Planck equation (Schulz and Lanzerotti, 1974):

$$\frac{\partial f}{\partial t} = \sum_{i=1}^{3} \frac{\partial}{\partial J_i} \left(\sum_{j=1}^{3} D_{J_i J_j} \frac{\partial f}{\partial J_j} \right), \tag{1.20}$$

where $J_1, J_2, J_3 = \mu, J, \Phi$, respectively, and $D_{J_i J_j}$ denote diffusion coefficients.

Equation (1.20) can be transformed into any coordinate system (I_1, I_2, I_3):

$$\frac{\partial f}{\partial t} = \frac{1}{G_{J \to I}} \sum_{i=1}^{3} \frac{\partial}{\partial I_i} \left(\sum_{j=1}^{3} G_{J \to I} \widetilde{D}_{I_i I_j} \frac{\partial f}{\partial I_j} \right), \tag{1.21}$$

where $G_{J \to I}$ is the Jacobian of the coordinate transformation, and $\widetilde{D}_{I_i I_j}$ are diffusion coefficients in coordinate system (I_1, I_2, I_3) (Haerendel, 1968):

$$\widetilde{D}_{I_i I_j} = \sum_{k,l=1}^{3} \frac{\partial I_i}{\partial J_k} D_{J_k J_l} \frac{\partial I_j}{\partial J_l}. \tag{1.22}$$

A convenient coordinate system for radiation belt modeling is (p, α, L^*). If we neglect processes that violate all three adiabatic invariants simultaneously and consider only processes that can violate only L^* and processes that violate only μ and J, equation (1.21) can be written in (p, α, L^*) coordinates as follows (Subbotin and Shprits, 2012):

$$\begin{aligned} \frac{\partial f}{\partial t} =& \frac{1}{G_{(\mu,J,L^*)}} \left. \frac{\partial}{\partial L^*} \right|_{\mu,J} G_{(\mu,J,L^*)} D_{L^*L^*} \left. \frac{\partial f}{\partial L^*} \right|_{\mu,J} + \\ & \frac{1}{G_{(p,\alpha,L^*)}} \left. \frac{\partial}{\partial p} \right|_{\alpha,L^*} G_{(p,\alpha,L^*)} \left(D_{pp} \left. \frac{\partial f}{\partial p} \right|_{\alpha,L^*} + D_{p\alpha} \left. \frac{\partial f}{\partial \alpha} \right|_{p,L^*} \right) + \\ & \frac{1}{G_{(p,\alpha,L^*)}} \left. \frac{\partial}{\partial \alpha} \right|_{p,L^*} G_{(p,\alpha,L^*)} \left(D_{\alpha\alpha} \left. \frac{\partial f}{\partial \alpha} \right|_{p,L^*} + D_{\alpha p} \left. \frac{\partial f}{\partial p} \right|_{\alpha,L^*} \right), \end{aligned} \tag{1.23}$$

where $D_{L^*L^*}, D_{pp}, D_{p\alpha}, D_{\alpha p}$, and $D_{\alpha\alpha}$ are bounce-averaged diffusion coefficients and Jacobians $G_{(\mu,J,L^*)}$ and $G_{(p,\alpha,L^*)}$ correspond to transformations from (μ, J, Φ) to (μ, J, L^*) and (p, α, L^*) coordinates, respectively. Expressions for $G_{(\mu,J,L^*)}$ and $G_{(p,\alpha,L^*)}$ can be found, for example, in Subbotin and Shprits (2012).

1.2.5 Modified Fokker-Planck Equation with Advection Terms

Equation (1.23) is applicable to radiation belt electrons (energies > 100 keV), since their drift trajectories are almost circular (see Section 1.2.1), and drift velocities are so high that inhomogeneities in drift phases are quickly smoothed out and the dependence of PSD on the drift phase can be neglected. Such an approximation is not valid for ring current electrons, as their azimuthal drift is much slower, and the radial extent of their drift trajectories depends strongly on local time, as shown in Figure 1.3. Shprits et al. (2015) extended equation (1.23) to ring current energies by including additional advection terms and taking into account dependence of PSD f on the drift phase:

$$\begin{aligned}\frac{\partial f}{\partial t} =& -v_\varphi \frac{\partial f}{\partial \varphi} - v_{R_0} \frac{\partial f}{\partial R_0} + \frac{1}{G_{(V,K,L^*)}} \frac{\partial}{\partial L^*} G_{(V,K,L^*)} D_{L^*L^*} \frac{\partial f}{\partial L^*} + \\ &+ \frac{1}{G_{(V,K,L^*)}} \frac{\partial}{\partial V} G_{(V,K,L^*)} \left(D_{VV} \frac{\partial f}{\partial V} + D_{VK} \frac{\partial f}{\partial K} \right) \\ &+ \frac{1}{G_{(V,K,L^*)}} \frac{\partial}{\partial K} G_{(V,K,L^*)} \left(D_{KV} \frac{\partial f}{\partial V} + D_{KK} \frac{\partial f}{\partial K} \right) - \frac{f}{\tau},\end{aligned} \tag{1.24}$$

where φ is MLT, R_0 is the radial distance at the geomagnetic equator, $G_{(V,K,L^*)} = -2\pi B_E R_E^2 \sqrt{8 m_0 V}/(K + 0.5)^3/L^{*2}$ is Jacobian of coordinate transformation from (μ, J, Φ) to (V, K, L^*) (Subbotin and Shprits, 2012), v_φ and v_{R_0} are bounce-averaged drift velocities, D_{VV}, D_{VK}, D_{KV}, and D_{KK} are bounce-averaged local diffusion coefficients, and τ is a lifetime parameter that can be used to specify electron loss to the atmosphere or interplanetary medium.

Let us briefly discuss some aspects of the application of the modified Fokker-Planck equation (1.24) with additional advection terms to modeling of the ring current and radiation belt dynamics. Equation (1.23), which is applicable only to radiation belt particles, has been discussed in detail by Shprits et al. (2008b, 2009); Subbotin and Shprits (2009); Subbotin et al. (2010); Kim et al. (2011); Subbotin et al. (2011a,b); Drozdov et al. (2017a), and Castillo et al. (2019).

Equation (1.24) describes the evolution of electron PSD and includes $\boldsymbol{E}\times\boldsymbol{B}$, gradient, and curvature drifts (the first two terms on the right-hand side), radial diffusion due to violation of the third invariant (third term), pitch-angle scattering and energy diffusion (fourth and fifth terms), and electron loss (sixth term). The advection term allows us to model the dynamics of ring current and radiation belt electrons simultaneously

and take into account coupling processes between these particle populations.

Modified adiabatic invariants V and K eliminate the need in interpolation of PSD between (μ, J, L^*) and (p, α, L^*) coordinates, as required by equation (1.23), since the radial diffusion portion of equation (1.23) must be solved using (μ, J, L^*) coordinates, the local diffusion portion must be solved using (p, α, L^*) coordinates, and a grid that is orthogonal in (μ, J, L^*) coordinates is not orthogonal in (p, α, L^*) coordinates (Subbotin and Shprits, 2009). A single grid in (V, K, L^*) coordinates is suitable for both radial and local diffusion modeling (Subbotin and Shprits, 2012). The grid eliminates the numerical error that is introduced by the interpolation. It also improves the performance of the numerical solution, as it requires a sufficiently smaller number of grid nodes for discretization of the cross-diffusion terms and avoids an interpolation step.

Adiabatic (reversible) changes in electron flux which are observed in situ can be included in equation (1.24) by remapping PSD if L^*, as a function of position and pitch-angle, changes due to adiabatic expansion or contraction of the geomagnetic field. Remapping of the PSD can be implemented as a simple one-dimensional interpolation of PSD as a function of L^* for constant φ, V, and K.

Diffusion coefficients D_{VV}, D_{VK}, D_{KV}, and D_{KK} are generally dependent on MLT, and equation (1.24) takes into account pitch-angle scattering and acceleration processes that are localized in MLT (e.g., due to resonance with hiss, chorus, or EMIC waves). To calculate the diffusion coefficients, MLT-dependent wave models are required (Spasojevic et al., 2015; Wang et al., 2019).

Simultaneous modeling of ring current and radiation belt electrons requires the use of an energy-dependent radial diffusion coefficient. Ring current electrons may not be able to complete a full drift orbit, as they are lost into the interplanetary medium (see Section 1.2.1). For such particles, the radial diffusion term should be ignored by, for example, zeroing out the radial diffusion coefficient for corresponding energy. Typical parameterizations of $D_{L^*L^*}$ were developed for radiation belts (Brautigam and Albert, 2000; Ozeke et al., 2014), and their extension to lower energies has to be made with care.

Drift velocities v_φ and v_{R_0} require specification of electric and magnetic fields in the whole computational domain. The convection electric field and magnetic field can be specified using empirical models (e.g., Volland, 1973; Stern, 1975; McIlwain, 1986; Weimer, 1996, 2001, 2005; Tsyganenko, 1989, 1995, 2002; Tsyganenko and Sitnov, 2005, 2007) or self-consistent modeling (e.g., Chen et al., 2006, 2015b; Toffoletto et al., 2003; Lemon et al., 2004). Global validation of accuracy of the models is complicated by a very limited number of satellite observations in the inner magnetosphere at any given moment, and the drift velocities are very likely a significant source of uncertain-

ties of the model (1.24). There is also ample evidence that a localized electric field can be responsible for rapid substorm- and storm-time electron transport in the inner magnetosphere (e.g., Lejosne et al., 2018; Gabrielse et al., 2012). There is currently a lack of empirical models of the localized electric fields that may also increase errors in the electron drift velocities during geomagnetically disturbed times.

1.3 Objectives and Structure of the Dissertation

The scope of the dissertation is:

- quantification of physical processes that control transport, loss, and acceleration of the radiation belt and ring current electrons;
- improvement of existing codes for modeling the evolution of radiation belt and ring current electrons;
- development of new tools for prediction of the dynamics of ring current electrons using sparse satellite measurements.

The four-dimensional Versatile Electron Radiation Belt code (VERB-4D code) is used as a main tool in the dissertaion. The VERB-4D code has been developed by Shprits et al. (2015) to solve the modified Fokker-Planck equation (1.24) with advection terms. The code has already been applied to the radiation belt electron dynamics during the 17 March 2013 geomagnetic storm, and the simulation results showed good agreement with Van Allen Probes observations for > 200 keV electrons.

In this dissertation, the following questions are addressed:

1. How do errors of numerical schemes affect the accuracy of ring current and radiation belt modeling?
2. How sensitive is the model of the ring current electron dynamics to the input parameters and empirical models?
3. Which physical processes control the dynamics of ring current electrons inside geostationary orbit during storm times?
4. Can the uncertainty in model prediction of the ring current electron dynamics be decreased by using the information from sparse in-situ measurements of electron flux?
5. Which physical mechanisms control ultrarelativistic electron precipitation from the outer radiation belt into the Earth's atmosphere?

To address question 1, we split the VERB-4D code into low-dimensional convection and high-energy diffusion parts. A set of analytical solutions of the low-dimensional problems is used to study accuracy and stability of the numerical schemes implemented in the code. We modeled electron transport from the plasma sheet to Geostationary Orbit (GEO) under quiet geomagnetic conditions and analyzed the influence of the order of the scheme for the convection equation on the results of simulations. The results are presented in Chapter 2, which is based on the publication Aseev et al. (2016).

To address questions 2 and 3, we extended the VERB-4D code to ring current energies and modeled the geomagnetic storm that occurred on 17 March 2013. We used a statistical model of electron flux at the spatial outer boundary at GEO developed by Denton et al. (2015) to estimate uncertainty levels of the numerical solution associated with errors in boundary conditions. To validate the model, the simulation results are compared with Van Allen Probes particle observations. The model parameters are varied to study the sensitivity of the model to the errors in input parameters. We also investigated the contribution of different physical processes to the dynamics of ring current electrons within GEO. The results are summarized in the publication-based Chapter 3 (Aseev et al., 2019).

To address question 4, we developed a data-assimilative code that blends together a two-dimensional model of ring current electron transport (advection portion with parameterized loss term in equation (1.24)) and Van Allen Probes flux observations by means of the Kalman filter. The synthetic data are used to understand whether the Kalman filter can correct uncertainties in model predictions due to errors in electron lifetimes, electric fields, and boundary conditions, using sparse satellite measurements. We studied the capabilities of the Kalman filter to correct model predictions in the MLT sectors in which satellite data are unavailable. The Kalman filter is also used to identify missing physical processes in the model. The results are presented in Chapter 4 that is based on the publication Aseev and Shprits (2019).

To address question 5, we computed ultrarelativistic electron PSD as a function of three adiabatic invariants, using Van Allen Probes observations. We analyzed the PSD as a function of L^* for constant μ and K and identified local minimums in PSD L^*-profiles. Such local minimums cannot be created by radial diffusion and are a signature of localized loss of electrons from the outer belt. We analyzed the correlation between the formation of the local minimums, ground observations of the EMIC waves, and narrowing of pitch-angle distributions of electron flux measured in situ by Van Allen Probes to understand if EMIC waves can be responsible for scattering of ultrarelativistic electrons into the Earth's atmosphere. The results are presented in the

publication-based Chapter 5 (Aseev et al., 2017).

In chapter 6, we summarize results of the dissertation and discuss future work.

Chapter 2

Numerical Applications of the Advective-Diffusive Codes for the Inner Magnetosphere

Published as:
Aseev, N. A., Shprits, Y. Y., Drozdov, A. Y., and Kellerman, A. C., 2016. Numerical Applications of the Advective-Diffusive Codes for the Inner Magnetosphere. *Space Weather*, 14(11):993–1010. doi:10.1002/2016SW001484

Abstract

In this study, we present analytical solutions for convection and diffusion equations. We introduce analytical solutions for the one-dimensional convection equation, two-dimensional convection problem, and one- and two-dimensional diffusion equations. Using obtained analytical solutions, we test the four-dimensional Versatile Electron Radiation Belt code (VERB-4D code) that solves the modified Fokker-Planck equation with additional convection terms. The ninth-order upwind numerical scheme for the one-dimensional convection equation shows much more accurate results than the results obtained with the third-order scheme. The universal limiter eliminates unphysical oscillations generated by high-order linear upwind schemes. Decrease in the spatial step leads to the convergence of a numerical solution of the two-dimensional diffusion equation with mixed terms to the analytical solution. We compare the results of the third- and ninth-order schemes applied to magnetospheric convection modeling. The results show significant differences in electron fluxes near geostationary orbit when different numerical schemes are used.

2.1 Introduction

The last decades gave rise to the swift development of codes modeling the near-Earth space environment. Ring current and radiation belt codes have particular importance since the codes provide predictive capabilities for the extremely variable environment where many satellites operate and can be damaged by charged particles penetrating satellite shielding.

Numerical details of existing ring current and radiation belt codes are rarely discussed in the literature, yet they are very important for the accuracy of simulation results and computational time requirements. Most of the codes are validated by comparison with data, while the basic validation of the accuracy of numerical methods has not been done or discussed in the literature. Inaccurate or unstable numerical methods may lead to significant errors, complicate the direct validation of the codes with data, or render the comparison with data meaningless. Accurate and stable numerical methods allow us to rely on results of the codes and even explain new physical phenomena.

The goal of this work is to present a convenient set of analytical solutions for testing of advective-diffusive codes for the inner magnetosphere and to demonstrate the fundamental features of the numerical schemes implemented in the VERB-4D code (Shprits et al., 2015). The VERB-4D code is an advective-diffusive code modeling of the dynamics of the Earth's electron radiation belts. Presented in this study are numerical methods and test results of these methods that can be extended to any advective-diffusive code for the Earth's inner magnetosphere.

The Earth's radiation belts consist of electrons and ions (mostly protons) trapped by the Earth's magnetic field. The energetic and relativistic electrons (from ≈ 100 to 900 keV) usually form a two-zone structure, while >900 keV electrons are only present in the outer zone (Fennell et al., 2015). The inner zone is located at radial distances between 1 and 2 R_E, where R_E denotes the Earth's radius, and is very stable (Williams and Smith, 1965; Pfitzer and Winckler, 1968). The outer zone can be extremely variable, and electron dynamics in the outer zone depends significantly on geomagnetic conditions (Rothwell and McIlwain, 1960; Craven, 1966). Electron flux between the inner and outer zones is usually several orders of magnitude lower than the flux in the belt zone, but it can be refilled or may even form a new belt (Baker et al., 2004; Shprits et al., 2011). This gap between the belts is referred to as a slot region (Russell and Thorne, 1970; Vernov et al., 1969).

Relativistic electrons in the radiation belts undergo three different types of periodic motion: gyration around geomagnetic field lines, bouncing between the mirror points,

and azimuthal drift around the Earth. Adiabatic invariants μ, J, and Φ are attributed to these types of motion, respectively (Kellogg, 1959; Roederer, 2012; Schulz and Lanzerotti, 1974; Walt, 1994). The invariants stay approximately constant when changes in the magnetic field happen slowly in comparison with the time scale of corresponding periodic motion. Thus, once being trapped, the particle will remain trapped forever under slow variations of environmental parameters. However, resonant interactions with plasma waves can violate the invariants if the characteristic disturbance time is comparable with the time scale of the corresponding type of periodic motion. Since the number of particles in the radiation belts is large, we can often describe particle behavior collectively in terms of Phase Space Density (PSD). Assuming that waves in the belts are incoherent at various radial distances and Magnetic Local Time (MLT) and that amplitudes of waves are much smaller than the background field, wave-particle interactions can be approximated as a diffusion process (Kennel and Engelmann, 1966; Lerche, 1968).

Diffusion processes in the radiation belts can be divided into radial and local diffusion. Radial diffusion (Kellogg, 1959; Fälthammar, 1965; Schulz and Eviatar, 1969) describes the violation of the invariant Φ by resonant interactions with Ultra-Low Frequency (ULF) waves (Lanzerotti and Morgan, 1973; Brautigam and Albert, 2000). It leads to inward or outward radial motion of charged particles, depending on the sign of PSD gradient. Inward radial diffusion is a dominant mechanism of electron energization (Hudson et al., 2001; Elkington et al., 2003) due to betatron and Fermi acceleration, and outward radial diffusion can lead to the loss driven by magnetopause shadowing (Shprits et al., 2006, 2008b). Such processes can be accompanied by two-dimensional local diffusion (Kennel and Engelmann, 1966; Lerche, 1968) that is responsible for the violation of μ and J. Pitch-angle diffusion scatters electrons into the loss cone and forces them to precipitate into the Earth's atmosphere. In turn, energy diffusion produces acceleration of electrons. Interactions with plasmaspheric hiss waves, lightning-generated whistlers, and anthropogenic Very Low Frequency (VLF) waves are responsible for the pitch-angle scattering inside the plasmasphere and produces only negligible energy diffusion. Acting outside the plasmasphere, chorus waves can be also responsible for the pitch-angle scattering. Local electron acceleration mostly happens on the night side due to the interactions with chorus waves. Interactions of high-energy electrons with Electromagnetic Ion-Cyclotron (EMIC) waves can also produce electron loss (Thorne and Kennel, 1971; Kersten et al., 2014; Usanova et al., 2014) which is most efficient at multi-MeV energies (Shprits et al., 2013a; Drozdov et al., 2015). Radial diffusion and local diffusion are reviewed in detail in Shprits et al. (2008a,b).

Another important process is magnetospheric convection (Dungey, 1961; Axford, 1969). The solar wind generates an electric field directing from dawn to dusk inside the magnetosphere (Schulz and Lanzerotti, 1974) and transports electrons from the plasma sheet inward by the $\mathbf{E} \times \mathbf{B}$ drift. Storm time injections of low-energy plasma sheet electrons provide seed population for the radiation belts and are crucial for the dynamics of ring current and radiation belts during disturbed geomagnetic conditions. For MeV electrons, advection due to gradient-curvature drift dominates over $\mathbf{E} \times \mathbf{B}$ transport.

The modified three-dimensional Fokker-Planck equation comprises both radial and local diffusion and describes the evolution of PSD. Originally, it is written in the (μ, J, Φ) coordinate system, but more convenient systems can be applied to the equation, using the corresponding transformation of coordinates and diffusion coefficients (Haerendel, 1968; Schulz and Lanzerotti, 1974). The Fokker-Planck equation can be supplemented by additional advection (often referred to as "convection") terms to take into account radial and azimuthal convection (Shprits et al., 2015).

The first code modeling the dynamics of the electron radiation belts was the Salammbô code (Beutier and Boscher, 1995). The original version of the code solved the three-dimensional Fokker-Planck equation in terms of adiabatic invariants. The Salammbô code incorporates radial diffusion, cosmic ray albedo neutron decay, pitch-angle scattering by plasmaspheric hiss, and Coulomb collisions. Unfortunately, details on numerical implementation and boundary conditions of the first version of the code were not provided in publications. The Versatile Electron Radiation Belt code (VERB code) (Shprits et al., 2008b, 2009; Subbotin and Shprits, 2009; Subbotin et al., 2010, 2011a,b) has been developed to solve the three-dimensional Fokker-Planck equation and takes into account radial, pitch-angle, energy, and mixed diffusion, and additional electron sources or sinks. The code utilizes the two-grid approach (Subbotin and Shprits, 2009). According to this approach, two different grids are used for the solution of radial and local diffusion equations. A variety of codes was developed on the basis of similar approaches (e.g., the DREAM3D code (Tu et al., 2013), the STEERB code (Zhang et al., 2014), and the BAS code (Glauert et al., 2014)). Though the two-grid approach is convenient for the formulation of boundary conditions, the approach may lead to an increase in computational time, possible computational instabilities, and numerical errors due to inaccuracies of the interpolation. To avoid the interpolation, a new set of variables was introduced (Subbotin and Shprits, 2012), and the one-grid approach was implemented in the VERB-4D code.

A number of ring current codes have been developed for the convection of electrons and ions. The RAM code (Jordanova et al., 1996, 1997) and the HEIDI code (Liemohn

et al., 2001; Ilie et al., 2012) solve the bounce-averaged kinetic equation. The equation describes the evolution of PSD as an advection process in coordinates consisting of radial distance, geomagnetic east longitude, kinetic energy, and cosine of the equatorial pitch angle. Such loss mechanisms as charge exchange, Coulomb collisions, wave-particle interactions, and absorption in the atmosphere are also taken into account. The RBE code (Fok et al., 2008) is a kinetic model that calculates the temporal variation of PSD of energetic electrons. The RBE code utilizes particle drifts, local diffusion due to wave-particle interactions, and the loss to the loss cone. The IMPTAM code (Ganushkina et al., 2006, 2012) is an advective code that follows the distributions of ions and electrons. Charge exchange with neutral hydrogen in the upper atmosphere, Coulomb collisions, and convective outflow through the magnetopause are included into the IMPTAM code.

A more comprehensive inner and middle magnetospheric model, the RCM code (Toffoletto et al., 2003), uses a many-fluid formalism to describe adiabatically drifting isotropic particle distributions in a self-consistently computed electric field and specified magnetic field. The successor of the RCM code, the RCM-E code (Lemon et al., 2004), is a combination of the RCM code and magneto-friction equilibrium solver (Hesse and Birn, 1993). The incorporated equilibrium solver provides a magnetic field model that is consistent with the computed pressures.

Complications of the mathematical description of the radiation belt dynamics results in application of numerical methods and techniques to the solution of high-dimensional problems. The difference in the associated time scales allows us to neglect mixed-diffusion terms corresponding to the third invariant and split the solution of the three-dimensional Fokker-Planck equation into independent solutions of the one-dimensional radial diffusion and the two-dimensional local diffusion equations. Convection terms can be added to the split three-dimensional Fokker-Planck equation as extra fractional steps. The separation into physical processes makes it possible to implement the numerical schemes, describing independently each of the processes. Therefore, the most efficient and accurate schemes can be chosen for each physical process characterizing ring current and radiation belt dynamics.

Inner magnetospheric codes usually approximate convection terms in smooth regions using the Lax-Wendroff scheme, which is second-order accurate in space and time (e.g., RAM code (Jordanova et al., 1996), HEIDI code (Liemohn et al., 2004), and RBE code (Fok et al., 1993)). (The order of a numerical scheme is the rate of convergence of the numerical solution to the exact solution, when the discretization step decreases (Godunov and Ryabenkii, 1987).) The codes switch to the first-order scheme in the presence of strong gradients, where this scheme behaves better. For diffusion simu-

lations, the most common are first- or second-order accurate in time and second-order accurate in space numerical schemes (e.g., DREAM3D code, STEERB code, BAS code, and VERB code).

In this work, we present convenient analytical solutions for testing of codes which model the ring current – radiation belt system in the inner magnetosphere. The solutions are presented for the one-dimensional convection equation describing either radial or azimuthal convection; the two-dimensional convection equation taking into account both radial and azimuthal convection; the one-dimensional diffusion equation simulating radial diffusion and the two-dimensional diffusion equation modeling local diffusion with mixed pitch-angle and energy terms. We present results of testing of implemented in the VERB-4D code numerical schemes on the basis of the provided analytical solutions. We study here how the accuracy of numerical schemes affects results of simulations. Comparison of the third- and ninth-order schemes applied to idealized quiet-time magnetospheric convection simulations is also presented.

The structure of the paper is organized as follows. In Section 2.2, we briefly describe the mathematical formulation of the modified Fokker-Planck equation and the numerical algorithms that constitute the core of the VERB-4D code. Section 2.3 is devoted to the convenient analytical solutions for code testing and to the results of some tests that have been performed with the VERB-4D code. The influence of the order of numerical schemes on magnetospheric convection modeling is discussed in Section 2.4. The main conclusions are presented in Section 2.5. Appendix 2.A describes the Courant-Friedrichs-Lewy condition, and Appendix 2.B contains details on the universal limiter which eliminates unphysical oscillations of the high-order linear numerical schemes for the convection equation.

2.2 Approach of the VERB-4D Code

The VERB-4D code solves the modified Fokker-Planck equation with additional convection terms, following the approach of Subbotin and Shprits (2012) and Shprits et al. (2015):

$$\begin{aligned}\frac{\partial f}{\partial t} = &-v_{\varphi}\frac{\partial f}{\partial \varphi} - v_{R_0}\frac{\partial f}{\partial R_0} + \frac{1}{G_{(V,K,L^*)}}\frac{\partial}{\partial L^*}G_{(V,K,L^*)}D_{L^*L^*}\frac{\partial f}{\partial L^*} + \\ &+ \frac{1}{G_{(V,K,L^*)}}\frac{\partial}{\partial V}G_{(V,K,L^*)}\left(D_{VV}\frac{\partial f}{\partial V} + D_{VK}\frac{\partial f}{\partial K}\right) + \\ &+ \frac{1}{G_{(V,K,L^*)}}\frac{\partial}{\partial K}G_{(V,K,L^*)}\left(D_{KV}\frac{\partial f}{\partial V} + D_{KK}\frac{\partial f}{\partial K}\right) - \frac{f}{\tau},\end{aligned} \tag{2.1}$$

where L^*, K, and V are adiabatic invariants, $L^* = 2\pi B_E R_E^2/\Phi$, R_E is the Earth's radius, B_E is the field at the geomagnetic equator at the Earth's surface, $K = J/\sqrt{8m_0\mu}$,

m_0 is particle rest mass, $V = \mu \cdot (K + 0.5)^2$, $f(\varphi, R_0, V, K)$ is the phase space density, t represents time, φ is MLT, R_0 is the radial distance from the center of the Earth at the geomagnetic equator, τ is the electron lifetime related to scattering into the loss cone and magnetopause shadowing, v_φ and v_{R_0} are bounce-averaged drift velocities, $D_{L^*L^*}$, D_{VV}, D_{VK}, D_{KV}, and D_{KK} are bounce-averaged diffusion coefficients, and $G_{(V,K,L^*)} = -2\pi B_E R_E^2 \sqrt{8 m_0 V}/(K + 0.5)^3/L^{*2}$ is the Jacobian of coordinate transformation from (μ, J, Φ) to (V, K, L^*) coordinates.

The VERB-4D code uses the operator splitting technique (Marchuk, 1990; Press et al., 1992; Subbotin and Shprits, 2009) that separates one-dimensional convection in MLT (first term of the right-hand side), one-dimensional convection in R_0 (second term), one-dimensional radial diffusion (third term), and two-dimensional local diffusion (fourth and fifth terms). A loss term (last term) is divided between processes in accordance with the nature of the loss (e.g., loss to the magnetopause is added after the convection step of calculations; loss to the loss cone is added to local diffusion).

The VERB-4D code solves equation (2.1) for PSD using only one grid in the (φ, R_0, V, K) coordinate system. While this system is convenient for modeling of convection and local diffusion processes, radial diffusion must be simulated in (φ, L^*, V, K) coordinates. To model radial diffusion, the VERB-4D code receives values of L^* as an input. The values of L^* are computed on the same (φ, R_0, V, K) grid, using a realistic magnetic field model, and updated each time when configuration of the magnetic field changes. Adiabatic changes due to compression and expansion of the magnetic field are implicitly taken into account, using one-dimensional cubic spline interpolation of PSD (Press et al., 1992) from previous to current values of L^* for all (φ, V, K) values if L^* changes.

Time and space discretization methods can be applied for low-dimensional subproblems which arise from the application of the operator splitting technique. Let us describe them in more detail. The VERB-4D code solves one-dimensional convection equation using the ninth-order upwind scheme. (Upwind schemes take into account the direction of the convective flow by calculating spatial derivative upstream (Godunov and Ryabenkii, 1987).) Godunov (1959) showed that high-order (higher than first order) linear numerical schemes for the one-dimensional convection equation suffer from artificial numerical oscillations leading to unphysical results. To eliminate the unphysical oscillations, the universal limiter is applied to high-order numerical schemes in the VERB-4D code (see Appendix 2.B and (Leonard, 1991; Leonard and Niknafs, 1991) for more details). The universal limiter detects regions of unphysical oscillations and decreases the accuracy of the scheme to the first order in such regions. The universal limiter can produce slight amplitude error near points of local extrema

of the transported profile, where changes in monotonicity are mistakenly recognized as short-wavelength unphysical oscillations. The discriminator developed by Leonard and Niknafs (1991) is also implemented in the VERB-4D code to diminish this amplitude error. Time discretization of the one-dimensional convection equation is explicit (the value of the function at each spatial grid point can be explicitly calculated from the previous time step), which makes implemented schemes conditionally stable. The conditional stability requires the Courant-Friedrichs-Lewy condition to be satisfied, imposing restrictions on the ratio of time step to spatial step (see Appendix 2.A).

The one-dimensional diffusion equation is solved implicitly (numerical solution at the current time step is calculated involving information of the modeled system at both current and previous time steps (Godunov and Ryabenkii, 1987)). The implicit scheme is unconditionally stable for any time step and has first-order accuracy in time and second-order accuracy in space. Such time and space discretization schemes require the inversion of tridiagonal matrix at each time step. The tridiagonal matrix algorithm (Press et al., 1992) is used in the VERB-4D code to solve corresponding system of linear equations. The algorithm has linear complexity in the number of spatial nodes, which makes this algorithm computationally efficient. The discretization of the two-dimensional diffusion equation that includes mixed-diffusion terms is also fully implicit, unconditionally stable, and has first-order accuracy in time and second-order accuracy in space. A direct solver implemented in LAPACK (Anderson et al., 1999) is used for a system of linear equations resulting from the space discretization of the second order.

The computational grid of the VERB-4D code is uniform in φ and R_0 coordinates, logarithmic in V coordinates, and either uniform or logarithmic in K coordinates. Since implemented schemes for convection equation are conditionally stable, the input time step is decreased automatically (if necessary) at the convection fractional steps to satisfy the Courant-Friedrichs-Lewy condition. The input time step is not changed at the diffusion fractional steps due to unconditional stability of corresponding schemes. This selective decrease in the time step reduces the total computational time.

2.3 Theoretical Framework for Testing of Inner Magnetospheric Models

To demonstrate stability, accuracy, and advantages of the techniques implemented in the VERB-4D code, we separate corresponding blocks in the code in order to investigate only the behavior of chosen numerical schemes. We use artificial analytical profiles as initial and boundary conditions in accordance with the physical nature of

simulated processes. We should note that all tests show properties of schemes in simple cases, since artificial profiles are obtained on the basis of strong assumptions (e.g., constant velocities or diffusion coefficients). The analytical solutions are useful for understanding the behavior of the schemes for smooth initial profiles and profiles with discontinuities or high gradients. Some results of testing of the numerical schemes implemented in the VERB-4D code along with utilized analytical solutions are presented in this section.

2.3.1 One-Dimensional Convection

In the simplest form, the one-dimensional convection equation with constant velocity can be written as

$$\frac{\partial f}{\partial t} + u\frac{\partial f}{\partial x} = 0, \tag{2.2}$$

where $f(x,t)$ is the distribution function, $t \in [0,\infty)$ represents time, $x \in (-\infty,+\infty)$ is the space coordinate, and $u = \text{const}$ is the flow velocity. The solution of equation (2.2) can be constructed in the following way (Evans, 1998):

$$f(x,t) = \widetilde{f}(x-ut), \tag{2.3}$$

where $\widetilde{f}$ is an arbitrary smooth function.

The one-dimensional convection equation (2.2) can be complemented with initial and boundary conditions to describe special physical cases. For instance, the solution of equation (2.2) with the initial condition

$$f(x,0) = h(x), \tag{2.4}$$

where $h(x)$ is a known function, is

$$f(x,t) = h(x-ut). \tag{2.5}$$

If the one-dimensional convection equation (2.2) is considered on the interval $x \in [a,b]$, where $a,b < \infty$, and is complemented only with the periodic boundary conditions

$$f(a,t) = f(b,t), \tag{2.6}$$

the solution of equation (2.2) is

$$f(x,t) = \widetilde{f}(x-ut), \tag{2.7}$$

where $\widetilde{f}$ is an arbitrary periodic function satisfying the following relation: $\widetilde{f}(b-ut) = \widetilde{f}(a-ut)$.

The choice of proper initial conditions for the one-dimensional convection equation (2.2) allows us to validate a particular numerical scheme. The step function is a basic test of monotonicity (monotonic profiles should stay monotonic) and reproduction

of discontinuities (Leonard, 1991). One period of squared sine function represents a relatively smooth profile with a continuously turning gradient and single local maximum (Leonard, 1991; Sweby, 1984). A semi-ellipse initial function (Zalesak, 1987) may force the numerical scheme to generate significant waviness near large gradients of the profile.

To test the block of the VERB-4D code modeling one-dimensional convection, let us consider the one-dimensional convection equation (2.2) with constant velocity and the periodic boundary conditions (2.6). In this set of tests, we study the influence of spatial resolution on accuracy of results, unphysical oscillations generated by the high-order linear upwind schemes, and elimination of such oscillations using the universal limiter. We do not utilize here the discriminator decreasing the amplitude error near local extrema. The particular solution of the general form (2.7) can be specified by the choice of initial conditions. Using dimensionless parameters, we set velocity $u = 1$ and left and right spatial boundaries $a = 0$ and $b = 7$, respectively. The initial profile consists of a step function, squared sine and semi-ellipse profiles. We run the VERB-4D code to calculate the profile at end time $T = 98$, corresponding to 14 rotations of the profile (one rotation has the length $b-a$). Spatial grids contain $N_x = 30$ and 70 nodes in our simulations. To guarantee the stability of the numerical scheme, we set up time step $\Delta t = 0.5\Delta x/u$ satisfying the Courant-Friedrichs-Lewy condition (see Appendix 2.A), where Δx is the spatial step of the grid. Simulation results are shown in Figure 2.1.

Figure 2.1a shows analytical and numerical solutions for grid size $N_x = 30$ if the universal limiter is not used. The green, red, and blue lines designate the analytical solution and numerical solutions obtained by using the third-order scheme and ninth-order scheme, respectively. The ninth-order scheme can reconstruct the general shape of sine and semi-ellipse, while the shape of the step function is not yet reproduced. The violation of monotonicity is observed as negative values produced by the ninth-order numerical scheme. The third-order scheme has very strong numerical diffusion and is not able to reproduce even the general shape of the analytical profile. The application of the universal limiter (Figure 2.1c) eliminates unphysical non-monotonic behavior, but numerical diffusion becomes more significant for both schemes. The increase in grid size to $N_x = 70$, without using the universal limiter (Figure 2.1b), demonstrates almost perfect reconstruction of sine and semi-ellipse profiles for the ninth-order scheme. However, the profile experiences unphysical oscillations at constant values of the analytical solution. The third-order scheme still suffers from large amplitude error, numerical diffusion, and unphysical oscillations. The universal limiter removes the oscillations (Figure 2.1d) for both third- and ninth-order schemes,

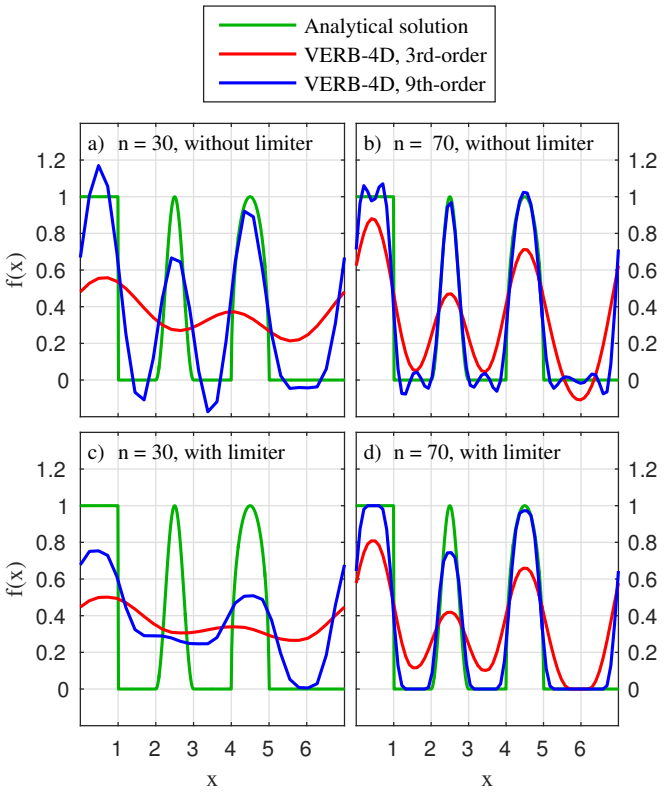

Figure 2.1: Comparison of the analytical solution (green line, from left to right: the step function, squared sine, and semi-ellipse) and VERB-4D code solutions (third-order (red line) and ninth-order (blue line) schemes) of the one-dimensional convection equation for different grid sizes (N_x = 30 (a,c) and 70 (b,d)), with (c,d) and without (a,b) the universal limiter, $u = 1$, $T = 98$ (14 rotations). $n \equiv N_x$.

though the limiter leads to the noticeable increase in the amplitude error of the sine function in the case of the ninth-order scheme. The amplitude error of the third-order scheme becomes even stronger.

Though the universal limiter allows us to use high-order schemes while avoiding unphysical oscillations, in some cases the limiter can introduce additional amplitude error. Other tests (not presented here) have shown that high-order schemes that use the universal limiter are more accurate than the lower-order schemes utilizing the universal limiter and that higher velocities and longer times of calculation lead to less accurate results.

The presented test was performed for idealized one-dimensional profiles, constant velocities, and uniform spatial grid. Physics-based simulations may be more complicated, requiring variable velocities, logarithmic grid, and additional source or loss terms. The test may not be fully applicable at some energies when particles are lost to the magnetopause or atmosphere in less than a few rotations, but they clearly illustrate the importance of accurate numerical schemes.

2.3.2 Two-Dimensional Convection

The solution of the two-dimensional convection equation

$$\frac{\partial f}{\partial t} + u\frac{\partial f}{\partial x} + w\frac{\partial f}{\partial y} = 0, \tag{2.8}$$

where $f(x,y,t)$ is the required function, $t \in [0,\infty)$ represents time, $x,y \in (-\infty,+\infty)$ are space coordinates, and u,w = const are velocities, can be generalized from solution (2.3) of the one-dimensional convection equation (2.2):

$$f(x,y,t) = \widetilde{f}(x-ut, y-wt), \tag{2.9}$$

where $\widetilde{f}$ is an arbitrary smooth function.

Moreover, if equation (2.8) is completed with the factorized initial conditions

$$f(x,y,0) = h_1(x)h_2(y), \tag{2.10}$$

where h_1 and h_2 are known functions, the solution of problem (2.8), (2.10) is reduced to two one-dimensional problems (2.2), (2.4) with $h(x) \equiv h_1(x)$ and $h_2(x)$ and can be found as follows

$$f(x,y,t) = h_1(x-ut)h_2(y-wt). \tag{2.11}$$

The latter fact allows us to deduce analytical solutions for the two-dimensional convection equation on the basis of the conclusions made for the one-dimensional equation.

As an example, we test here how significantly the numerical error depends on the order of the scheme and the duration of the simulation. We turn on the universal limiter and discriminator, aiming to study the realistic behavior of the profile. We impose the periodic boundary conditions in x and constant boundary conditions in y equal to 0 for two-dimensional convection equation (2.8). The periodic boundary conditions in x correspond to convection in MLT, and constant boundary conditions in y correspond to convection in R_0. Initial conditions are factorized into two one-dimensional profiles including step-function, squared sine, and semi-ellipse profiles. The computational domain is taken as a rectangle area $[0,7]\times[0,250]$ using dimensionless coordinates. The velocities in x and y are $u = 1$ and $w = 2$, respectively. Spatial steps in x and y are equal to 0.1. Time step is chosen using the same approach as for the one-dimensional test above.

The results of simulations are presented in Figures 2.2 and 2.3 for dimensionless end times $T = 7$ and 70, respectively. The analytical solutions are shown in Figures 2.2a, 2.2d, 2.3a, and 2.3d for $T = 7$ and $T = 70$. The use of the ninth-order scheme (Figures 2.2e and 2.3e) results in smaller numerical diffusion than the use of the third-order scheme (Figures 2.2b and 2.3b). The differences between analytical

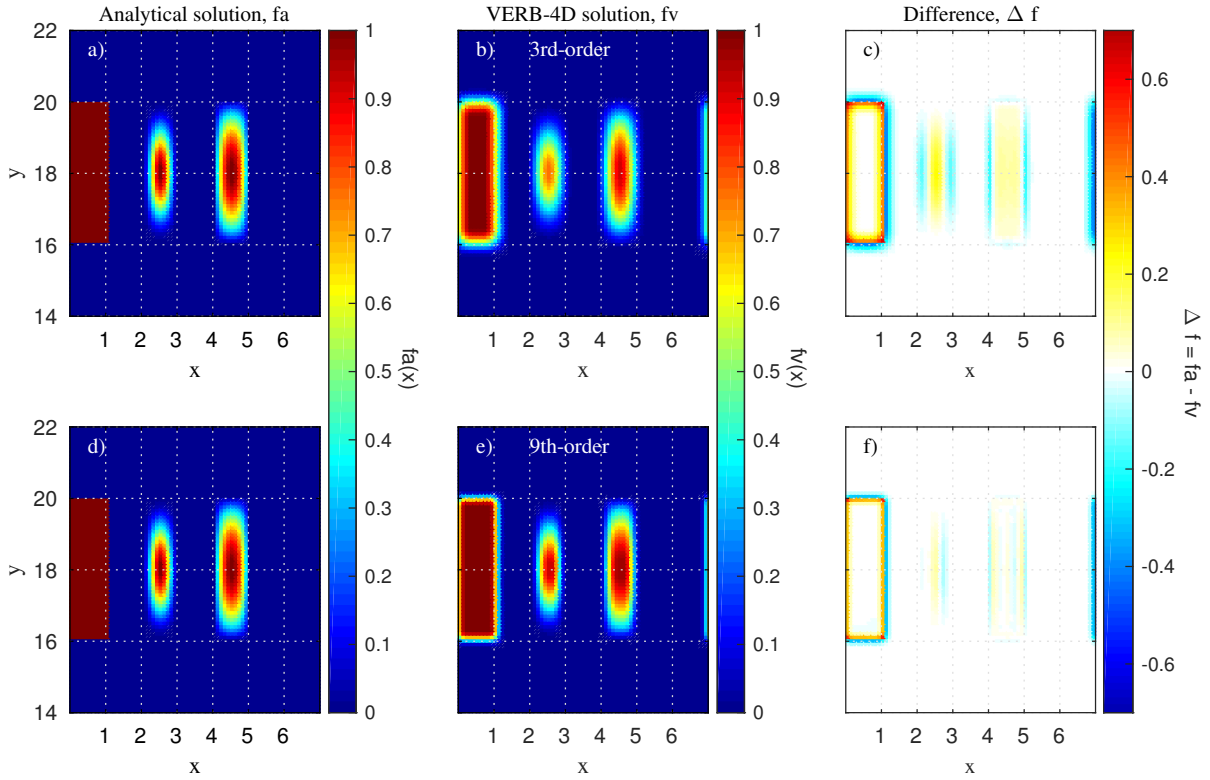

Figure 2.2: Comparison of the analytical solution (a,d) and VERB-4D code solutions (third-order (b) and ninth-order (e) schemes) of the two-dimensional convection equation and differences between analytical solution and each numerical solution (c,f) for end time $T = 7$ (1 rotation in x), $u = 1$, $w = 2$, and spatial steps in x and y are equal to 0.1. Step, squared sine, and semi-ellipse are shown at each plot from left to right.

and numerical solutions are shown in Figures 2.2c, 2.2f, 2.3c, and 2.3f. Figures 2.2c, 2.2f, 2.3c, and 2.3f show significant numerical errors close to the step function in all considered cases. In the case of the third-order scheme, sine and semi-ellipse profiles obtained numerically also show numerical errors comparable with the error on the edges of the step function. Numerical error on the edges of sine and semi-ellipse profiles predominantly appears in x direction (Figures 2.2c, 2.2f, 2.3c, and 2.3f), since gradients in y direction are smaller and numerical diffusion in y is weaker, leading to lower error. For longer computational times, the errors accumulate due to inaccuracies of time and space discretization and increase.

2.3.3 One-Dimensional Diffusion and Two-Dimensional Diffusion with Mixed Terms

Now let us consider the one-dimensional diffusion equation with constant diffusion coefficient $D > 0$:

$$\frac{\partial f}{\partial t} - D\frac{\partial^2 f}{\partial x^2} = 0, \tag{2.12}$$

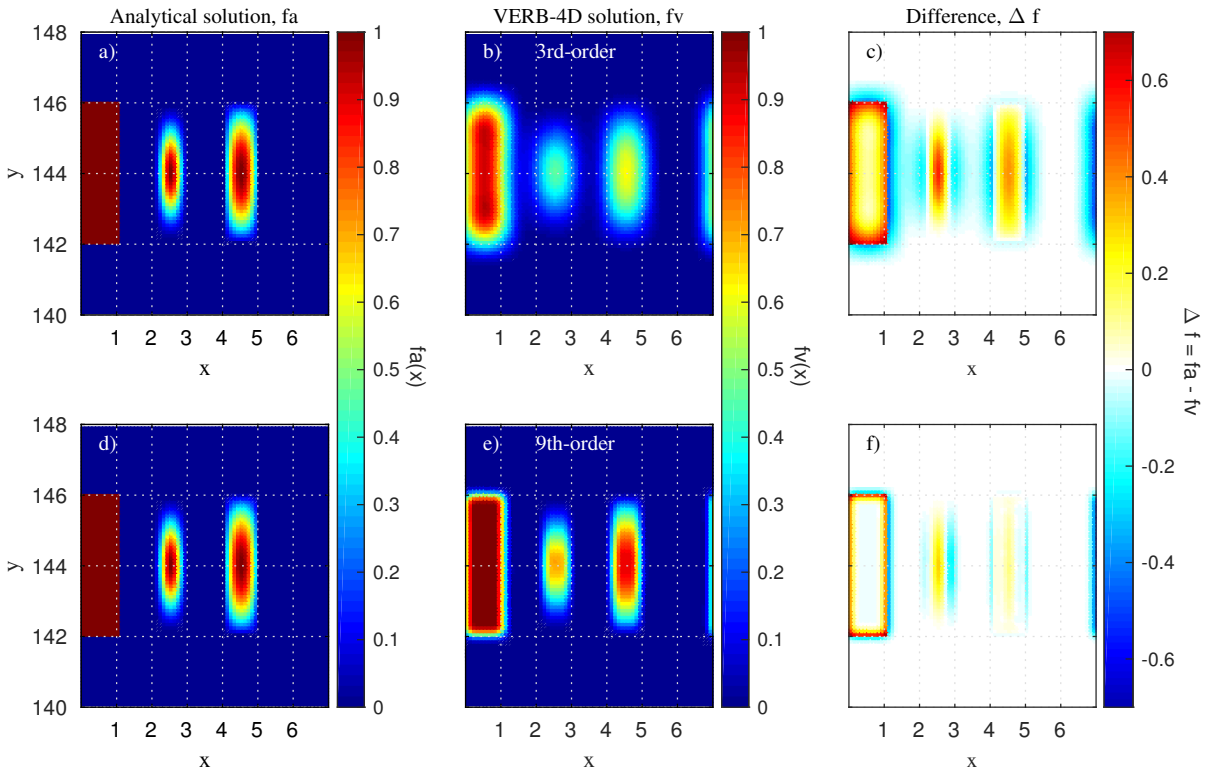

Figure 2.3: Same as Figure 2.2 but for longer end time $T = 70$.

where $f(x,t)$ is the required function, $t \in [0,+\infty)$ is time, and $x \in (-\infty,+\infty)$ is a space coordinate. If we take a Gaussian with a non-zero parameter σ as an initial condition

$$f(x,0) = e^{-x^2/2\sigma}, \tag{2.13}$$

the solution of equation (2.12) is represented in the form of a widening Gaussian (Strang, 2007):

$$f(x,t) = \frac{1}{\sqrt{1+2Dt/\sigma}} e^{-x^2/(2\sigma+4Dt)}. \tag{2.14}$$

A Gaussian (2.13) is appropriate for investigation of a numerical scheme on smooth solutions, since it is infinitely differentiable.

To explore the behavior of a numerical scheme on discontinuous functions, it is convenient to set the initial conditions in addition to one-dimensional diffusion equation (2.12) as a step function

$$f(x,0) = \begin{cases} 1, & |x| < x_0, \\ 0, & |x| > x_0, \end{cases} \tag{2.15}$$

where x_0 is a known number. In this case, the analytical solution can be found in the following form (Polyanin, 2001):

$$f(x,t) = \frac{1}{2}\left[\operatorname{erf}\left(\frac{x_0 - x}{2\sqrt{Dt}}\right) + \operatorname{erf}\left(\frac{x_0 + x}{2\sqrt{Dt}}\right)\right], \tag{2.16}$$

where

$$\mathrm{erf(x)} = \frac{2}{\sqrt{\pi}} \int_0^x e^{-\tilde{x}^2} d\tilde{x}. \tag{2.17}$$

All conclusions relating to the one-dimensional diffusion problem can be generalized in the case of the two-dimensional diffusion equation with constant diffusion coefficients D_{xx} and D_{yy}

$$\frac{\partial f}{\partial t} - D_{xx}\frac{\partial^2 f}{\partial x^2} - D_{yy}\frac{\partial^2 f}{\partial y^2} = 0. \tag{2.18}$$

We solve (2.18) for $t \in [0, +\infty)$, $x, y \in (-\infty, +\infty)$, $D_{xx}, D_{yy} > 0$. This generalization can be demonstrated by introducing factorized initial conditions for equation (2.18)

$$f(x, y, 0) = f_1(x) f_2(y), \tag{2.19}$$

where $f_1(x)$ and $f_2(y)$ are known functions. The solution of the problem (2.18), (2.19) is also factorized to solutions $f_1(x, t)$ and $f_2(y, t)$ of the corresponding one-dimensional diffusion equations in each space coordinate with constant positive diffusion coefficients D_{xx} and D_{yy}:

$$f(x, y, t) = f_1(x, t) f_2(y, t). \tag{2.20}$$

To obtain the analytical form of the solution, one can use either the widening Gaussian (2.14) or function (2.16) as $f_1(x, 0) \equiv f_1(x)$ and $f_2(y, 0) \equiv f_2(y)$.

It is also customary to obtain the analytical solution for the two-dimensional diffusion equation with mixed terms. Assuming constant diffusion coefficients D_{xx}, $D_{xy} = D_{yx}$, and D_{yy}, the equation takes the form

$$\frac{\partial f}{\partial t} - D_{xx}\frac{\partial^2 f}{\partial x^2} - D_{yy}\frac{\partial^2 f}{\partial y^2} - 2D_{xy}\frac{\partial^2 f}{\partial x \partial y} = 0, \tag{2.21}$$

where $t \in [0, +\infty)$, $x, y \in (-\infty, +\infty)$, $D_{xx}, D_{yy} > 0$, $D_{xx} D_{yy} > D_{xy}^2$.

The mixed-diffusion term D_{xy} in (2.21) can be eliminated using the following technique (Albert and Young, 2005). Applying the linear transformation of coordinates $(x, y) \to (\xi, \eta)$

$$\xi = a_\xi x + b_\xi y, \;\; \eta = a_\eta x + b_\eta y, \tag{2.22}$$

where $a_\xi b_\eta - b_\xi a_\eta \neq 0$, diffusion coefficients in new coordinates can be written as (Haerendel, 1968; Schulz and Lanzerotti, 1974)

$$\begin{aligned} D_{\xi\xi} &= a_\xi^2 D_{xx} + 2a_\xi b_\xi D_{xy} + b_\xi^2 D_{yy}, \\ D_{\eta\eta} &= a_\eta^2 D_{xx} + 2a_\eta b_\eta D_{xy} + b_\eta^2 D_{yy}, \\ D_{\xi\eta} &= a_\xi a_\eta D_{xx} + (a_\xi b_\eta + b_\xi a_\eta) D_{xy} + b_\xi b_\eta D_{yy}. \end{aligned} \tag{2.23}$$

The diffusion coefficient $D_{\xi\eta}$ can be eliminated if the following condition is satisfied:

$$a_\xi a_\eta D_{xx} + (a_\xi b_\eta + b_\xi a_\eta) D_{xy} + b_\xi b_\eta D_{yy} = 0. \tag{2.24}$$

The positivity of $D_{\xi\xi}$ and $D_{\eta\eta}$ is guaranteed by the inequality $D_{xx}D_{yy} > D_{xy}^2$.

The diffusion equation with mixed terms (2.21) can be simplified to equation (2.18) with corresponding diffusion coefficients $D_{\xi\xi}$ and $D_{\eta\eta}$ if D_{xx}, D_{yy} and D_{xy} in equation (2.21) satisfy restriction (2.24). Therefore, an analytical solution of the diffusion equation (2.18) without mixed terms can be used to construct an analytical solution of the two-dimensional diffusion equation (2.21) with mixed terms. For instance, if the initial condition for (2.21) is the following function with positive parameters σ_1 and σ_2

$$f(x,y,0) = e^{-(a_\xi x + b_\xi y)^2/2\sigma_1} e^{-(a_\eta x + b_\eta y)^2/2\sigma_2}, \tag{2.25}$$

the solution of the problem (2.21), (2.25) can be found as follows:

$$\begin{aligned} f(x,y,t) \;=\; & \left[1 + 2\frac{\left(a_\xi^2 D_{xx} + 2a_\xi b_\xi D_{xy} + b_\xi^2 D_{yy}\right)t}{\sigma_1}\right]^{-\frac{1}{2}} \\ & \times \left[1 + 2\frac{\left(a_\eta^2 D_{xx} + 2a_\eta b_\eta D_{xy} + b_\eta^2 D_{yy}\right)t}{\sigma_2}\right]^{-\frac{1}{2}} \\ & \times e^{-(a_\xi x + b_\xi y)^2/(2\sigma_1 + 4(a_\xi^2 D_{xx} + 2a_\xi b_\xi D_{xy} + b_\xi^2 D_{yy})t)} \\ & \times e^{-(a_\eta x + b_\eta y)^2/(2\sigma_2 + 4(a_\eta^2 D_{xx} + 2a_\eta b_\eta D_{xy} + b_\eta^2 D_{yy})t)} \end{aligned} \tag{2.26}$$

for all a_ξ, b_ξ, a_η, and b_η satisfying (2.24) and $a_\xi b_\eta - b_\xi a_\eta \neq 0$.

Our next set of tests is devoted to the investigation of the convergence of the numerical solution of the two-dimensional diffusion equation (2.21) with mixed terms to the analytical solution. We set $D_{xx} = D_{yy} = 10$ and $D_{xy} = 7$, using dimensionless units to satisfy the condition $D_{xx}D_{yy} > D_{xy}^2$. The function (2.25) with parameters $a_\xi = a_\eta = b_\eta = 1/\sqrt{2}$, $b_\xi = -1/\sqrt{2}$, $\sigma_1 = \sigma_2 = 200$ is chosen as the initial condition for equation (2.21). Note that the chosen parameters a_ξ, b_ξ, a_η, and b_η along with the diffusion coefficients D_{xx}, D_{yy}, D_{xy} satisfy condition (2.24). Zero values of the required function are chosen as constant boundary conditions at infinities. To emulate spatial infinities, we use square $[-200, 200] \times [-200, 200]$ since the sizes of the square are considerably larger than the characteristic size of the initial function, and the required function can be approximated with zero at the borders of the square.

Figure 2.4 presents analytical solutions (Figures 2.4a, 2.4d, and 2.4g), numerical solutions (Figures 2.4b, 2.4e, and 2.4h), and their differences (Figures 2.4c, 2.4f, and 2.4i) for grid sizes 25×25, 50×50, and 100×100 for the end time $T = 70$ and the time step 0.14. The VERB-4D code solutions represent anisotropic diffusion in (ξ, η) coordinates (2.22) rotated 45° clockwise about (x, y) axes. Indeed, diffusion with mixed terms in

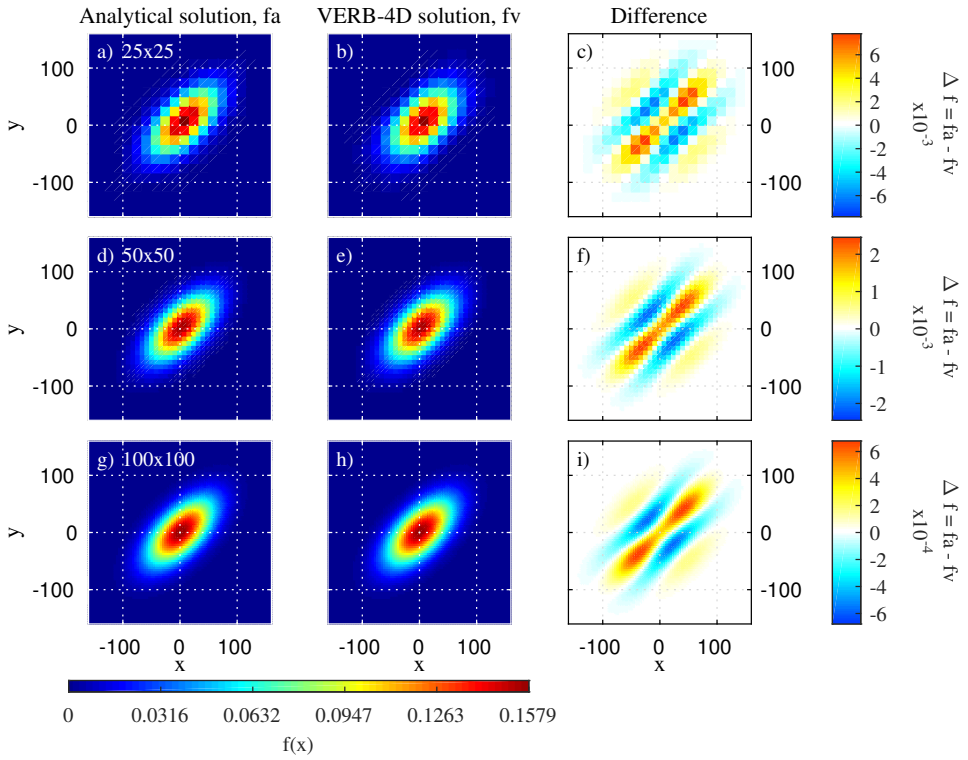

Figure 2.4: Comparison of analytical solution (a,d,g) and VERB-4D code solution (b,e,h) of the two-dimensional diffusion equation with mixed terms, and their difference (c,f,i) for grid sizes 25×25, 50×50, and 100×100, $x \in [-200, 200]$, $y \in [-200, 200]$, $T = 70$, $D_{xx} = D_{yy} = 10$, $D_{xy} = 7$, $\sigma = 200$.

(x, y) coordinates are equivalent to anisotropic diffusion without mixed terms in (ξ, η) coordinates, since $D_{\xi\xi} = 3$, $D_{\eta\eta} = 17$, and $D_{\xi\eta} = 0$ (see equations (2.23)). Numerical errors have the same shape in all cases (Figures 2.4c, 2.4f, and 2.4i). The VERB-4D code solution underestimates the analytical one along the line $y = x$ and overestimates it along the lines $y = x \pm 50$. The absolute difference decreases about 3.5 times when the spatial step decreases 2 times in each variable. Therefore, a numerical solution of the VERB-4D code converges to the analytical solution.

As expected, further tests (not presented here) showed stability of numerical solution to an increasing time step, since the implemented numerical scheme for the two-dimensional diffusion with mixed terms is fully implicit.

2.4 Influence of Numerical Schemes on Magnetospheric Convection Modeling

We performed a set of simulations in order to investigate the influence of the order of the scheme for the convection equation on magnetospheric convection modeling. Here we turn on the universal limiter and the discriminator that are applied to the third-

and ninth-order schemes. We assign diffusion coefficients $D_{L^*L^*}$, D_{VV}, D_{VK}, D_{KV}, and D_{KK} in the Fokker-Planck equation (2.1) to zero and take into account only convection terms and loss due to magnetopause shadowing based on the Shue model (Shue et al., 1997). The computational domain in R_0 and φ is set as a rectangle in polar coordinates $[6.6R_E, 10R_E] \times [0, 2\pi]$. Boundary conditions in φ are periodic. Zero derivative boundary conditions are used at $6.6R_E$. Constant boundary conditions at $R_0 = 10R_E$ are parameterized using kappa function with $\kappa = 3.3$, the electron density taken from Tsyganenko and Mukai (2003), and the parameterization of electron temperature provided by N. Ganushkina (personal communication, 2015). An empty magnetosphere is taken as an initial condition. Azimuthal and radial velocities v_φ and v_{R_0} are calculated using the centered dipole approximation and the Volland-Stern electric field model (Stern, 1975; Volland, 1973) with the Kp-dependent intensity according to Maynard and Chen (1975).

To study the impact of the numerical scheme on the results of magnetospheric convection modeling, we assume quiet-time geomagnetic conditions (Kp = 2, IMF $B_z = 0$ nT, solar wind number density is equal to 7 cm^{-3}, and solar wind velocity is equal to 400 km/s). Several pulses of the localized electric field are launched, as described below, to investigate the response of different numerical schemes to sharp changes in velocities and PSD. The localized electric field is associated with the dipolarization process in the magnetosphere (Baumjohann et al., 1990; Angelopoulos et al., 1992). Propagating in the eastward direction, electromagnetic pulses are calculated following Li et al. (1998) and Sarris et al. (2002). In the spherical coordinate system, the localized electric field takes the form:

$$\mathbf{E}_\phi = -\hat{e}_\phi E_0 / E_{max} \, (1 + c_1 \cos(\phi - \phi_0))^{n_p} \exp(-l^2), \tag{2.27}$$

where $\hat{e}_\phi$ is the unit vector in the direction of the increase of azimuth angle ϕ, $l = [r - r_i + v_{front}(r)(t - t_a)]/d_{pulse}$ is the location of the maximum intensity of the pulse, $v_{front}(r) = a_{front} + b_{front} r$ describes the pulse front velocity as a function of radial distance r, d_{pulse} is the width of the pulse, $c_1 > 0$ and $n_p > 0$ are coefficients determining the local time dependence of the electric field amplitude, $t_a = (c_2/v_a)(1 - \cos(\phi - \phi_0))$ represents the delay of the pulse depending on the azimuth angle, ϕ_0 is the azimuth angle of the fastest transport to given r, c_2 is the magnitude of the delay, v_a is the longitudinal speed of the pulse, and r_i is a parameter affecting the arrival time of the pulse. The parameter E_{max} is introduced to eliminate unphysical values in excess of 1000 mV/m for the maximum E_ϕ, according to Ganushkina et al. (2006). Following Sarris et al. (2002), we use $\phi_0 = 0$, $c_1 = 1$, $c_2 = 0.5 \;\; R_E$, $a_{front} = 53.15$ km/s, $b_{front} = 0.0093$ s^{-1}, $n_p = 8$, $v_a = 20$ km/s, $r_i = 100 \; R_E$, $d_{pulse} = 4 \cdot 10^7$ m, and $E_0 = 4$ mV/m.

The evolution of PSD is calculated for 3.5 days. The launched electric field pulses

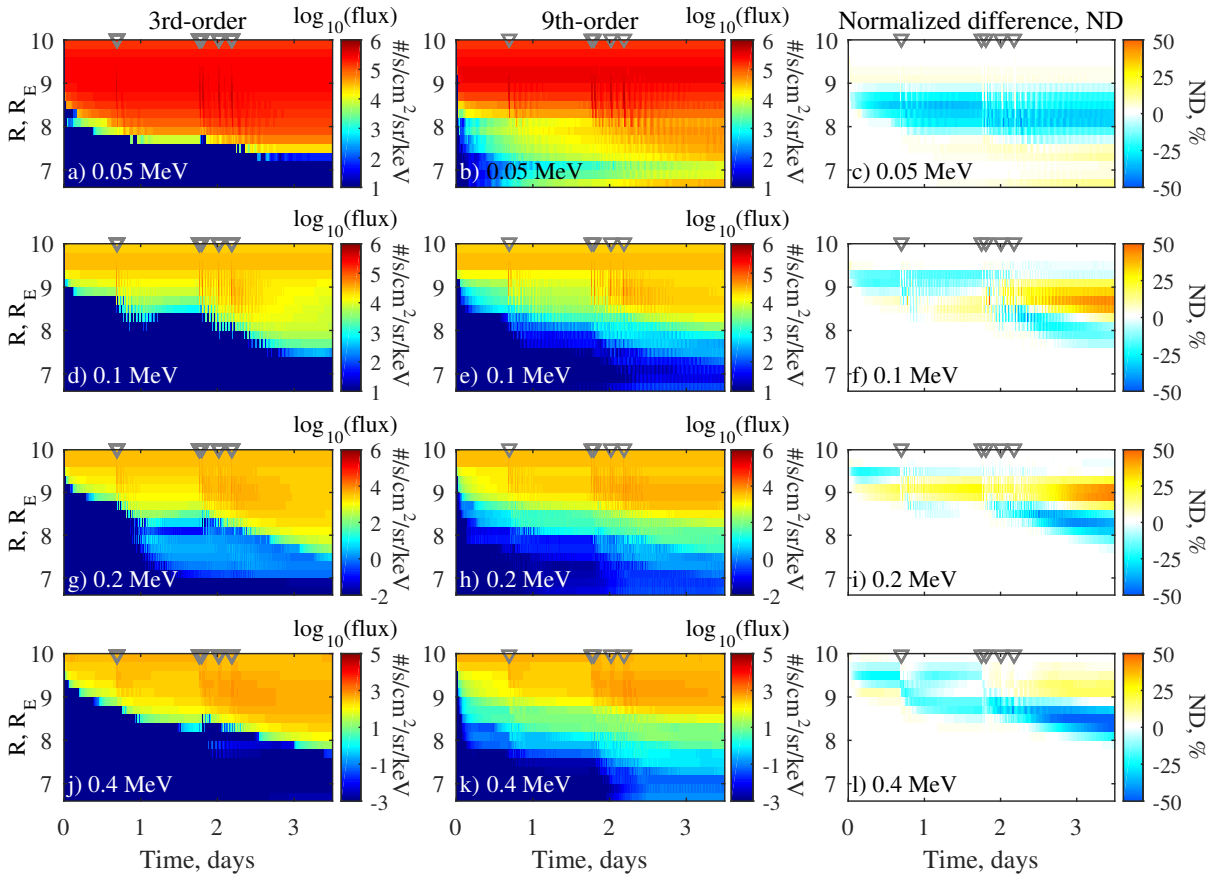

Figure 2.5: Electron fluxes obtained by using the third- (a,d,g,j) and ninth-order (b,e,h,k) schemes and the normalized difference (c,f,i,l) for 50° pitch angle, MLT = 3 h. Times of arrival of localized electric field are marked with gray triangles. $R \equiv R_0$.

reach the computational domain at $t = 0.68$, 1.76, 1.8, 2.01, and 2.18 days. Spatial step is equal to $0.2R_E$ in R_0 and $\pi/6$ in φ, corresponding to the spatial grid in R_0 and φ of the size of 18×13.

Figure 2.5 presents the evolution of fluxes in time for different R_0 calculated with the third- and ninth-order schemes for 0.05, 0.1, 0.2, and 0.4 MeV electrons. Figures 2.5a, 2.5d, 2.5g, and 2.5j show fluxes obtained with the third-order upwind scheme, and Figures 2.5b, 2.5e, 2.5h, and 2.5k show electron fluxes calculated using the ninth-order scheme. To compare these results for particular energies, we introduce the Normalized Difference (ND) metric (Subbotin and Shprits, 2009):

$$\mathrm{ND} = \frac{f_{9th}(t,R_0) - f_{3rd}(t,R_0)}{\max\limits_{\text{over } R_0 \text{ for fixed t}} (f_{3rd}(t,R_0) + f_{9th}(t,R_0))/2} \times 100\%, \tag{2.28}$$

where f_{3rd} and f_{9th} are PSD (or fluxes) obtained, using third- and ninth-order schemes. Figures 2.5c, 2.5f, 2.5i, and 2.5l present normalized differences for energies E_{kin} under consideration. Times of arrival of localized electric field are marked with gray triangles at the top of each plot. Considerable differences, about 50% in terms of the ND metric,

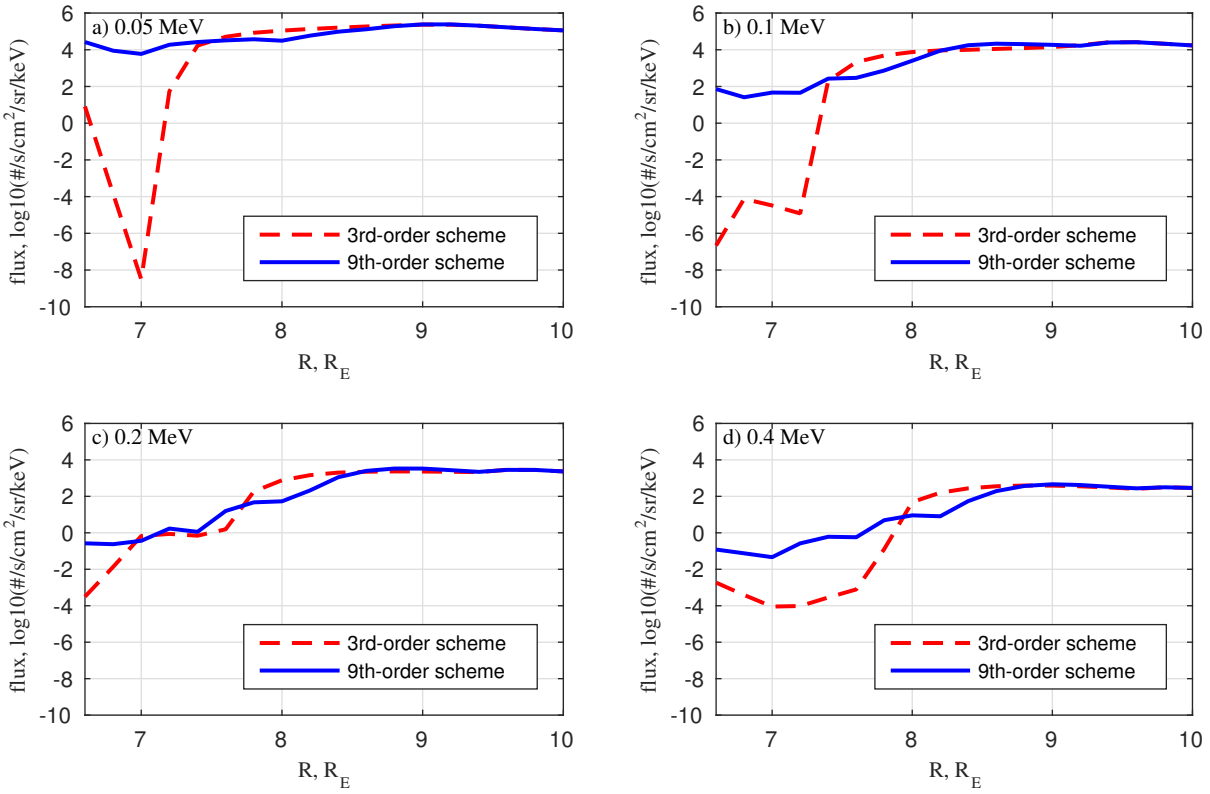

Figure 2.6: Dependence of numerically calculated profiles of electron fluxes on the scheme order for a simulation at t = 3 day, MLT = 3 h, pitch angle $\alpha = 50°$. Plots a,b,c,d correspond to electron energies E_{kin} = 0.05, 0.1, 0.2, and 0.4 MeV, respectively. The dashed line denotes results obtained with the third-order scheme, and the solid line shows the results obtained with the ninth-order scheme. $R \equiv R_0$.

appear after the third day at $R_0 \approx 8.5R_E$ for 0.1 MeV electrons and at $R_0 \approx 9R_E$ for 0.2 MeV electrons, where the ninth-order scheme results in more prominent flux than the third-order one. On the contrary, the third-order scheme results in higher fluxes for 0.4 MeV particles at $R_0 \approx 8.4R_E$, where the normalized difference is equal to about −50%. The ND of the order of $-(25-35)$% at $R_0 \approx 8-9R_E$ characterizes results for 0.05 MeV particles during the whole interval of calculations.

It is instructive to compare the flux profiles at the end of the third day of the simulation (Figure 2.6). Both schemes show approximately the same results at $R_0 \approx 9-10R_E$. The difference becomes more pronounced at lower radial distances. Fluxes obtained with the ninth-order scheme are up to one order lower at $8\pm0.5R_E$ for all energies. The ninth-order scheme gives significantly higher results at the lowest R_0 (below 7.5 R_E for E_{kin} = 0.05 and E_{kin} = 0.1 MeV, below 7 R_E for E_{kin} = 0.2 MeV, and below 8 R_E for E_{kin} = 0.4 MeV).

To conclude, the ninth-order scheme leads to higher fluxes in comparison with the third-order scheme below $R_0 \approx 8R_E$ at the end of the calculation. It can, therefore, be said that the ninth-order scheme results in faster transport of electrons to lower

R_0. Though we have not compared results of the simulation with observations in this study, we can rely more on the ninth-order scheme, as the scheme shows more accurate results and better reproduces the analytical solutions (see Section 2.3).

2.5 Summary and Conclusions

Presented numerical simulations show the importance of detailed stability and accuracy verification tests for the inner magnetospheric models. Numerical instabilities may produce inadequate results and render the code unusable. Violation of accuracy can lead to more intricate issues, when numerical errors and uncertainties of physical models are indistinguishable, or may lead to erroneous physical conclusions or estimation of the missing physics. Low-accuracy numerical schemes require a finer grid than the more accurate schemes to achieve the same results and consequently have a negative impact on the performance of the code. For these reasons, the verification of numerical schemes is an essential step before the validation of the code with observations.

In this work, we presented a set of convenient analytical solutions and verification tests for advective-diffusive codes. Accuracy and stability of numerical schemes for the inner magnetosphere modeling can be studied, choosing the appropriate initial and boundary conditions and comparing the simulation results with analytical solutions. Though the presented analytical profiles are constructed under strong assumptions such as constant velocities or constant diffusion coefficients, the basic behavior of the implemented numerical schemes can be investigated, using both smooth and discontinuous solutions.

We performed a comprehensive analysis of numerical methods and techniques underlying the VERB-4D code. Below is the list of the main findings:

1. It is crucially important to use accurate numerical schemes in the inner magnetospheric models. Our simulations have shown (Figures 2.5 and 2.6) that accuracy of numerical schemes significantly affects simulation results of an advection code.

2. Low-order numerical schemes for the convection equation can lead to large errors. For instance, the third-order scheme results in stronger numerical dissipation and a higher amplitude error than the ninth-order scheme (Figures 2.1, 2.2, and 2.3).

3. Our tests of the convection and diffusion solvers implemented in the VERB-4D code have shown the convergence of the numerical solution to the analytical one.

4. The VERB-4D code shows stable behavior independent of the input time step.

2.A Courant-Friedrichs-Lewy Condition

Stability of numerical schemes is a key aspect in the construction of robust methods for solving partial differential equations. Unstable schemes can magnify small inaccuracies of initial conditions or numerical solutions, resulting in a large total numerical error and rendering even high-order schemes inapplicable for complex physical problems. Stable schemes can be either conditionally or unconditionally stable. As the name implies, unconditionally stable schemes are stable for any parameters of modeled system and numerical methods (i.e., velocity, spatial step, etc.), while conditionally stable schemes restrict these parameters.

We present here the simplest condition for a wide class of schemes for solving one-dimensional convection equation, the Courant-Friedrichs-Lewy condition (Godunov and Ryabenkii, 1987). We consider equation (2.2) with constant positive velocity u. Assume that spatial boundary is confined in the interval $[a, b]$. We introduce a uniform spatial grid $\{x_i\}_{i=1}^{N_x}$, $x_i = a + (i-1)\cdot\Delta x$, $\Delta x = (b-a)/(N_x - 1)$, $i = 1, \ldots, N_x$. Time discretization is performed at moments $t_k = k\cdot\Delta t$. Discrete values of required function are denoted as $f(x_i, t_k) = f_i^k$.

The first-order explicit conditionally stable scheme for one-dimensional convection equation (2.2) can be written as follows:

$$\frac{f_i^{k+1} - f_i^k}{\Delta t} + u\frac{f_i^k - f_{i-1}^k}{\Delta x} = 0. \tag{2.29}$$

The scheme (2.29) is stable if the following condition is satisfied:

$$\frac{u\Delta t}{\Delta x} \leq 1. \tag{2.30}$$

Condition (2.30) is referred to as the Courant-Friedrichs-Lewy condition, and the number $u\Delta t/\Delta x$ is referred to as the Courant number. The Courant-Friedrichs-Lewy condition is also valid for more accurate high-order schemes and can be generalized for equations with variable velocities. If low-order schemes, which require small spatial steps for high accuracy, are used, relatively small time steps should inevitably be employed. In this case, computational time can be increased significantly, which particularly has a negative impact on long-term simulations.

2.B Elimination of Unphysical Oscillations Using the Universal Limiter

Following, in general, Leonard (1991), we briefly describe the method of the construction of high-order numerical schemes for the one-dimensional convection equation (2.2), free of unphysical oscillations. Equation (2.2) is considered at the spatial

domain $[a, b]$ and the time interval $[0, +\infty)$. For generality, the velocity $u = u(x, t)$ is assumed to be variable in both space and time. The spatial domain is uniformly divided into N_x nodes: $x_i = a + (i-1) \cdot \Delta x$, $i = 1, \ldots, N_x$. The required function is considered at the nodes $\{x_i\}_{i=1}^{N_x}$ and calculated at discrete times $t_k = k \cdot \Delta t$: $f(x_i, t_k) = f_i^k$, $k = 1, ...$

The value of the function at the node x_i and the moment t_{k+1} can be represented as follows:

$$f_i^{k+1} = f_i^k - (c_{i+1/2}^k f_{i+1/2}^k - c_{i-1/2}^k f_{i-1/2}^k), \tag{2.31}$$

where $c_{i\pm1/2}^k = u(x_i \pm \Delta x/2, t_k)\Delta t/\Delta x$ is the Courant number, and $f_{i\pm1/2}^k = f(x_i \pm \Delta x/2, t_k)$. Since the discretized function $f(x, t)$ is defined only at the nodes x_i, the values $f_{i\pm1/2}^k$ have to be approximated on the basis of known values f_i^k.

The value of $f_{i+1/2}^k$ for the arbitrary odd N-th order ($N > 1$) upwind scheme satisfies the recursive expression

$$f_{i+1/2}^{k,(N)} = f_{i+1/2}^{k,(N-1)} + \frac{\prod_{j=1}^{(N-1)/2} ((c_{i+1/2}^k)^2 - j^2)}{N!} \left[D_{i+1/2}^{k,(N-1)} - \frac{\operatorname{sign}(c_{i+1/2}^k)}{2} \delta_{i+1/2}^{k,(N)} \right], \tag{2.32}$$

where $f_{i+1/2}^{k,(N)}$ is the value of $f_{i+1/2}^k$ corresponding to the N-th order scheme, $f_{i+1/2}^{k,(0)} = \frac{1}{2}(f_{i+1}^k + f_i^k)$, $\operatorname{sign}(c_{i+1/2}^k)$ is the sign of the Courant number, and coefficients $D_{i+1/2}^{k,(N-1)}$ and $\delta_{i+1/2}^{k,(N)}$ can be expanded into the following sums:

$$D_{i+1/2}^{k,(N-1)} = \frac{1}{2} \sum_j a_j f_{i+j}^k, \tag{2.33}$$

$$\delta_{i+1/2}^{k,(N)} = \sum_j b_j f_{i+j}^k \tag{2.34}$$

with finite number of non-zero coefficients a_j and b_j. Values of a_j and b_j can be obtained from Tables 2.1 and 2.2.

In case of even $N > 2$, $f_{i+1/2}^k$ can be approximated as follows:

$$f_{i+1/2}^{k,(N)} = f_{i+1/2}^{k,(N-2)} + \frac{\prod_{j=1}^{N/2-1} ((c_{i+1/2}^k)^2 - j^2)}{(N-1)!} \left[D_{i+1/2}^{k,(N-2)} - \frac{c_{i+1/2}^k}{N} \delta_{i+1/2}^{k,(N-1)} \right]. \tag{2.35}$$

Using expressions (2.32) and (2.35) together with (2.31), one can calculate the evolution of the required function from the moment t_k to t_{k+1}.

It is well known that high-order (higher than second order) linear numerical schemes for the one-dimensional convection equation suffer from artificial unphysical oscillations (Godunov, 1959). Leonard (1991) developed the universal limiter eliminating unphysical oscillations. The universal limiter is applicable to a numerical scheme of arbitrary order. The limiter is based on the three stages: (I) calculation

Table 2.1: Coefficients for calculation $2 \cdot D_{i+1/2}^{k,(N)}$.

N	a_5	a_4	a_3	a_2	a_1	a_0	a_{-1}	a_{-2}	a_{-3}	a_{-4}
0	0	0	0	0	+1	+1	0	0	0	0
1	0	0	0	+1	0	-1	0	0	0	
2	0	0	0	+1	-1	-1	+1	0	0	0
3	0	0	+1	-2	0	+2	-1	0	0	
4	0	0	+1	-3	+2	+2	-3	+1	0	0
5	0	+1	-4	+5	0	-5	+4	-1	0	
6	0	+1	-5	+9	-5	-5	+9	-5	+1	0
7	+1	-6	+14	-14	0	+14	-14	+6	-1	
8	+1	-7	+20	-28	+14	+14	-28	+20	-7	+1
…	…	…	…	…	…	…	…	…	…	…

$f_{i+1/2}^k$ using (2.32) and (2.35) for all i, (II) modification of $f_{i+1/2}^k$ if unphysical oscillations are detected, and (III) updating f_i^k according to (2.31). Details of the universal limiter are presented in the following algorithm.

1. Set $i = 1$.
2. **While** $i \le N_x$ **do**:
   (a) **if** $c_{i+1/2}^k = 0$: set $i \to i+1$ and **go to** step 2;
   (b) calculate $f_{i+1/2}^k$ for the desired order scheme using (2.32) and (2.35);
   (c) among adjacent to $x_i + \Delta x/2$ nodes x_j designate nearest upstream (C), next to the nearest upstream (U), and nearest downstream (D) nodes on the basis of $\text{sign}(c_{i+1/2}^k)$;
   (d) compute DEL $= f_D^k - f_U^k$ and ADEL $= |\text{DEL}|$;
   (e) compute ACURV $= |f_D^k - 2f_C^k + f_U^k|$;
   (f) **if** ACURV $\ge$ ADEL: set $f_{i+1/2}^k \to f_C^k$; $i \to i+1$; **go to** step 2;
   (g) compute the reference value $f_{ref} = f_U^k + (f_C^k - f_U^k)/c_{i+1/2}^k$;
   (h) **if** DEL > 0: $f_{i+1/2}^k \to \max(f_{i+1/2}^k, f_C^k)$; $f_{i+1/2}^k \to \min(f_{i+1/2}^k, \min(f_{ref}, f_D^k))$;
   (i) **else** $f_{i+1/2}^k \to \min(f_{ref}, f_C^k)$; $f_{i+1/2}^k \to \max(f_{i+1/2}^k, \max(f_{ref}, f_D^k))$;
   (j) $i \to i+1$;
   (k) **go to** step 2.
3. Update the function f_i^k for all i according to expression (2.31).

The universal limiter can produce slight amplitude error near points of local extremum, where changes in monotonicity are mistakenly recognized as short-wavelength unphysical oscillations. The discriminator proposed by Leonard and Niknafs (1991) analyzes the behavior of the function near each node x_i and decides

Table 2.2: Coefficients for calculation $\delta_{i+1/2}^{k,(M)}$.

M	b_5	b_4	b_3	b_2	b_1	b_0	b_{-1}	b_{-2}	b_{-3}	b_{-4}
0	0	0	0	0	+1	0	0	0	0	
1	0	0	0	0	+1	-1	0	0	0	0
2	0	0	0	+1	-2	+1	0	0	0	
3	0	0	0	+1	-3	+3	-1	0	0	0
4	0	0	+1	-4	+6	-4	+1	0	0	
5	0	0	+1	-5	+10	-10	+5	-1	0	0
6	0	+1	-6	+15	-20	+15	-6	+1	0	
7	0	+1	-7	+21	-35	+35	-21	+7	-1	0
8	+1	-8	+28	-56	+70	-56	+28	-8	+1	
9	+1	-9	+36	-84	+126	-126	+84	-36	+9	-1
…	…	…	…	…	…	…	…	…	…	…

on the basis of value and sign of gradient at the adjacent nodes if the associated oscillation relates to a local extremum. If a local extremum is detected, the discriminator relaxes the universal limiter constraints, and stages 2c-2i of the algorithm above are skipped.

Finally, we note that if formulas (2.32) and (2.35) are used near the boundaries of the spatial domain $[a, b]$, the expansions (2.33) and (2.34) may require values of f_i^k beyond the range $i = 1, \ldots, N_x$ (e.g., f_{-1}^k, $f_{N_x+1}^k$, etc.). In this case, the necessary number of 'ghost' points has to be introduced in accordance with the order of the desired numerical scheme. Values of the function $f(x,t)$ at these points should be chosen depending on the type of boundary conditions.

Acknowledgments

This project received funding support from Helmholtz-Gemeinschaft, NASA grant NNX15AI94G, NSF grant AGS-1203747 and the UC Office of the President, UC Lab Fees Research Program Award ID #12-LR-235337. We would like to thank Dmitri Subbotin for his contributions to the development of the VERB code. We would like to thank Natalia Ganushkina for provided parameterization of electron temperature. We would like to thank the anonymous reviewers for their insightful comments and suggestions that have contributed to improve this paper. No data was used in producing this manuscript.

Chapter 3

Transport and Loss of Ring Current Electrons Inside Geosynchronous Orbit during the 17 March 2013 Storm

Published as:
Aseev, N. A., Shprits, Y. Y., Wang, D., Wygant, J., Drozdov, A. Y., Kellerman, A. C., and Reeves, G. D., 2019. Transport and Loss of Ring Current Electrons Inside Geosynchronous Orbit during the 17 March 2013 Storm. *Journal of Geophysical Research: Space Physics*, 124(2):915–933. doi:10.1029/2018JA026031

Abstract

Ring current electrons (1-100 keV) have received significant attention in recent decades, but many questions regarding their major transport and loss mechanisms remain open. In this study, we model the enhancement of phase space density that occurred during the 17 March 2013 storm, using the four-dimensional Versatile Electron Radiation Belt code (VERB-4D code). Our model includes global convection, radial diffusion, and scattering into the Earth's atmosphere driven by whistler-mode hiss and chorus waves. We study the sensitivity of the model to the boundary conditions, global electric field, electric field associated with subauroral polarization streams, electron loss rates, and radial diffusion coefficients. The results of the code are almost insensitive to the model parameters above 4.5 R_E, which indicates that the general dynamics of the electrons between 4.5 R_E and the geostationary orbit can be explained by global convection. We found that the major discrepancies between the model and data can stem from the inaccurate electric field model and uncertainties in lifetimes. We show that additional mechanisms that are responsible for radial transport are required to explain the dynamics of $\geq$ 40 keV electrons, and the inclusion of the radial diffusion

rates which are typically assumed in radiation belt studies leads to a better agreement with the data. The overall effect of subauroral polarization streams on the electron phase space density profiles seems to be smaller than the uncertainties in other input parameters. This study is an initial step towards understanding of the dynamics of these particles inside the geostationary orbit.

3.1 Introduction

The ring current electrons (energies from ~1 to a few 100 keV) can contribute to surface charging of satellites and may provide from 10 to 25% of the ring current energy during storm times (Frank, 1967a; Liu et al., 2005; Zhao et al., 2016). The injections of ~ 10 keV electrons in the inner magnetosphere during enhanced magnetospheric convection excite chorus waves (Hwang et al., 2007; Thorne, 2010) which resonate with relativistic electrons in the radiation belts and provide an effective mechanism of their pitch-angle scattering (Horne and Thorne, 2003; Albert, 2005; Shprits et al., 2008b; Thorne, 2010) and local acceleration (Horne and Thorne, 1998; Summers et al., 1998; Horne et al., 2005; Li et al., 2007; Reeves et al., 2013). Electrons of 1-10 keV energies can be deposited into protective shielding of satellites operating within the ring current region, cause surface charging, and ultimately damage satellite electronics (DeForest, 1972; Baker, 2000; Choi et al., 2011; Thomsen et al., 2013; Ganushkina et al., 2017).

Despite the important role of the ring current electrons, their transport and loss processes within the Geostationary Orbit (GEO) remain poorly understood, primarily due to the limited number of measurements. Only several years ago, Van Allen Probes opened up a whole new opportunity for quantitative tests of models and theory. Reeves et al. (2016) analyzed Van Allen Probes electron flux measurements and showed the coherence of the particle dynamics across a broad range of energies from a few tens of keV up to MeV. They found that at any given L-shell, the number of enhancement events increases with the decrease in electron energy, and the enhancements have an upper energy limit that varies from event to event. Zhao et al. (2016) examined the dynamics of the ring current electrons during storm times in comparison with the ions. Their results indicate that the electrons frequently penetrate deep into the inner magnetosphere and stay in the low-L region for a long time, while the loss of tens of keV protons is much faster at low L-shells. They also found that the contribution of the ring current electrons to the Dst index is noticeably smaller than that of the ions. Using Van Allen Probes observations between December 2012 and September 2013, Turner et al. (2015) found 47 events with signatures of electron injections at L-shells ≤ 4, which were limited in energy to ≤ 250 keV and followed the observations of

the injections at higher L-shells. They also noted that it is often difficult to distinguish electron injections from the enhanced convection during storms.

It still remains unclear which mechanisms are responsible for the earthward transport of ring current electrons within GEO. It was suggested that the global dawn-dusk electric field, driven by the dayside reconnection and antisunward magnetic field line convection, together with co-rotation-driven radial electric field, defines the electron drift path in the inner magnetosphere (e.g., Axford, 1969; Lyons and Williams, 1984, and references therein). Supporting this theory, Korth et al. (1999) found that lines demarcating enhanced electron flux at GEO match the Alfvén boundaries (the boundaries between open and closed drift trajectories) calculated using the Volland-Stern global electric field model (Volland, 1973; Stern, 1975). Using Polar data, Friedel et al. (2001) showed that electrons are organized by the Alfvén boundaries within GEO, shrinking and allowing deeper access of plasma during storm times.

It was proposed that energetic electrons can be injected in the magnetotail during geomagnetically active times by substorm-related localized Bursty Bulk Flows (BBFs) (Angelopoulos et al., 1992, 1994; Runov et al., 2009, 2011). Gabrielse et al. (2012) showed that the injections are driven by narrow channels of enhanced electric field associated with the BBFs. However, the efficiency of this transport mechanism to inject particles inside GEO still remains uncertain. Dubyagin et al. (2011) found that a significant fraction of flow bursts is unable to penetrate within 9 R_E, and Ohtani et al. (2006) concluded that only a small portion of BBFs can reach geostationary distances. Further studies (Sergeev et al., 2012; Liu et al., 2016) established that many BBFs are not accompanied by particle injections. Liu et al. (2016) showed that only 20 of 71 events of dipolarization fronts detected within GEO between 1 November 2012 and 1 November 2013 were associated with energetic electron injections, typically not propagating closer than ~6 R_E.

An increase in the large-scale electric field between $L = 3$ and $L = 6$, where L is McIlwain L-shell, for moderate to active geomagnetic conditions ($Kp > 3$) was reported by Rowland and Wygant (1998). They showed that, during the strongest geomagnetic activity, the enhanced electric field can be observed inside $L = 3$. Later, their results were confirmed by Califf et al. (2014). The enhancement was attributed to Subauroral Polarization Streams (SAPS) (e.g., Foster and Burke, 2002; Foster and Vo, 2002), the northward middle-latitude ionospheric electric field that arises from the separation between earthward ion and electron plasma sheet boundaries (Southwood and Wolf, 1978) and usually pronounced in the evening sector. Although initial steps were made in order to understand how SAPS affect electrons in the inner magnetosphere (Su et al., 2016; Califf et al., 2017; Lejosne et al., 2018), more comprehensive modeling studies

including electron transport and loss processes are required.

Understanding the dynamics of the ring current electron population is a challenging task, since the electron distribution significantly depends not only on time and radial coordinate, as it does for the radiation belts, but also on Magnetic Local Time (MLT). Multi-spacecraft measurements covering different MLT sectors are therefore required to observe the electron population in its global evolution. However, measuring this electron population is complicated by different external effects, such as surface charging and contamination by photoelectrons and penetrating radiation (see Denton et al., 2017, and references therein). Numerical modeling helps us gain insight into the dynamics of ring current electrons under the scarcity of satellite measurements.

In recent years, a number of ring current models have been developed (e.g., RCM code (Toffoletto et al., 2003; Lemon et al., 2004; Chen et al., 2015b), RAM code (Jordanova et al., 1996; Jordanova and Miyoshi, 2005; Jordanova et al., 2016), CIMI code (Fok et al., 1999, 2011, 2014), IMPTAM code (Ganushkina et al., 2013, 2014, 2015), and HEIDI code (Liemohn et al., 2001; Ilie et al., 2012)). The models include the ring current electron population and typically take into account the processes which are important for electron dynamics, such as global convection, localized particle injections, radial diffusion due to drift resonance with ULF waves, and local scattering rates of the electrons. All models face similar challenges in describing the dynamics of the electrons. Due to the complexity of the system, it is often difficult to analyze model errors. For instance, the underestimation of observed particle fluxes can be driven by overestimated scattering rates, as well as unrealistic transport processes or by the combination of both factors. Such model errors are the main hindrance for understanding which physical processes are responsible for the dynamics of the ring current electrons.

In this study, we use the VERB-4D code (Shprits et al., 2015; Aseev et al., 2016) to understand the mechanisms which control transport and loss of ring current electrons within GEO during the 17 March 2013 storm. By varying different model parameters, we examine the sensitivity of the model and determine the most significant processes which drive the electron transport and loss. To validate the model, we compare simulation results with Van Allen Probes measurements.

The manuscript is organized as follows. In Section 3.2, we present Van Allen Probes measurements during the 17 March 2013 storm. We describe the modeling approach in Section 3.3. We show simulation results and study the sensitivity of the code in Section 3.4. In Section 3.5, we discuss the results, and the main conclusions of the study are summarized in Section 3.6.

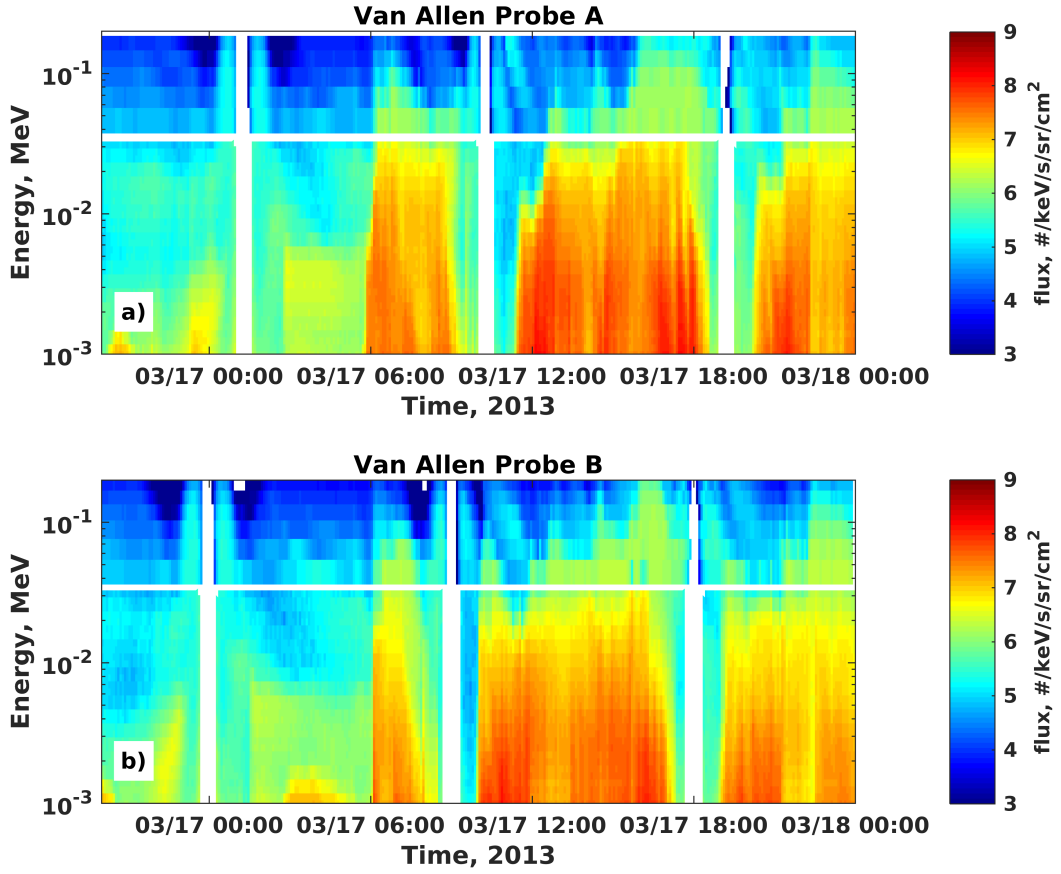

Figure 3.1: Combined HOPE and MagEIS spectrum for 90° local pitch angle for Van Allen Probes A (a) and B (b). The HOPE data above 30 keV are not shown, and the white horizontal line marks the energy boundary between the instruments.

3.2 Observations of the 17 March 2013 Storm

We use the combined Van Allen Probe Helium, Oxygen, Proton, and Electron (HOPE) Mass Spectrometer (Funsten et al., 2013) and Magnetic Electron Ion Spectrometer (MagEIS) (Blake et al., 2013) Level 3 particle data during the 17 March 2013 geomagnetic storm to calculate electron Phase Space Density (PSD) as a function of the first and second adiabatic invariants μ and K. The HOPE and MagEIS data match up well during the storm (e.g., see Figure 3.1, which illustrates electron flux spectrum during the storm), and we have not performed an additional intercalibration between the instruments. The apogee of the satellites is located at ~1 h MLT, and an inbound satellite pass traverses the postmidnight and prenoon MLT sectors, while an outbound pass crosses postnoon and premidnight sectors. We use T04S magnetic field model (Tsyganenko and Sitnov, 2005) incorporated into the IRBEM library (Boscher et al., 2012) to calculate invariants μ and K from observed local pitch angles and energies.

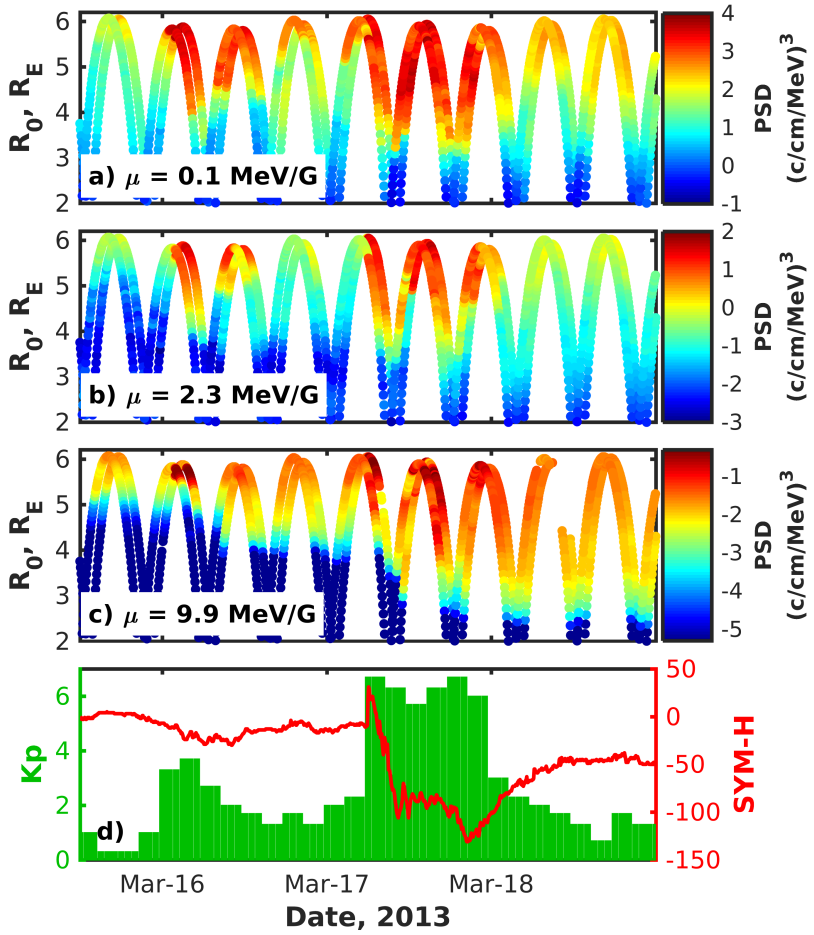

Figure 3.2: (a-c) Electron PSD derived from Van Allen Probes observations for μ = 0.1, 2.3, and 9.9 MeV/G and K = 0.3 $G^{1/2}R_E$ during the 17 March 2013 storm. (d) The Kp (green) and SYM-H (red) indices.

To determine values of μ, we also use magnetic field measurements made by Electric and Magnetic Field Instrument Suite and Integrated Science (EMFISIS) (Kletzing et al., 2013) on board the satellite. Since values of μ and K vary along the satellite trajectory, we use bilinear interpolation to calculate PSD for given constant μ and K.

Figure 3.2a-3.2c shows five-minute-averaged electron PSD which are obtained from the data for the first adiabatic invariant μ = 0.1, 2.3, and 9.9 MeV/G and second invariant K = 0.3 $G^{1/2}R_E$ during the 17 March 2013 storm. The chosen values of the invariants approximately correspond to energies 0.3, 9, and 30 keV at GEO and 1, 30, and 100 keV at L=4 (see Figure 3.3 illustrating energy and pitch-angle dependence on the L-shell). The corresponding pitch angles vary from ~34° at GEO to 40° at L=3, which ensures that Van Allen Probes data are available even if the satellite is significantly off the geomagnetic equator, which can happen during active times.

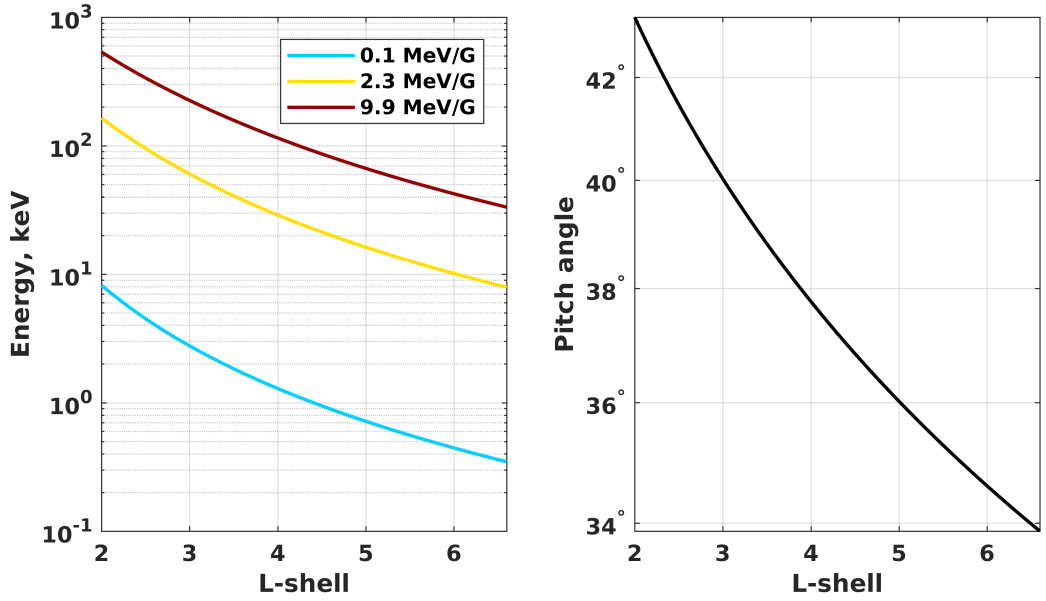

Figure 3.3: Energies and pitch angles corresponding to different values of the first adiabatic invariant μ. The second invariant $K = 0.3\ \mathrm{G}^{1/2}\mathrm{R}_E$ is constant. The energies and pitch angles are calculated using the dipole field.

The geomagnetic storm was driven by a coronal mass ejection that hit the Earth's magnetosphere at 6:00 (see Lyons et al. (2016) for more detail). In response to the storm, the Kp index (Figure 3.2d) showed values above 6– for 18 hours, and the SYM-H index (Figure 3.2d) reached −130 nT, indicating significant enhancement of the ring current. Ring current electrons were injected down to R_0 = 2.5-3 R_E, showing the increase in the PSD until the main phase of the storm ended on ~18 March (see Figure 3.2a-3.2c). We note that R_0 denotes here the distance from the center of the Earth to the point of the minimum magnetic field found along the field line at which the spacecraft resides (for this, we used Olson and Pfitzer (1977) and IGRF (Thébault et al., 2015) magnetic field models). The recovery phase was characterized by the sharp decrease in 0.1 and 2.3 MeV/G electron PSD and a more gradual decrease in 9.9 MeV/G electron PSD.

Although the storm-time dynamics of electrons for considered values of μ and K may look similar, it can be driven by different energy-dependent mechanisms. Particles with a half-drift period longer than the main phase of the storm have direct convective access to the ring current region (Lyons and Williams, 1980). The higher-energy particles have shorter drift periods and more efficiently interact with electric field fluctuations, which lead to the inward displacement driven by radial diffusion (Cornwall, 1968; Lyons and Schulz, 1989). Lyons and Schulz (1989) showed that particles with energies $\gtrapprox$ 40 keV are closer to diffusive access, while $\lessapprox$ 40 keV particles

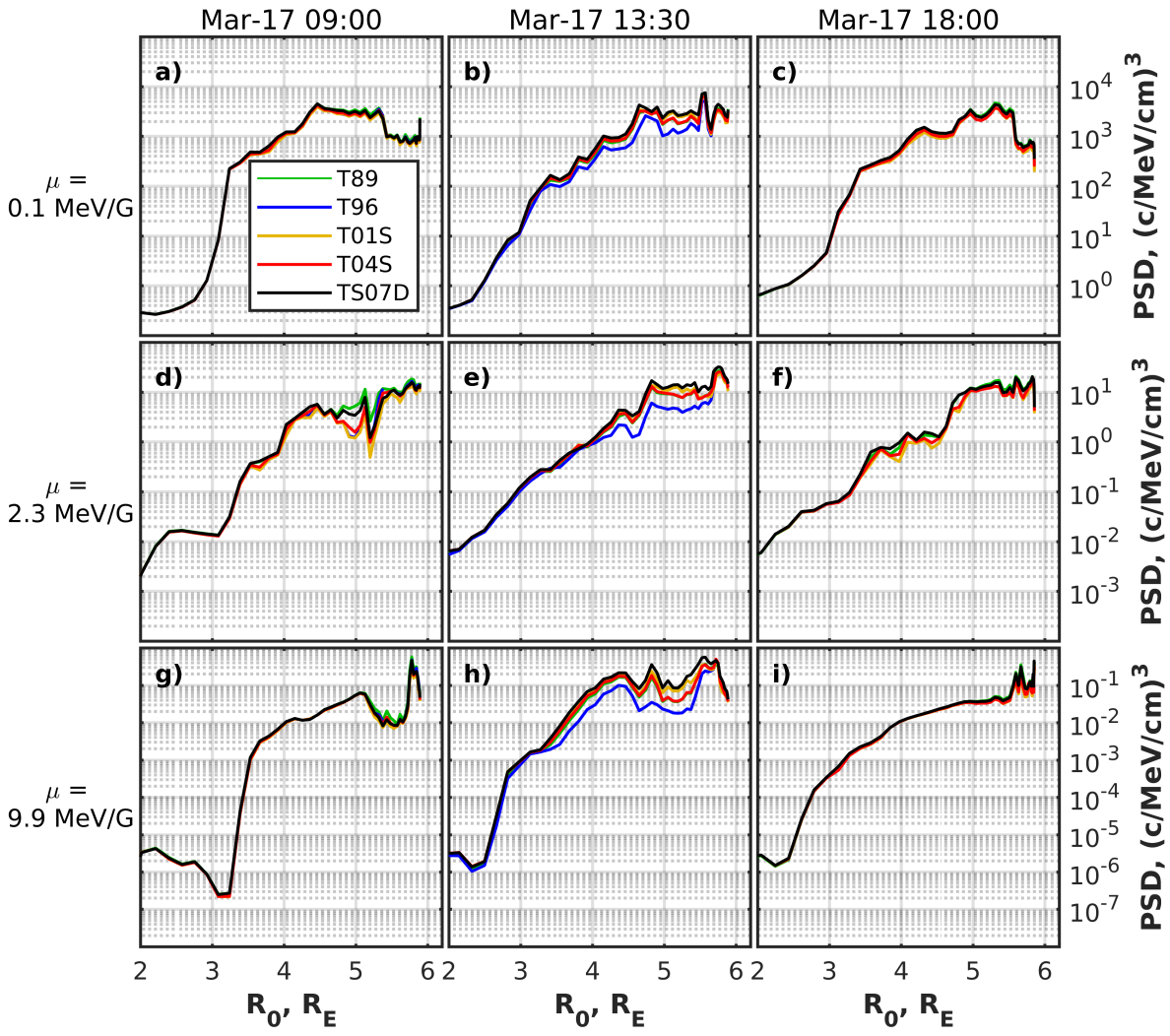

Figure 3.4: Profiles of electron PSD for $K = 0.3$ $G^{1/2}R_E$ and $\mu = 0.1$ MeV/G (a-c), 2.3 MeV/G (d-f), and 9.9 MeV/G (g-i) calculated using different magnetic field models for three subsequent Van Allen Probe B passes. Columns correspond to the passes beginning at 9:00, 13:30, and 18:00 on 17 March (from left to right).

have convective access.

The calculated PSD may depend on the used magnetic field model since the calculation of the invariant K requires an integration along a field line that crosses the spacecraft location. Errors in the field model may lead to the uncertainties in the computed PSD. To study the effects of different magnetic field models, we also calculated PSD, using the Tsyganenko (1989) (T89), Tsyganenko (1995) (T96), Tsyganenko (2002) (T01S), and Tsyganenko and Sitnov (2007) (TS07D) models.

Figure 3.4 shows the calculated PSD profiles as a function of R_0 for three consecutive Van Allen Probe B passes during the main phase of the storm. For the first satellite

pass beginning at 9:00 on 17 March, the magnetic field models have almost no effect on μ = 0.1 and 9.9 MeV/G electron PSD, while a small difference in PSD is observed for 2.3 MeV/G particles between ~4.6 and 5.3 R_E. For the next pass beginning at 13:30, the PSD profiles which were calculated using T89, T01S, T04S, and TS07D models slightly differ above ~4.8 R_E for all values of the first invariant, and the T96 model results in generally lower PSD, which are up to one order of magnitude smaller than the profiles calculated using the TS07D model. The PSD values along the following pass at 18:00 show insignificant differences for all profiles. As will be shown later, the differences in the PSD obtained from the Van Allen Probe measurements are much smaller than the uncertainties in the numerical model of the ring current electrons, and the errors which the T04S model introduces can be neglected, given a much larger model uncertainty.

3.3 Model Description

We use the VERB-4D code to model the dynamics of the ring current electrons. The code solves the modified Fokker-Planck equation with additional advection terms (Shprits et al., 2015; Aseev et al., 2016). It allows simultaneous modeling of ring-current and radiation belt dynamics by combining electron drift, radial diffusion, pitch-angle and energy diffusion and loss processes that can be parameterized with the lifetime τ (e.g., magnetopause shadowing is accounted by setting up τ to 1/2 drift period, and loss to the atmosphere is accounted by setting up the lifetimes within the loss cone to 1/4 bounce time):

$$\begin{aligned}\frac{\partial f}{\partial t} = &-v_\varphi \frac{\partial f}{\partial \varphi} - v_{R_0} \frac{\partial f}{\partial R_0} + \frac{1}{G_{(V,K,L^*)}} \frac{\partial}{\partial L^*} G_{(V,K,L^*)} D_{L^*L^*} \frac{\partial f}{\partial L^*} + \\ &+ \frac{1}{G_{(V,K,L^*)}} \frac{\partial}{\partial V} G_{(V,K,L^*)} \left(D_{VV} \frac{\partial f}{\partial V} + D_{VK} \frac{\partial f}{\partial K} \right) + \\ &+ \frac{1}{G_{(V,K,L^*)}} \frac{\partial}{\partial K} G_{(V,K,L^*)} \left(D_{KV} \frac{\partial f}{\partial V} + D_{KK} \frac{\partial f}{\partial K} \right) - \frac{f}{\tau},\end{aligned} \tag{3.1}$$

where f is the PSD, t represents time, φ is MLT, R_0 is the radial distance to a given point at the geomagnetic equator, V, K, and L^* are modified adiabatic invariants (Subbotin and Shprits, 2012), $V = \mu \cdot (K+0.5)^2$, μ is the first adiabatic invariant, τ is electron lifetime related to scattering into the loss cone and magnetopause shadowing, v_φ and v_{R_0} are bounce-averaged drift velocities, $D_{L^*L^*}$, D_{VV}, D_{VK}, D_{KV}, and D_{KK} are bounce-averaged diffusion coefficients, $G_{(V,K,L^*)} = -2\pi B_E R_E^2 \sqrt{8 m_0 V}/(K+0.5)^3/L^{*2}$ is the Jacobian of the coordinate transformation from adiabatic invariants (μ, J, Φ) to (V, K, L^*) (Subbotin and Shprits, 2012), B_E is the field at the equator at the Earth's surface, m_0 is electron rest mass.

The VERB-4D code has been designed to simplify the implementation of the most important physical processes responsible for the electron dynamics and allows us to efficiently perform ensemble simulations or study sensitivity of the code to different input parameters. The numerical schemes implemented in the code have been thoroughly tested (Aseev et al. (2016) and Chapter 2), and it is guaranteed that the numerical errors do not affect physical interpretation of the results.

The spatial boundaries are set up at R_0 = 1 and 6.6 R_E with 0.5 h and 0.2 R_E grid steps in MLT and radial distance, respectively. To construct a grid in V and K, we create a logarithmic grid in energy and pitch angles limited by 200 eV and 30 keV and 0.7° and 89.3° at GEO with 60 nodes in energy and 61 nodes in pitch angle. Adiabatic invariants are then calculated on this grid, using the dipole field model. We choose these energy limits at GEO to fit in the statistical boundary condition model described below.

To model the enhancement of PSD during the main phase of the storm, we set up initial conditions from the Van Allen Probe-B inbound pass starting at 20:00 on 16 March and ending at midnight on 17 March. We use PSD derived from HOPE and MagEIS measurements, assume symmetry in MLT, and assign the calculated initial conditions to 20:00 16 March. Boundary conditions in MLT are periodic. At the lower boundary R_0 = 1 R_E, we assume zero PSD since all particles are lost in the atmosphere. To specify the outer boundary at R_0 = 6.6, we use a statistical model of electron fluxes developed by Denton et al. (2016). The model is based on 82 satellite-years of observations at GEO made by magnetospheric plasma analyzer instruments on board Los Alamos National Laboratory satellites. The model provides spin-averaged electron fluxes as a function of energy, MLT and the Kp index and covers the energy range from ~40 eV to 40 keV at GEO. Along with the mean and median values of the fluxes, 5th, 25th, 75th, and 95th percentile limits are also given. To obtain directional flux from the spin-averaged flux, we assume its sinusoidal dependence on the pitch angle.

We take into account electron scattering driven by hiss and chorus waves by using parameterized electron lifetimes included in the parameter τ instead of local diffusion terms (fourth and fifth terms on the right-hand side of equation (3.1)). In this case, boundary conditions in the invariants V and K are not required, since there is no feedback from local diffusion terms. We use the MLT-averaged model of electron lifetimes within the plasmasphere developed by Orlova et al. (2016). Outside the plasmasphere, we utilize the MLT-dependent scattering rates obtained by Gu et al. (2012). The plasmapause location is calculated using the Carpenter and Anderson (1992) model.

We use the realistic Tsyganenko (1989) (T89) magnetic field model and the Weimer (2005) (W05) polar cap potential model to calculate electron **E**×**B** and gradient-

curvature drift velocities at the geomagnetic equator. The polar cap potential is mapped along the equipotential dipole field lines down to the geomagnetic equator. At the equator, the electric field is numerically calculated, using a central differencing scheme (we refer to the calculated electric field as the W05 electric field model). Compared to the commonly used Kp-driven Volland-Stern electric field model, the W05 model is parameterized with solar wind parameters, which ensures more realistic variability of the global electric field, naturally driven by the dayside reconnection. In the current work, we feed 15-minute averaged solar wind parameters to the W05 model.

We utilize Kp-parameterized radial diffusion rates by Brautigam and Albert (2000). We note that similar results are obtained with the parameterization developed by Ozeke et al. (2014). To simultaneously account for the direct convective and diffusive access of electrons to the ring current region, we smoothly zero out the diffusion rates for electron energies smaller than the threshold of 40 keV proposed by Lyons and Schulz (1989).

3.4 Results

In this section, we show the results of the VERB-4D code and compare them with the PSD calculated along Van Allen Probes trajectories. We present the confidence intervals of the model which are associated with the uncertainties in the outer boundary conditions. We also study the sensitivity of the results to the input parameters such as convection electric field, electron loss rates, radial diffusion coefficients, and SAPS electric fields.

We start all simulations which are presented in this section at 20:00 on 16 March 2013 with a time step of 15 minutes. We stop the simulations at 00:00 on 18 March 2013 to model the storm-time enhancement of PSD across a given range of energies. We then interpolate the global distribution of PSD provided by the VERB-4D code along Van Allen Probes trajectories, using linear interpolation in time, radial distance, and MLT. The target values of μ and K invariants to compare with satellite data were chosen to match the corresponding grid values of the VERB-4D code.

3.4.1 Model-Data Comparison along Van Allen Probes Orbits

We use the mean value of the Denton et al. (2015) statistical flux distribution and the W05 electric field to model the storm-time dynamics of the ring current electrons. Other input parameters are the same as described in Section 3.3.

Figure 3.5 shows the comparison between Van Allen Probes data and the results of the VERB-4D code for μ = 0.1, 2.3, and 9.9 MeV/G and K = 0.3 $G^{1/2}R_E$ electrons. The

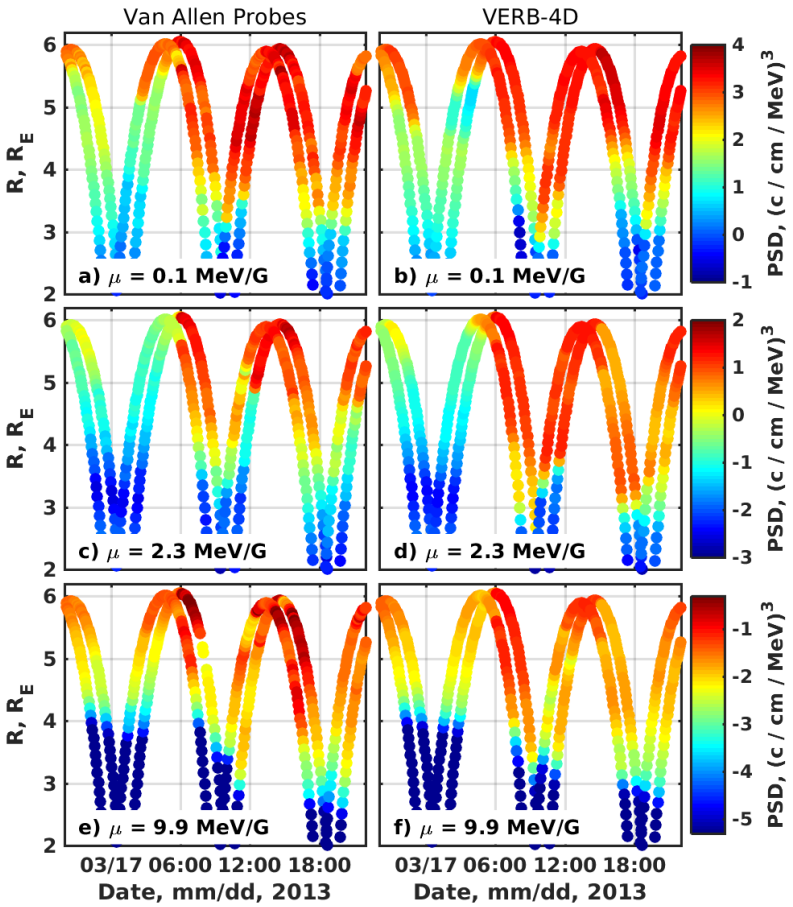

Figure 3.5: Comparison of Van Allen Probes PSD (left column) with the VERB-4D code results (right column) for μ = 0.1, 2.3, and 9.9 MeV/G and K = 0.3 $G^{1/2}R_E$. The figure represents an in-situ comparison, made at the location of the spacecraft. The mean boundary flux is used. A leftmost orbit along a given inbound or outbound pass corresponds to Van Allen Probe B trajcetory. $R \equiv R_0$.

leftmost orbit along a given inbound or output pass in Figure 3.5 corresponds to the Van Allen Probe B trajectory since Van Allen Probe B moves ahead of Van Allen Probe A for the chosen time interval.

The storm-time dynamics of the 0.1 MeV/G electrons (Figure 3.5a) is reproduced relatively well by the VERB-4D code (Figure 3.5b). The code captures the time and radial extent of the PSD enhancement. The measurements along the pass starting at 6:00 on 17 March 2013, just before the storm onset, show the increase in electron PSD from ~6 R_E to as low as 3.5-4 R_E, and the code is able to reproduce the increase, predicting the radial extent of the enhancement ~0.1-0.2 R_E farther away from the Earth than is seen in the data. In agreement with the data, the model results show the earthward penetration of the electrons along the next satellite pass at ~9:00 down to 3 R_E for Van Allen Probe B and to 3.5 R_E for Van Allen Probe A. For the next two passes,

the model agrees well with the observations between ~4 R_E and 6 R_E and generally underestimates PSD between 3 and 4 R_E.

The comparison between the code and the data for μ = 2.3 and 9.9 MeV/G electrons between ~6:00 and 10:00 reveals an interesting fact that the enhancements in the modeled PSD extend closer to the Earth than the data show, while the code agrees well with the data for μ = 0.1 MeV/G electrons. The increase in 2.3 MeV/G PSD is observed down to ~4 R_E (Figure 3.5c), and the code predicts higher PSD between 3 and 4 R_E (Figure 3.5d). The observed enhancement in 9.9 MeV/G electron PSD extends down to 4.5-5 R_E (Figure 3.5e) for the same time interval, while the enhancement in the code spreads down to 3.5-4 R_E (Figure 3.5f). Such a mismatch in the model predictions between 0.1 MeV/G and higher energy electrons can be explained by the strong convection electric field or shorter lifetimes of the 0.1 MeV/G electrons which are implemented in the model.

For the outbound satellite pass between ~10:00 and 13:00, the code overestimates the observations for μ = 2.3 MeV/G electrons from ~3.5 to 4.9 R_E, which can be due to the stronger earthward propagation that occurred during the previous pass. We note that Van Allen Probe A shows the sudden increase in electron PSD at 4.9 R_E that occurred at 12:00, as the satellite moves to the apogee. Such an increase cannot be attributed to the energy boundary between HOPE and MagEIS instruments, since the boundary is located at ~3.2 R_E for the given first and second adiabatic invariants. The nature of the increase is not clear, since Van Allen Probe B traversing a similar region shows much higher PSD between 4 and 4.9 R_E than Van Allen Probe A observes. The model overestimates PSD between 3 and 4.5 R_E along the next two satellite passes after 13:00 and agrees better at higher radial distances.

The model results for the μ = 9.9 MeV/G particles matches well the observations between 3 and 4 R_E after 10:00, despite the overestimated PSD at the previous satellite pass. Above 4 R_E, the model generally shows slightly lower PSD values than observed in the data.

The results presented in this section indicate that the model is capable of qualitatively and quantitatively reproducing the dynamics of the ring current electron population above 4.5 R_E. The model can capture the features of the enhancements in that region, although the magnitude of PSD may slightly differ from the observations. The differences between the model and data above 4.5 R_E can be explained by the simplified Kp-dependent model of the spatial outer boundary conditions. Below 4.5 R_E, the discrepancies between the model and the data are generally higher, which can be indicative of the uncertainties in electric and magnetic fields or in electron lifetimes. In the next sections, we study the discrepancies between the model and the data in more

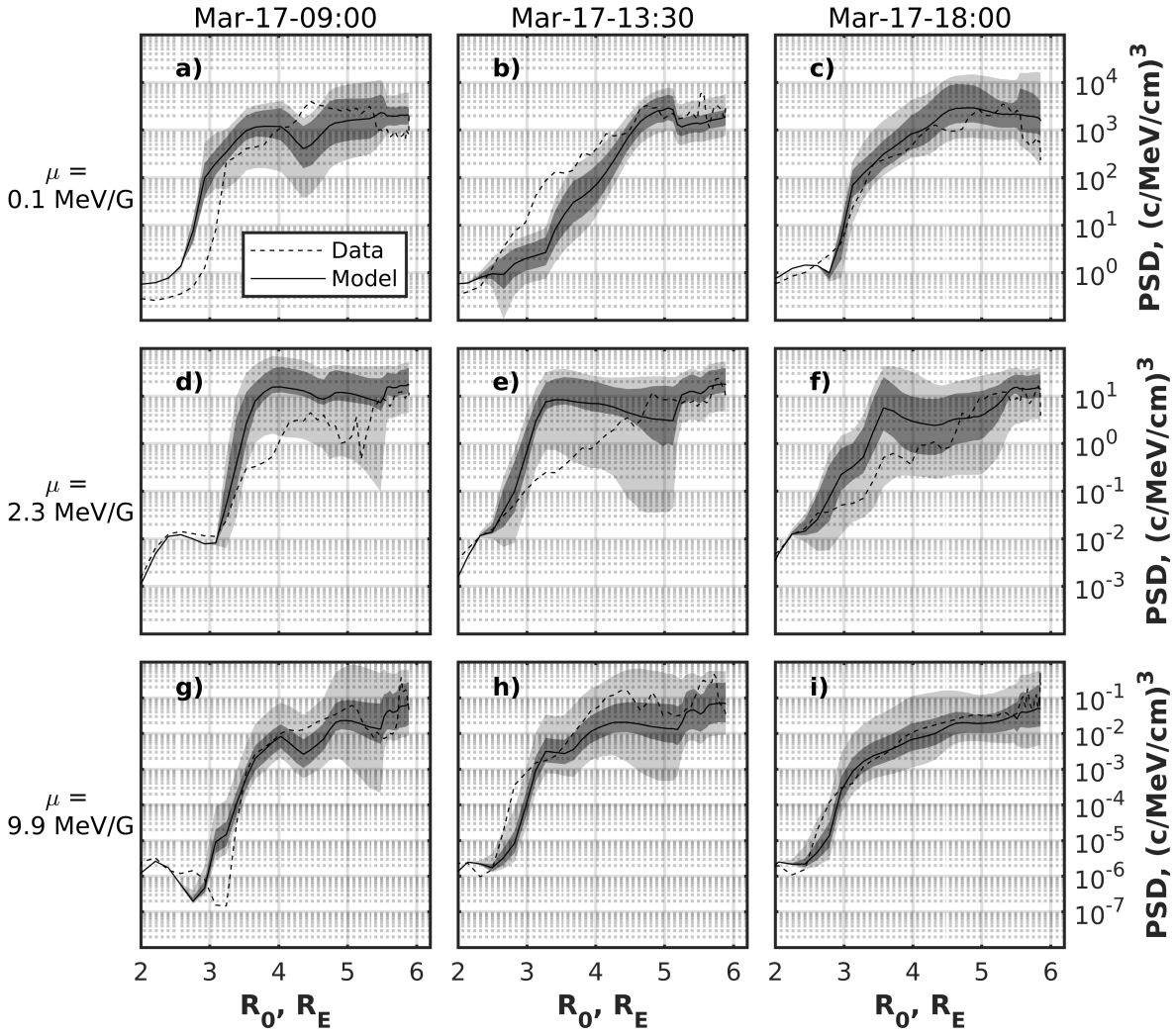

Figure 3.6: Comparison between Van Allen Probe B data (dashed lines) with the VERB-4D code results (solid lines) for K = 0.3 $G^{1/2}R_E$ and μ = 0.1 MeV/G (a-c), 2.3 MeV/G (d-f), and 9.9 MeV/G (g-i). Columns correspond to satellite passes beginning at 9:00, 13:30, and 18:00 on 17 March (from left to right). The dark-grey regions are limited by the 25th and 75th percentiles of the outer radial boundary conditions. The light-grey regions are limited by the 5th and 95th percentiles.

detail by analyzing the sensitivity of the code to the input parameters.

3.4.2 Sensitivity to the Outer Boundary Conditions

To study the sensitivity of the model to the boundary conditions and provide approximate confidence interval of the model, we perform simulations with 5th, 25th, 75th, and 95th percentiles of statistical distribution of electron flux at GEO (Denton et al., 2015), keeping all other input parameters the same as in Section 3.4.1. Figure 3.6 presents PSD profiles for μ = 0.1, 2.3, and 9.9 MeV/G and K = 0.3 $G^{1/2}R_E$, together

with percentile limits for three subsequent Van Allen Probe B passes starting at 9:00 on 17 March. The figure shows that, most of the time, satellite data are within the percentile limits, generally showing better agreement above R_0 = 3.5 R_E across all adiabatic invariants. Note that PSD varies by up to 4 orders of magnitude, and the model covers rather well this variability within the confidence interval. Below 3.5 R_E, μ = 0.1 MeV/G electron PSD profiles diverge from simulation results, demonstrating deeper earthward displacement by approximately 0.3 R_E for the satellite pass that started at 9:00 (Figure 3.6a) and lower PSD values for the next pass (Figure 3.6b), underestimating the inner boundary by approximately 0.3 R_E. The results for 2.3 MeV/G electrons are generally higher than the data for the first two presented satellite passes between 3 and 4 R_E, yet the satellite observations show much better agreement at others radial distances. The values and shapes of PSD profiles for μ = 9.9 MeV/G are very close to the 25th and 75th percentile limits across all radial distances.

Although the magnitude of the modeled PSD depends on the outer boundary conditions which are used in the simulations, the shape of the profiles remains mostly unchanged. This fact does not necessarily imply that the boundary conditions have no effect on the shape of the profiles or the observed smaller-scale features. Since we use different percentile values of the electron flux at GEO as the boundary conditions, the increase or decrease in the magnitude of the boundary conditions takes place along all MLT sectors at the same time. The percentile values thus provide approximate lower and upper limits of the PSD magnitude and do not affect the shape of the profiles.

The fact that the Van Allen Probe observations do not fit in the 5th and 95th percentile limits indicates that the discrepancies between the model and data, which is evident in Figure 3.6a below 3 R_E and in Figures 3.6b and 3.6e between 3 and 4 R_E, are most probably caused by other model parameters, such as electric field or electron loss rates.

3.4.3 Role of the Electric Field Model

The differences between the observed PSD and the results of the VERB-4D code (e.g., see Figure 3.5) can partially stem from the inaccuracies of the electric field model. In this section, we study the role of the global electric field in the simulations.

Figure 3.7 presents the comparison between the local electric field measured by the Van Allen Probe Electric Field and Waves (EFW) instrument (Wygant et al., 2013) and the W05 electric field model interpolated in time and space along the satellite trajectory. The presented electric fields are in a reference frame co-rotating with the Earth. We use a 6-minute moving average of the observed electric fields. We eliminate intervals when spacecraft charging affects the measurements and when the satellites

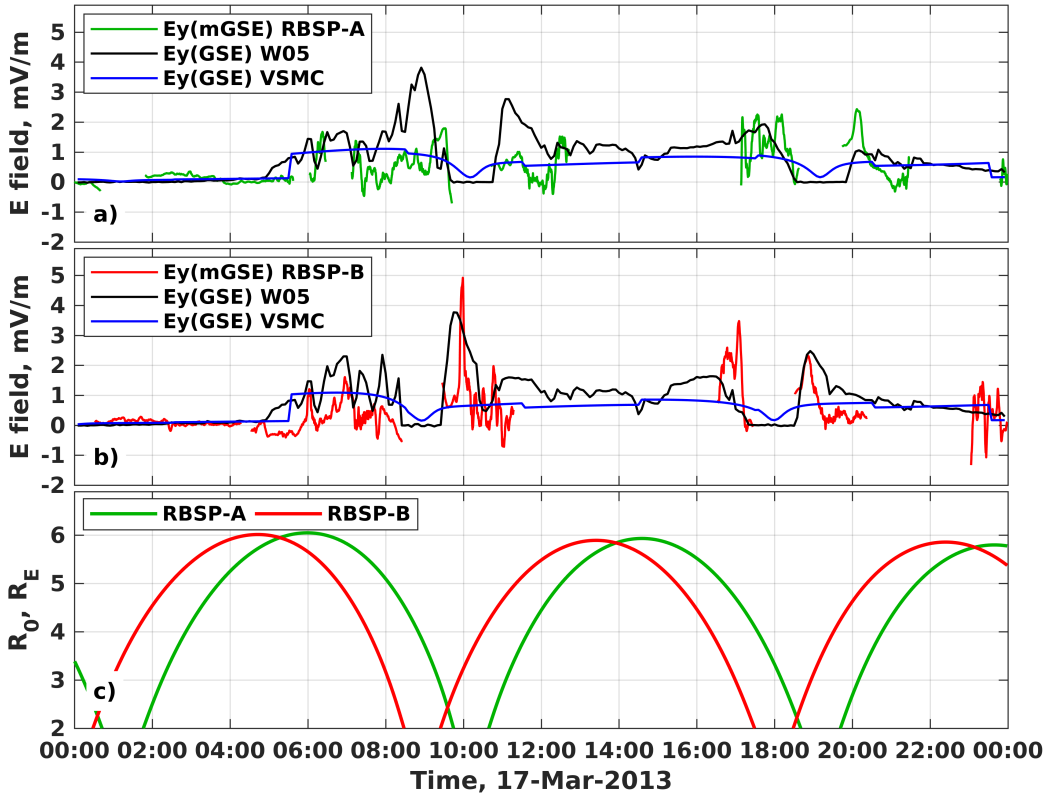

Figure 3.7: (a-b) Comparison between electric fields measured by Van Allen Probes A and B (green and red lines), the W05 electric field model (black lines), and the VSMC electric field model (blue lines). The electric fields are presented in the reference frame co-rotating with the Earth. The model electric fields are calculated along the satellite trajectories. (c) Van Allen Probes R_0 (the distance from the center of the Earth to the point of the minimum magnetic field along the magnetic field line crossing the spacecraft location).

reside in the Earth's shadow and observations are compromised. Figure 3.7 shows the measured E_y component in the MGSE coordinate system (Wygant et al., 2013) and the E_y component in GSE system obtained from the W05 model. The MGSE system has been developed to isolate the more accurately measured components of the electric field, and the Y-axis in GSE system is most nearly aligned with the Y-axis in MGSE system.

The W05 electric field is similar to the Van Allen Probe observations between ~6:00 and 8:00 on 17 March 2013, slightly overestimating the measurements. When Van Allen Probe A moves towards perigee, it observes an increase in the electric field magnitude from 8:00, when the spacecraft is at 5 R_E, to ~9:30, when the spacecraft resides at 3 R_E. The W05 model also predicts an increase in the electric field, but the model shows a distinct peak at 9:00 (~ 3.5 R_E) that is ~3.5 times higher than observed electric

field (Figure 3.7a). The W05 electric field at the next satellite pass also shows a peak at the same location. Van Allen Probe B shows a similar enhancement at ~10:00, which is, however, more narrow than the W05 model predicts (see Figure 3.7b). Overall, the model electric field noticeably overestimates the measurements between 8:00 and 10:00. Such an overestimation can explain the fact that the model results are higher than the data for 2.3 and 9.9 MeV/G particles below 4-4.5 R_E along the inbound satellite pass beginning at 6:00 (see Figure 3.5).

To understand how the global electric field can affect simulation results, we perform a simulation, using the Kp-dependent Volland-Stern electric field model (Volland, 1973; Stern, 1975; Maynard and Chen, 1975) (VSMC) and keep all other parameters the same as in Section 3.4.1. The comparison of the VSMC electric field with the EFW measurements is shown in Figure 3.7. Since the Kp index reaches ~6 and stays approximately constant for 18 hours, the VSMC model shows almost no variations which are constantly seen in the data. Compared to the W05 model, the E_y component of the VSMC electric field is mostly lower, and the models agree better at higher radial distances.

Figure 3.8 presents the comparison of the resulting PSD for μ = 0.1, 2.3, 9.9 MeV/G and K = 0.3 $G^{1/2}R_E$ electrons interpolated along Van Allen Probe B trajectory for different electric field models. The electric field models have almost no effect on the profiles of 9.9 MeV/G electrons, due to the gradient and curvature drifts, which are relatively strong for these particles. The magnitudes of 0.1 and 2.3 MeV/G electron PSD for W05 and VSMC electric field models are very similar above ~4.5 R_E. This result is consistent with Figure 3.7, showing that both electric field models do not differ much at higher radial distances. Below 4.5 R_E, where the VSMC electric field is much smaller than the W05 field, the electron profiles obtained with the VSMC model are significantly lower compared to the profiles obtained with the W05 model. The VSMC electric field model leads to larger differences in 0.1 and 2.3 MeV/G electron PSD profiles and data between ~2.5 and 4-4.5 R_E. We note a peak in the 0.1 MeV/G profiles that is observed near 3 R_E, which can be formed due to a stronger loss and slow earthward transport from GEO if the VSMC model is used.

Figures 3.9 and 3.10 illustrate the global evolution of the modeled PSD for μ = 2.3 MeV/G and K = 0.3 $G^{1/2}R_E$ electrons for different electric field models and several time moments during the main phase of the storm. At 6:00 on 17 March 2013, just before the storm, the PSD obtained with the W05 model show the increase propagating from GEO to ~5 R_E at the night side (Figure 3.9a), while the VSMC model only predicts the increase down to ~6 R_E (Figure 3.10a). In general, the W05 model leads to propagation of the electrons down to 3 R_E at a later time, up to 1 R_E deeper than in

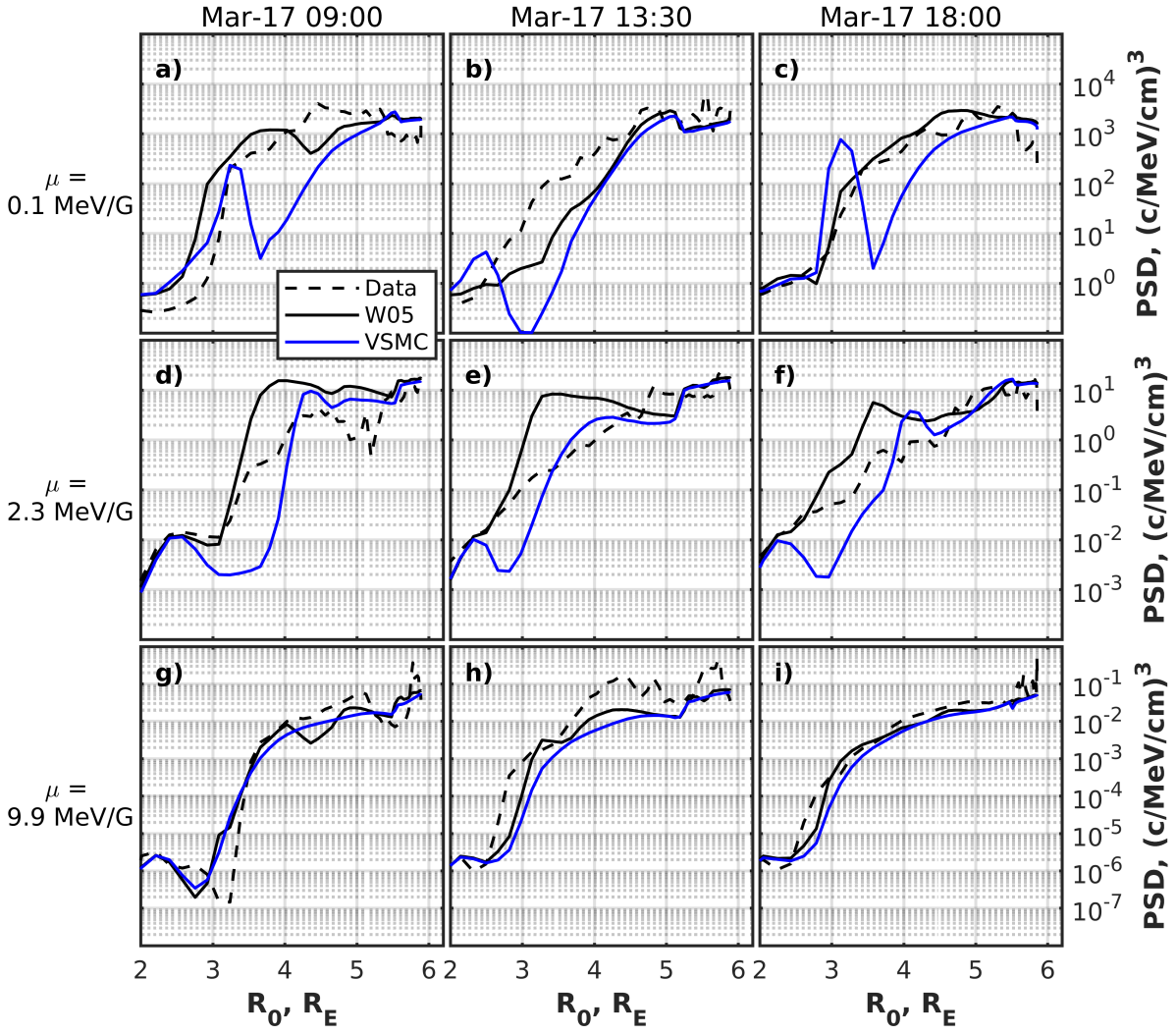

Figure 3.8: Comparison between Van Allen Probe B PSD (dashed lines) with the VERB-4D code results if the W05 electric field model is used (black solid line), and if the VSMC electric field model is used (blue solid lines) for K = 0.3 $G^{1/2}R_E$ and μ = 0.1 MeV/G (a-c), 2.3 MeV/G (d-f), and 9.9 MeV/G (g-i). Columns correspond to satellite passes beginning at 9:00, 13:30, and 18:00 on 17 March (from left to right).

the case of the VSMC model. The enhanced PSD obtained with the W05 model fill the region between 3 and 5 R_E in the MLT sector between 21 and 12 h from 9:00 to 18:00 (Figures 3.9b-3.9e). Such an enhancement is also evident in Figure 3.6 as a peak in 2.3 MeV/G electron PSD profiles computed with the VERB-4D code. The VSMC model predicts lower PSD in the same region (Figures 3.10b-3.10e). Both models give qualitatively and quantitatively similar results above 4.5-5 R_E, in good agreement with the data, as shown in Figure 3.8. Another region of the difference in the modeled global distributions is around the duskside from 14 to 21 h MLT. This region contains the

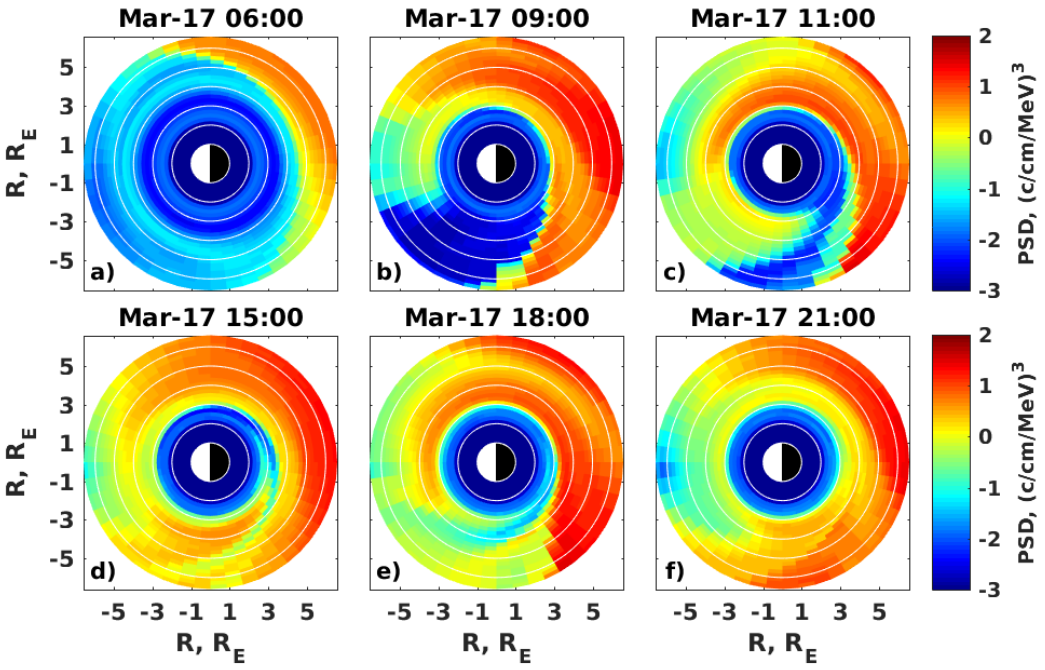

Figure 3.9: Global PSD distribution of μ = 2.3 MeV/G and K = 0.3 $G^{1/2}R_E$ electrons obtained with the VERB-4D code if the W05 electric field model is used. $R \equiv R_0$.

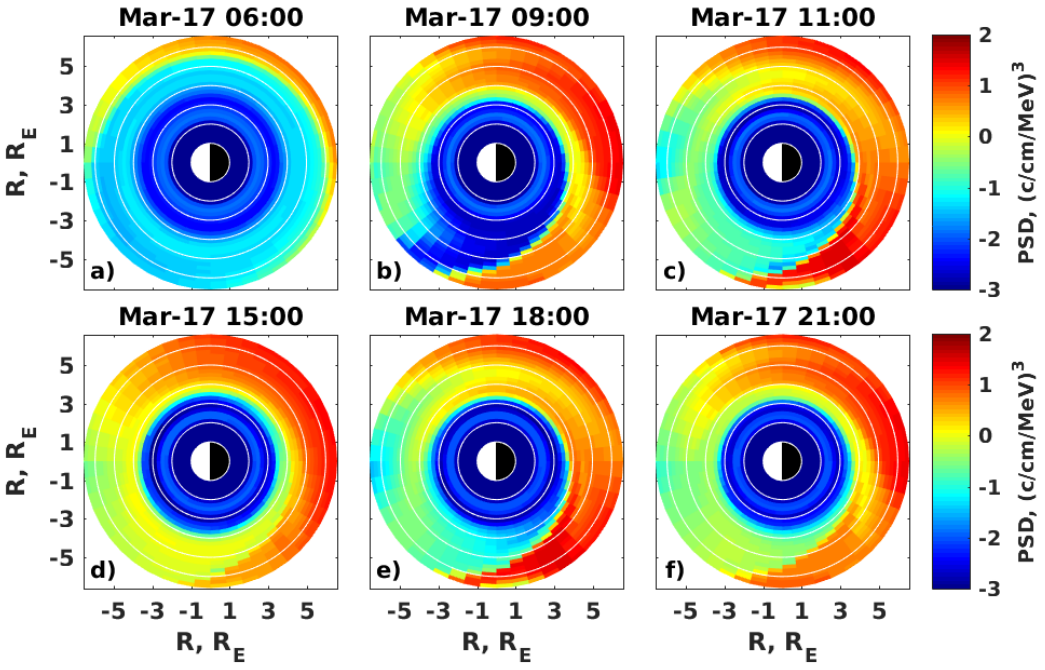

Figure 3.10: Global PSD distribution of μ = 2.3 MeV/G and K = 0.3 $G^{1/2}R_E$ electrons obtained with the VERB-4D code if the VSMC electric field model is used. $R \equiv R_0$.

stagnation point that separates open and closed drift paths, and the small difference in the electric field model can affect the trapping of particles in the code and potentially lead to the over- or underestimation of the measurements. We note that Van Allen Probes do not cross this region during the considered event, and the difference in the dynamics there have to be addressed in future studies.

3.4.4 Sensitivity to the Electron Lifetime Model

In this section, we study the sensitivity of the code results to the electron lifetime model. We perform several simulations with the same model parameters as described in Section 3.4.1, and vary the electron lifetimes outside the plasmasphere. We multiply and divide the lifetimes by 2 and 10, and if the lifetimes are lower than the strong diffusion limit predicts, we assume the strong diffusion approximation.

Figure 3.11 presents the resulting profiles interpolated along the Van Allen Probe B trajectory for different electron lifetimes. The μ = 0.1 MeV/G profiles are the most sensitive to the changes in the lifetimes. The two-fold increase or decrease in the lifetimes may lead to the difference in PSD larger than 1 order of magnitude and different shape of the profiles (e.g., Figure 3.11b). The μ = 2.3 MeV/G profiles are less sensitive to the increase in the electron lifetimes (Figures 3.11d-3.11f), while the profiles differ more significantly if the lifetimes are decreased. The two-fold decrease in the lifetimes results in similar shape and magnitude of the profiles, while the ten-fold decrease leads to unrealistically low model results. The profiles of μ = 9.9 MeV/G particles are not noticeably changed due to the increase and two-fold decrease in electron lifetimes, and the ten-fold decrease in electron lifetimes produces results much smaller than the data. The model results are generally less sensitive to the electron lifetimes above 4.5 R_E for all μ values, while the difference between the simulations grows with decreasing radial distance.

3.4.5 Effects of Radial Diffusion

To demonstrate the role of the radial diffusion, we perform an additional simulation with all input parameters which have been used in Section 3.4.1 and set up the radial diffusion coefficient $D_{L^*L^*}$ to zero. Figure 3.12 shows the comparison between the simulations with and without the radial diffusion term for μ = 9.9 MeV/G and K = 0.3 $G^{1/2}R_E$ electrons. We note that the diffusion coefficient for 0.1 and 2.3 MeV/G electrons is zero by the setup of the model, and the results of both simulations are identical for these particle populations. The simulation with the radial diffusion term agrees better with the data for all considered satellite passes. The difference between the simulations is most evident along a satellite pass starting at 9:00 (Figure 3.12).

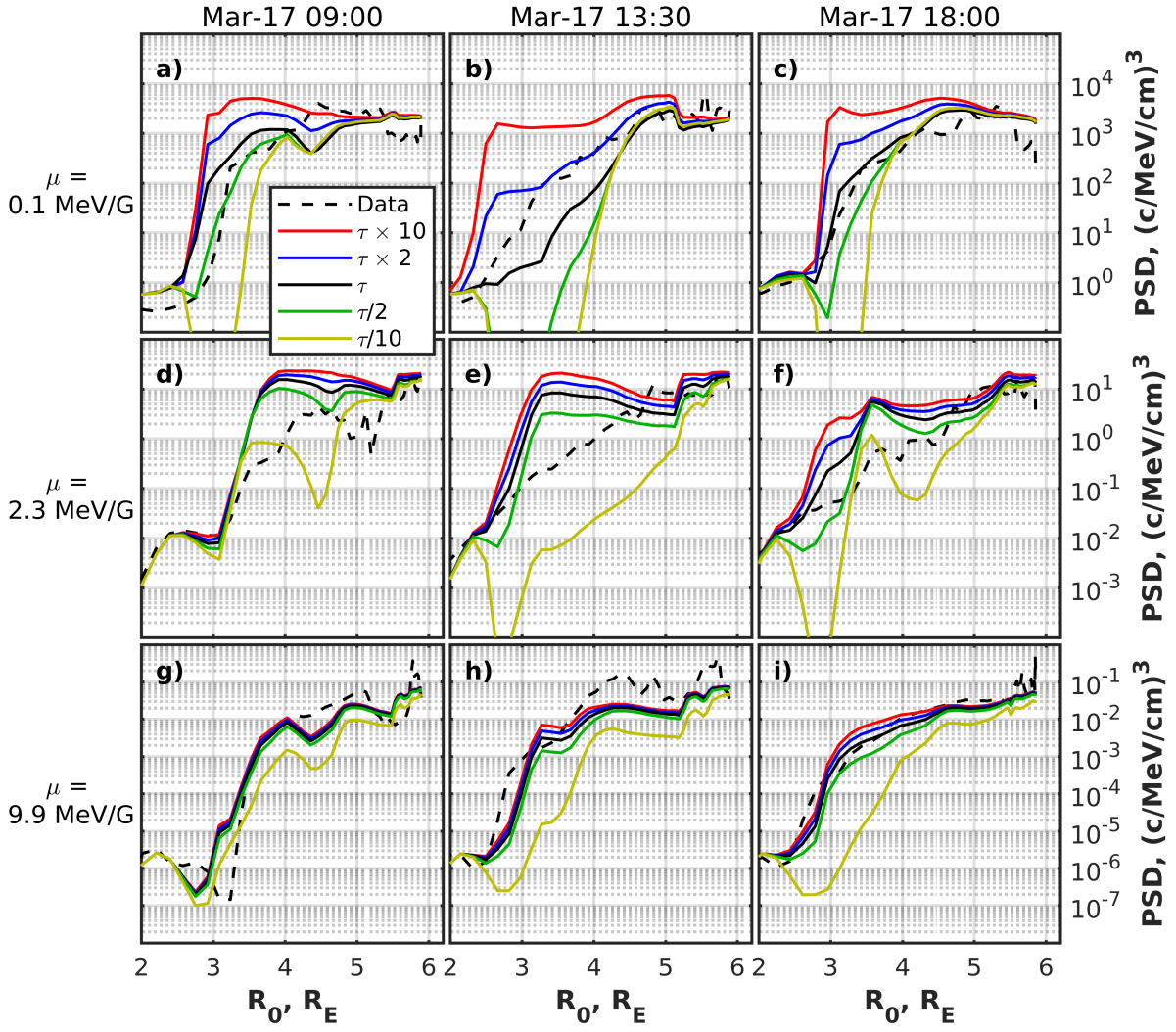

Figure 3.11: Comparison between Van Allen Probe B PSD (dashed lines) with the VERB-4D code results for different electron lifetimes outside the plasmasphere (solid lines) for K = 0.3 $G^{1/2}R_E$ and μ = 0.1 MeV/G (a-c), 2.3 MeV/G (d-f), and 9.9 MeV/G (g-i). Columns correspond to satellite passes beginning at 9:00, 13:30, and 18:00 on 17 March (from left to right).

The radial diffusion term results in deeper propagation of the PSD profiles, compared to the simulation when radial diffusion is not included in the code. The simulations give almost the same results above 4.5 R_E, and the discrepancies are observed at lower radial distances.

3.4.6 Effects of SAPS

The SAPS electric field can potentially affect the dynamics of the ring current electrons below ~4 R_E. To estimate an effect of SAPS, we performed a simulation with the included Kp-dependent model of SAPS, using the approach developed by Goldstein

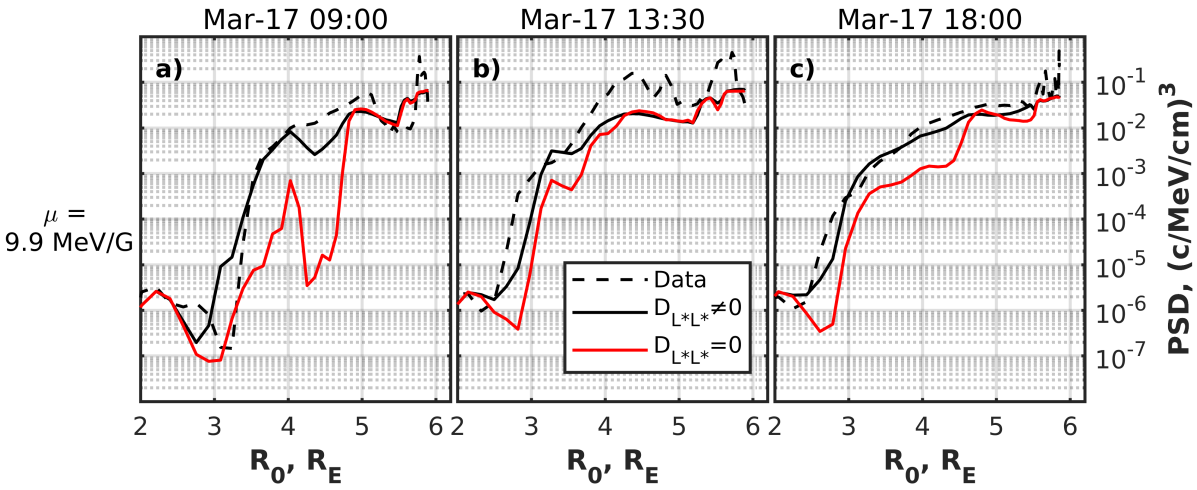

Figure 3.12: Comparison between Van Allen Probe B PSD (dashed lines) with the VERB-4D code results with and without radial diffusion term (black and red solid lines, respectively) for K = 0.3 $G^{1/2}R_E$ and μ = 9.9 MeV/G electrons. Columns correspond to satellite passes beginning at 9:00, 13:30, and 18:00 on 17 March (from left to right).

et al. (2005). Figure 3.13 presents the results in the same format as Figure 3.8. The overall effect of SAPS is relatively small for μ = 9.9 MeV/G particles. SAPS lead to the deeper earthward propagation of the 2.3 MeV/G electron PSD profiles than the model without SAPS. The difference between two simulations for 0.1 MeV/G electrons is noticeable between 3 and 4 R_E at 13:30 on 17 March 2013, and results obtained with the SAPS model included diverge strongly from the data along this satellite pass (Figure 3.13b). The implemented model of SAPS has no effect on the shape of the profiles (except for the profiles in Figure 3.13b), leading to a small earthward shift of the PSD profiles. We note that the Kp-driven SAPS model creates very slow changes in the electric field, and the effect may be more pronounced with a more variable realistic field.

3.5 Discussion

The comparison between the VERB-4D code and Van Allen Probes data demonstrates that the model results are almost insensitive to the input parameters such as electric field model, electron scattering rates, boundary conditions, radial diffusion, and the SAPS model, for μ = 0.1, 2.3, and 9.9 MeV/G and K = 0.3 $G^{1/2}$ electrons above $\sim$ 4.5 R_E. The observed PSD fit in the approximate confidence intervals associated with the uncertainties in boundary conditions and are almost always within the 25th and 75th percentile limits above 4.5 R_E (see Figure 3.6). The simulations with the W05 and VSMC electric field models give similar results in that region, with PSD being slightly higher in the case of the W05 model (see Figure 3.8). Between 4.5 R_E and

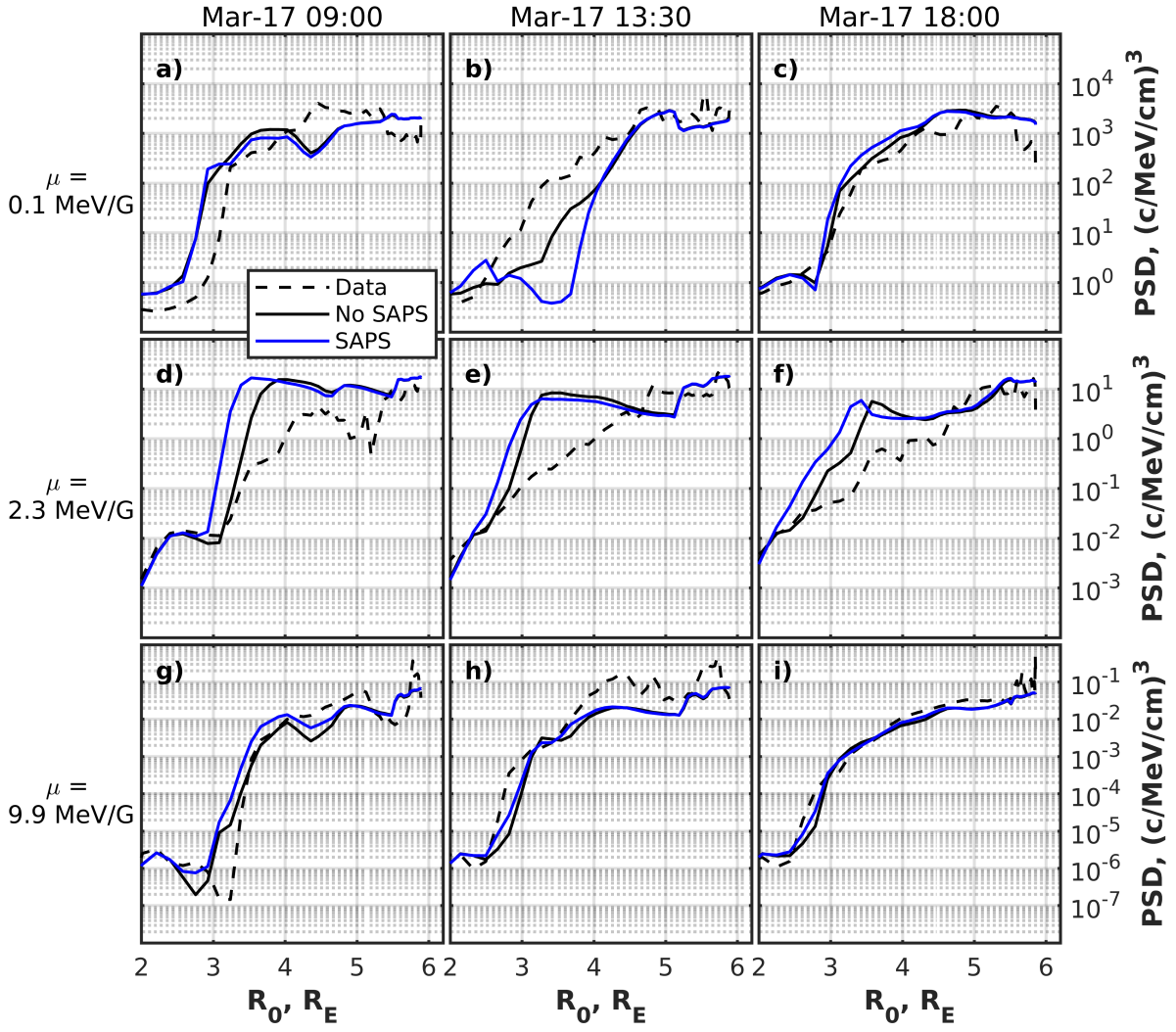

Figure 3.13: Comparison between Van Allen Probe B data (dashed lines) with the VERB-4D code results with and without SAPS included (blue and black solid lines, respectively) for K = 0.3 $G^{1/2}R_E$ and μ = 0.1 MeV/G (a-c), 2.3 MeV/G (d-f), and 9.9 MeV/G (g-i). Columns correspond to satellite passes beginning at 9:00, 13:30, and 18:00 on 17 March (from left to right).

GEO, the code results are almost insensitive to the electron lifetimes, and the SAPS have no effect on the PSD profiles. A good agreement between the model and the observations above 4.5 R_E indicate that realistic boundary conditions which are transported inward by the global-scale electric and magnetic field can generally explain the PSD enhancement in that region. The use of more accurate boundary conditions from the observations as well as localized electric and magnetic fields may help reproduce smaller-scale features observed in the data.

The model results differ from the data more noticeably below 4.5 R_E, and the biggest discrepancies are likely explained by the errors in electric field and electron lifetime

models. The in-situ comparison between the electric field measured by Van Allen Probes and the field computed with the W05 model shows that the model electric field agrees better with the observations at higher radial distances and overestimates the measurements at lower distances down to as low as 3 R_E at the beginning of the storm (see Figure 3.7). The unrealistically strong electric field at lower radial distances is a possible reason for the overestimation of electron PSD below 4 R_E for 2.3 and 9.9 MeV/G electrons from 8:00 to 10:00 (see Figure 3.5). The peak in 2.3 MeV/G electron PSD profiles between 3 and 4 R_E (Figures 3.6d-3.6f) is not observed in the data and is most probably caused by the uncertainties in the W05 electric field model, since the VSMC model leads to the less pronounced peak and even underestimation of the measurements at lower radial distances (see Figures 3.8d-3.8f). The 0.1 MeV/G electron PSD profiles are the most sensitive to the electron lifetimes, and the simultaneous overestimation of the observed PSD for 2.3 MeV/G electrons and underestimation for 0.1 MeV/G electrons along Van Allen Probe B trajectory beginning at 13:30 on 17 March 2013 (Figures 3.6b and 3.6e) may be caused by the combined effects of uncertainties in the lifetimes and electric field. We note that a ten-fold decrease in electron lifetimes leads to unrealistic results for all considered adiabatic invariants.

The quantification of the radial diffusion of the ring current electrons needs to be further investigated in future studies. With regard to the 17 March 2013 storm, the global-scale convection does not reproduce the radial extent of the 9.9 MeV/G profiles below 4-5 R_E, while the inclusion of the radial diffusion term leads to much better agreement with the measurements (see Figure 3.12). We note here that, in general, radial diffusion is not the only candidate for explaining the dynamics of these particles. For instance, the SAPS electric field can also contribute to their transport. Although the simplest Kp-dependent model of the SAPS (Goldstein et al., 2005) that we tested in this study produces only a slight earthward shift of the profiles (Figure 3.13), more realistic models, including self-consistent treatment of the electric field (Yu et al., 2017), potentially may cause more noticeable effects. The localized particle injections due to penetrating dipolarization fronts can also contribute to the electron radial transport, but their effects are typically observed at higher radial distances.

The use of the local diffusion term and MLT-dependent chorus wave models can further improve the simulation results. Since most of the chorus wave models have been designed for the radiation belts, they assume that the wave amplitude and normal angle distribution do not vary within rather wide day and night MLT sectors (e.g., Spasojevic and Shprits, 2013; Agapitov et al., 2015, 2018). While such an assumption can be justified in three-dimensional radiation belt codes, four-dimensional models of the ring current electrons may require more accurate MLT-dependent chorus wave pa-

rameterizations. We also emphasize the importance of the plasmasphere model that separates hiss and chorus wave-driven scattering of electrons. Inaccuracy in the demarcation boundary between the regions dominated by different waves and different plasma conditions introduces additional uncertainty in the simulations. More advanced MLT-dependent models (e.g., derived from the neural network-based model of plasmasphere (e.g., Zhelavskaya et al., 2017)) will be included in our future studies.

3.6 Summary

In this study, we modeled the storm-time enhancement of ring current electron PSD during the 17 March 2013 storm for μ = 0.1, 2.3, and 9.9 MeV/G and K = 0.3 $G^{1/2}R_E$ electrons, which covers the energies from 1 to 100 keV at L = 4, using the VERB-4D code. Our model includes magnetospheric convection driven by global magnetic and electric fields, radial diffusion, and electron scattering rates due to interaction with whistler-mode hiss and chorus waves. We compared the simulation results with Van Allen Probes data and studied the sensitivity of the model to the input parameters including the global electric field, outer boundary conditions at GEO, electron lifetimes outside of the plasmasphere, radial diffusion, and SAPS. The main conclusions are stated below.

1. For the considered event, simulation results are relatively insensitive to all tested input parameters above 4.5 R_E for all considered adiabatic invariants, and the general dynamics of the particles between 4.5 and 6.6 R_E appear to be driven by the transport of the particles from GEO under the action of the global electric and magnetic fields.

2. Although the sensitivity of the model to the localized electric fields has not been tested in this study, our results indicate that the discrepancies between the model and data between 4.5 R_E and GEO can be explained by uncertainties in boundary conditions, and additional physical processes, such as the localized fields, may not be needed to reproduce the general evolution of the ring current electrons in that region.

3. The main discrepancies between the model and data below 4.5 R_E can be explained by errors in the global electric field and electron lifetimes.

4. The global convective transport cannot reproduce the radial extent of the 9.9 MeV/G electron profiles below ~4.5 R_E, and the inclusion of the radial diffusion term with the diffusion rates by Brautigam and Albert (2000) leads to better agreement with the data.

5. The Kp-driven SAPS model (Goldstein et al., 2005) leads to relatively small changes in the electron profiles, which seem to be less significant than the uncertainties related to lifetimes or electric field.

This study presents the initial step towards understanding of the complicated transport and loss processes of low-energy electrons within GEO. The future extension of this study will include modeling of lower energy electrons, improvement of the loss and fields model, and understanding of the contribution of localized electric fields beyond and inside GEO.

Acknowledgments

The authors acknowledge use of NASA/GSFC's Space Physics Data Facility's OMNIWeb service, and OMNI data. The Kp index was provided by GFZ Potsdam. The authors are grateful to the RBSP-ECT team for the provision of Van Allen Probes observations. All RBSP-ECT data are publicly available at the web site http://www.RBSP-ect.lanl.gov/. This research was supported by the Helmholtz-Gemeinschaft (HGF) [10.13039/501100001656], NASA grants NNX15AI94G and NNX16AG78G, NSF grant AGS-1552321, and project PROGRESS funded by EC | Horizon 2020 Framework Programme (H2020) [10.13039/100010661] (637302)). The research has been partially funded by Deutsche Forschungsgemeinschaft (DFG) through grant CRC 1294 Data Assimilation, Project B06. Processing and analysis of the ECT data was supported by Energetic Particle, Composition, and Thermal Plasma (RBSP-ECT) investigation funded under NASA's Prime contract no. NAS5-01072. The work by the EFW team was conducted under JHU/APL contract 922613 (RBSP-EFW). This work used computational and storage services associated with the Hoffman2 Shared Cluster provided by UCLA Institute for Digital Research and Education's Research Technology Group. The authors thank the developers of the IRBEM library which was adapted for use in the current study, and Daniel Weimer for the provision of the codes for the global electric field model. The authors are grateful to Sharon Uy for her help in editing the paper. The authors thank Irina Zhelavskaya and Frederic Effenberger for useful discussions.

Chapter 4

Reanalysis of Ring Current Electron Phase Space Densities using Van Allen Probe Observations, Convection Model, and Log-Normal Kalman Filter

Published as:
Aseev, N. A. and Shprits, Y. Y., 2019. Reanalysis of Ring Current Electron Phase Space Densities Using Van Allen Probe Observations, Convection Model, and Log-Normal Kalman Filter. *Space Weather*, 17(4):619–638. doi:10.1029/2018SW002110

Abstract

Models of ring current electron dynamics unavoidably contain uncertainties in boundary conditions, electric and magnetic fields, electron scattering rates, and plasmapause location. Model errors can accumulate with time and result in significant deviations of model predictions from observations. Data assimilation offers useful tools which can combine physics-based models and measurements to improve model predictions. In this study, we systematically analyze the performance of the Kalman filter applied to a log-transformed convection model of ring current electrons and Van Allen Probes data. We consider long-term dynamics of μ = 2.3 MeV/G and K = 0.3 $G^{1/2}R_E$ electrons from 1 February 2013 to 16 June 2013. By using synthetic data, we show that the Kalman filter is capable of correcting errors in model predictions associated with uncertainties in electron lifetimes, boundary conditions, and convection electric fields. We demonstrate that reanalysis retains features which cannot be fully reproduced by the convection model, such as storm-time earthward propagation of the electrons down to

2.5 R_E. The Kalman filter can adjust model predictions to satellite measurements, even in regions where data are not available. We show that the Kalman filter can adjust model predictions in accordance with observations for μ = 0.1, 2.3, and 9.9 MeV/G and constant K = 0.3 $G^{1/2}R_E$ electrons. The results of this study demonstrate that data assimilation can improve performance of ring current models, better quantify model uncertainties, and help us to understand more deeply the physics of the ring current particles.

4.1 Introduction

The ring current electron population (energies from ~1 to a few 100 keV) is very dynamic and shows strong storm-time variations in Magnetic Local Time (MLT) and radial distance over timescales shorter than one hour. Prediction of ring current electron dynamics is of crucial importance for space weather applications, but numerical modeling of this particle population is complicated by uncertainties in electric and magnetic fields, boundary conditions, wave-particle interactions, location of the plasmapause, and magnetopause position. The errors in each component may add up with time and lead to deviation of model results from a true state of the system. An opposite effect may also take place if the errors cancel each other out. In this case, a coincidental agreement between the model and observations for a particular event or for a particular location in space may be misleading.

A lack of detailed MLT-dependent in-situ wave and particle observations renders it challenging to quantify model errors in dominant electron loss and transport processes. The ring current models either rely on global statistical electric and magnetic field parameterizations, which may differ from real fields, or use computationally expensive self-consistent treatment of the fields. Uncertainties in the fields beyond the Geostationary Orbit (GEO) stem from localized dipolarization fronts (Angelopoulos et al., 1992, 1994), which are believed to efficiently inject electrons earthward (e.g., Birn et al., 1998; Gabrielse et al., 2012; Turner et al., 2016; Gabrielse et al., 2017), but the importance of which in the overall electron transport has not been studied in detail. Within GEO, measured electric fields below L = 5.5 appeared to be stronger and more dynamic than the conventional co-rotation and convection field model suggested (Rowland and Wygant, 1998; Califf et al., 2014). Another important source of model errors originates from uncertainties in the models of different plasma waves, such as whistler-mode chorus or plasmaspheric hiss. The errors in wave amplitude and wave-normal angle distributions can lead to incorrect electron scattering rates and inaccurate electron flux predictions.

Data assimilation can offer useful tools which help adjust model predictions in ac-

cordance with data and identify uncertainties in the model. Data assimilation methods have been widely used in radiation belt physics (Shprits et al., 2007; Koller et al., 2007; Ni et al., 2009; Daae et al., 2011; Kondrashov et al., 2011; Schiller et al., 2012), but only a few studies on the application of data assimilation methods to the ring current have been performed. Nakano et al. (2008) used a particle filter approach to assimilate energetic neutral atom data into the Comprehensive Ring Current Model (Fok et al., 2001). They showed that the particle filter can reconstruct the ion distribution in the ring current. Godinez et al. (2016) combined Van Allen Probe Magnetic Electron Ion Spectrometer (MagEIS) ion differential flux data with the RAM code to estimate the ring current pressure by means of the Ensemble Kalman Filter (EnKF). They demonstrated that data assimilation can help reproduce missing enhancement of pressure in the inner magnetospheric region during an isolated substorm event observed on 18 July 2013. These studies give encouraging results of the applicability of data assimilation methods for the ring current model, which have to be further validated.

The scarcity of in-situ satellite measurements may hinder application of data assimilation methods in space sciences. Models of the Earth's magnetosphere, ionosphere, radiation belts, and ring current are typically multidimensional and involve many degrees of freedom. Spacecraft data are limited in space, and the effects of data assimilation methods can also be localized due to the poor data coverage. The multidimensionality of the models also leads to high computational costs and complicates numerical implementation of data assimilation methods. To tackle such issues, some assumptions about the model have to be made, or more sophisticated methods have to be developed. For instance, Bourdarie and Maget (2012) applied the ensemble Kalman filter to perform electron radiation belt reanalysis, using a sparse data set. Shprits et al. (2013a) proposed a suboptimal method on the basis of the operator splitting technique to reconstruct three-dimensional dynamics of the radiation belts, using Combined Release and Radiation Effects Satellite (CRRES) data. They showed that the results of their method are very close to the optimal results of the full Kalman filter. Merkin et al. (2016) demonstrated that the assimilation of ionospheric magnetic perturbations into the coupled magnetosphere-ionosphere LFM-RCM codes correctly modifies ionospheric currents and magnetic perturbations and nudges them towards the synthetic observations.

In this study, we present reanalysis of the ring current electron dynamics, using a log-transformed convection model blended with Van Allen Probes measurements by means of the Kalman filter. We limit the computational domain to GEO (6.6 R_E) to decrease the computational complexity and increase relative coverage of the domain by the observations. We use the convection portion of the four-dimensional Versatile

Electron Radiation Belt code (VERB-4D code) (Shprits et al., 2015; Aseev et al., 2016) and Volland-Stern electric field and dipole field models to drive the transport of ring current electrons. Such an approach allows us to efficiently perform long-term simulations and systematically analyze the applicability of the Kalman filter to the ring current electron modeling.

The presented study is organized as follows. In Section 4.2, we describe the data and methods which are used in the study. In Section 4.3, we present results of numerical experiments with synthetic data which are used to study the performance of the Kalman filter. We illustrate applicability of the Kalman filter in Section 4.4, using real Van Allen Probes observations. We discuss the results in Section 4.5. Section 4.6 summarizes conclusions of the study.

4.2 Data and Methods

4.2.1 Data

In this study, we use Van Allen Probes data, the "gold standard" of particle and field measurements in the inner magnetosphere. We model evolution of electron Phase Space Density (PSD) for constant first and second adiabatic invariants, and it is, therefore, necessary to convert local Van Allen Probes observations to the model space. To calculate the invariants and PSD along the satellite orbits, we use Helium, Oxygen, Proton, and Electron (HOPE) Mass Spectrometer (Funsten et al., 2013), MagEIS (Blake et al., 2013), and Electric and Magnetic Field Instrument Suite and Integrated Science (EMFISIS) (Kletzing et al., 2013) on board the satellites.

Figure 4.1 illustrates Van Allen Probes orbits for the selected period from 1 February 2013 to 16 June 2013. The apogee of the satellites is located at the night side and moves westward from 2.5 h MLT on 1 February 2013 to 21.5 h MLT on 1 June 2013. Van Allen Probes provide observations along one orbit inside a localized MLT sector which may pose difficulties for data assimilation methods to reconstruct global distribution of electron PSD. Note that there is no data on the day side above $\sim$2 R_E for the considered time period, and one of the goals of this paper is to investigate if the Kalman filter can adjust the model to the observations in the regions where data are not available.

We calculate 5-minute averages of the measured electron fluxes and then convert the fluxes to PSD, according to the formula (Rossi and Olbert, 1970)

$$f = \frac{J_n}{p^2}, \tag{4.1}$$

where J_n is the electron differential directional flux, p is the particle momentum, and

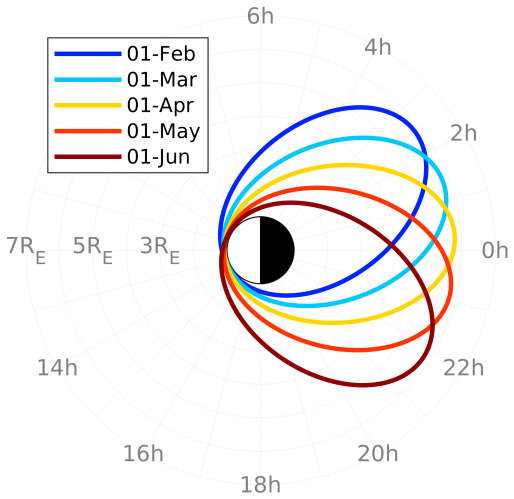

Figure 4.1: Schematic illustration of Van Allen Probes orbits during the considered period from 1 February 2013 to 16 June 2013.

f is PSD.

We use local magnetic field measurements to compute the first invariant μ. We calculate the second adiabatic invariant K, using T01S magnetic field model incorporated into the IRBEM library (Boscher et al., 2012). We use bilinear interpolation to calculate PSD for given μ and K along the satellite orbits during the time interval from 1 February 2013 to 16 June 2013. This time interval allows us to study the response of the ring current electrons to numerous substorms and storms, including the strongest events observed on 17 March 2013 and 1 June 2013, as well as post-storm decay of electron PSD. In this study, we compute PSD for μ = 0.1, 2.3, and 9.9 MeV/G and constant K = 0.3 $G^{1/2}R_E$ electrons. The selected invariants cover a typical range of ring current electron energies from ~1 to 100 keV at L = 4 (see Figure 4.2).

4.2.2 Convection Model

We adopt the approach of the VERB-4D code to model the dynamics of the ring current electron population (see a detailed description of the VERB-4D code and underlying equations in Aseev et al. (2016) and Chapter 2). We use the simplified version of the code, referred to as the VERB-CS code (CS is deciphered as "Convection Simplified") which solves the convection equation

$$\frac{\partial f}{\partial t} + v_\varphi \frac{\partial f}{\partial \varphi} + v_{R_0} \frac{\partial f}{\partial R_0} + \frac{f}{\tau} = 0, \tag{4.2}$$

where f is PSD, t denotes time, φ is MLT, R_0 is a radial distance at the geomagnetic equator, v_φ and v_{R_0} are drift velocities, and τ are electron lifetimes.

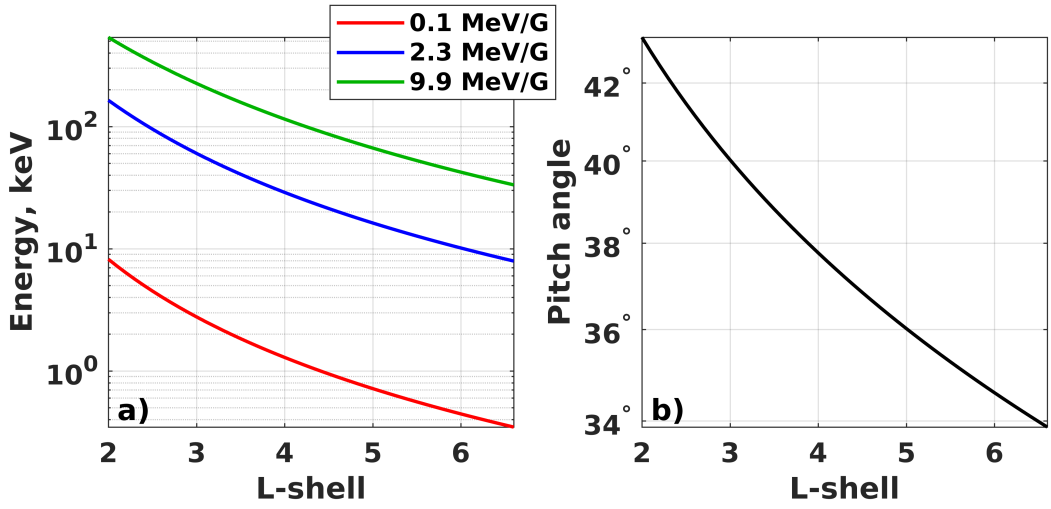

Figure 4.2: (a) Dependence of energy on L-shell calculated for μ = 0.1, 2.3, and 9.9 MeV/G (red, blue, and green lines, respectively) and constant K = 0.3 $G^{1/2}R_E$. (b) Dependence of pitch angle on L-shell for K = 0.3 $G^{1/2}R_E$. The dipole magnetic field model is used.

Equation (4.2) is solved for constant values of first and second adiabatic invariants. The equation describes electron transport in radial distance and MLT due to **E**×**B** and gradient-curvature drifts (second and third terms on the left-hand side) and electron scattering into the Earth's atmosphere (fourth term). We note that the four-dimensional equation which is solved by the VERB-4D code is reduced to a two-dimensional case by using parameterized lifetime τ. Such an approach simplifies the implementation of the Kalman filter and allows us to efficiently calculate long-term evolution of electron PSD and test the performance of the Kalman filter.

Equation (4.2) has to be complemented by initial and boundary conditions. The boundary conditions are periodic in MLT and constant in R_0. We set up $f = 0$ at $R_0 = 1$, assuming that all electrons are lost in the Earth's atmosphere. We use a statistical model of electron fluxes at GEO developed by Denton et al. (2015) to set up the outer boundary conditions at R_0 = 6.6 R_E. The model is based on 82 satellite-years of observations at GEO made by magnetospheric plasma analyzer (Bame et al., 1993) on board Los Alamos National Laboratory Satellites. The model provides Kp-dependent spin-averaged electron fluxes for all MLT sectors and energies from ~40 eV to ~40 keV. We compute directional flux from the spin-averaged flux, assuming sinusoidal dependence on a pitch angle, and convert the flux to PSD, using equation (4.1) and assuming the dipole field approximation to calculate particle momentum from the first adiabatic invariant. To specify initial conditions, we calculate PSD, using Van Allen Probes HOPE and MagEIS measurements, and calculate the MLT average of PSD over ±5 hours from the start time of a simulation. We extend initial conditions from

Van Allen Probes apogee to GEO, using constant PSD.

Drift velocities are calcuated using the dipole magnetic field approximation and the Volland-Stern Kp-dependent electric field model (Volland, 1973; Stern, 1975; Maynard and Chen, 1975). Inside the plasmasphere, we use a model of electron lifetimes developed by Orlova et al. (2016). Electron lifetimes due to local interaction with chorus waves outside the plasmasphere are adopted from Orlova and Shprits (2014). The plasmapause is calculated using Carpenter and Anderson (1992) model.

4.2.3 Log-Transformed Convection Model

Equation (4.2) can be integrated numerically under the presence of strong gradients in f by using high-order discretization schemes and limiters which preserve the monotonicity of the solution and its sign (Leonard, 1991; Aseev et al., 2016). Electron PSD is a non-negative quantity, but the Kalman filter cannot guarantee its sign conservation (e.g., Cohn, 1997). Cohn (1997) also discussed that an error distribution of positive physical quantities cannot be strictly Gaussian, since there exists a non-zero probability of assigning to them negative values, which may pose problems for the optimality of the Kalman filter. An alternative log-transformed formulation of equation (4.2) can be used to account for these difficulties. We note that the similar approach has been applied to the radiation belt dynamics by Kondrashov et al. (2011).

We transform PSD f to a new variable g

$$g = \log f. \tag{4.3}$$

Equation (4.2) can now be rewritten in terms of the new variable g as

$$\frac{\partial g}{\partial t} + v_{\varphi}\frac{\partial g}{\partial \varphi} + v_{R_0}\frac{\partial g}{\partial R_0} + \frac{1}{\tau} = 0. \tag{4.4}$$

We note that the transformation (4.3) guarantees the positivity of electron PSD. Log-transformed convection equation (4.4) contains the same convection terms as equation (4.2), and we adapt the VERB-CS code to the log-transformed formulation.

Following the approach of the VERB-4D code, we use the ninth-order explicit numerical scheme and the universal limiter (Leonard, 1991) in the VERB-CS code to solve convection equation (4.4). A time step of the model is 15 minutes, and it is adjusted to satisfy the Courant stability condition, depending on time-variable drift velocities. We use a spatial grid with 1 h step in MLT and 0.2 R_E step in radial distance.

4.2.4 Kalman Filter

Log-transformed model (4.4) includes a number of uncertainties in the parameters such as electric and magnetic fields, electron lifetimes, plasmapause position, and

boundary conditions. The model errors can be accumulated with time, and model predictions can be substantially different from the real state of the system. The Kalman filter adjusts model predictions to the available satellite measurements. In this section, we describe a Kalman filter technique applied to log-transformed convection model (4.4). We assume that "natural" state and observation variables are the logarithm of PSD defined by equation (4.3), and the dynamics of the ring current electrons is described by log-transformed convection model (4.4).

Let us denote a discretized state variable g at time t_{k-1} as a vector $\mathbf{g}^f_{k-1}$. The state vector $\mathbf{g}^f_{k-1}$ is propagated in time by a nonlinear model operator $\widehat{M}_{k-1}$:

$$\mathbf{g}^f_k = \widehat{M}_{k-1}\left(\mathbf{g}^f_{k-1}\right). \tag{4.5}$$

The model operator $\widehat{M}_{k-1}$ can be derived from time and space discretization of equation (4.4).

When applied to a true state $\mathbf{g}^t_{k-1}$ defined on the same model grid as $\mathbf{g}^f_{k-1}$, the model operator advances $\mathbf{g}^t_{k-1}$ in time with some error $\boldsymbol{\epsilon}^m_{k-1}$:

$$\mathbf{g}^t_k = \widehat{M}_{k-1}\left(\mathbf{g}^t_{k-1}\right) + \boldsymbol{\epsilon}^m_{k-1}. \tag{4.6}$$

Error $\boldsymbol{\epsilon}^m_{k-1}$ may include uncertainties in model parameters and errors associated with numerical schemes and sub-grid processes.

A satellite observation vector $\mathbf{g}^{obs}_k$ at time k also contains random error $\boldsymbol{\epsilon}^{obs}_k$ which includes measurement errors (e.g., due to background contamination (e.g., Smirnov et al., 2019, and references therein), noisy detectors, spacecraft charging, or low counting statistics) and error of representativeness due to unresolved scales:

$$\mathbf{g}^{obs}_k = \widehat{H}_k\left(\mathbf{g}^t_k\right) + \boldsymbol{\epsilon}^{obs}_k, \tag{4.7}$$

where $\widehat{H}_k$ is an observation operator. The operator $\widehat{H}_k$ maps model variables into an observation space. The observation space may differ from the model space, which is the case of in-situ particle measurements made in flux counts. We assume that the conversion from counts to PSD is perfect, and we consider PSD as an actually measured quantity. Such an assumption does not influence results of our study, but significantly simplifies implementation of the Kalman filter.

Observations also do not typically coincide with the model grid, and the operator $\widehat{H}_k$ may involve interpolation. If it is not possible to make observations in the whole model domain, the size of the vector $\mathbf{g}^{obs}_k$ can be smaller than the size of the state vector $\mathbf{g}^f_k$.

For purposes of data assimilation, we bin Van Allen Probes observations in space, using model grid nodes as bin centers. The size of each bin corresponds to grid steps

in MLT and radial distance. We then calculate mean values of electron PSD inside each bin. The resulting observation vector $\mathbf{g}_k^{obs}$ is defined on model grid nodes, and the observation operator $\widehat{H}_k$ is, therefore, a matrix that contains 0 and 1. We denote this matrix as $\mathbf{H}_k$, and the satellite observation vector can be represented as

$$\mathbf{g}_k^{obs} = \mathbf{H}_k \mathbf{g}_k^t + \boldsymbol{\epsilon}_k^{obs}. \tag{4.8}$$

The Kalman filter gives an optimal solution $\mathbf{g}_k^a$ of the filtering problem (4.6), (4.8) which is referred to as analysis:

$$\mathbf{g}_k^a = \left\langle \mathbf{g}_k^t \middle| \left\{ \mathbf{g}_1^{obs}, \mathbf{g}_2^{obs}, \ldots, \mathbf{g}_k^{obs} \right\} \right\rangle, \tag{4.9}$$

where the right-hand side denotes the conditional mean of the true state $\mathbf{g}_k^t$ at time t_k given the observations $\left\{ \mathbf{g}_1^{obs}, \mathbf{g}_2^{obs}, \ldots, \mathbf{g}_k^{obs} \right\}$ made by the time t_k. The model and observation errors $\boldsymbol{\epsilon}_k^m$ and $\boldsymbol{\epsilon}_k^{obs}$ are assumed to be Gaussian variables with zero mean and white (uncorrelated) in time:

$$\boldsymbol{\epsilon}_k^m \sim \mathcal{N}(\mathbf{0}, \mathbf{Q}_k), \ \left\langle \boldsymbol{\epsilon}_k^m (\boldsymbol{\epsilon}_l^m)^T \right\rangle = \mathbf{0}, \ \ k \neq l, \tag{4.10}$$

$$\boldsymbol{\epsilon}_k^{obs} \sim \mathcal{N}(\mathbf{0}, \mathbf{R}_k), \ \left\langle \boldsymbol{\epsilon}_k^{obs} (\boldsymbol{\epsilon}_l^{obs})^T \right\rangle = \mathbf{0}, \ \ k \neq l, \tag{4.11}$$

where $\mathcal{N}$ denotes multivariate Gaussian distribution, $\mathbf{Q}_k$ and $\mathbf{R}_k$ are model and observation error covariance matrices, respectively, $\mathbf{0}$ is a vector with all elements equal to zero, and $\langle\ \rangle$ denotes the expectation operator. Errors $\boldsymbol{\epsilon}_k^m$ and $\boldsymbol{\epsilon}_k^{obs}$ and the initial true state also have to be mutually uncorrelated (e.g., see Cohn, 1997).

The Kalman filter technique consists of forecast and analysis steps. Let us define the forecast error covariance matrix $\mathbf{P}_k^f$ as

$$\mathbf{P}_k^f = \left\langle \left(\mathbf{g}_k^t - \mathbf{g}_k^f \right) \left(\mathbf{g}_k^t - \mathbf{g}_k^f \right)^T \middle| \left\{ \mathbf{g}_1^{obs}, \mathbf{g}_2^{obs}, \ldots, \mathbf{g}_{k-1}^{obs} \right\} \right\rangle \tag{4.12}$$

and the analysis error covariance matrix $\mathbf{P}_k^a$ as

$$\mathbf{P}_k^a = \left\langle \left(\mathbf{g}_k^t - \mathbf{g}_k^a \right) \left(\mathbf{g}_k^t - \mathbf{g}_k^a \right)^T \middle| \left\{ \mathbf{g}_1^{obs}, \mathbf{g}_2^{obs}, \ldots, \mathbf{g}_k^{obs} \right\} \right\rangle. \tag{4.13}$$

At the forecast step, the Kalman filter propagates the analysis $\mathbf{g}_{k-1}^a$ in time and updates the forecast error covariance matrix $\mathbf{P}_k^f$:

$$\mathbf{g}_k^f = \widehat{M}_{k-1} \left(\mathbf{g}_{k-1}^a \right), \tag{4.14}$$

$$\mathbf{P}_k^f = \mathbf{L}_{k-1} \mathbf{P}_{k-1}^a \mathbf{L}_{k-1}^T + \mathbf{Q}_{k-1}, \tag{4.15}$$

where matrix $\mathbf{L}_{k-1}$ is referred to as a linear tangent model which is obtained by linearizing operator $\widehat{M}_{k-1}$.

At the analysis step, the forecast $\mathbf{g}_k^f$ is corrected according to the observations:

$$\mathbf{g}_k^a = \mathbf{g}_k^f + \mathbf{K}_k \mathbf{d}_k, \tag{4.16}$$

where $\mathbf{d}_k = \mathbf{g}_k^{obs} - \mathbf{H}_k \mathbf{g}_k^f$ is an innovation vector, and matrix $\mathbf{K}_k$ is referred to as Kalman gain:

$$\mathbf{K}_k = \mathbf{P}_k^f \mathbf{H}_k^T \left(\mathbf{H}_k \mathbf{P}_k^f \mathbf{H}_k^T + \mathbf{R}_k \right)^{-1}. \tag{4.17}$$

The analysis error covariance $\mathbf{P}_k^a$ is also updated at this step as follows:

$$\mathbf{P}_k^a = \mathbf{P}_k^f - \mathbf{K}_k \mathbf{H}_k \mathbf{P}_k^f. \tag{4.18}$$

Equations (4.14)-(4.18) constitute a complete set of equations describing the Kalman filter. To compute reanalysis of the ring current electrons, we solve these equations every 30 minutes, which corresponds to every second time step of the log-transformed convection model.

We note that we use the first-order explicit upwind numerical scheme to obtain the linear tangent model $\mathbf{L}_k$, and the ninth-order scheme for operator $\widehat{M}_k$. Such an approach allows us to simplify implementation of the Kalman filter while preserving accuracy of the convection model, but it can potentially affect optimality of the reanalysis.

We adopt the approach of Kondrashov et al. (2011) and set up the model and observation covariance matrices $\mathbf{Q}_k$ and $\mathbf{R}_k$ as diagonal with elements $\log(1+\alpha_m)$ and $\log(1+\alpha_{obs})$, respectively. In this study, we assume equal model and observation errors $\alpha_m = \alpha_{obs} = 0.5$. The use of equal errors suggests that both model and data contribute equally to the reanalysis, and reanalysis performance is not dominated by either data or model.

4.3 Experiments with Synthetic Data

In this section, we present results of numerical experiments with "synthetic" data. To generate the synthetic data, we run the log-transformed VERB-CS code with predefined parameters (a control simulation) and assume that the results of the model represent a true state of the system. We then define synthetic data as the results of the control simulation specified at the grid nodes closest to Van Allen Probes A and B trajectories in a given assimilation window. By varying different parameters of the VERB-CS code, we can study deviation of the reanalysis from the known "true" state of the system and performance of the Kalman filter.

For the control simulation, we run the model for $\mu = 2.3$ MeV/G and K = 0.3 $G^{1/2}$ R_E electrons. The parameters of the convection model are described in Sections 4.2.2 and 4.2.3. The model time step is 15 minutes, and data assimilation is performed every 30 minutes.

4.3.1 Metrics

We assess accuracy of the ring current electron PSD reanalysis in fraternal twin experiments by using two metrics which are described in this section. Since a "true" state of the system is produced by the model in the control simulation, the "true" state is available on the same model grid as reanalysis, and assessment of reanalysis accuracy is essentially a comparison between outputs of two simulations.

To understand how well reanalysis reconstructs radial extent of electron PSD and how corresponding errors depend on geomagnetic activity, we use logarithmic difference ε_{log10} between MLT-averaged true state and model (or reanalysis) output:

$$\varepsilon_{log10}(t, R_{0j}) = log_{10}\left(\frac{1}{N_\varphi}\sum_{i=1}^{N_\varphi} f_{true}(t, \varphi_i, R_{0j})\right) - log_{10}\left(\frac{1}{N_\varphi}\sum_{i=1}^{N_\varphi} f_{model}(t, \varphi_i, R_{0j})\right), \quad (4.19)$$

where f_{true} denotes PSD obtained in the control simulation (true state), f_{model} is the predicted stated (model or reanalysis), i and j are grid nodes in MLT and radial distance, respectively, and N_φ is the number of nodes in the MLT grid.

Electron PSD varies in space and time by several orders of magnitude, and the use of the logarithmic difference helps us represent scale-dependent errors by illustrating the ratio between the true state and reanalysis. We note that it is impossible to devise a universal metric that would characterize the ability of the model to simultaneously reconstruct all features of the resulting PSD, such as variations in time, MLT, and radial distance, and ε_{log10} may hide information about MLT dependence of errors or even mask some errors in the calculation. The limitations of the metric have to be taken into account during analysis of the results of fraternal twin experiments.

To compute a second, quantitative measure of the general reconstruction of the true state, we follow Morley (2016) and Morley et al. (2018). We require such a measure being a scalar describing accuracy of the reconstruction of the PSD distribution in space. The measure has to be computed for each time step of the model to represent its dependence on geomagnetic conditions. We first calculate "PSD matching ratio" (Yu et al., 2014; Morley et al., 2018) $\xi_{i,j}(t)$ for each grid node

$$\xi_{i,j}(t) = 10^{\eta_{i,j}(t)}, \quad (4.20)$$

where

$$\eta_{i,j}(t) = \left| log_{10}\left(\frac{f_{data}(t, \varphi_i, R_{0j})}{f_{model}(t, \varphi_i, R_{0j})}\right)\right|, \quad (4.21)$$

and we use the same notation as in equation (4.19).

The value of $\xi_{i,j}$ represents a factor by which the model (or reanalysis) PSD differ from the true state at a point (φ_i, R_{0j}), regardless of whether the true state is overesti-

mated or underestimated by the model. Model prediction coincides with the true state at a point (φ_i, R_{0j}) if $\xi_{i,j} = 1$.

We calculate an average of $\xi_{i,j}(t)$ over MLT and radial distance to quantitatively estimate the accuracy of global reconstruction of the true state:

$$\widetilde{\zeta}(t) = \frac{1}{N_\varphi}\frac{1}{N_{R_0}}\sum_{i=1}^{N_\varphi}\sum_{j=1}^{N_{R_0}}\xi_{i,j}(t), \tag{4.22}$$

where N_{R_0} is the number of nodes in the radial grid.

The metric $\widetilde{\zeta}$ is symmetric with respect to the swap of true and predicted PSD states. The metric $\widetilde{\zeta}$ differs from the metric that Morley (2016) developed, which was named "Median Symmetric Accuracy " (MdSA). Morley (2016) (1) considered a scalar variable changing with time, (2) calculated the median of the matching ratio, (3) substracted 1 from the median, and (4) multiplied the result by 100 to obtain an equivalent percentage error.

We do not use percentage representation in this study since the model error may exceed one order of magnitude in some fraternal twin experiments, and the percentage representation is not useful. For this reason, we do not substract 1 from $\widetilde{\zeta}$ and do not multiply it by 100, so $\widetilde{\zeta} \geq 1$ and $\widetilde{\zeta} \equiv 1$ corresponds to the perfect match between model and data.

We tested the MdSA metric applied to the fraternal twin experiments and found that the median may not reflect well the accuracy of the reanalysis. If the true state coincides (or almost coincides) with the prediction in more than half of the grid points, which is often true in the case of reanalysis in experiments with errors in boundary conditions and electron lifetimes, the MdSA is zero (or almost zero). Therefore, a perfect match between the true state and reanalysis cannot be distinguished from the case when the model arbitrarily deviates from the true state in less than half of the grid points. The use of mean in the metric $\widetilde{\zeta}$ eliminates such a problem.

The metric $\widetilde{\zeta}$ assigns the same weights to grid points closer to the Earth, where fewer changes in PSD are expected, and points near the outer radial boundary, where the system is the most dynamic and PSD is usually higher. By re-weighting the mean in equation (4.22), the metric $\widetilde{\zeta}$ can be adjusted to a particular application. In this study, we do not re-weight the metric and use equation (4.22). We note that such a metric is most suitable for assessing the accuracy of the reanalysis in the fraternal twin experiments, and other studies may require a different metric, depending on the problem and desired feature to be reproduced by the model.

We refer to metric $\widetilde{\zeta}$ as the Mean Fractional Symmetric Error (MFSE). Its name is intentionally made to resemble the name "median symmetric accuracy" introduced by Morley (2016), since MFSE inherits its main features from the MdSA. The use of the

word "error" instead of "accuracy" is more intuitive since the MFSE decreases with increase in model accuracy.

4.3.2 Errors in Electron Lifetimes

In a fraternal twin experiment, the model that is used for data assimilation differs from the model that produces a synthetic "true" state. By changing parameters of the log-transformed convection model, we can artificially introduce a model error and study the performance of the Kalman filter, using the "imperfect" model. In this section, we combine the Kalman filter and the VERB-CS code with 10-fold increased lifetimes τ. We keep all other parameters the same for both versions of the model.

Figure 4.3 illustrates results of the fraternal twin experiment, using the "imperfect" model with "inaccurate" electron lifetimes. Figure 4.3a shows MLT-averaged PSD as a synthetic truth, and Figure 4.3b presents simulation results with the electron lifetimes $\tau \cdot 10$ if the Kalman filter is not applied. The increase in the electron lifetimes by one order leads to drastically different model results. The electrons which are transported down to 3-6 R_E during geomagnetically disturbed times stay longer inside the geostationary orbit, and the resulting PSD can be higher by several orders of magnitude compared to the synthetic data.

Figure 4.3c shows MLT-averaged reanalysis results obtained by combining an "imperfect" model, the Kalman filter, and synthetic data. The reanalysis is visually indistinguishable from the synthetic "true" state (Figure 4.3a). The reanalysis retains the same pronounced features: shorter post-storm PSD decay times and the local minimum between 3 R_E and 5 R_E. Figure 4.3d shows the logarithmic difference ε_{log10} between the MLT-averaged synthetic "true" state and the reanalysis. The logarithmic difference is generally negative, since the model overestimates the "true" state, and the magnitude of the logarithmic difference does not exceed ~0.2 and increases with increase in the Kp index (see Figure 4.3f).

The model MFSE $\widetilde{\zeta}_{model}$ (see the red line in Figure 4.3e) grows with time and falls noticeably when the Kp index sharply increases. During such periods, the radial component of electron drift velocity also increases, and electrons penetrate closer to the Earth, partially compensating inaccuracies driven by errors in electron lifetimes. The maximum of $\widetilde{\zeta}_{model}$ almost reaches 100, which indicates that the model overestimates the "true" state by two orders of magnitude on average. In the case of reanalysis, $\widetilde{\zeta}_{reanalysis}$ slightly deviates from 1 and never reaches 2 (see the blue line in Figure 4.3e). This fact suggests that the Kalman filter can efficiently correct errors in the model predictions.

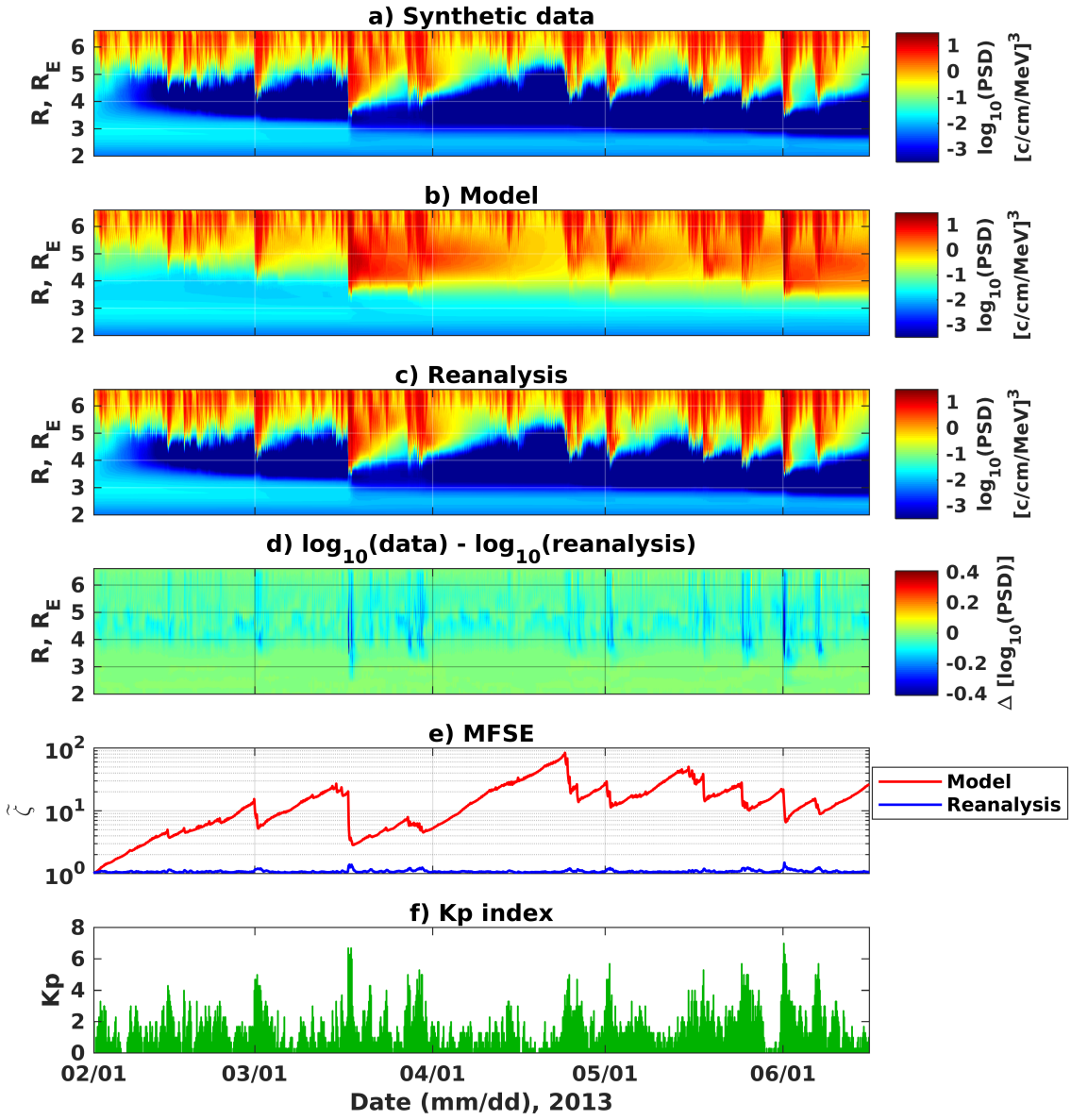

Figure 4.3: (a) MLT-averaged synthetic "true" state obtained by running the VERB-CS code for μ = 2.3 MeV/G and K = 0.3 $G^{1/2}R_E$ electrons. (b) MLT-averaged model results when the electron lifetimes are 10 times higher than in the model used to calculate the "true" state. (c) MLT-averaged reanalysis results. (d) Logarithmic difference ε_{log10} between the MLT-averaged synthetic "true" state and reanalysis. (e) Evolution of the MFSE. (f) The Kp index. $R \equiv R_0$.

4.3.3 Errors in Boundary Conditions

Modeling of the ring current electron dynamics requires the knowledge of MLT-dependent outer boundary conditions. Errors in the boundary conditions due to limited MLT coverage of different spacecraft can be a significant source of uncertainty in the

model. Interpolation of satellite data in time and space can only provide general large-scale MLT distribution of electron flux, and smaller-scale particle transport may not be reproduced properly. It is, therefore, important to understand if model errors due to inaccurate boundary conditions can be corrected by the Kalman filter. In this section, we present results of the fraternal twin experiment in which we decrease the boundary conditions 10 times in the VERB-CS code used for data assimilation, compared to the model that we use to obtain the synthetic data.

Figure 4.4 presents results of the fraternal twin experiment with the inaccuracies in boundary conditions. Figure 4.4a shows the MLT-averaged synthetic "true" state, and Figure 4.4b shows results of the convection model in which boundary conditions are 10 times lower than the boundary conditions which are used for obtaining the synthetic "true" state. The decrease in the boundary conditions affects only magnitude of the resulting electron PSD, and the qualitative picture of PSD evolution is similar to the synthetic data.

Figure 4.4c shows the reanalysis results, using the "imperfect" model with "inaccurate" boundary conditions, and Figure 4.4d shows the logarithmic difference ε_{log10} between the "truth" and the reanalysis. The reanalysis underestimates the "true" state by ~1 order above 6 R_E. It is an expected result, since Van Allen Probes apogee is located near 6 R_E, and there are not enough synthetic measurements for correcting model results beyond 6 R_E. The difference can also reach one order below 6 R_E when the Kp index sharply increases (compare numerous earthward-looking red spikes in Figure 4.4d and the Kp index in Figure 4.4f). During these periods, the convection electric field is enhanced, and electrons are transported from geostationary distances toward the Earth so fast that the Kalman filter needs more time to "pull" the model state toward the synthetic truth.

The model MFSE $\widetilde{\zeta}_{model}$ (see the red line in Figure 4.4e) increases with time and reaches ~4 at the end of the simulation, which corresponds to an average 4-fold underestimation of the synthetic "true" state. During periods of sharp increases in the Kp index, $\widetilde{\zeta}_{model}$ noticeably rises, since the errors in boundary conditions propagate inward faster. The reanalysis MFSE $\widetilde{\zeta}_{reanalysis}$ (see the blue line in Figure 4.4e) is much smaller compared to $\widetilde{\zeta}_{model}$. It does not fall below its background value, which is slightly higher than 1, due to permanent underestimation of the "true" state above ~6 R_E. Note that $\widetilde{\zeta}_{reanalysis}$ also increases with the increase in the Kp index, and may even reach $\widetilde{\zeta}_{model}$.

This fraternal twin experiment reveals two important aspects of the data assimilation, using only Van Allen Probes data. First, errors in boundary conditions cannot be corrected above 6 R_E without other data sources, and, second, the Kalman filter adjusts the imperfect model with inaccurate boundary conditions to the synthetic state

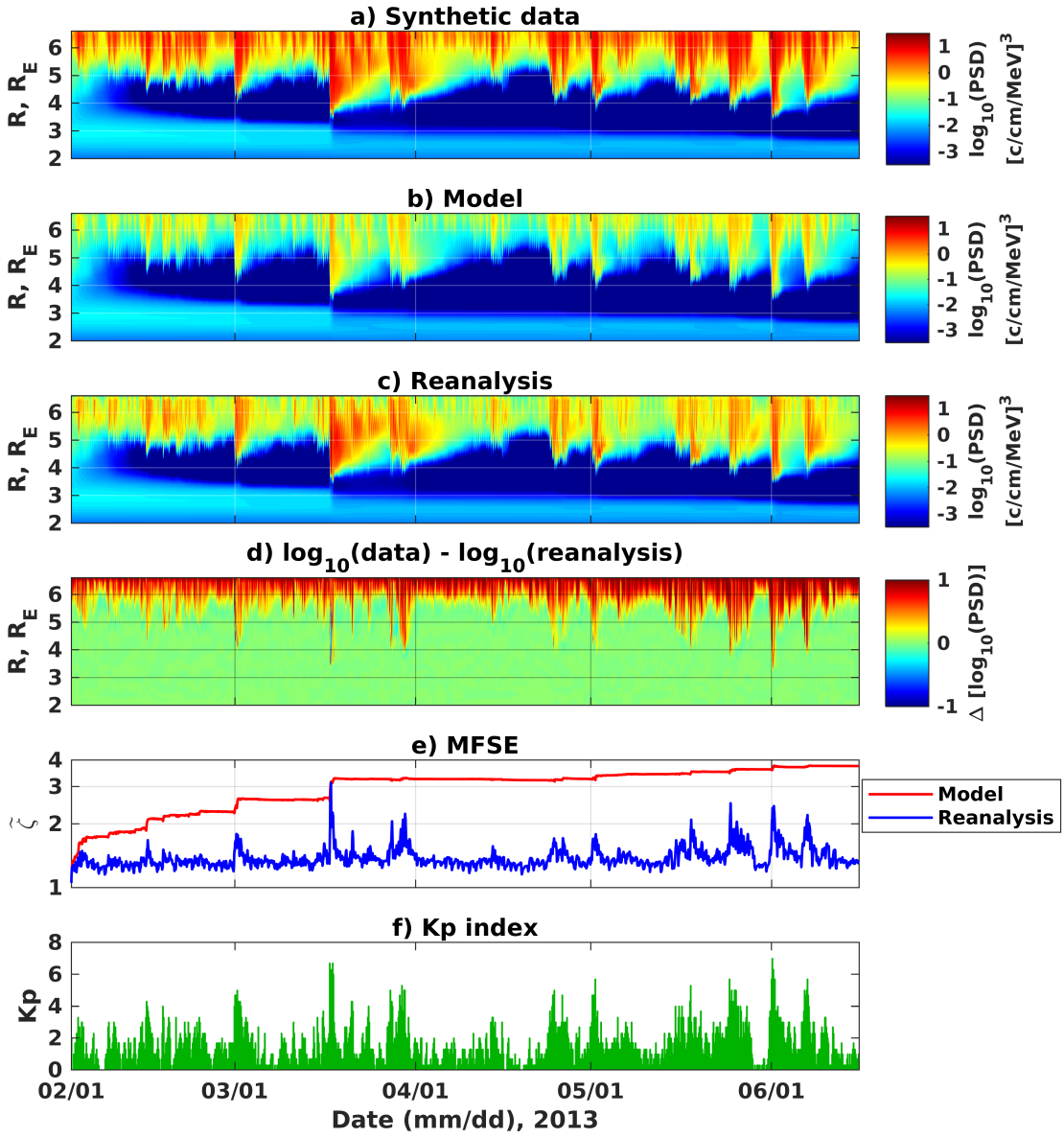

Figure 4.4: (a) MLT-averaged synthetic "true" state obtained by running the VERB-CS code for μ = 2.3 MeV/G and K = 0.3 $G^{1/2}R_E$ electrons. (b) MLT-averaged model results when the boundary conditions are 10 times lower than in the model used to calculate the "true" state. (c) MLT-averaged reanalysis results. (d) Logarithmic difference ε_{log10} between the MLT-averaged synthetic "true" state and reanalysis. (e) Evolution of the MFSE. (f) The Kp index. $R \equiv R_0$.

on the time scales comparable to the duration of a storm. We note, however, that the considered fraternal twin experiment is an extreme case of errors in boundary conditions, and errors in real problems can be significantly lower if satellite measurements or statistical models are used to produce the reanalysis.

4.3.4 Errors in Convection Electric Field

Determination of the global convection electric field is one of the most challenging tasks in modeling of the ring current electron dynamics. Due to unavailability of global in-situ electric field measurements, ring current codes have to rely on empirical models or self-consistent calculations of the electric field. Uncertainties in the electric field model directly result in uncertainties in drift velocities, affect electron transport timescales, and may lead to significant errors in the distribution of electron PSD. In this fraternal twin experiment, we study whether the Kalman filter can improve predictions of ring current electron PSD in the case of an inaccurate electric field model. We multiply the convection electric field by 4 and assimilate the synthetic "true" state provided by the "perfect" model. We note that the co-rotation electric field remains unchanged.

Figure 4.5 shows results of the fraternal twin experiment. The synthetic "true" state (Figure 4.5a) is obtained with the same parameters as has been used in the previous experiments. Figure 4.5b presents results of the VERB-CS code with the four-fold increase in the convection electric field. The results of the "imperfect" model show fast earthward propagation of the ring current electrons since the convection electric field is responsible for radial transport of the particles in the model. The difference between the "true" state and the model is most prominent between 2.5 and 6 R_E. The model overestimates the "true" state by several orders of magnitude, and the difference grows with enhanced geomagnetic activity. One of the most noticeable features in the model results (Figure 4.5b) is an enhancement of electron PSD at ~3 R_E that occurs during the 17 March 2013 geomagnetic storm and lasts until the end of the simulations, being intermittently refilled during periods of increases in the Kp index.

Figure 4.5c presents reanalysis results which combine the "imperfect" model and synthetic data obtained along the orbits of Van Allen Probes being flown through the synthetic "true" state. The reanalysis contains features observed both in synthetic data (Figure 4.5a) and model predictions (Figure 4.5b). The reanalysis eliminates long-term features produced by the model, such as the "unrealistic" enhancement at 3 R_E. However, the Kalman filter is not able to correct the shorter-term behavior of the model on the time scales of approximately less than a day. The logarithmic difference ε_{log10} between the data and the model (see Figure 4.5d) is highest near the inner edge of the enhanced PSD and exceeds one order of magnitude. The difference is shifted earthward with the increase in the Kp index, when the model electric field sharply becomes larger. This fact suggests that more measurements at different radial distances and MLT sectors are required to reconstruct global convective transport and loss of the electrons for typical storm time scales.

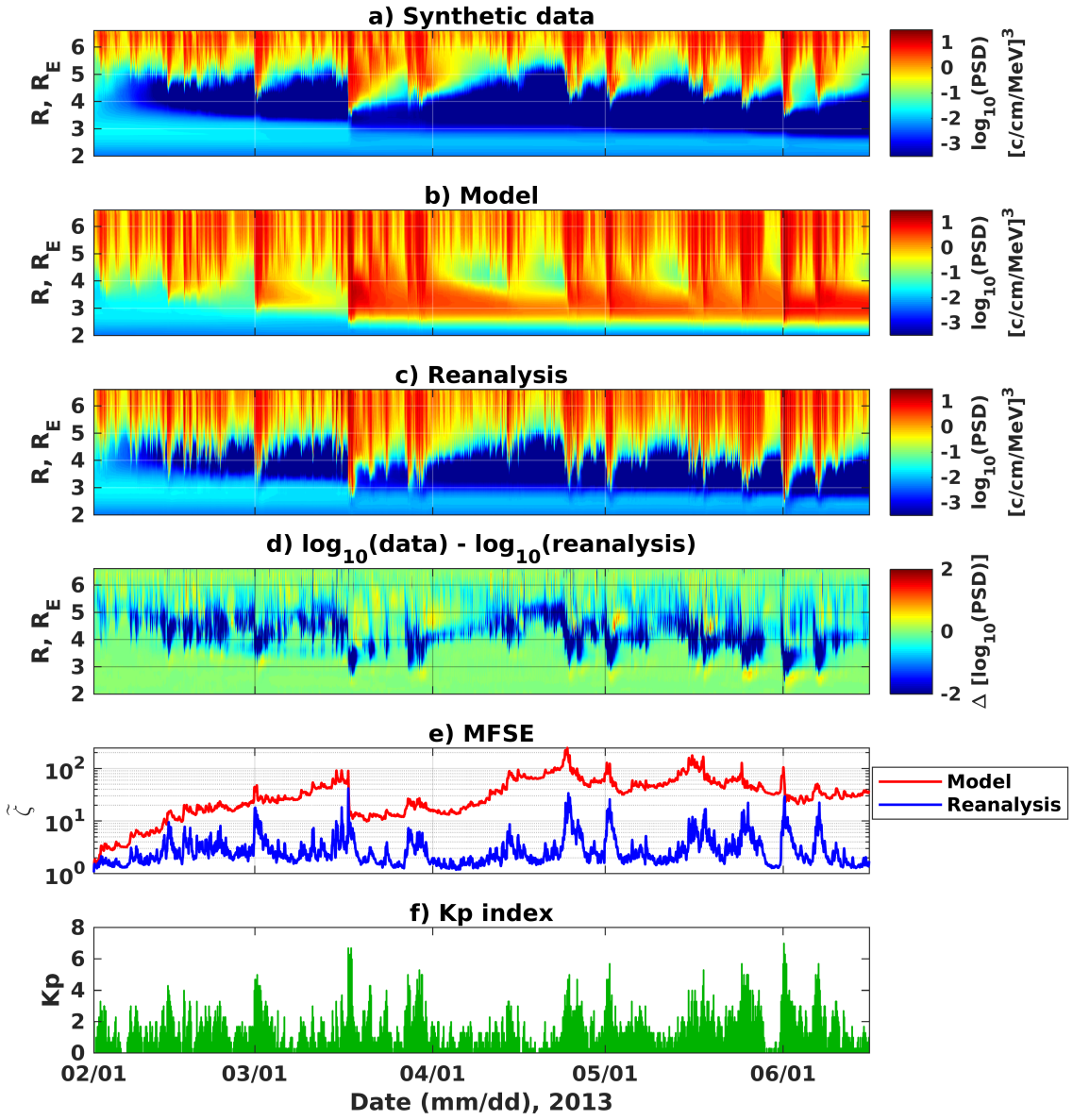

Figure 4.5: (a) MLT-averaged synthetic "true" state obtained by running the VERB-CS code for μ = 2.3 MeV/G and K = 0.3 $G^{1/2}R_E$ electrons. (b) MLT-averaged model results when the convection electric field is 4 times higher than in the model used to calculate the "true" state. (c) MLT-averaged reanalysis results. (d) Logarithmic difference ε_{log10} between the MLT-averaged synthetic "true" state and reanalysis. (e) Evolution of the MFSE. (f) The Kp index. $R \equiv R_0$.

The reanalysis MFSE $\widetilde{\zeta}_{reanalysis}$ (see Figure 4.5e) is noticeably decreased in comparison to the model $\widetilde{\zeta}_{model}$. During periods of the increase in the Kp index, $\widetilde{\zeta}_{reanalysis}$ also grows sharply and can be comparable to $\widetilde{\zeta}_{model}$. We note that $\widetilde{\zeta}_{reanalysis}$ in this experiment is generally larger than in the previous experiments, being sometimes higher than 10. The correction of errors associated with overestimated drift velocities seems

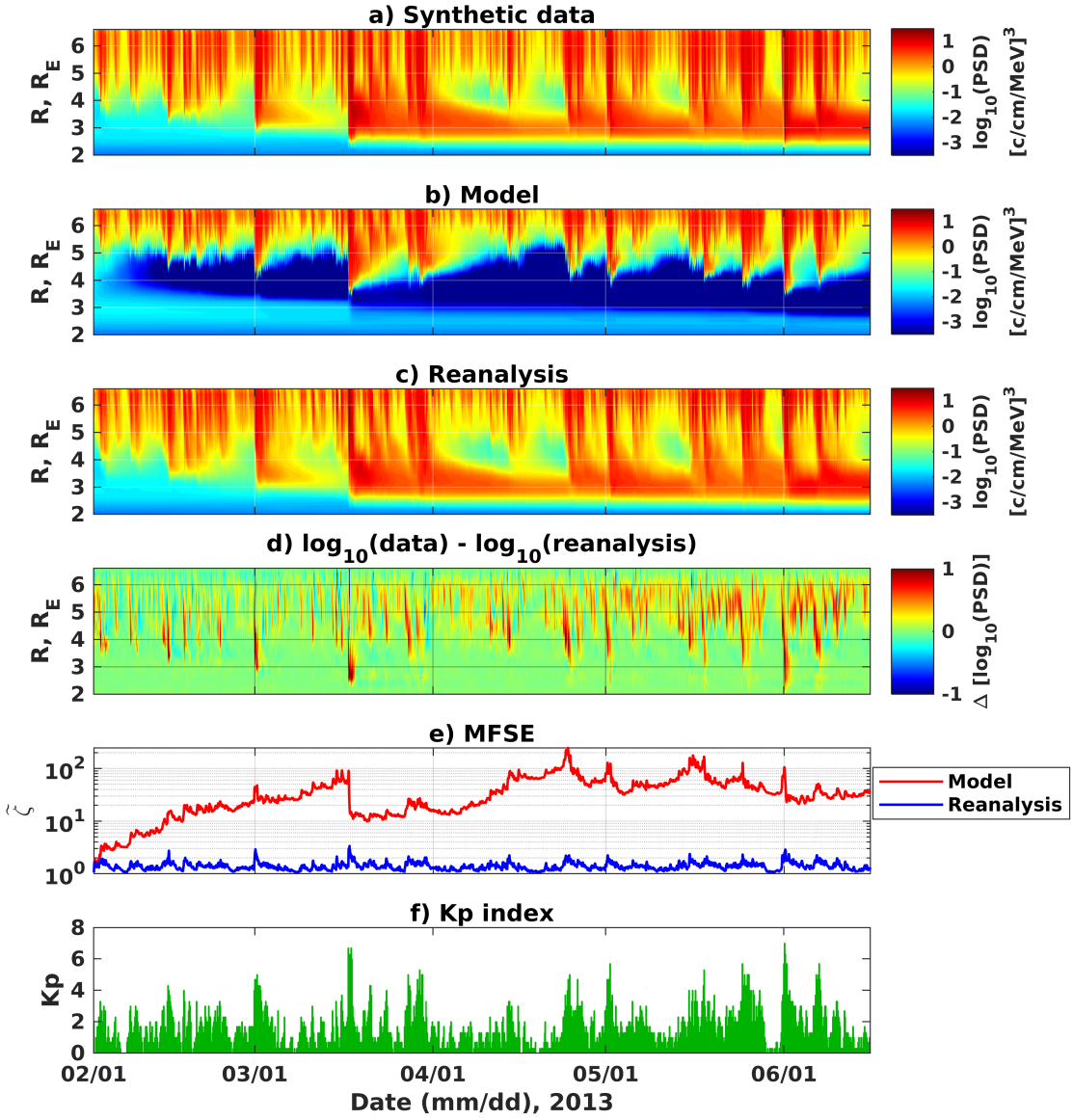

Figure 4.6: (a) MLT-averaged synthetic "true" state obtained by running the VERB-CS code for μ = 2.3 MeV/G and K = 0.3 $G^{1/2}R_E$ elecrtons. (b) MLT-averaged model results when the convection electric field is 4 times smaller than in the model used to calculate the "true" state. (c) MLT-averaged reanalysis results. (d) Logarithmic difference ε_{log10} between the MLT-averaged synthetic "true" state and reanalysis. (e) Evolution of the MFSE. (f) The Kp index. $R \equiv R_0$.

to be more challenging for the Kalman filter than the correction of errors in boundary conditions and electron lifetimes.

We also performed an experiment with the convection electric field being four times smaller in the model that was used for data assimilation than in the model that provided synthetic data. Figure 4.6 shows the results of the experiment. We note that

we simply swapped the models used in the previous experiment for performing data assimilation (Figure 4.5b) and obtaining a synthetic "true" state (Figure 4.5a) to avoid very low PSD values in the synthetic data due to slow radial transport. The results indicate that the overall difference between the synthetic data and reanalysis is much smaller in the case, when the model electric field is underestimated, than in the case of overestimation.

4.4 Reanalysis of Ring Current Electrons using Van Allen Probes Data

The experiments with synthetic data give a promising result that the Kalman filter can improve predictions of the ring current electron dynamics by decreasing model errors associated with uncertainties in electron lifetimes, outer boundary conditions, and drift velocities, and provide reasonable reanalysis results, using only Van Allen Probes synthetic "measurements." In this section, we apply the Kalman filter to combine the VERB-CS code with real Van Allen Probes measurements by means of data assimilation.

4.4.1 Long-Term Reanalysis from 1 February 2013 to 16 June 2013

We adopt the model parameters described in Sections 4.2.2 and 4.2.3, which have been used to produce the synthetic "true" state for the fraternal twin experiments. The model relies on several simplifications which likely introduce noticeable errors. Errors in the electron drift velocities are associated with the magnetic dipole field approximation, which is not valid during storm times at high radial distances, and the Kp parameterization of the convection electric field, which is naturally driven by the dayside reconnection and varies on time scales much shorter than the cadence of the Kp index. Uncertainties in boundary conditions stem from the used statistical model, conversion from the spin-averaged to directional flux, and calculation of the PSD under the dipole field approximation. Parameterized electron lifetimes and a simplified plasmapause model may also contribute to the overall model error.

Figure 4.7a presents evolution of μ = 2.3 MeV/G and K = 0.3 $G^{1/2}R_E$ electron PSD derived from Van Allen Probes HOPE and MagEIS measurements between 1 February 2013 and 16 June 2013. The PSD values are binned in time and radial distance with 10 hour and 0.2 R_E steps, respectively. The PSD varies by more than 3 orders of magnitude within GEO, and electrons can be propagated down to 2.5 R_E during geomagnetic storms (see the Kp-index in Figure 4.7e).

Figure 4.7b shows MLT-averaged VERB-CS code results for the considered period

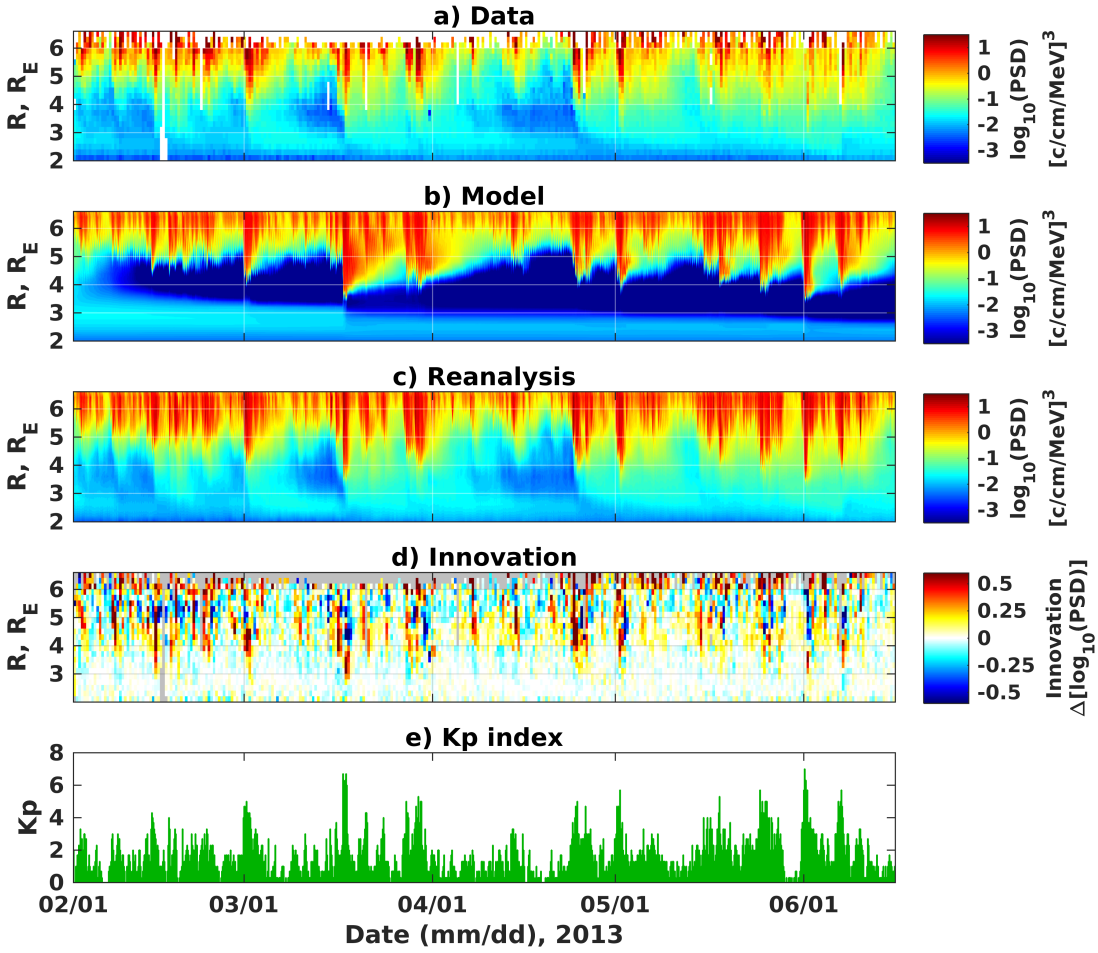

Figure 4.7: (a) Evolution of electron PSD for μ = 2.3 MeV/G and K = 0.3 $G^{1/2}R_E$ obtained from Van Allen Probes data and binned in time and radial distance. (b) MLT-averaged model results when the Kalman filter is not applied. (c) MLT-averaged reanalysis results. (d) Innovation vector binned in time and radial distance. (e) The Kp index. $R \equiv R_0$.

of time. Note that these results contain real model errors, yet they have been treated as the synthetic truth in the fraternal twin experiments. The model results noticeably differ from the observed PSD. The model underestimates the data between 3 R_E and ~4.5-5 R_E by several orders of magnitude (see the dark-blue color in Figure 4.7b). The observed storm-time enhancements of electron PSD are reproduced by the model above ~4.5 R_E. However, the model overestimates the post-storm PSD for some events, such as those on 17 March 2013 and 29 March 2013. The model-data comparison suggests that violated balance between transport and loss processes may lead to significant deviations of the predicted PSD on time scales from several weeks to months.

Figure 4.7c presents MLT-averaged reanalysis results combining the VERB-CS code and Van Allen Probes observations. The Kalman filter corrects for inaccuracies in the

model and improves the results to better match the observations. The reanalysis captures observed penetration of the ring current electrons from GEO to 2.5 R_E, which cannot be reproduced by the model, and the overall radial extent of the reanalysis shows the same variability, as seen in the data. The reanalysis results resemble the observations and significantly differ from the model below ~5 R_E. The features of both model and data can be seen in the reanalysis above 5 R_E, where the electron PSD reaches the highest values.

The correction that the Kalman filter adds to the model is most clearly seen in an innovation vector. The innovation is a difference between observations and forecast transformed into the observation space (vector $\mathbf{d}_k$ in equation (4.16)). We note that the innovation in our formulation is the natural logarithm of the ratio between observed PSD and the model, since we use the natural logarithm of PSD as a model and observation variables (see equation (4.3)). For simplicity, we transform the ratio from natural to common logarithm. Negative values of the innovation indicate that the model overestimates the data, and positive values mean that the observed PSD is higher than those predicted by the model.

Figure 4.7d shows the innovation transformed back into the model MLT-R_0 space. The abundance of both positive and negative values of the innovation indicates that the model may underestimate, as well as overestimate, the data. For the events when electrons are transported down to 2.5-3 R_E, the innovation shows high positive values below 4 R_E, implying that the radial transport in the model is less efficient than in reality. The ring current electron PSD experiences intermittent enhancements and decreases between 4 R_E and 6 R_E, and the innovation shows the highest magnitude and more frequent variations in that region.

Figure 4.8a presents the innovation binned in the Kp index and radial distance, and Figure 4.8b shows the number of samples used to calculate the innovation. During relatively quiet geomagnetic times (Kp < 4−), the innovation shows the smallest deviations from zero. The innovation is almost zero between 2 R_E and 4 R_E, and the deviations are higher above 4 R_E. The innovation is significantly bigger during disturbed geomagnetic conditions (Kp ≥ 4) than during quiet times. The innovation shows high positive values between 3 R_E and 4 R_E when Kp ≥ 4, which indicates that the model cannot reproduce fast earthward propagation of ring current electrons. This fact, together with almost zero innovation in this region during quiet times, suggests that the underestimation of electron PSD below 4-5 R_E produced by the model (see Figure 4.7b) is associated with the errors in the storm-time electron transport. At higher radial distances, the uncertainties in boundary conditions start playing a more important role during disturbed times, and the model both underestimates and overestimates the

data.

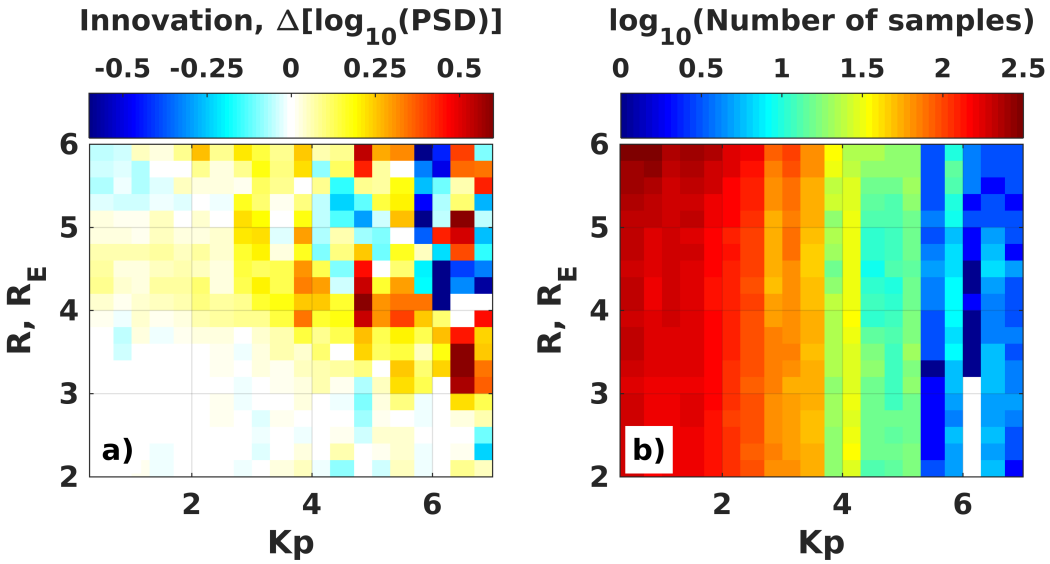

Figure 4.8: (a) Innovation vector for μ = 2.3 MeV/G and K = 0.3 $G^{1/2}R_E$ binned in the Kp index and radial distance. (b) Number of samples which are used to calculate the mean value in each bin.

4.4.2 Reanalysis during the 1 June 2013 Storm

In the previous sections, we have analyzed the performance of the Kalman filter on time scales of months. We have shown that the Kalman filter is able to improve model predictions, but may not perform well during storm times. In this section, we apply the Kalman filter during the storm observed on 1 June 2013 to study the ability of the Kalman filter to reconstruct MLT-dependent distribution of the ring current electron PSD on time scales of several days when the magnetospheric convection is most intense. During the chosen storm, the Kp index reached 7, and the Dst index went down to -124 nT at ~08:00 UT on 1 June 2013 (see Figure 4.9).

We initialize the VERB-CS code at 00:00 UT 30 May 2013 by MLT-averaging Van Allen Probes HOPE and MagEIS data over ±5 hours, which approximately corresponds to one satellite orbit. We model evolution of μ = 2.3 MeV/G and K = 0.3 $G^{1/2}R_E$ electron PSD and use the same parameters of the convection model which are described in Sections 4.2.2 and 4.2.3 and have been used in previous numerical simulations.

Figure 4.10 illustrates the global PSD evolution during the storm. The first row (Figures 4.10a-4.10e) shows the model results if the Kalman filter is not applied, the second row (Figures 4.10f-4.10j) presents the reanalysis, and the last row (Figures 4.10k-4.10o) shows the logarithm of the ratio between the reanalysis and the model. Both reanalysis and model are initialized with the same PSD (see Figures 4.10a, 4.10f, and 4.10k). The model results do not noticeably differ from the reanalysis 30 hours after the beginning

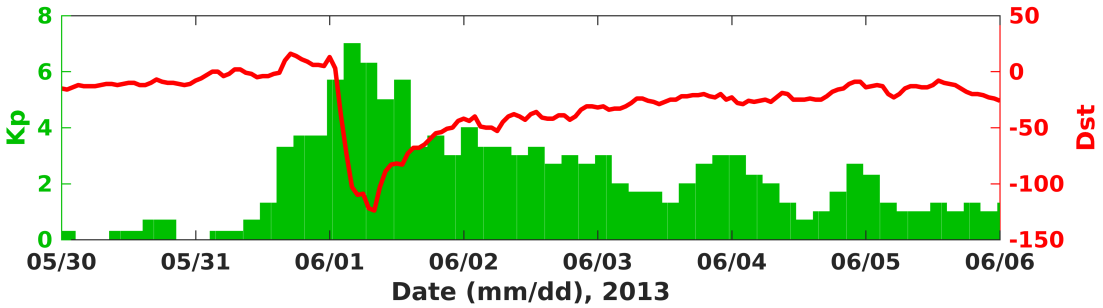

Figure 4.9: The Kp (green) and Dst (red) indices during the geomagnetic storm observed on 1 June 2013.

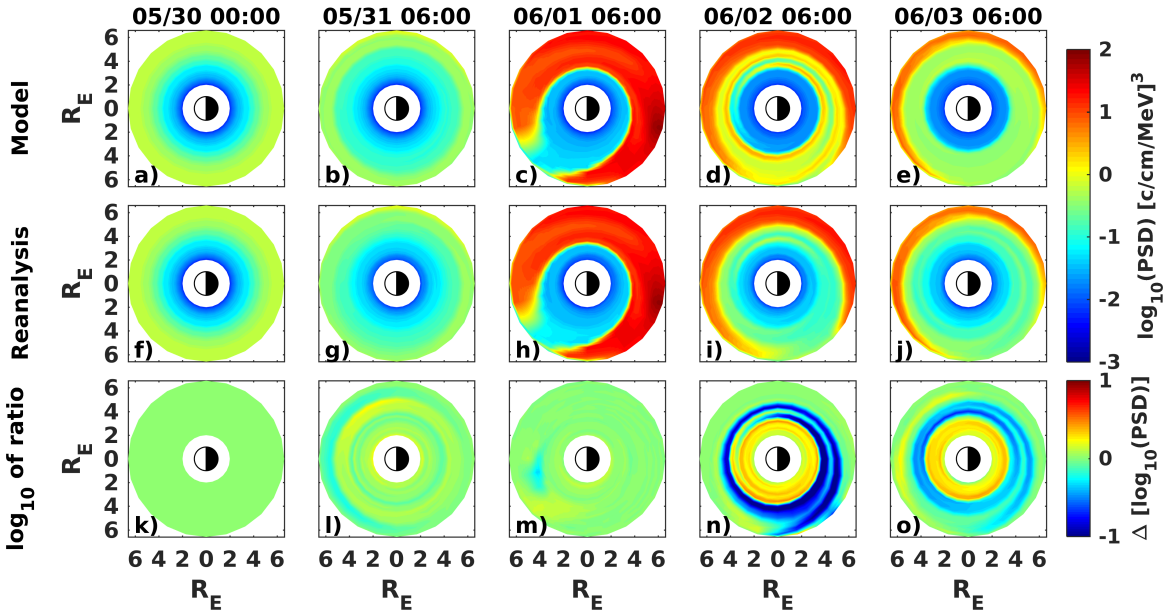

Figure 4.10: Global evolution of PSD for μ = 2.3 MeV/G and K = 0.3 $G^{1/2}R_E$ electrons during the geomagnetic storm observed on 1 June 2013: (a-e) model results when the Kalman filter is not applied, (f-j) reanalysis, (k-o) the difference between common logarithms of reanalysis and model results.

of the simulation (see Figures 4.10b, 4.10g, and 4.10l), most likely due to the fact that geomagnetic conditions were very quiet.

During the main phase of the storm, the model results and the reanalysis are almost identical (see Figures 4.10c, 4.10h, and 4.10m) which may indicate that the Kalman filter is not able to correct the model errors during the storm main phase when PSD is significantly enhanced and electrons are rapidly transported earthward. One day later, at 6:00 UT on 2 June 2013, the model predicts lower PSD values below 3 R_E than the reanalysis shows (see Figure 4.10n). The reanalysis is generally lower than the model results between 3 R_E and 5 R_E (compare Figures 4.10d and 4.10i), and a spiral-like structure of enhanced PSD, which is observed in the model results at ~4 R_E (Figure 4.10d) is almost absent in the reanalysis (Figure 4.10i). The difference between the reanalysis and the model becomes slightly smaller two days after the main phase

of the storm (see Figure 4.10o).

The presented results indicate that assimilation of Van Allen Probes point measurements is able to correct the errors in the predictions of the log-transformed convection model across different MLT sectors, in accordance with the observations. The Kalman filter adjusts the model to local Van Allen Probes observations within the assimilation window, and the model spreads the locally modified PSD across different MLT sectors and radial distances. This mechanism is responsible for pronounced differences in regions which are not covered by the satellite observations (e.g., $R_0 > 2$ on the day side for the considered period of time). A lack of data near GEO and in different MLT sectors leads to the limitations described in the fraternal twin experiments in Sections 4.3.3 and 4.3.4: the reanalysis is likely dominated by the model contribution rather than the data during storm times and near GEO, during both quiet and disturbed geomagnetic conditions.

4.4.3 Reanalysis for Different Values of μ

Adiabatic invariants are natural variables which are used to formulate equations describing radiation belt and ring current electron dynamics. However, it is more instructive to predict the evolution of electron flux as a function of energy and pitch angle for real applications such as calculating fluences, which help estimate potential effects of surface and deep dielectric charging of satellites. Calculation of electron flux for given energy and pitch angle requires the knowledge of PSD for a range of first and second adiabatic invariants. In this section, we apply the developed data assimilation framework for reconstruction of electron PSD for different values of μ which cover a typical energy range of the ring current electrons.

We use the same approach described in Section 4.2, to assimilate PSD obtained from Van Allen Probes HOPE and MagEIS data for μ = 0.1 and 9.9 MeV/G and constant K = 0.3 $G^{1/2}R_E$, using the convection model and the Kalman filter. The selected adiabatic invariants roughly correspond to 1 and 100 keV at ~4 R_E, respectively (see Figure 4.2).

Figure 4.11 presents reanalysis of μ = 0.1 MeV/G and K = 0.3 $G^{1/2}R_E$ PSD in the same format as Figure 4.7. The PSD obtained with the model (Figure 4.11b) is generally higher than the observations (Figure 4.11a) below ~4.5 R_E. The model shows fast earthward transport during periods of the Kp index $\gtrsim$ 4, and the inner extent of the PSD produced by the model is located closer to the Earth by 1-1.5 R_E. The reanalysis (see Figure 4.11c) is able to adjust the model to the measurements, with the biggest corrections made between 3 and 4.5 R_E during storm times (see Figure 4.11d). As in the case of the fraternal twin experiment with artificially increased velocities presented in

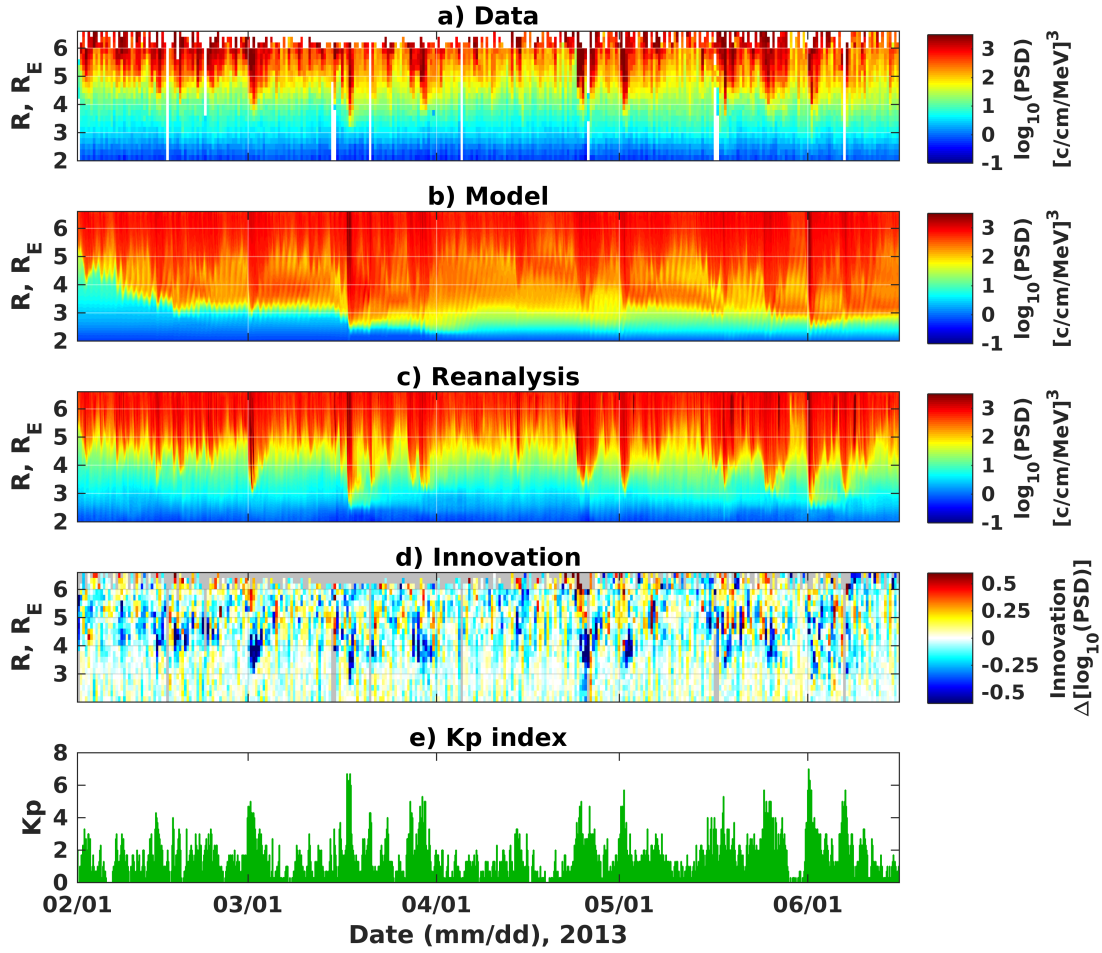

Figure 4.11: (a) Evolution of electron PSD for μ = 0.1 MeV/G and K = 0.3 $G^{1/2}R_E$ obtained from Van Allen Probes data and binned in time and radial distance. (b) MLT-averaged model results when the Kalman filter is not applied. (c) MLT-averaged reanalysis results. (d) Innovation vector binned in time and radial distance. (e) The Kp index. $R \equiv R_0$.

Section 4.3.4, the Kalman filter is more effective on the time scales longer than ~1 day. During geomagnetic storms, the reanalysis mostly resembles the model rather than the data, which is most probably caused by a lack of global in-situ measurements. We also note that MLT-averaging may also affect the comparison of the results presented in Figure 4.11.

Figure 4.12 shows reanalysis for μ = 9.9 MeV/G and K = 0.3 $G^{1/2}R_E$ electrons. Such values of the adiabatic invariants correspond to relatively high energies, and the electrons are transported radially by the diffusion process (Lyons and Schulz, 1989). Convection equation (4.2) does not take into account radial diffusion, and the model results (Figure 4.12b) significantly underestimate observations (Figure 4.12a). The reanalysis (Figure 4.12c) shows that even in the case of a missing physical process in the model

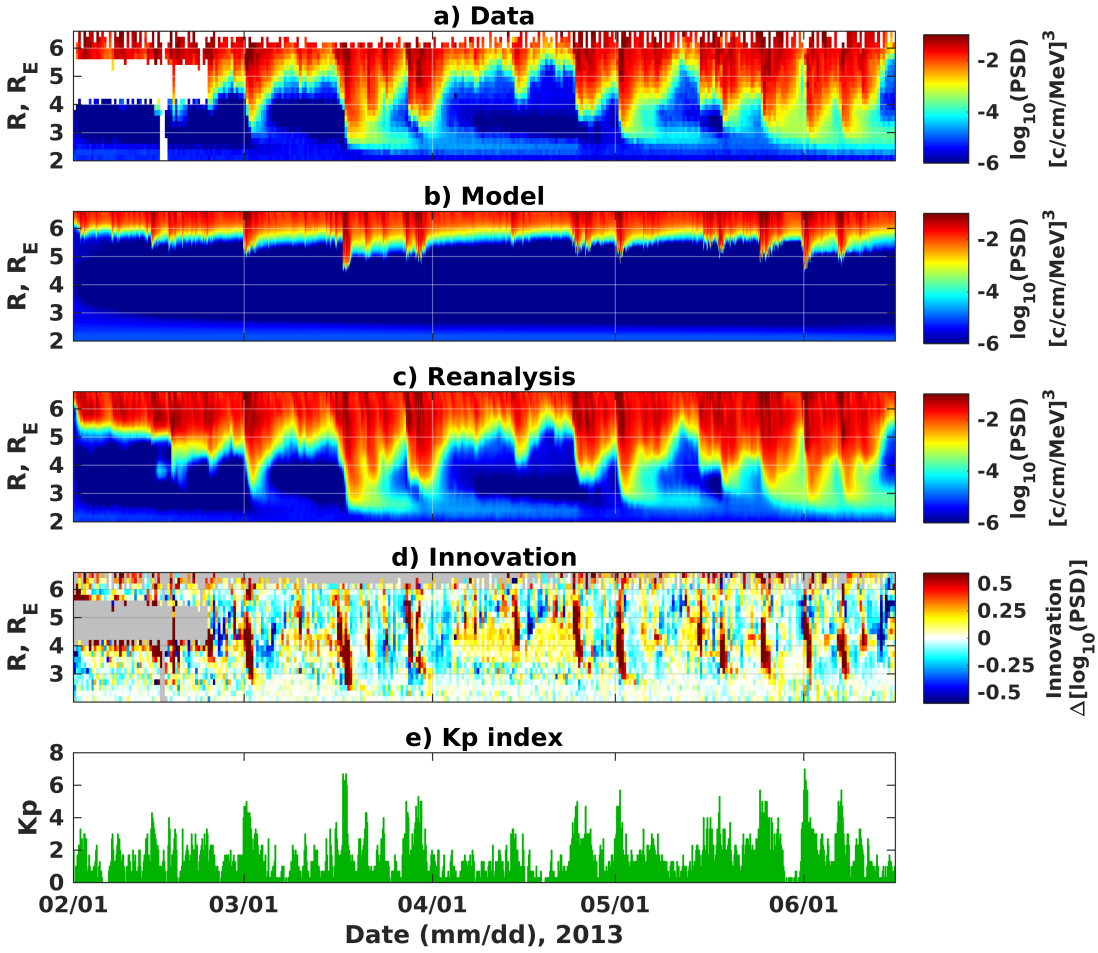

Figure 4.12: (a) Evolution of electron PSD for μ = 9.9 MeV/G and K = 0.3 $G^{1/2}R_E$ obtained from Van Allen Probes data and binned in time and radial distance. (b) MLT-averaged model results when the Kalman filter is not applied. (c) MLT-averaged reanalysis results. (d) Innovation vector binned in time and radial distance. (e) The Kp index. $R \equiv R_0$.

equation, the Kalman filter can correct model predictions, using Van Allen Probes data. As expected, the innovation is highest and positive for periods of the high Kp index, which indicates that the Kalman filter recognizes the underestimation of data by the model and adjusts the predictions accordingly.

4.5 Discussion

In this work, we used the log-transformed VERB-CS code, which was specially developed for this study on the basis of the approach of the VERB-4D code, Van Allen Probes in-situ measurements, and the Kalman filter to reconstruct the global dynamics of ring current electron PSD from 1 February 2013 to 16 June 2013. We used the model with Kp-dependent boundary conditions, drift velocities and electron lifetimes to effi-

ciently perform the long-term simulations and study the performance of the Kalman filter. While the simplified model can deviate from the data on timescales of weeks or months, the reanalysis agrees better with the observations. Numerical experiments with synthetic data showed that the Kalman filter can be efficiently applied to correct errors in model predictions associated with electron lifetimes, outer boundary conditions, and drift velocities. We showed that the Kalman filter adjusts predictions of the convection model to the observations across different MLT sectors, using only local Van Allen Probes measurements.

We demonstrated that the Kalman filter is a powerful tool that can be used in real applications and long-term studies of the ring current electron dynamics. Existing models include many physical processes such as charged particle transport and wave-particle interactions and numerous parameters and parameterizations which may contain significant uncertainties (e.g., plasmapause and magnetopause location, drift velocities, and spatial outer boundary conditions). Our results suggest that the Kalman filter can provide global reanalysis, which is more accurate than either interpolated data or a global model.

Reanalysis of the ring current electron dynamics can be used to identify the missing physical processes in the model. By inspecting the innovation, it is possible to determine in which regions and under which conditions the model overestimates or underestimates observations and study the balance between transport and loss processes. As an example, we show that the earthward transport of μ = 2.3 MeV/G and K = 0.3 $G^{1/2}R_E$ electrons below ~4 R_E during storm times cannot be reproduced by the simplified Kp-dependent convection model.

The Kalman filter can correct model predictions for typical ring current electron energies from 1 to 100 keV. Convection model (4.2) can be further applied to a range of different values of first and second adiabatic invariants and blended with Van Allen Probes data by means of the Kalman filter to reconstruct electron fluxes for particular energy and pitch angle inside GEO. Such an extension is beyond the scope of this manuscript and will be performed in our future studies.

Since in-situ particle measurements are localized in a narrow region of space at a particular time, assimilation of Van Allen Probes observations has inherited several limitations. During the main phase of geomagnetic storms, electron PSD is significantly enhanced, and ring current electrons undergo fast earthward transport. The Kalman filter may require a time period comparable to that of a typical storm main phase to reconstruct global distribution of electron PSD. As a result, the reanalysis of global storm-time electron distribution can be primarily driven by the model rather then observations during a storm main phase. The lack of data near GEO also renders

the reanalysis to rely on the model. The performance of the Kalman filter can be significantly improved by simultaneously assimilating multiple satellite observations, such as those made by ERG, THEMIS, LANL GEO, or GOES missions. More detailed global evolution of electrons fluxes or PSD can be obtained by assimilating POES and MetOp satellite data which simultaneously provide measurements at different MLT sectors and across different L-shells with high temporal resolution. We note that data assimilation of multiple spacecraft data requires careful intercalibration and specification of observation errors for each satellite.

The Kalman filter relies on the assumption of Gaussian distribution of model and observation errors. In this work, we use the logarithm of PSD as model and observation variables. The choice of the log-transformed variables is made to eliminate the computational issues which are associated with the possibility of the Kalman filter to produce negative PSD values. By using the log-transformed variables, we implicitly assume log-normal distribution of model and observation errors. Although non-negativity of PSD indicates that the distribution of errors cannot be strictly Gaussian, log-normal distribution of the errors is also not guaranteed. The quantification of model and observation errors is a challenging problem which we will address in future studies.

The two-dimensional log-transformed convection model that we use in this study can be potentially incorporated in the more sophisticated space weather codes and frameworks. For instance, the VERB-4D code includes both ring current and radiation belt electron transport, loss and acceleration processes driven by convection, radial diffusion, and local wave-particle interactions. Methods of data assimilation have been already developed for the radiation belt portion of the code (Shprits et al., 2013a; Kellerman et al., 2014), and the approach presented in this study supplements the developed methods to globally reconstruct the four-dimensional state of the ring current and radiation belt electrons by means of the Kalman filter and the VERB-4D code.

4.6 Summary and Conclusions

We presented the long-term reanalysis of the ring current electron dynamics, using Van Allen Probes observations, the log-normal Kalman filter, and the two-dimensional VERB-CS code. We showed that the Kalman filter can be applied to reconstruct global evolution of ring current electron PSD using Van Allen Probes point measurements. The main conclusions are summarized below.

1. Even when only Van Allen Probes data are used, the Kalman filter is capable of decreasing errors in model predictions which are associated with electron lifetimes, boundary conditions, and drift velocities.

2. Reanalysis retains features which are observed in data and cannot be fully reproduced by the model such as the earthward propagation of μ = 2.3 MeV/G and K = 0.3 $G^{1/2}R_E$ electrons down to ~2.5 R_E and shorter loss timescales.

3. The innovation allows us to study performance of the model and identify model uncertainties. With regard to the Kp-dependent convection model applied to μ = 2.3 MeV/G and K = 0.3 $G^{1/2}R_E$ electrons, the magnitude of the innovation increases (and hence, the model accuracy decreases) with radial distance and the Kp index.

4. Assimilation of Van Allen Probes measurements globally adjusts model predictions in accordance with the observations, even in sectors in which the data are not available.

5. The Kalman filter can adjust model predictions for μ = 0.1, 2.3, and 9.9 MeV/G and constant K = 0.3 $G^{1/2}R_E$, using Van Allen Probes data, which corresponds to a typical energy range of ring current electrons.

6. Assimilation of multiple spacecraft data is required to reconstruct the ring current electron dynamics during storm main phases and near GEO.

The results obtained in this study indicate that the Kalman filter can efficiently combine a physics-based model of the ring current electrons and sparse satellite observations to improve model predictions. The further studies will include more sophisticated models, multi-spacecraft data, and combined reanalysis of the ring current and radiation belt electron dynamics.

Acknowledgments

The authors acknowledge use of NASA/GSFC's Space Physics Data Facility's OMNIWeb service, and OMNI data. The Kp index was provided by GFZ Potsdam. The executable for reproducing the results is available upon request. The authors are grateful to the RBSP-ECT team for the provision of Van Allen Probes observations. All RBSP-ECT data are publicly available at the web site http://www.RBSP-ect.lanl.gov/. This research was supported by the Helmholtz-Gemeinschaft (HGF) [10.13039/501100001656], NASA grant NNX15AI94G, and project PROGRESS funded by EC – Horizon 2020 Framework Programme (H2020) [10.13039/100010661] (637302)). The research has been partially funded by Deutsche Forschungsgemeinschaft (DFG) through grant CRC 1294 Data Assimilation, Project B06. This work used computational and storage services associated with the Hoffman2 Shared Cluster provided by UCLA Institute for Digital Research and Education's Research Technology

Group. The authors thank the developers of the IRBEM library which was adapted for use in the current study. The authors thank Sharon Uy for her help with editing the manuscript. The authors are grateful to anonymous reviewers for the insightful comments which helped improve the manuscript.

Chapter 5

Signatures of Ultrarelativistic Electron Loss in the Heart of the Outer Radiation Belt Measured by Van Allen Probes

Published as:
Aseev, N. A., Shprits, Y. Y., Drozdov, A. Y., Kellerman, A. C., Usanova, M. E., Wang, D., and Zhelavskaya, I. S., 2017. Signatures of Ultrarelativistic Electron Loss in the Heart of the Outer Radiation Belt Measured by Van Allen Probes. *Journal of Geophysical Research: Space Physics*, 122(10):10,102–10,111. doi:10.1002/2017JA024485

Abstract

Up until recently, signatures of the ultrarelativistic electron loss driven by Electromagnetic Ion-Cyclotron (EMIC) waves in the Earth's outer radiation belt have been limited to direct or indirect measurements of electron precipitation or the narrowing of normalized pitch-angle distributions in the heart of the belt. In this study, we demonstrate additional observational evidence of ultrarelativistic electron loss that can be driven by resonant interaction with EMIC waves. We analyzed the profiles derived from Van Allen Probes particle data as a function of time and three adiabatic invariants between 9 October and 29 November 2012. New local minimums in the profiles are accompanied by the narrowing of normalized pitch-angle distributions and ground-based detection of EMIC waves. Such a correlation may be indicative of ultrarelativistic electron precipitation into the Earth's atmosphere caused by resonance with EMIC waves.

5.1 Introduction

Wave-particle interactions causing loss and acceleration of electrons in the Earth's radiation belts have been extensively studied since the beginning of the space era (Thorne and Kennel, 1971; Imhof et al., 1977; Millan and Thorne, 2007; Shprits et al., 2008a,b; Xiao et al., 2009; Thorne, 2010; Xiao et al., 2010). Recently, particular attention has been paid to the dynamics of very energetic ultrarelativistic electrons (energies above ~1-2 MeV) (e.g., Baker et al., 2013b; Shprits et al., 2013b; Xiao et al., 2015; Shprits et al., 2017). However, major mechanisms controlling this population are still under debate. The purpose of this study is to provide additional observational evidence of ultrarelativistic electron loss due to local resonant interaction with EMIC waves.

The launch of Van Allen Probes, formerly known as Radiation Belt Storm Probes (RBSP), on 30 August 2012, has led to significant progress in understanding of the dynamics of ultrarelativistic electron population. The Relativistic Electron-Proton Telescope (REPT) (Baker et al., 2013a), which is a part of the Energetic Particle, Composition, and Thermal Plasma (ECT) Suite (Spence et al., 2013) on board the satellites, allows measuring the electron distribution of energies from ~2 to ~10 MeV and above and covers both inner and outer belt regions from 1.2 R_E to 5.8 R_E. A few days after the launch, Van Allen Probes detected the unusual three-zone radiation belt structure (Baker et al., 2013b). The third belt (narrow "storage ring" (Baker et al., 2013b)), persisting for almost a month, was formed by ultrarelativistic electrons at $L^* = \sim 3.25$ after the flux dropout on ~3 September 2012. Shprits et al. (2013b) analyzed this unique event, modeling the electron dynamics with the Versatile Electron Radiation Belt code (VERB code) (Shprits et al., 2009; Subbotin and Shprits, 2009). They showed that EMIC wave-induced electron scattering is responsible for the formation of the third belt, and the expanded plasmasphere placed the belt in a different plasma environment, where electromagnetic waves weakly affect ultrarelativistic electrons, and the third belt remained for tens of days. Long-term modeling results obtained by Drozdov et al. (2015), using the VERB code, showed that observed 3.6 MeV electron fluxes are significantly overestimated if EMIC waves are not included in the simulations. Further comparison of the simulation results with the observations of the 17 January 2013 storm (Shprits et al., 2016) confirmed that EMIC waves cause fast local loss of the ultrarelativistic electrons in the outer belt.

Previous theoretical studies suggested that EMIC waves can efficiently scatter sub-MeV and MeV electrons (Thorne and Kennel, 1971; Horne and Thorne, 1998; Summers and Thorne, 2003; Ukhorskiy et al., 2010). Supporting the theoretical findings, a number of observational case studies used VLF transmitter and receiver systems, riometers,

balloons, and polar satellites to measure ultrarelativistic electron precipitation associated with simultaneous detection of EMIC waves by ground-based or satellite magnetometers (Clilverd et al., 2007, 2015; Rodger et al., 2008, 2015; Miyoshi et al., 2008; Blum et al., 2015). Using a recently developed algorithm for determination of precipitation events of sub-MeV and MeV electrons from POES and MetOp satellite (Carson et al., 2013), Hendry et al. (2016) showed that 60% to 90% of precipitation events coincide with the waves detected on the ground. Yet the observational studies of electron precipitation into the atmosphere suggested that sub-MeV and MeV electrons can be scattered by EMIC waves, such studies consider only the electron population inside the loss cone, leaving aside the effects of the waves on the pitch-angle distribution of particles in the heart of the belt.

Usanova et al. (2014) investigated the correlation between ground-based observations of EMIC waves from the Canadian Array for Real-time Investigations of Magnetic Activity (CARISMA) (Mann et al., 2008) and the variability of the ultrarelativistic outer belt measured in situ by Van Allen Probes. They found the correlation between the observations of EMIC waves and narrowing of the normalized pitch-angle distributions, which is a clear tell-tale signature of EMIC wave-induced precipitation.

Another mechanism of electron loss affecting all populations of radiation belt particles is the loss into the interplanetary medium driven by outward radial diffusion (Shprits et al., 2006; Ohtani et al., 2009; Turner et al., 2012). This mechanism is most effective during compression of the magnetosphere when particles previously trapped in the Earth's magnetic field at high radial distances find themselves drifting along the open trajectories that cross the magnetopause. These particles become lost into the interplanetary medium on time scales of the drift period, creating sharp negative gradients near the outer boundary of the outer belt. The sharp gradients, in turn, result in fast particle transport away from Earth due to enhanced outward radial diffusion driven by drift resonance of particles with ULF waves. The loss into the interplanetary medium should be carefully separated from the precipitation into the atmosphere if any loss mechanism in the belts is investigated.

In this study, we present additional evidence for the ultrarelativistic electron loss in the heart of the outer belt that can be driven by resonant interaction with EMIC waves and complement the signatures of effects of EMIC waves found by Usanova et al. (2014) for the time period from 9 October to 29 November 2012. We analyze Phase Space Density (PSD) derived from Van Allen Probes observations as a function of time and three adiabatic invariants μ, K and L^* (Schulz and Lanzerotti, 1974; Roederer, 2012) to distinguish reversible (adiabatic) changes resulting from slow expansion and compression of the magnetic field from nonreversible (non-adiabatic) changes leading

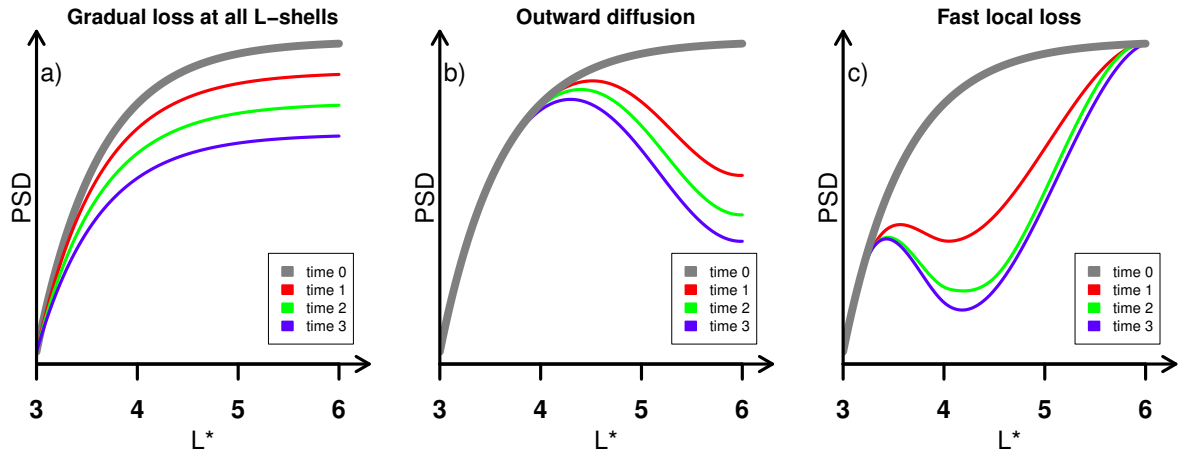

Figure 5.1: Signatures of the electron loss from the outer radiation belt: (a) gradual loss at all L-shells due to resonant interaction with whistler-mode waves, (b) magnetopause shadowing, and (c) EMIC-wave driven loss. Adapted from Shprits et al. (2017).

to particle loss or acceleration. The mechanisms causing nonreversible changes can be further differentiated if the PSD is considered as a function of L^* and time for constant μ and K (Selesnick and Blake, 2000; Green and Kivelson, 2004; Reeves et al., 2013). In particular, local minimums in relativistic and ultrarelativistic electron PSD profiles are a distinctive feature of fast local loss which can be driven by EMIC waves (Shprits et al., 2017). The signatures of the EMIC wave-induced loss are recognizably different from the signatures of gradual electron loss at all L-shells driven by whistler-mode waves and magnetopause shadowing that is characterized by a negative PSD gradient at higher L-shells (see Figure 5.1). To provide observational evidence that EMIC waves scatter ultrarelativistic electrons into the Earth's atmosphere, we analyze such local minimums, narrowing of pitch-angle distributions, and the occurrence of EMIC waves on the ground.

5.2 Van Allen Probes Measurements from 9 October to 29 November 2012

The interval of enhanced ultrarelativistic electron flux in the outer belt between 9 October and 29 November 2012 was teemed with multiple events of enhanced EMIC wave activity observed on the ground (Usanova et al., 2014) and gave us a good opportunity to gain insight into the processes driving the electron loss. Figure 5.2 illustrates the dynamics of differential ultrarelativistic electron fluxes from 9 October to 29 November. Note that the fluxes were averaged over the solid angle subtended by a whole sphere. Figure 5.2a shows the evolution of Dst and Kp indices, and Figures 5.2b-5.2d present the fluxes measured by the REPT instrument on board Van Allen Probes.

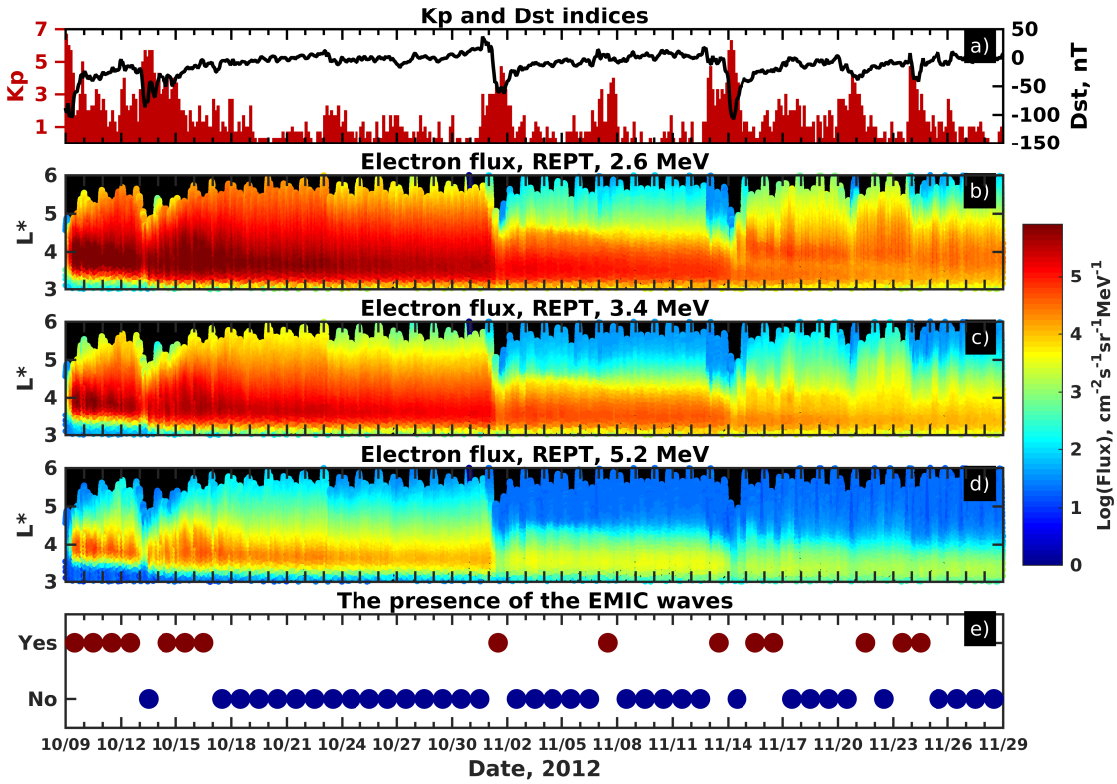

Figure 5.2: (a) Kp and Dst indices between 9 October and 29 November 2012, provided by OMNIWeb. (b-d) Differential electron fluxes measured by REPT on board Van Allen Probes in 2.6, 3.4, and 5.2 MeV energy channels as a function of time and L^* computed using the TS07D magnetic field model (Tsyganenko and Sitnov, 2007). (e) The presence of EMIC waves measured by CARISMA stations at L = 4–4.5.

Figure 5.2e, adopted from Usanova et al. (2014), demonstrates the occurrence of EMIC waves on the ground measured by CARISMA stations at L = 4-4.5. The red circles in Figure 5.2e denote the days when EMIC waves were observed, while blue circles indicate the days when no EMIC waves activity was detected.

The prominent storm-time flux dropouts are observed on 13 October, 1 November and 13-14 November. The dropouts are accompanied by enhanced EMIC waves activity and minimums in the Dst index, which indicates that EMIC wave-induced scattering, adiabatic changes associated with the changes in the magnetic field configuration, magnetopause shadowing, and the loss into the interplanetary medium driven by outward radial diffusion can be responsible for such flux variations. Interestingly, EMIC waves are also observed not only during dropouts, but also during the enhancement of the belt (e.g., 14-16 October) and intervals when the flux remains almost unchanged (e.g., 7 November 2012). It is therefore necessary to distinguish between competing loss and acceleration processes while performing analysis of effects of EMIC waves on

ultrarelativistic electrons in the belt.

5.3 Data and Methods

In order to extract signatures of EMIC wave-driven ultrarelativistic electron loss from in-situ Van Allen Probes measurements, we applied the method proposed by Shprits et al. (2017). The method relies on the fact that, interacting locally with electrons, EMIC waves produce pronounced local minimums in PSD profiles for constant first and second adiabatic invariants. Unless smoothed out by radial diffusion or local acceleration, the minimums can persist for hours and days, and they can be derived from Van Allen Probes ECT suite observations.

We used 5-minute averaged Magnetic Electron Ion Spectrometer (MagEIS) (Blake et al., 2013) and REPT data to calculate electron PSD as a function of adiabatic invariants. The first adiabatic invariant μ has been calculated, using local magnetic field observations measured by the Electric and Magnetic Field Instrument Suite and Integrated Science (EMFISIS) (Kletzing et al., 2013) on board the satellites. To determine the invariants K and L^* corresponding to the local pitch angles and position of satellites, we utilized the TS07D magnetic field model (Tsyganenko and Sitnov, 2007), which is implemented in the IRBEM library (Boscher et al., 2012). We calculated PSD for $K = 0.1\ G^{1/2}R_E$, since this value of the second invariant roughly corresponds to $51° - 55°$ pitch angles in the heart of the outer belt, and EMIC waves can efficiently resonate with the ultrarelativistic electrons of such pitch angles (Summers and Thorne, 2003). We used bilinear cubic interpolation to calculate PSD for particular values of μ and K for constant L^*.

5.4 Signatures of EMIC Wave-Driven Ultrarelativistic Electron Loss

Figure 5.3 illustrates the formation of local minimums on 2-3 November, after the dropout of electron fluxes on 1 November (see Figures 5.2b-5.2d). Figures 5.3a-5.3c show the evolution of relativistic (μ = 300 MeV/G) and ultrarelativistic (μ = 2500 and 4500 MeV/G) PSD profiles. Figures 5.3d-5.3f present energies corresponding to the chosen adiabatic invariants in the dipole field approximation. Pre-dropout ultrarelativistic profiles, derived from RBSP-A measurements at around 08:45, 2 November, have wide pronounced peaks at $L^* = 4$ and negative gradients above $L^* = \sim 4.3$ (see dark blue lines in Figures 5.3b and 5.3c). The next two passes of RBSP-A show an enhancement of both relativistic and ultarelativistic electron PSD at higher L-shells. The formation of local minimums can be noticed at the following satellite pass at $L^* = \sim 4.7$ around 22:10. The passes at ~07:10 and ~11:45 on 3 November show enhancement of

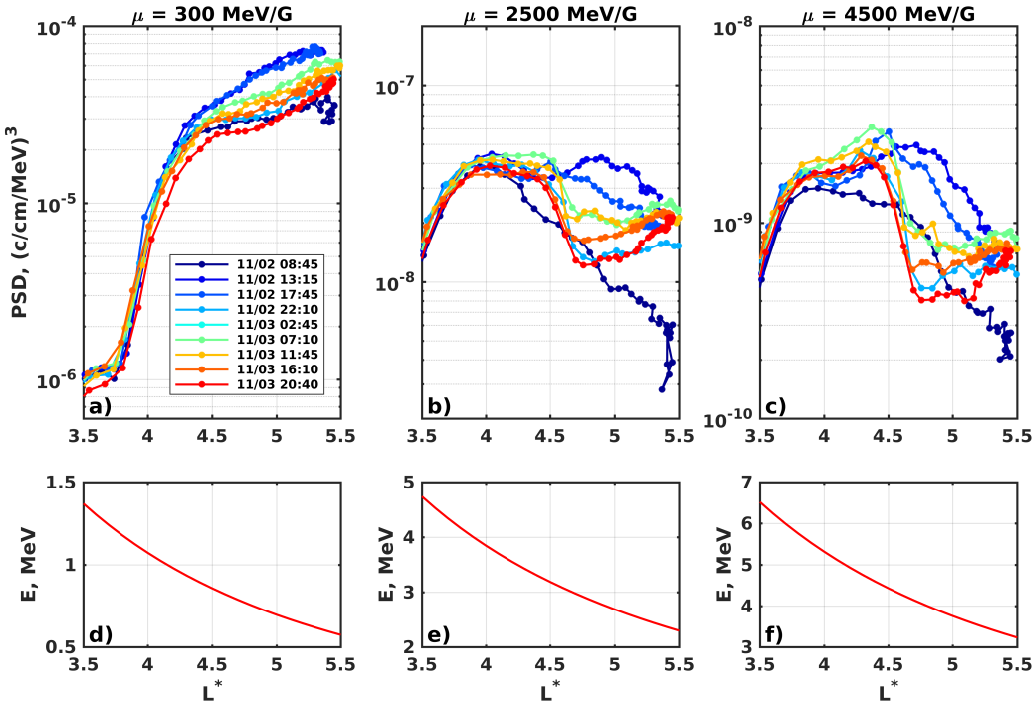

Figure 5.3: (a-c) Evolution of PSD profiles derived from RBSP-A flux measurements as a function of L^* for $K = 0.1G^{1/2}R_E$ and μ = 300, 2500 and 4500 MeV/G on 2-3 November 2012 using the TS07D magnetic field model.The colors represent the end times of successive inbound and outbound satellite passes. (d-f) Energies corresponding to the chosen μ and K calculated in the dipole field approximation.

ultrarelativistic electron PSD above $L^* = \sim 4.5$ without noticeable changes in the depth and width of the minimums. The subsequent passes demonstrate fast deepening of local minimums at $L^* = 4.7$, while profiles at $L^* = 5.5$ do not show significant variations. Relativistic electron profiles, presented in Figure 5.3a, preserve monotonic behavior for the considered interval, showing only a slow gradual decrease.

To take into account uncertainties associated with calculations of K and L^* that globally depend on magnetic field configuration, we analyzed PSD profiles computed using T89 (Tsyganenko, 1989), T96 (Tsyganenko, 1995), T01S (Tsyganenko, 2002), and T04S (Tsyganenko and Sitnov, 2005) magnetic field models. We note that the results are not shown here (see supplementary material of Aseev et al. (2017) for the figures). The results indicate that the local minimums in ultrarelativistic electron PSD profiles are observed independently of any known advanced magnetic field model, while relativistic electron profiles demonstrate a monotonic decrease with L^*.

The simultaneous formation of local minimums in ultrarelativistic electron PSD profiles at $L^* = 4.7$, the decrease between $L^* = 4.5$ and 5, and slight changes at $L^* = 5.5$ imply a fast local loss process operating in a narrow region of L-shells. The observed minimums could not be produced by magnetopause shadowing or by the local interac-

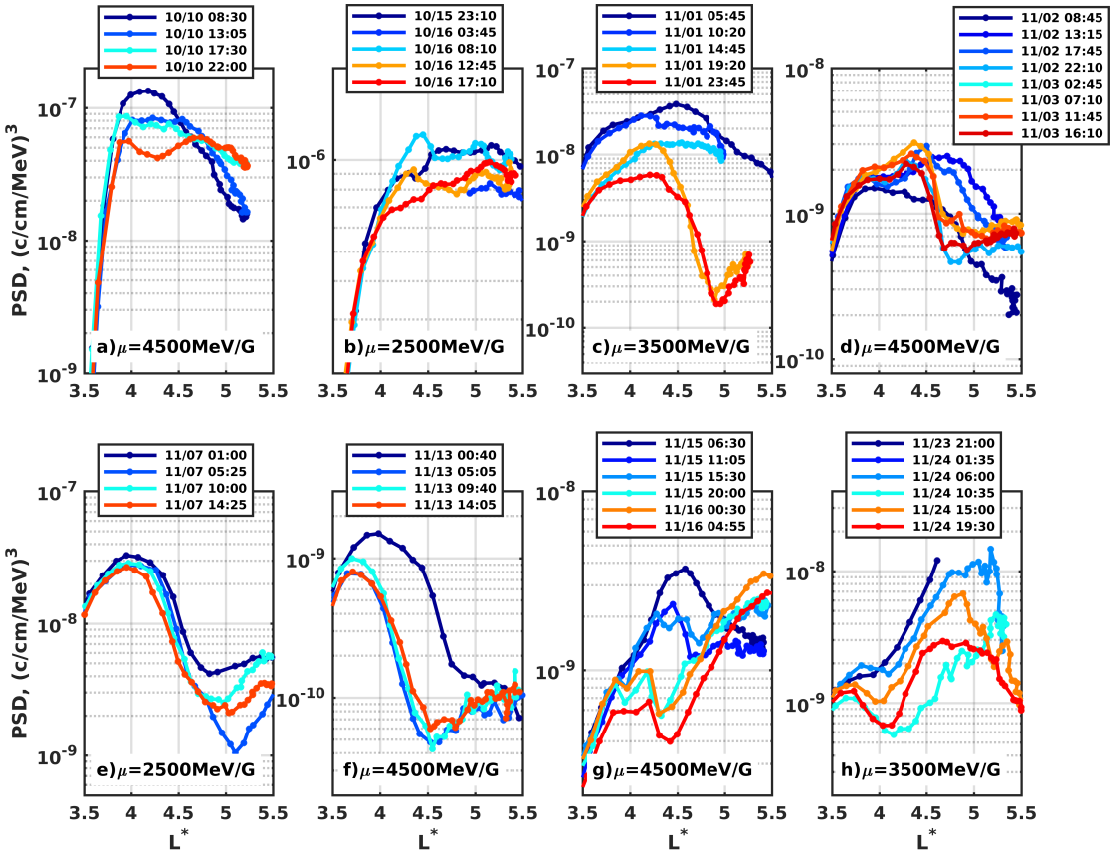

Figure 5.4: (a-h) Evolution of PSD profiles during periods when the most pronounced minimums were detected. The profiles are derived from RBSP-A flux measurements as a function of L^* for $K = 0.1$ $G^{1/2}R_E$ and constant μ computed using the TS07D magnetic field model. Colors represent the end times of successive inbound and outbound satellite passes.

tion with hiss or chorus waves, which is effective on much longer time scales than Van Allen Probes orbital period and is characterized by a very weak dependence on radial distance (Orlova and Shprits, 2014; Orlova et al., 2016; Shprits et al., 2017). Resonating with ultrarelativistic electrons, EMIC waves can locally scatter electrons into the loss cone and form the minimums, as presented in Figures 5.3b and 5.3c. The absence of such minimums in the profiles of less energetic electrons (Figure 5.3a) is additional evidence of an EMIC wave-driven nature of loss, since less energetic electrons do not interact with EMIC waves, according to the concept of minimum resonant energy (e.g., Summers and Thorne, 2003).

We analyzed PSD profiles for μ = 2500, 3500, and 4500 MeV/G from 9 October to 29 November 2016 and found 8 events when noticeable local minimums were formed for at least one value of μ in the chosen range. Figures 5.4a-5.4h show the profiles for the values of the first invariant μ corresponding to the most pronounced minimums observed. The minimums differ in their position, depth, and width. The minimums are

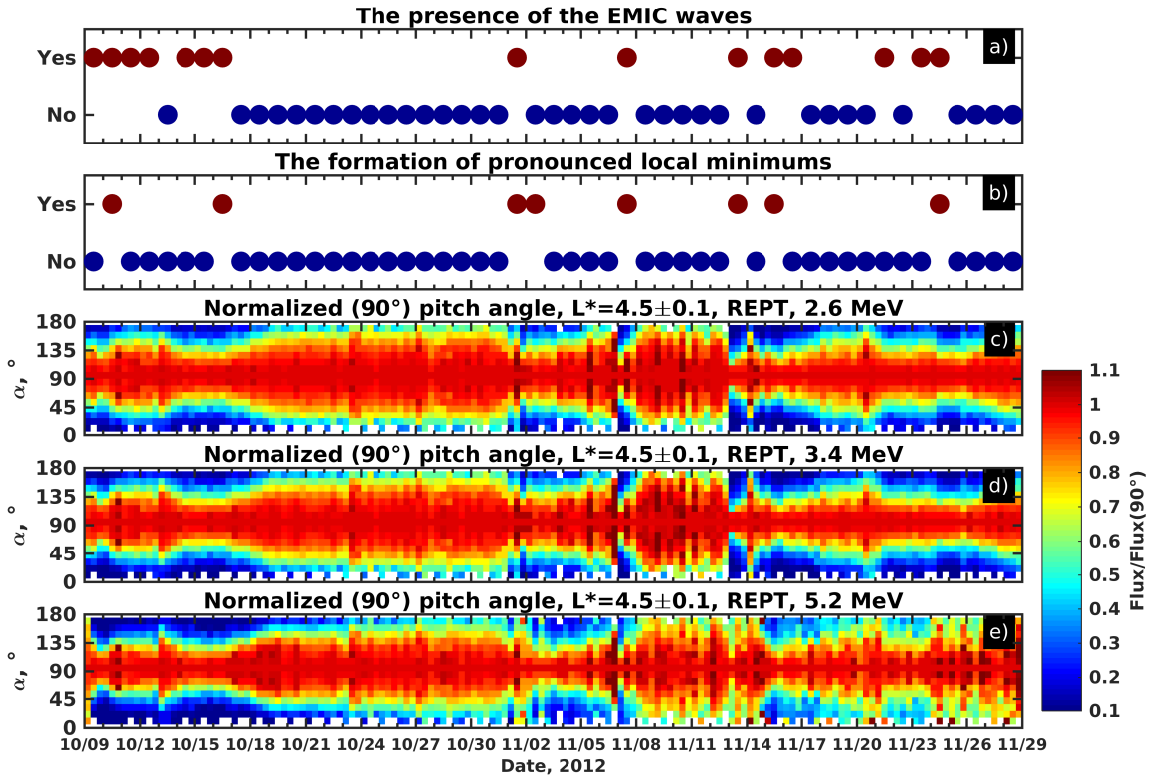

Figure 5.5: (a) The presence of EMIC waves measured by CARISMA stations between 9 October and 29 November 2012. (b) The formation of new local minimums in PSD profiles for the same time period. (c-e) The pitch-angle distributions of directional differential fluxes normalized by the equatorial flux as a function of time and pitch angle measured by Van Allen Probes in 2.6, 3.4, and 5.2 MeV energy channels at $L^* = 4.5 \pm 0.1$.

located between $L^* = 4$ and 5, and the width varies from ~0.3 to ~1 (in L-shell units). The minimums appear simultaneously with the prominent dropouts (Figures 5.4c, 5.4f and 5.4h) of PSD or when no large variations of PSD were detected (Figures 5.4a, 5.4b, 5.4d, 5.4e, and 5.4g). To decrease uncertainties associated with the magnetic field model, we also analyzed PSD profiles calculated using the T04S magnetic field model for identified events. Supplementary Figure 5 of Aseev et al. (2017) shows that the change in the magnetic field model mostly does not affect local minimums, though their shape can be slightly different.

Figure 5.5 summarizes the signatures of EMIC wave effects on ultrarelativistic electrons in the outer belt for the studied period. Figure 5.5a illustrates the occurrence of EMIC waves on the ground and is similar to Figure 5.2e. Figure 5.5b shows the presence of new pronounced local minimums in $\mu = 2500$, 3500, or 4500 MeV/G profiles. Red markers ('Yes') indicate days when the new local minimum was formed for at least one value in the chosen range, and blue markers ('No') represent days without

local minimums. Figures 5.5c-5.5e illustrate the pitch-angle distributions of differential fluxes normalized by the equatorial flux at $L^* = 4.5$ in the energy channels 2.6, 3.4, and 5.2 MeV.

New local minimums are formed during intervals of high EMIC wave activity, showing strong correlation with the detection of EMIC waves on the ground (compare red dots in Figures 5.5a and 5.5b). The formation of local minimums also coincides with the narrowing of pitch-angle distributions, produced by the resonant interaction with EMIC waves (Usanova et al., 2014). The simultaneous formation of local minimums, narrowing of the distributions, and EMIC wave detection on the ground is the observational evidence that EMIC waves not only change the shape of the normalized pitch-angle distribution but may also result in particle loss.

5.5 Discussion

In this study, we analyzed 51 days of data measured by REPT on board Van Allen Probes and found 8 events of the formation of minimums in ultrarelativistic electron PSD profiles. The events were accompanied by the narrowing of normalized pitch-angle distributions and EMIC wave detection on the ground (see Figure 5.5). Such correlation shows from the statistical point of view that the new local minimums have an EMIC wave-driven nature, as was found from the physical principles by Shprits et al. (2017). Complementing the findings of Usanova et al. (2014), which demonstrate that the narrowing of the pitch-angle distributions coincide with EMIC wave measurements, the formation of new local minimums may indicate EMIC wave-induced scattering of ultrarelativistic electrons.

The new local minimums not only provide evidence of ultrarelativistic electron loss, but they can also help identify EMIC wave occurrence in space. Since the minimums are the response of the electrons to the wave activity, they are the explicit manifestation of EMIC waves even if wave measurements are not available or spacecraft is not in the region of the waves. Therefore, the new minimums can be used to support direct observations of the waves or to reveal EMIC waves that cannot be observed on the ground or in situ. Seven of eight local minimums found between 9 October and 29 November 2012 serve as additional evidence of EMIC wave presence, while only one local minimum, which appeared on 2 November after the previous minimum on 1 November vanished, was not accompanied by EMIC waves and can be considered a potential indirect signature of the waves (see Figure 5.5).

The duration of EMIC waves can be estimated from electron flux observations (converted to PSD) in the case of deepening minimums, as was discussed by Shprits et al. (2017). The deepening minimum in ultrarelativistic electron PSD profiles indicates

that local loss induced by EMIC waves dominates over the acceleration process driven by radial diffusion that tends to smooth out the minimum. In this case, EMIC waves are present in the region of the deepening minimum at least as long as the deepening minimum is observed. However, if the minimum does not change its depth or the depth decreases, it is hard to distinguish EMIC wave effects on radiation belt electrons from the radial diffusion influence using only flux observations, and more detailed analysis involving EMIC wave parameters and radial diffusion rates is required. For this reason, we do not consider the question of EMIC wave duration in the current study and concentrate only on EMIC wave presence, which can be evident from the event of new local minimum formation.

The analysis of minimums can be complicated by different loss and acceleration processes that occur simultaneously with EMIC waves. For instance, Figure 5.4b shows the acceleration of particles after the minimum is formed at ~12:45 on 16 October. In this case, the acceleration over the wide L^* range may accompany the loss of ultrarelativistic particles at $L^* = \sim 4.6$. Electron acceleration may render the minimums more shallow, which is harder to detect visually or by using an automated algorithm.

For some events, EMIC waves were observed at times when local minimums are not seen in the data. That can be explained by the action of radial diffusion smoothing out the minimums, competition with local acceleration, or non-optimal spectral properties of the waves for the efficient electron scattering. For instance, if the local minimum is formed at high L-shells, it can be suddenly destroyed by magnetopause shadowing, as detected on 12 November (see Figure 5.6). Acceleration due to inward radial diffusion or local interaction with night side chorus waves can lead to the increase in PSD and smoothing out the minimums (see Figure 5.7 illustrating the disappearance of the minimums on 2 November). If competing processes significantly distort the minimums on time scales less than half of Van Allen Probes period, the local minimums can be hardly observed, and, therefore, their formation is detected more rarely than EMIC waves.

The local minimums and narrowing of pitch-angle distributions are observed during the intervals of prominent storm-time flux dropouts, indicating that EMIC waves can contribute to the noticeable flux decrease. It is necessary, however, to estimate the relative importance of EMIC wave-induced loss in the outer belt and the loss into the interplanetary medium driven by outward radial diffusion. Figure 5.8 shows the last closed drift shell calculated for equatorially mirroring electrons using the TS07D magnetic field model. To calculate the last closed drift shell, we find the magnetic field line farthest from the Earth which has only one local minimum at the noon magnetic longitude and calculate L^* corresponding to a given K value. This approach is imple-

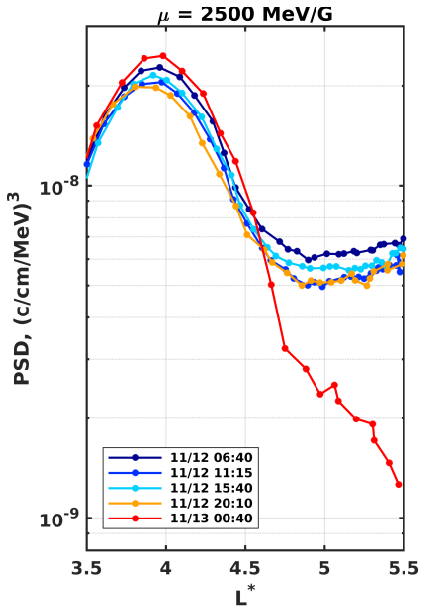

Figure 5.6: Evolution of ultrarelativistic electron PSD profiles as a function of L^* for $K = 0.1$ $G^{1/2}R_E$ and $\mu = 2500$ MeV/G. The adiabatic invariants K and L^* are calculated using the TS07D magnetic field model. The local minimums observed on 12 November are destroyed by loss to interplanetary medium that occurred around midnight on 13 November. Colors represent the end times of successive inbound and outbound satellite passes.

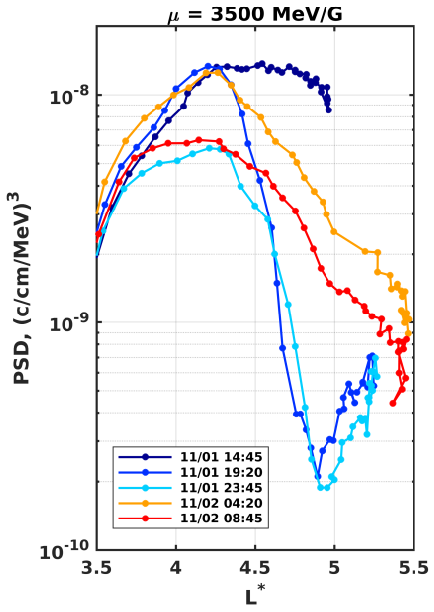

Figure 5.7: Evolution of ultrarelativistic electron PSD profiles as a function of L^* for $K = 0.1$ $G^{1/2}R_E$ and $\mu = 3500$ MeV/G. The adiabatic invariants K and L^* are calculated using the TS07D magnetic field model. The local minimum disappears after the electron acceleration at high L-shells. Colors represent the end times of successive inbound and outbound satellite passes.

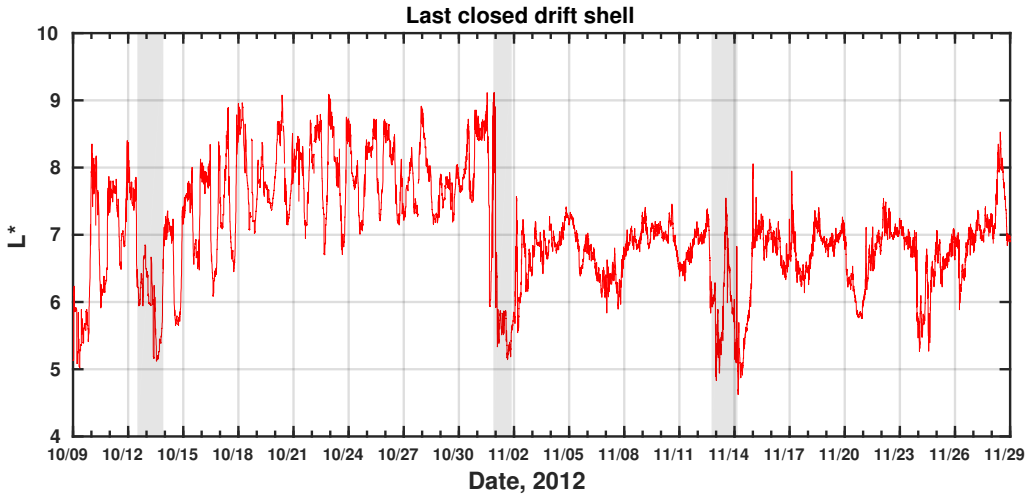

Figure 5.8: The last closed drift shell computed for equatorially mirroring particles using the TS07D magnetic field model. The gray shadowed regions correspond to significant storm-time dropouts of ultrarelativitic electron fluxes at $L^* = 5$.

mented because of the limitations of the IRBEM library computational framework in dealing with double minimum field lines and provides an approximation of the last closed drift shell which likely is at slightly higher L-shells. A gray background color in Figure 5.8 marks the periods when the significant storm-time dropouts of the ultrarelativistic electron fluxes were observed at $L^* = 5$. As can be clearly seen from the figure, all storm-time events were accompanied by the sharp decrease of the last closed drift shell, which may indicate the enhanced electron loss into the interplanetary medium.

Figure 5.9 illustrates electron fluxes measured by the RBSP-A at $L^* = 5$ and averaged over the satellite orbital period for the storms that occurred on 13 October, 1 November, and 13-14 November. The storms on 13 October and 13-14 November are characterized by a simultaneous dropout in electron fluxes from ~100-200 keV to several MeV energies (gray shaded regions in Figures 5.9a and 5.9d and Figures 5.9c and 5.9f), which can be indicative of the radiation belt variations associated with changes in magnetic field configuration. The event on 1 November, however, shows a significant decrease of multi-MeV electron fluxes and a simultaneous increase in ~100-800 keV fluxes (see Figures 5.9b and 5.9e). The flux enhancement can be driven by electron injections from the plasma sheet into the radiation belt region, concealing any possible effects of magnetopause shadowing on such electron population. Modeling studies (e.g., Kersten et al., 2014; Drozdov et al., 2015; Shprits et al., 2016) are required for further understanding the balance between EMIC wave loss, loss into the interplanetary medium, and the electron source population injected at the night side.

We emphasize the existence of essential coherence between EMIC wave observations and new local minimums in PSD profiles of ultrarelativistic electrons. Further

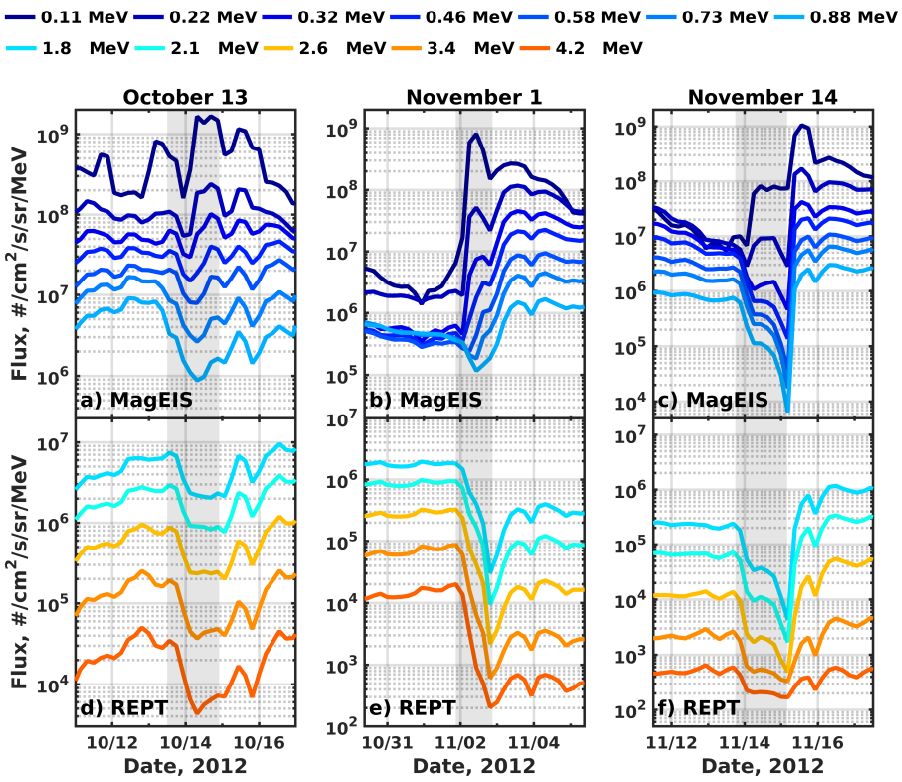

Figure 5.9: Evolution of electron fluxes at $L^* = 5 \pm 0.25$ measured by MagEIS and REPT instruments on board the RBSP-A during the most significant storm-time dropouts which occurred on 13 October (a,d), 1 November (b,e), and 13-14 November (c,f). The fluxes are averaged over the satellite orbital period. The gray shaded regions correspond to significant storm-time dropouts of ultrarelativistic electron fluxes.

studies are required for detailed understanding of correlations between the waves and the minimums, conditions under which the minimums are formed, as well as dependence of local minimum parameters on EMIC wave properties.

Acknowledgments

The authors used geomagnetic indices provided by OMNIWeb and are grateful to the RBSP-ECT team for the provision of Van Allen Probes observations (http://rbsp-ect.lanl.gov/). This research was supported by the Helmholtz Association Recruiting Initiative, NSF GEM AGS-1203747, NASA grants NNX12AE34G and NNX16AF91G, and project PROGRESS funded by EU Horizon 2020 No 637302. The authors are grateful to Sharon Uy for her help in editing the paper. The authors thank anonymous reviewers for their insightful comments that helped improve the manuscript.

Chapter 6

Summary and Future Work

6.1 Summary

In recent decades, numerous studies have been based on numerical codes that model radiation belt and ring current dynamics. Although such studies often make conclusions on the importance of a certain physical process by comparing simulation results with satellite observations, much less attention is given to the quantification of numerical errors, uncertainties in the input parameters, and sensitivity of model results to such parameters. Uncertainties associated with numerical schemes and input parameters complicate physical interpretation of the results and may lead to wrong conclusions drawn from the comparison with observations. In this dissertation, particular attention is paid to the accuracy and stability of numerical codes that are used to quantify physical processes controlling the dynamics of ring current and radiation belts.

A significant part of the dissertation is based on the VERB-4D code that has been developed for modeling radiation belt and ring current electron dynamics (Shprits et al., 2015). We pursued the following goals:

1. Understand how accuracy of numerical schemes may affect results of ring current and radiation belt modeling.

2. Understand how sensitive the model of ring current electrons is to input parameters, and find the parameters the model is most sensitive to.

3. Quantify transport and loss processes that control dynamics of the ring current electrons inside GEO, using the VERB-4D code.

4. Develop a data-assimilative code that would correct prediction of the model of ring current electron transport and loss by using information from sparse satellite observations.

5. Understand which physical process is responsible for scattering ultrarelativistic

electrons from the outer radiation belt to the Earth's atmosphere by analyzing satellite measurements.

We demonstrated that numerical schemes of the VERB-4D code show stable and accurate behavior. We showed that the use of low-order numerical schemes for the convection equation may lead to significant numerical errors, given the same spatial and temporal discretization. We demonstrated that it is important to use a numerical limiter to model drift motion of ring current and radiation belt electrons, since the limiter eliminates oscillations that are generated by high-order numerical schemes for the convection equation and may lead to unphysical results. We modeled transport of energetic electrons from the plasma sheet to GEO under typical quiet magnetospheric conditions and showed that the electron flux obtained with the third-order scheme for convection equation can be several orders of magnitude smaller than the flux obtained with the ninth-order scheme.

We used the VERB-4D code to model dynamics of ring current electrons inside GEO during the 17 March 2013 geomagnetic storm. We used the statistical model of the electron source at GEO developed by Denton et al. (2015) to estimate confidence intervals of the model (5th, 25th, 75th, and 95th percentiles) which are associated with the outer spatial boundary conditions. We compared simulation results with Van Allen Probes measurements. We found that the results above 4.5 R_E are most sensitive to the boundary conditions. The satellite data above that radial distance are within or close to 25th and 75th percentile limits. Our results indicate that the discrepancy between model and data above 4.5 R_E can be explained by errors in boundary conditions and that the general dynamics of the ring current electrons during the storm is driven by global-scale convection and co-rotation electric fields and magnetic field. Below 4.5 R_E, the simulation results are most sensitive to the convection electric field model and electron lifetimes. We showed that the inclusion of the diffusion rates using Brautigam and Albert (2000) parameterization for >40 keV electrons leads to better agreement of the results with Van Allen Probes observations. The estimated effect of SAPS electric field on ring current electron dynamics appeared to be much smaller than the discrepancy between model and data. Improvements in convection electric field and electron lifetime or wave models are of the highest priority for increasing the accuracy of the prediction of the ring current electron dynamics in the inner magnetosphere.

We developed a data-assimilative tool that allows us to combine a convection model of ring current electron transport that is based on the VERB-4D code and Van Allen Probes measurements, using the Kalman filter. We used synthetic data to study whether the Kalman filter can improve model predictions, given only sparse satellite

measurements. The synthetic data were obtained from a control 135-day simulation, and we varied different input parameters to understand whether the Kalman filter can correct model uncertainties in electron lifetimes, convection electric field, and boundary conditions. The accuracy of the reanalysis is highest during quiet geomagnetic conditions, since the reanalysis is unable to fully capture the dynamics of ring current electrons during storm times due to an insufficient amount of data per MLT sector. The lack of satellite data also complicates the reconstruction of the electron PSD above Van Allen Probes apogee in the case of errors in boundary conditions. We applied the Kalman filter to real Van Allen Probes measurements and showed that the reanalysis is able to capture observed features of electron PSD that cannot be reproduced by the model. One of such features is fast earthward propagation of the electrons down to 2.5 R_E. We analyzed the innovation vector and found that model predictions of μ = 2.3 MeV/G and K = 0.3 $G^{1/2}$ R_E electron PSD systematically underestimate the observations below 4 R_E during storms, which indicates that the electric field model or electron lifetime parameterizations that we used should be improved. We showed that the Kalman filter adjusts model predictions even in MLT sectors where data are not available, and it is applicable to the observations for a wide range of energies. Our results are promising for application of data assimilation techniques in nowcast and forecast of ring current dynamics.

We computed PSD for ultrarelativistic electrons, using Van Allen Probes data. We analyzed PSD as a function of L^* for constant μ and K from 9 October to 29 November 2012 and found 8 events of the formation of local minimums. The minimums are indicative of local scattering of ultrarelativistic electrons from the radiation belts into the Earth's atmosphere (Shprits et al., 2017). Most of the found local minimums were accompanied by the narrowing of the pitch-angle distributions and observations of EMIC waves on the ground. Such a correlation shows from the statistical point of view that the loss of the electrons can be driven by resonant interaction with EMIC waves. Since EMIC waves are sporadic and hard-to-detect in situ, the local minimums in the PSD profiles can also serve as indirect evidence of the presence of EMIC waves in the inner magnetosphere.

6.2 Key scientific findings and developed tools

The main results of the dissertation are briefly summarized below.

1. We demonstrated that the order of numerical schemes significantly affects the results of modeling electron transport from the plasma sheet to GEO, which can complicate comparison of the model with observations and interpretation of the

results.

2. We showed that earthward transport of ring current electrons from GEO to 4.5 R_E during the 17 March 2013 geomagnetic storm can be explained by the advective transport in global electric and magnetic fields.

3. We showed that the model of ring current electron dynamics below 4.5 R_E is most sensitive to parameterized lifetimes and the global electric field. We demonstrated that the effect of the Kp-driven SAPS model is small as compared to the uncertainties of the model.

4. We developed a data-assimilative code that blends together a two-dimensional convection model of the ring current electron transport and in-situ particle measurements by means of the Kalman filter. The developed code significantly improves prediction of the ring current electron transport, even when sparse Van Allen Probes measurements are used for the data assimilation, and allows us to reconstruct the global dynamics of the ring current electrons from sparse measurements.

5. We showed that the Kalman filter can correct errors in the ring current model predictions due to uncertainties in electron lifetimes, boundary conditions, and drift velocities, using only Van Allen Probes measurements.

6. We found a high correlation between the ground observations of EMIC waves and the formation of local minimums in the radial PSD profiles of ultrarelativistic electrons. A high correlation between the minimums in PSD profiles and occurrence of EMIC waves indicates that the EMIC waves are responsible for the electron loss from the outer radiation belt into the Earth's atmosphere.

6.3 Future Work

The results of the dissertation are planned to be extended in the future. In this section, we outline some directions of our future work.

We will use the VERB-4D code to understand coupling processes between ring current and radiation belt electrons. It is believed that the ring current electrons are a seed population for the radiation belts (Jaynes et al., 2015). Although a number of observational studies showed correlation between flux enhancements of ring current and radiation belt electrons (e.g., Li et al., 2005; Turner and Li, 2008; Boyd et al., 2016), there is still a lack of modeling studies explaining how ring current electrons can be accelerated to radiation belt energies. The VERB-4D code will allow us to investigate transport, loss, and acceleration of ring current electrons and their interplay

with radiation belt particles. We will use recently developed hiss and chorus wave models (e.g., Spasojevic et al., 2015; Wang et al., 2019) to calculate MLT-dependent pitch-angle, energy, and mixed-diffusion coefficients. Results presented in Chapter 5 indicate that EMIC waves should be also incorporated in the simulations to account for the loss of ultrarelativistic electrons. We will include the diffusion coefficients into the VERB-4D code, which will allow us to take into account different acceleration and pitch-angle scattering rates at different MLT sectors. We will also incorporate more accurate electric and magnetic field models into the code to improve the accuracy of drift velocities, L^*, and conversion of adiabatic invariants into energy and pitch-angle space and back. We will improve the accuracy of the boundary conditions at GEO by using in-situ measurements of recently launched GOES-16 and GOES-17 satellites and test the applicability of the newly developed model of electron flux by Denton et al. (2019).

We will investigate the feasibility of long-term ring current electron modeling. Numerical codes were used in several studies to model the electron dynamics during particular events (e.g., Chen et al., 2015b, 2019; Jordanova et al., 2016; Yu et al., 2019), only a few modeled long-term dynamics at GEO (Ganushkina et al., 2019), and none presented long-term physics-based predictions inside GEO. Results of the dissertation suggest that a simple Kp-dependent model of electron transport and loss accumulates significant error on timescales higher than several days and, therefore, is not suitable for long-term modeling (see results of Chapter 4). To increase the accuracy of the model predictions, empirical models of convection electric field and electron lifetimes will be improved (see results of Chapter 3).

We will develop a new data assimilation code that will allow us to blend different satellite observations of ring current and radiation belt electrons with a full four-dimensional Fokker-Planck equation with convection terms (1.24). The four-dimensional reanalysis can help us cross-calibrate observations from different satellite missions, improve predictions of the model, and identify model errors or missing physical processes that couple ring current and radiation belts. To decrease computational complexity, we will use the operator splitting technique that reduces the four-dimensional equation to a series of one- and two-dimensional problems. We will then combine the data assimilation method presented in Chapter 4 for the convection part of the equation with the suboptimal data assimilation technique developed by Shprits et al. (2013a) for radiation belts. Dependence of reanalysis on drift phase (MLT) requires assimilation of satellite data from different MLT sectors. To increase data coverage, we will use measurements from a number of satellite missions that operate near the equator (e.g., ERG, THEMIS, Cluster, and GOES missions). We will also explore the

feasibility of the assimilation of data from the POES mission that includes satellites flying at low-Earth orbit at different MLT sectors. For this, we will apply methods for reconstruction of dependence of differential flux on equatorial pitch angle and energy, which are suggested, for example, by Peck et al. (2015); Shi et al. (2016), and Allison et al. (2018). We will apply the developed data assimilation codes to predict ring current electron dynamics in real-time and complement the currently operating at GFZ system that forecasts dynamics of the Earth's radiation belts.

Bibliography

Agapitov, O. V., Artemyev, A. V., Mourenas, D., Mozer, F. S., and Krasnoselskikh, V., 2015. Empirical Model of Lower Band Chorus Wave Distribution in the Outer Radiation Belt. *Journal of Geophysical Research: Space Physics*, 120(12):10–425. doi:10.1002/2015JA021829.

Agapitov, O. V., Mourenas, D., Artemyev, A. V., Mozer, F. S., Hospodarsky, G., Bonnell, J., and Krasnoselskikh, V., 2018. Synthetic Empirical Chorus Wave Model from Combined Van Allen Probes and Cluster Statistics. *Journal of Geophysical Research: Space Physics*, 123(1):297–314. doi:10.1002/2017JA024843.

Albert, J. M., 2005. Evaluation of Quasi-Linear Diffusion Coefficients for Whistler Mode Waves in a Plasma with Arbitrary Density Ratio. *Journal of Geophysical Research: Space Physics*, 110(A3). doi:10.1029/2004JA010844.

Albert, J. M. and Young, S. L., 2005. Multidimensional Quasi-Linear Diffusion of Radiation Belt Electrons. *Geophysical research letters*, 32(14). doi:10.1029/2005GL023191.

Allison, H. J., Horne, R. B., Glauert, S. A., and Del Zanna, G., 2018. Determination of the Equatorial Electron Differential Flux from Observations at Low Earth Orbit. *Journal of Geophysical Research: Space Physics*, 123(11):9574–9596. doi:10.1029/2018JA025786.

Anderson, E., Bai, Z., Bischof, C., Blackford, S., Dongarra, J., Du Croz, J., Greenbaum, A., Hammarling, S., McKenney, A., and Sorensen, D. *LAPACK Users' Guide*, volume 9. Siam, 1999.

Angelopoulos, V., Baumjohann, W., Kennel, C. F., Coroniti, F. V., Kivelson, M. G., Pellat, R., Walker, R. J., Lühr, H., and Paschmann, G., 1992. Bursty Bulk Flows in the Inner Central Plasma Sheet. *Journal of Geophysical Research: Space Physics*, 97(A4):4027–4039. doi:10.1029/91JA02701.

Angelopoulos, V., Kennel, C. F., Coroniti, F. V., Pellat, R., Kivelson, M. G., Walker, R. J., Russell, C. T., Baumjohann, W., Feldman, W. C., and Gosling, J. T., 1994. Statistical

Characteristics of Bursty Bulk Flow Events. *Journal of Geophysical Research: Space Physics*, 99(A11):21257–21280. doi:10.1029/94JA01263.

Aseev, N. A. and Shprits, Y. Y., 2019. Reanalysis of Ring Current Electron Phase Space Densities Using Van Allen Probe Observations, Convection Model, and Log-Normal Kalman Filter. *Space Weather*, 17(4):619–638. doi:10.1029/2018SW002110.

Aseev, N. A., Shprits, Y. Y., Drozdov, A. Y., and Kellerman, A. C., 2016. Numerical Applications of the Advective-Diffusive Codes for the Inner Magnetosphere. *Space Weather*, 14(11):993–1010. doi:10.1002/2016SW001484.

Aseev, N. A., Shprits, Y. Y., Drozdov, A. Y., Kellerman, A. C., Usanova, M. E., Wang, D., and Zhelavskaya, I. S., 2017. Signatures of Ultrarelativistic Electron Loss in the Heart of the Outer Radiation Belt Measured by Van Allen Probes. *Journal of Geophysical Research: Space Physics*, 122(10):10,102–10,111. doi:10.1002/2017JA024485.

Aseev, N. A., Shprits, Y. Y., Wang, D., Wygant, J., Drozdov, A. Y., Kellerman, A. C., and Reeves, G. D., 2019. Transport and Loss of Ring Current Electrons Inside Geosynchronous Orbit during the 17 March 2013 Storm. *Journal of Geophysical Research: Space Physics*, 124(2):915–933. doi:10.1029/2018JA026031.

Axford, W. I., 1969. Magnetospheric Convection. *Reviews of Geophysics*, 7(1-2):421–459. doi:10.1029/RG007i001p00421.

Baker, D. N., 2000. The Occurrence of Operational Anomalies in Spacecraft and Their Relationship to Space Weather. *IEEE Transactions on Plasma Science*, 28(6):2007–2016. doi:10.1109/27.902228.

Baker, D. N., Belian, R. D., Higbie, P. R., Klebesadel, R. W., and Blake, J. B., 1987. Deep Dielectric Charging Effects Due to High-Energy Electrons in Earth's Outer Magnetosphere. *Journal of electrostatics*, 20(1):3–19. doi:10.1016/0304-3886(87)90082-9.

Baker, D. N., Kanekal, S., Blake, J. B., Klecker, B., and Rostoker, G., 1994. Satellite Anomalies Linked to Electron Increase in the Magnetosphere. *Eos, Transactions American Geophysical Union*, 75(35):401–405. doi:10.1029/94EO01038.

Baker, D. N., Pulkkinen, T. I., Li, X., Kanekal, S. G., Blake, J. B., Selesnick, R. S., Henderson, M. G., Reeves, G. D., Spence, H. E., and Rostoker, G., 1998. Coronal Mass Ejections, Magnetic Clouds, and Relativistic Magnetospheric Electron Events: ISTP. *Journal of Geophysical Research: Space Physics*, 103(A8):17279–17291. doi:10.1029/97JA03329.

Baker, D. N., Kanekal, S. G., Li, X., Monk, S. P., Goldstein, J., and Burch, J. L., 2004. An Extreme Distortion of the Van Allen Belt Arising from the Hallowe'en Solar Storm in 2003. *Nature*, 432(7019):878. doi:10.1038/nature03116.

Baker, D. N., Kanekal, S. G., Hoxie, V. C., Batiste, S., Bolton, M., Li, X., Elkington, S. R., Monk, S., Reukauf, R., Steg, S., Westfall, J., Belting, C., Bolton, B., Braun, D., Cervelli, B., Hubbell, K., Kien, M., Knappmiller, S., Wade, S., Lamprecht, B., Stevens, K., Wallace, J., Yehle, A., Spence, H. E., and Friedel, R., nov 2013a. The Relativistic Electron-Proton Telescope (REPT) Instrument on Board the Radiation Belt Storm Probes (RBSP) Spacecraft: Characterization of Earth's Radiation Belt High-Energy Particle Populations. *Space Science Reviews*, 179(1-4):337–381. ISSN 0038-6308. doi:10.1007/s11214-012-9950-9.

Baker, D. N., Kanekal, S. G., Hoxie, V. C., Henderson, M. G., Li, X., Spence, H. E., Elkington, S. R., Friedel, R. H. W., Goldstein, J., Hudson, M. K., Reeves, G. D., Thorne, R. M., Kletzing, C. A., and Claudepierre, S. G., 2013b. A Long-Lived Relativistic Electron Storage Ring Embedded in Earth's Outer Van Allen Belt. *Science*, 340(6129). doi:10.1126/science.1233518.

Bame, S. J., McComas, D. J., Thomsen, M. F., Barraclough, B. L., Elphic, R. C., Glore, J. P., Gosling, J. T., Chavez, J. C., Evans, E. P., and Wymer, F. J., 1993. Magnetospheric Plasma Analyzer for Spacecraft with Constrained Resources. *Review of scientific instruments*, 64(4):1026–1033. doi:10.1063/1.1144173.

Baumjohann, W. and Treumann, R. A. *Basic Space Plasma Physics*. World Scientific Publishing Company, 2012.

Baumjohann, W., Paschmann, G., and Lühr, H., 1990. Characteristics of High-Speed Ion Flows in the Plasma Sheet. *Journal of Geophysical Research: Space Physics*, 95(A4): 3801–3809. doi:10.1029/JA095iA04p03801.

Beutier, T. and Boscher, D., 1995. A Three-Dimensional Analysis of the Electron Radiation Belt by the Salammbô Code. *Journal of Geophysical Research: Space Physics*, 100 (A8):14853–14861. doi:10.1029/94JA03066.

Birn, J., Thomsen, M. F., Borovsky, J. E., Reeves, G. D., McComas, D. J., Belian, R. D., and Hesse, M., 1998. Substorm Electron Injections: Geosynchronous Observations and Test Particle Simulations. *Journal of Geophysical Research: Space Physics*, 103(A5): 9235–9248. doi:10.1029/97JA02635.

Blake, J. B., Carranza, P. A., Claudepierre, S. G., Clemmons, J. H., Crain, W. R., Dotan, Y., Fennell, J. F., Fuentes, F. H., Galvan, R. M., George, J. S., et al., 2013.

The Magnetic Electron Ion Spectrometer (MagEIS) Instruments Aboard the Radiation Belt Storm Probes (RBSP) Spacecraft. *Space Science Reviews*, 179(1-4):383–421. doi:10.1007/s11214-013-9991-8.

Blum, L. W., Halford, A., Millan, R., Bonnell, J. W., Goldstein, J., Usanova, M., Engebretson, M., Ohnsted, M., Reeves, G., Singer, H., Clilverd, M., and Li, X., 2015. Observations of Coincident EMIC Wave Activity and Duskside Energetic Electron Precipitation on 18-19 January 2013. *Geophysical Research Letters*, 42(14):5727–5735. ISSN 00948276. doi:10.1002/2015GL065245.

Bortnik, J., Thorne, R. M., and Meredith, N. P., 2007. Modeling the Propagation Characteristics of Chorus Using CRRES Suprathermal Electron Fluxes. *Journal of Geophysical Research: Space Physics*, 112(A8). doi:10.1029/2006JA012237.

Bortnik, J., Thorne, R. M., and Meredith, N. P., 2008. The Unexpected Origin of Plasmaspheric Hiss from Discrete Chorus Emissions. *Nature*, 452(7183):62. doi:10.1038/nature06741.

Boscher, D., Bourdarie, S., O'Brien, P., and Guild, T. IRBEM-lib Library (http://irbem.sourceforge.net), 2012.

Bossen, M., McPherron, R. L., and Russell, C. T., 1976. A Statistical Study of Pc 1 Magnetic Pulsations at Synchronous Orbit. *Journal of Geophysical Research*, 81(34): 6083–6091. doi:10.1029/JA081i034p06083.

Bourdarie, S. A. and Maget, V. F. Electron Radiation Belt Data Assimilation with an Ensemble Kalman Filter Relying on the Salammbô Code. In *Annales Geophysicae*, volume 30, page 929, 2012. doi:10.5194/angeo-30-929-2012.

Boyd, A. J., Spence, H. E., Huang, C.-L., Reeves, G. D., Baker, D. N., Turner, D. L., Claudepierre, S. G., Fennell, J. F., Blake, J. B., and Shprits, Y. Y., 2016. Statistical Properties of the Radiation Belt Seed Population. *Journal of Geophysical Research: Space Physics*, 121(8):7636–7646. doi:10.1002/2016JA022652.

Brautigam, D. H. and Albert, J. M., 2000. Radial Diffusion Analysis of Outer Radiation Belt Electrons during the October 9, 1990, Magnetic Storm. *Journal of Geophysical Research: Space Physics*, 105(A1):291–309. doi:10.1029/1999JA900344.

Califf, S., Li, X., Blum, L., Jaynes, A., Schiller, Q., Zhao, H., Malaspina, D., Hartinger, M., Wolf, R. A., Rowland, D. E., et al., 2014. THEMIS measurements of quasi-static electric fields in the inner magnetosphere. *Journal of Geophysical Research: Space Physics*, 119(12):9939–9951. doi:10.1002/2014JA020360.

Califf, S., Li, X., Zhao, H., Kellerman, A., Sarris, T. E., Jaynes, A., and Malaspina, D. M., 2017. The Role of the Convection Electric Field in Filling the Slot Region between the Inner and Outer Radiation Belts. *Journal of Geophysical Research: Space Physics*, 122(2):2051–2068. doi:10.1002/2016JA023657.

Cao, X., Shprits, Y. Y., Ni, B., and Zhelavskaya, I. S., 2017. Scattering of Ultra-Relativistic Electrons in the Van Allen Radiation Belts Accounting for Hot Plasma Effects. *Scientific reports*, 7(1):17719. doi:10.1038/s41598-017-17739-7.

Carpenter, D. L., 1963. Whistler Evidence of a 'Knee' in the Magnetospheric Ionization Density Profile. *Journal of Geophysical Research*, 68(6):1675–1682. doi:10.1029/JZ068i006p01675.

Carpenter, D. L. and Anderson, R. R., 1992. An ISEE/whistler Model of Equatorial Electron Density in the Magnetosphere. *Journal of Geophysical Research: Space Physics*, 97(A2):1097–1108. doi:10.1029/91JA01548.

Carson, B. R., Rodger, C. J., and Clilverd, M. A., 2013. POES Satellite Observations of EMIC-wave Driven Relativistic Electron Precipitation during 1998-2010. *Journal of Geophysical Research: Space Physics*, 118(1):232–243. ISSN 21699380. doi:10.1029/2012JA017998.

Castillo, A. M., Shprits, Y. Y., Ganushkina, N., Drozdov, A., Aseev, N., Wang, D., and Dubyagin, S., 2019. Simulations of the Inner Magnetospheric Energetic Electrons Using the IMPTAM-VERB Coupled Model. *Journal of Atmospheric and Solar-Terrestrial Physics*, 191. doi:10.1016/j.jastp.2019.05.014.

Cervantes, S., Shprits, Y. Y., Aseev, N. A., Drozdov, A. Y., Castillo, A., and Stolle, C., 2019. Identifying Radiation Belt Electron Source and Loss Processes by Assimilating Spacecraft Data in a Three-Dimensional Diffusion Model. *Journal of Geophysical Research: Space Physics*. doi:10.1029/2019JA027514.

Chen, L., Bortnik, J., Li, W., Thorne, R. M., and Horne, R. B., 2012. Modeling the Properties of Plasmaspheric Hiss: 1. Dependence on Chorus Wave Emission. *Journal of Geophysical Research: Space Physics*, 117(A5). doi:10.1029/2011JA017201.

Chen, M. W., Liu, S., Schulz, M., Roeder, J. L., and Lyons, L. R., 2006. Magnetically Self-Consistent Ring Current Simulations during the 19 October 1998 Storm. *Journal of Geophysical Research: Space Physics*, 111(A11). doi:10.1029/2006JA011620.

Chen, M. W., Lemon, C. L., Guild, T. B., Keesee, A. M., Lui, A., Goldstein, J., Rodriguez, J. V., and Anderson, P. C., 2015a. Effects of Modeled Ionospheric Conductance and Electron Loss on Self-Consistent Ring Current Simulations during the 5–7

April 2010 Storm. *Journal of Geophysical Research: Space Physics*, 120(7):5355–5376. doi:10.1002/2015JA021285.

Chen, M. W., Lemon, C. L., Orlova, K., Shprits, Y., Hecht, J., and Walterscheid, R. L., 2015b. Comparison of Simulated and Observed Trapped and Precipitating Electron Fluxes during a Magnetic Storm. *Geophysical Research Letters*, 42(20):8302–8311.

Chen, M. W., Lemon, C. L., Hecht, J., Sazykin, S., Wolf, R. A., Boyd, A., and Valek, P., 2019. Diffuse Auroral Electron and Ion Precipitation Effects on RCM-E Comparisons with Satellite Data During the March 17, 2013 Storm. *Journal of Geophysical Research: Space Physics*. doi:10.1029/2019JA026545.

Choi, H.-S., Lee, J., Cho, K.-S., Kwak, Y.-S., Cho, I.-H., Park, Y.-D., Kim, Y.-H., Baker, D. N., Reeves, G. D., and Lee, D.-K., 2011. Analysis of GEO Spacecraft Anomalies: Space Weather Relationships. *Space Weather*, 9(6). doi:10.1029/2010SW000597.

Claudepierre, S. G., Elkington, S. R., and Wiltberger, M., 2008. Solar Wind Driving of Magnetospheric ULF Waves: Pulsations Driven by Velocity Shear at the Magnetopause. *Journal of Geophysical Research: Space Physics*, 113(A5). doi:10.1029/2007JA012890.

Claudepierre, S. G., Wiltberger, M., Elkington, S. R., Lotko, W., and Hudson, M. K., 2009. Magnetospheric Cavity Modes Driven by Solar Wind Dynamic Pressure Fluctuations. *Geophysical Research Letters*, 36(13). doi:10.1029/2009GL039045.

Clilverd, M. A., Rodger, C. J., Millan, R. M., Sample, J. G., Kokorowski, M., McCarthy, M. P., Ulich, T., Raita, T., Kavanagh, A. J., and Spanswick, E., 2007. Energetic Particle Precipitation into the Middle Atmosphere Triggered by a Coronal Mass Ejection. *Journal of Geophysical Research: Space Physics*, 112(A12). ISSN 2156-2202. doi:10.1029/2007JA012395.

Clilverd, M. A., Duthie, R., Hardman, R., Hendry, A. T., Rodger, C. J., Raita, T., Engebretson, M., Lessard, M. R., Danskin, D., and Milling, D. K., may 2015. Electron Precipitation from EMIC Waves: A Case Study from 31 May 2013. *Journal of Geophysical Research: Space Physics*, 120(5):3618–3631. ISSN 21699380. doi:10.1002/2015JA021090.

Cohn, S. E., 1997. An Introduction to Estimation Theory. *Journal of the Meteorological Society of Japan. Ser. II*, 75(1B):257–288. doi:10.2151/jmsj1965.75.1B_257.

Cornwall, J. M., 1968. Diffusion Processes Influenced by Conjugate-Point Wave Phenomena. *Radio science*, 3(7):740–744. doi:10.1002/rds196837740.

Craven, J. D., 1966. Temporal Variations of Electron Intensities at Low Altitudes in the Outer Radiation Zone as Observed with Satellite Injun 3. *Journal of Geophysical Research*, 71(23):5643–5663. doi:10.1029/JZ071i023p05643.

Daae, M., Shprits, Y. Y., Ni, B., Koller, J., Kondrashov, D., and Chen, Y., 2011. Reanalysis of Radiation Belt Electron Phase Space Density Using Various Boundary Conditions and Loss Models. *Advances in Space Research*, 48(8):1327–1334. doi:10.1016/j.asr.2011.07.001.

DeForest, S. E., 1972. Spacecraft Charging at Synchronous Orbit. *Journal of Geophysical Research*, 77(4):651–659. doi:10.1029/JA077i004p00651.

Denton, M. H., Thomsen, M. F., Jordanova, V. K., Henderson, M. G., Borovsky, J. E., Denton, J. S., Pitchford, D., and Hartley, D. P., 2015. An Empirical Model of Electron and Ion Fluxes Derived from Observations at Geosynchronous Orbit. *Space Weather*, 13(4):233–249. doi:10.1002/2015SW001168.

Denton, M. H., Henderson, M. G., Jordanova, V. K., Thomsen, M. F., Borovsky, J. E., Woodroffe, J., Hartley, D. P., and Pitchford, D., 2016. An Improved Empirical Model of Electron and Ion Fluxes at Geosynchronous Orbit Based on Upstream Solar Wind Conditions. *Space Weather*, 14(7):511–523. doi:10.1002/2016SW001409.

Denton, M. H., Reeves, G. D., Larsen, B. A., Friedel, R. F. W., Thomsen, M. F., Fernandes, P. A., Skoug, R. M., Funsten, H. O., and Sarno-Smith, L. K., 2017. On the Origin of Low-Energy Electrons in the Inner Magnetosphere: Fluxes and Pitch-Angle Distributions. *Journal of Geophysical Research: Space Physics*, 122(2):1789–1802. doi:10.1002/2016JA023648.

Denton, M. H., Taylor, M. G. G. T., Rodriguez, J. V., and Henderson, M. G., 2019. Extension of an Empirical Electron Flux Model from 6 to 20 Earth Radii Using Cluster/RAPID Observations. *Space Weather*, 17(5):778–792. doi:10.1029/2018SW002121.

Drozdov, A. Y., Shprits, Y. Y., Orlova, K. G., Kellerman, A. C., Subbotin, D. A., Baker, D. N., Spence, H. E., and Reeves, G. D., 2015. Energetic, Relativistic, and Ultra-relativistic Electrons: Comparison of Long-Term VERB Code Simulations with Van Allen Probes Measurements. *Journal of Geophysical Research: Space Physics*, 120(5):3574–3587. doi:10.1002/2014JA020637.

Drozdov, A. Y., Shprits, Y. Y., Aseev, N. A., Kellerman, A. C., and Reeves, G. D., 2017a. Dependence of Radiation Belt Simulations to Assumed Radial Diffusion Rates Tested for Two Empirical Models of Radial Transport. *Space Weather*, 15(1):150–162. doi:10.1002/2016SW001426.

Drozdov, A. Y., Shprits, Y. Y., Usanova, M. E., Aseev, N. A., Kellerman, A. C., and Zhu, H., 2017b. EMIC Wave Parameterization in the Long-Term VERB Code Simulation. *Journal of Geophysical Research: Space Physics*, 122(8):8488–8501. doi:10.1002/2017JA024389.

Drozdov, A. Y., Aseev, N., Effenberger, F., Turner, D. L., Saikin, A., and Shprits, Y. Y., 2019. Storm-Time Depletions of Multi-MeV Radiation Belt Electrons Observed at Different Pitch Angles. *Journal of Geophysical Research: Space Physics*, 124(11):8943–8953. doi:10.1029/2019JA027332.

Dubyagin, S., Sergeev, V., Apatenkov, S., Angelopoulos, V., Runov, A., Nakamura, R., Baumjohann, W., McFadden, J., and Larson, D., 2011. Can Flow Bursts Penetrate into the Inner Magnetosphere? *Geophysical Research Letters*, 38(8). doi:10.1029/2011GL047016.

Dungey, J. W., 1961. Interplanetary Magnetic Field and the Auroral Zones. *Physical Review Letters*, 6(2):47. doi:10.1103/PhysRevLett.6.47.

Dungey, J. W. The Theory of the Quiet Magnetosphere. In *Solar-Terrestrial Physics*, page 91, 1967.

Elkington, S. R., Hudson, M. K., and Chan, A. A., 1999. Acceleration of Relativistic Electrons Via Drift-Resonant Interaction with Toroidal-Mode Pc-5 ULF Oscillations. *Geophysical research letters*, 26(21):3273–3276. doi:10.1029/1999GL003659.

Elkington, S. R., Hudson, M. K., and Chan, A. A., 2003. Resonant Acceleration and Diffusion of Outer Zone Electrons in an Asymmetric Geomagnetic Field. *Journal of Geophysical Research: Space Physics*, 108(A3). doi:10.1029/2001JA009202.

Engebretson, M. J., Keiling, A., Fornacon, K.-H., Cattell, C. A., Johnson, J. R., Posch, J. L., Quick, S. R., Glassmeier, K.-H., Parks, G. K., and Reme, H., 2007. Cluster Observations of Pc 1–2 Waves and Associated Ion Distributions during the October and November 2003 Magnetic Storms. *Planetary and Space Science*, 55(6):829–848. doi:10.1016/j.pss.2006.03.015.

Engebretson, M. J., Posch, J. L., Wygant, J. R., Kletzing, C. A., Lessard, M. R., Huang, C.-L., Spence, H. E., Smith, C. W., Singer, H. J., Omura, Y., et al., 2015. Van Allen Probes, NOAA, GOES, and Ground Observations of an Intense EMIC Wave Event Extending over 12 H in Magnetic Local Time. *Journal of Geophysical Research: Space Physics*, 120(7):5465–5488. doi:10.1002/2015JA021227.

Evans, L. C., 1998. Partial Differential Equations, Grad. *Graduate Studies in Math*, 19.

Fälthammar, C.-G., 1965. Effects of Time-Dependent Electric Fields on Geomagnetically Trapped Radiation. *Journal of Geophysical Research*, 70(11):2503–2516. doi:10.1029/JZ070i011p02503.

Fennell, J. F., Claudepierre, S. G., Blake, J. B., O'Brien, T. P., Clemmons, J. H., Baker, D. N., Spence, H. E., and Reeves, G. D., 2015. Van Allen Probes Show That the Inner Radiation Zone Contains No MeV Electrons: ECT/MagEIS Data. *Geophysical Research Letters*, 42(5):1283–1289. doi:10.1002/2014GL062874.

Fok, M.-C., Kozyra, J. U., Nagy, A. F., Rasmussen, C. E., and Khazanov, G. V., 1993. Decay of Equatorial Ring Current Ions and Associated Aeronomical Consequences. *Journal of Geophysical Research: Space Physics*, 98(A11):19381–19393. doi:10.1029/93JA01848.

Fok, M.-C., Moore, T. E., and Delcourt, D. C., 1999. Modeling of Inner Plasma Sheet and Ring Current during Substorms. *Journal of Geophysical Research: Space Physics*, 104(A7):14557–14569. doi:10.1029/1999JA900014.

Fok, M.-C., Wolf, R. A., Spiro, R. W., and Moore, T. E., 2001. Comprehensive Computational Model of Earth's Ring Current. *Journal of Geophysical Research: Space Physics*, 106(A5):8417–8424. doi:10.1029/2000JA000235.

Fok, M.-C., Horne, R. B., Meredith, N. P., and Glauert, S. A., 2008. Radiation Belt Environment Model: Application to Space Weather Nowcasting. *Journal of Geophysical Research: Space Physics*, 113(A3). doi:10.1029/2007JA012558.

Fok, M.-C., Glocer, A., Zheng, Q., Horne, R. B., Meredith, N. P., Albert, J. M., and Nagai, T., 2011. Recent Developments in the Radiation Belt Environment Model. *Journal of Atmospheric and Solar-Terrestrial Physics*, 73(11-12):1435–1443. doi:10.1016/j.jastp.2010.09.033.

Fok, M.-C., Buzulukova, N. Y., Chen, S.-H., Glocer, A., Nagai, T., Valek, P., and Perez, J., 2014. The Comprehensive Inner Magnetosphere-Ionosphere Model. *Journal of Geophysical Research: Space Physics*, 119(9):7522–7540. doi:10.1002/2014JA020239.

Foster, J. C. and Burke, W. J., 2002. SAPS: A New Categorization for Sub-Auroral Electric Fields. *Eos, Transactions American Geophysical Union*, 83(36):393–394. doi:10.1029/2002EO000289.

Foster, J. C. and Vo, H. B., 2002. Average Characteristics and Activity Dependence of the Subauroral Polarization Stream. *Journal of Geophysical Research: Space Physics*, 107(A12). doi:10.1029/2002JA009409.

Frank, L. A., 1967a. Several Observations of Low-Energy Protons and Electrons in the Earth's Magnetosphere with OGO 3. *Journal of Geophysical Research*, 72(7):1905–1916. doi:10.1029/JZ072i007p01905.

Frank, L. A., 1967b. On the Extraterrestrial Ring Current during Geomagnetic Storms. *Journal of Geophysical Research*, 72(15):3753–3767. doi:10.1029/JZ072i015p03753.

Friedel, R. H. W., Korth, H., Henderson, M. G., Thomsen, M. F., and Scudder, J. D., 2001. Plasma Sheet Access to the Inner Magnetosphere. *Journal of Geophysical Research: Space Physics*, 106(A4):5845–5858. doi:10.1029/2000JA003011.

Funsten, H. O., Skoug, R. M., Guthrie, A. A., MacDonald, E. A., Baldonado, J. R., Harper, R. W., Henderson, K. C., Kihara, K. H., Lake, J. E., Larsen, B. A., et al., 2013. Helium, Oxygen, Proton, and Electron (HOPE) Mass Spectrometer for the Radiation Belt Storm Probes Mission. *Space Science Reviews*, 179(1-4):423–484. doi:10.1007/s11214-013-9968-7.

Gabrielse, C., Angelopoulos, V., Runov, A., and Turner, D. L., 2012. The Effects of Transient, Localized Electric Fields on Equatorial Electron Acceleration and Transport Toward the Inner Magnetosphere. *Journal of Geophysical Research: Space Physics*, 117(A10). doi:10.1029/2012JA017873.

Gabrielse, C., Angelopoulos, V., Harris, C., Artemyev, A., Kepko, L., and Runov, A., 2017. Extensive Electron Transport and Energization Via Multiple, Localized Dipolarizing Flux Bundles. *Journal of Geophysical Research: Space Physics*, 122(5):5059–5076. doi:10.1002/2017JA023981.

Ganushkina, N., Jaynes, A., and Liemohn, M., 2017. Space Weather Effects Produced by the Ring Current Particles. *Space Science Reviews*, 212(3-4):1315–1344. doi:10.1007/s11214-017-0412-2.

Ganushkina, N. Y., Pulkkinen, T. I., Milillo, A., and Liemohn, M., 2006. Evolution of the Proton Ring Current Energy Distribution during 21–25 April 2001 Storm. *Journal of Geophysical Research: Space Physics*, 111(A11). doi:10.1029/2006JA011609.

Ganushkina, N. Y., Liemohn, M. W., Pulkkinen, T. I., et al., 2012. Storm-time Ring Current: Model-Dependent Results. doi:10.5194/angeo-30-177-2012.

Ganushkina, N. Y., Amariutei, O. A., Shprits, Y. Y., and Liemohn, M. W., 2013. Transport of the Plasma Sheet Electrons to the Geostationary Distances. *Journal of Geophysical Research: Space Physics*, 118(1):82–98. doi:10.1029/2012JA017923.

Ganushkina, N. Y., Liemohn, M. W., Amariutei, O. A., and Pitchford, D., 2014. Low-energy Electrons (5–50 kev) in the Inner Magnetosphere. *Journal of Geophysical Research: Space Physics*, 119(1):246–259. doi:10.1002/2013JA019304.

Ganushkina, N. Y., Amariutei, O. A., Welling, D., and Heynderickx, D., 2015. Nowcast Model for Low-Energy Electrons in the Inner Magnetosphere. *Space Weather*, 13(1): 16–34. doi:10.1002/2014SW001098.

Ganushkina, N. Y., Sillanpää, I., Welling, D., Haiducek, J., Liemohn, M., Dubyagin, S., and Rodriguez, J. V., 2019. Validation of Inner Magnetosphere Particle Transport and Acceleration Model (IMPTAM) with Long-Term GOES MAGED Measurements of kev Electron Fluxes at Geostationary Orbit. *Space Weather*, 17(5):687–708. doi:10.1029/2018SW002028.

Glauert, S. A., Horne, R. B., and Meredith, N. P., 2014. Three-dimensional Electron Radiation Belt Simulations Using the BAS Radiation Belt Model with New Diffusion Models for Chorus, Plasmaspheric Hiss, and Lightning-Generated Whistlers. *Journal of Geophysical Research: Space Physics*, 119(1):268–289. doi:10.1002/2013JA019281.

Godinez, H. C., Yu, Y., Lawrence, E., Henderson, M. G., Larsen, B., and Jordanova, V. K., 2016. Ring Current Pressure Estimation with RAM-SCB Using Data Assimilation and Van Allen Probe Flux Data. *Geophysical Research Letters*, 43(23). doi:10.1002/2016GL071646.

Godunov, S. K., 1959. A Difference Method for Numerical Calculation of Discontinuous Solutions of the Equations of Hydrodynamics. *Matematicheskii Sbornik*, 89(3): 271–306.

Godunov, S. K. and Ryabenkii, V. S. *Difference Schemes: an Introduction to the Underlying Theory*, volume 19. Elsevier, 1987.

Goldstein, H., Poole, C., and Safko, J. Classical Mechanics, 2002.

Goldstein, J., Sandel, B. R., Thomsen, M. F., Spasojević, M., and Reiff, P. H., 2004. Simultaneous Remote Sensing and in Situ Observations of Plasmaspheric Drainage Plumes. *Journal of Geophysical Research: Space Physics*, 109(A3). doi:10.1029/2003JA010281.

Goldstein, J., Burch, J. L., and Sandel, B. R., 2005. Magnetospheric Model of Subauroral Polarization Stream. *Journal of Geophysical Research: Space Physics*, 110(A9). doi:10.1029/2005JA011135.

Green, J. C. and Kivelson, M. G., 2004. Relativistic Electrons in the Outer Radiation Belt: Differentiating between Acceleration Mechanisms. *Journal of Geophysical Research: Space Physics*, 109(A3). doi:10.1029/2003JA010153.

Gringauz, K. I. The Structure of the Earth's Ionized Gas Envelope Based on Local Charged Particle Concentrations Measured in the USSR. In *Space Research II*, page 574, 1961.

Gu, X., Shprits, Y. Y., and Ni, B., 2012. Parameterized Lifetime of Radiation Belt Electrons Interacting with Lower-Band and Upper-Band Oblique Chorus Waves. *Geophysical Research Letters*, 39(15). doi:10.1029/2012GL052519.

Gurnett, D. A. and Bhattacharjee, A. *Introduction to Plasma Physics: With Space, Laboratory and Astrophysical Applications*. Cambridge University Press, 2017.

Haerendel, G. Diffusion Theory of Trapped Particles and the Observed Proton Distribution. Technical report, Max-Planck-Institut fuer Physik und Astrophysik, Garching, Ger., 1968.

Hendry, A. T., Rodger, C. J., Clilverd, M. A., Engebretson, M. J., Mann, I. R., Lessard, M. R., Raita, T., and Milling, D. K., jun 2016. Confirmation of EMIC Wave-Driven Relativistic Electron Precipitation. *Journal of Geophysical Research: Space Physics*, 121 (6):5366–5383. ISSN 21699380. doi:10.1002/2015JA022224.

Hesse, M. and Birn, J., 1993. Three-dimensional Magnetotail Equilibria by Numerical Relaxation Techniques. *Journal of Geophysical Research: Space Physics*, 98(A3):3973–3982. doi:10.1029/92JA02905.

Horne, R. B. and Thorne, R. M., 1998. Potential Waves for Relativistic Electron Scattering and Stochastic Acceleration during Magnetic Storms. *Geophysical Research Letters*, 25(15):3011–3014. doi:10.1029/98GL01002.

Horne, R. B. and Thorne, R. M., 2003. Relativistic Electron Acceleration and Precipitation during Resonant Interactions with Whistler-Mode Chorus. *Geophysical research letters*, 30(10). doi:10.1029/2003GL016973.

Horne, R. B., Thorne, R. M., Shprits, Y. Y., Meredith, N. P., Glauert, S. A., Smith, A. J., Kanekal, S. G., Baker, D. N., Engebretson, M. J., Posch, J. L., et al., 2005. Wave Acceleration of Electrons in the Van Allen Radiation Belts. *Nature*, 437(7056):227. doi:10.1038/nature03939.

Hudson, M. K., Elkington, S. R., Lyon, J. G., Wiltberger, M., and Lessard, M., 2001. Radiation Belt Electron Acceleration by ULF Wave Drift Resonance: Simulation of 1997 and 1998 Storms. *Space Weather*, 125:289–296. doi:10.1029/GM125p0289.

Hwang, J.-A., Lee, D.-Y., Lyons, L. R., Smith, A. J., Zou, S., Min, K. W., Kim, K.-H., Moon, Y.-J., and Park, Y., 2007. Statistical Significance of Association between Whistler-Mode Chorus Enhancements and Enhanced Convection Periods during High-Speed Streams. *Journal of Geophysical Research: Space Physics*, 112(A9). doi:10.1029/2007JA012388.

Ilie, R., Liemohn, M. W., Toth, G., and Skoug, R. M., 2012. Kinetic Model of the Inner Magnetosphere with Arbitrary Magnetic Field. *Journal of Geophysical Research: Space Physics*, 117(A4). doi:10.1029/2011JA017189.

Imhof, W. L., Reagan, J. B., and Gaines, E. E., nov 1977. Fine-scale spatial structure in the pitch angle distributions of energetic particles near the midnight trapping boundary. *Journal of Geophysical Research*, 82(32):5215–5221. ISSN 01480227. doi:10.1029/JA082i032p05215.

Jaynes, A. N., Baker, D. N., Singer, H. J., Rodriguez, J. V., Loto'aniu, T. M., Ali, A. F., Elkington, S. R., Li, X., Kanekal, S. G., Claudepierre, S. G., et al., 2015. Source and Seed Populations for Relativistic Electrons: Their Roles in Radiation Belt Changes. *Journal of Geophysical Research: Space Physics*, 120(9):7240–7254. doi:10.1002/2015JA021234.

Johnson, M. H. and Kierein, J., 1992. Combined Release and Radiation Effects Satellite (CRRES): Spacecraft and Mission. *Journal of Spacecraft and Rockets*, 29(4):556–563. doi:10.2514/3.55641.

Jordanova, V. K. and Miyoshi, Y., 2005. Relativistic Model of Ring Current and Radiation Belt Ions and Electrons: Initial Results. *Geophysical research letters*, 32(14). doi:10.1029/2005GL023020.

Jordanova, V. K., Kistler, L. M., Kozyra, J. U., Khazanov, G. V., and Nagy, A. F., 1996. Collisional Losses of Ring Current Ions. *Journal of Geophysical Research: Space Physics*, 101(A1):111–126. doi:10.1029/95JA02000.

Jordanova, V. K., Kozyra, J. U., Nagy, A. F., and Khazanov, G. V., 1997. Kinetic Model of the Ring Current-Atmosphere Interactions. *Journal of Geophysical Research: Space Physics*, 102(A7):14279–14291. doi:10.1029/96JA03699.

Jordanova, V. K., Tu, W., Chen, Y., Morley, S. K., Panaitescu, A.-D., Reeves, G. D., and Kletzing, C. A., 2016. RAM-SCB Simulations of Electron Transport and Plasma Wave Scattering during the October 2012 "Double-Dip" Storm. *Journal of Geophysical Research: Space Physics*, 121(9):8712–8727. doi:10.1002/2016JA022470.

Kellerman, A. C., Shprits, Y. Y., Kondrashov, D., Subbotin, D., Makarevich, R. A., Donovan, E., and Nagai, T., 2014. Three-dimensional Data Assimilation and Reanalysis of Radiation Belt Electrons: Observations of a Four-Zone Structure Using Five Spacecraft and the VERB Code. *Journal of Geophysical Research: Space Physics*, 119(11): 8764–8783. doi:10.1002/2014JA020171.

Kellogg, P. J., 1959. Van Allen Radiation of Solar Origin. *Nature*, 183. doi:10.1038/1831295a0.

Kennel, C. F. and Engelmann, F., 1966. Velocity Space Diffusion from Weak Plasma Turbulence in a Magnetic Field. *The Physics of Fluids*, 9(12):2377–2388. doi:10.1063/1.1761629.

Kersten, T., Horne, R. B., Glauert, S. A., Meredith, N. P., Fraser, B. J., and Grew, R. S., 2014. Electron Losses from the Radiation Belts Caused by EMIC Waves. *Journal of Geophysical Research: Space Physics*, 119(11):8820–8837. doi:10.1002/2014JA020366.

Kim, H.-J. and Chan, A. A., 1997. Fully Adiabatic Changes in Storm Time Relativistic Electron Fluxes. *Journal of Geophysical Research: Space Physics*, 102(A10):22107–22116. doi:10.1029/97JA01814.

Kim, K.-C., Shprits, Y., Subbotin, D., and Ni, B., 2011. Understanding the Dynamic Evolution of the Relativistic Electron Slot Region Including Radial and Pitch Angle Diffusion. *Journal of Geophysical Research: Space Physics*, 116(A10). doi:10.1029/2011JA016684.

Kletzing, C. A., Kurth, W. S., Acuna, M., MacDowall, R. J., Torbert, R. B., Averkamp, T., Bodet, D., Bounds, S. R., Chutter, M., Connerney, J., et al., 2013. The Electric and Magnetic Field Instrument Suite and Integrated Science (EMFISIS) on RBSP. *Space Science Reviews*, 179(1-4):127–181. doi:10.1007/s11214-013-9993-6.

Koller, J., Chen, Y., Reeves, G. D., Friedel, R. H. W., Cayton, T. E., and Vrugt, J. A., 2007. Identifying the Radiation Belt Source Region by Data Assimilation. *Journal of Geophysical Research: Space Physics*, 112(A6). doi:10.1029/2006JA012196.

Kondrashov, D., Ghil, M., and Shprits, Y., 2011. Lognormal Kalman Filter for Assimilating Phase Space Density Data in the Radiation Belts. *Space Weather*, 9(11). doi:10.1029/2011SW000726.

Korth, H., Thomsen, M. F., Borovsky, J. E., and McComas, D. J., 1999. Plasma Sheet Access to Geosynchronous Orbit. *Journal of Geophysical Research: Space Physics*, 104 (A11):25047–25061. doi:10.1029/1999JA900292.

Kronberg, E. A., Ashour-Abdalla, M., Dandouras, I., Delcourt, D. C., Grigorenko, E. E., Kistler, L. M., Kuzichev, I. V., Liao, J., Maggiolo, R., Malova, H. V., et al., 2014. Circulation of Heavy Ions and Their Dynamical Effects in the Magnetosphere: Recent Observations and Models. *Space Science Reviews*, 184(1-4):173–235. doi:10.1007/s11214-014-0104-0.

Lanzerotti, L. J. and Morgan, C. G., 1973. ULF Geomagnetic Power near L= 4: 2. Temporal Variation of the Radial Diffusion Coefficient for Relativistic Electrons. *Journal of geophysical research*, 78(22):4600–4610. doi:10.1029/JA078i022p04600.

Lejosne, S., Kunduri, B. S. R., Mozer, F. S., and Turner, D. L., 2018. Energetic Electron Injections Deep Into the Inner Magnetosphere: A Result of the Subauroral Polarization Stream (SAPS) Potential Drop. *Geophysical Research Letters*, 45(9):3811–3819.

Lemaire, J. F. and Gringauz, K. I. *The Earth's Plasmasphere*. Cambridge University Press, 2005.

Lemon, C., Wolf, R. A., Hill, T. W., Sazykin, S., Spiro, R. W., Toffoletto, F. R., Birn, J., and Hesse, M., 2004. Magnetic Storm Ring Current Injection Modeled with the Rice Convection Model and a Self-Consistent Magnetic Field. *Geophysical research letters*, 31(21). doi:10.1029/2004GL020914.

Leonard, B. P., 1991. The ULTIMATE Conservative Difference Scheme Applied to Unsteady One-Dimensional Advection. *Computer methods in applied mechanics and engineering*, 88(1):17–74.

Leonard, B. P. and Niknafs, H. S., 1991. Sharp Monotonic Resolution of Discontinuities Without Clipping of Narrow Extrema. *Computers & Fluids*, 19(1):141–154. doi:10.1016/0045-7930(91)90011-6.

Lerche, I., 1968. Quasilinear Theory of Resonant Diffusion in a Magneto-Active, Relativistic Plasma. *The Physics of Fluids*, 11(8):1720–1727. doi:10.1063/1.1692186.

Li, J., Bortnik, J., An, X., Li, W., Angelopoulos, V., Thorne, R. M., Russell, C. T., Ni, B., Shen, X., Kurth, W. S., et al., 2019. Origin of Two-Band Chorus in the Radiation Belt of Earth. *Nature communications*, 10(1):1–9. doi:10.1038/s41467-019-12561-3.

Li, W., Shprits, Y. Y., and Thorne, R. M., 2007. Dynamic Evolution of Energetic Outer Zone Electrons Due to Wave-Particle Interactions during Storms. *Journal of Geophysical Research: Space Physics*, 112(A10). doi:10.1029/2007JA012368.

Li, W., Ma, Q., Thorne, R. M., Bortnik, J., Kletzing, C. A., Kurth, W. S., Hospodarsky, G. B., and Nishimura, Y., 2015. Statistical Properties of Plasmaspheric

Hiss Derived from Van Allen Probes Data and Their Effects on Radiation Belt Electron Dynamics. *Journal of Geophysical Research: Space Physics*, 120(5):3393–3405. doi:10.1002/2015JA021048.

Li, X., Baker, D. N., Temerin, M., Reeves, G. D., and Belian, R. D., 1998. Simulation of Dispersionless Injections and Drift Echoes of Energetic Electrons Associated with Substorms. *Geophysical Research Letters*, 25(20):3763–3766. doi:10.1029/1998GL900001.

Li, X., Baker, D. N., Temerin, M., Reeves, G., Friedel, R., and Shen, C., 2005. Energetic Electrons, 50 kev to 6 MeV, at Geosynchronous Orbit: Their Responses to Solar Wind Variations. *Space Weather*, 3(4). doi:10.1029/2004SW000105.

Liemohn, M. W., Kozyra, J. U., Clauer, C. R., and Ridley, A. J., 2001. Computational Analysis of the Near-Earth Magnetospheric Current System during Two-Phase Decay Storms. *Journal of Geophysical Research: Space Physics*, 106(A12):29531–29542. doi:10.1029/2001JA000045.

Liemohn, M. W., Ridley, A. J., Gallagher, D. L., Ober, D. M., and Kozyra, J. U., 2004. Dependence of Plasmaspheric Morphology on the Electric Field Description during the Recovery Phase of the 17 April 2002 Magnetic Storm. *Journal of Geophysical Research: Space Physics*, 109(A3). doi:10.1029/2003JA010304.

Liu, J., Angelopoulos, V., Zhang, X.-J., Turner, D. L., Gabrielse, C., Runov, A., Li, J., Funsten, H. O., and Spence, H. E., 2016. Dipolarizing Flux Bundles in the Cis-Geosynchronous Magnetosphere: Relationship between Electric Fields and Energetic Particle Injections. *Journal of Geophysical Research: Space Physics*, 121(2):1362–1376. doi:10.1002/2015JA021691.

Liu, S., Chen, M. W., Roeder, J. L., Lyons, L. R., and Schulz, M., 2005. Relative Contribution of Electrons to the Stormtime Total Ring Current Energy Content. *Geophysical research letters*, 32(3). doi:10.1029/2004GL021672.

Lyon, J. G., Fedder, J. A., and Mobarry, C. M., 2004. The Lyon–Fedder–Mobarry (LFM) Global MHD Magnetospheric Simulation Code. *Journal of Atmospheric and Solar-Terrestrial Physics*, 66(15-16):1333–1350. doi:10.1016/j.jastp.2004.03.020.

Lyons, L. R. and Schulz, M., 1989. Access of Energetic Particles to Storm Time Ring Current through Enhanced Radial "Diffusion". *Journal of Geophysical Research: Space Physics*, 94(A5):5491–5496. doi:10.1029/JA094iA05p05491.

Lyons, L. R. and Thorne, R. M., 1973. Equilibrium Structure of Radiation Belt Electrons. *Journal of Geophysical Research*, 78(13):2142–2149. doi:10.1029/JA078i013p02142.

Lyons, L. R. and Williams, D. J., 1980. A Source for the Geomagnetic Storm Main Phase Ring Current. *Journal of Geophysical Research: Space Physics*, 85(A2):523–530. doi:10.1029/JA085iA02p00523.

Lyons, L. R. and Williams, D. J. *Quantitative Aspects of Magnetospheric Physics*. D. Reidel Publishing Company, Dordrecht-Boston-Lancaster, 1984.

Lyons, L. R., Gallardo-Lacourt, B., Zou, S., Weygand, J. M., Nishimura, Y., Li, W., Gkioulidou, M., Angelopoulos, V., Donovan, E. F., Ruohoniemi, J. M., et al., 2016. The 17 March 2013 Storm: Synergy of Observations Related to Electric Field Modes and Their Ionospheric and Magnetospheric Effects. *Journal of Geophysical Research: Space Physics*, 121(11). doi:10.1002/2016JA023237.

Ma, Q., Mourenas, D., Artemyev, A., Li, W., Thorne, R. M., and Bortnik, J., 2016. Strong Enhancement of 10–100 kev Electron Fluxes by Combined Effects of Chorus Waves and Time Domain Structures. *Geophysical Research Letters*, 43(10):4683–4690. doi:10.1002/2016GL069125.

Mann, I. R., Milling, D. K., Rae, I. J., Ozeke, L. G., Kale, A., Kale, Z. C., Murphy, K. R., Parent, A., Usanova, M., Pahud, D. M., Lee, E.-A., Amalraj, V., Wallis, D. D., Angelopoulos, V., Glassmeier, K.-H., Russell, C. T., Auster, H.-U., and Singer, H. J., dec 2008. The Upgraded CARISMA Magnetometer Array in the THEMIS Era. *Space Science Reviews*, 141(1-4):413–451. ISSN 0038-6308. doi:10.1007/s11214-008-9457-6.

Marchuk, G. I., 1990. Splitting and Alternating Direction Methods. *Handbook of numerical analysis*, 1:197–462.

Mauk, B. H. and McPherron, R. L., 1980. An Experimental Test of the Electromagnetic Ion Cyclotron Instability within the Earth's Magnetosphere. *The Physics of Fluids*, 23 (10):2111–2127. doi:10.1063/1.862873.

Maynard, N. C. and Chen, A. J., 1975. Isolated Cold Plasma Regions: Observations and Their Relation to Possible Production Mechanisms. *Journal of Geophysical Research*, 80(7):1009–1013. doi:10.1029/JA080i007p01009.

McCollough, J. P., Elkington, S. R., and Baker, D. N., 2009. Modeling EMIC Wave Growth during the Compression Event of 29 June 2007. *Geophysical Research Letters*, 36(18). doi:10.1029/2009GL039985.

McIlwain, C. E., 1986. A Kp Dependent Equatorial Electric Field Model. *Advances in Space Research*, 6(3):187–197. doi:10.1016/0273-1177(86)90331-5.

McPherron, R. L., 2005. Magnetic Pulsations: Their Sources and Relation to Solar Wind and Geomagnetic Activity. *Surveys in Geophysics*, 26(5):545–592. doi:10.1007/s10712-005-1758-7.

Merkin, V. G., Kondrashov, D., Ghil, M., and Anderson, B. J., 2016. Data Assimilation of Low-Altitude Magnetic Perturbations into a Global Magnetosphere Model. *Space Weather*, 14(2):165–184. doi:10.1002/2015SW001330.

Millan, R. M. and Thorne, R. M., 2007. Review of Radiation Belt Relativistic Electron Losses. *Journal of Atmospheric and Solar-Terrestrial Physics*, 69(3):362–377. ISSN 13646826. doi:10.1016/j.jastp.2006.06.019.

Miyoshi, Y., Sakaguchi, K., Shiokawa, K., Evans, D., Albert, J., Connors, M., and Jordanova, V., 2008. Precipitation of Radiation Belt Electrons by EMIC Waves, Observed from Ground and Space. *Geophysical Research Letters*, 35(23):L23101. ISSN 0094-8276. doi:10.1029/2008GL035727.

Miyoshi, Y., Shinohara, I., Takashima, T., Asamura, K., Higashio, N., Mitani, T., Kasahara, S., Yokota, S., Kazama, Y., Wang, S.-Y., et al., 2018. Geospace Exploration Project ERG. *Earth, Planets and Space*, 70(1):101. doi:10.1186/s40623-018-0862-0.

Morley, S. K., 2016. Alternatives to Accuracy and Bias Metrics Based on Percentage Errors for Radiation Belt Modeling Applications. *Los Alamos National Laboratory report*, pages LA–UR.

Morley, S. K., Brito, T. V., and Welling, D. T., 2018. Measures of Model Performance Based on the Log Accuracy Ratio. *Space Weather*, 16(1):69–88. doi:10.1002/2017SW001669.

Nakano, S., Ueno, G., Ebihara, Y., Fok, M.-C., Ohtani, S., Brandt, P. C., Mitchell, D. G., Keika, K., and Higuchi, T., 2008. A Method for Estimating the Ring Current Structure and the Electric Potential Distribution Using Energetic Neutral Atom Data Assimilation. *Journal of Geophysical Research: Space Physics*, 113(A5). doi:10.1029/2006JA011853.

Ni, B., Thorne, R. M., Shprits, Y. Y., and Bortnik, J., 2008. Resonant Scattering of Plasma Sheet Electrons by Whistler-Mode Chorus: Contribution to Diffuse Auroral Precipitation. *Geophysical Research Letters*, 35(11). doi:10.1029/2008GL034032.

Ni, B., Shprits, Y., Thorne, R., Friedel, R., and Nagai, T., 2009. Reanalysis of Relativistic Radiation Belt Electron Phase Space Density Using Multisatellite Observations: Sensitivity to Empirical Magnetic Field Models. *Journal of Geophysical Research: Space Physics*, 114(A12). doi:10.1029/2009JA014438.

Ni, B., Thorne, R. M., Meredith, N. P., Horne, R. B., and Shprits, Y. Y., 2011. Resonant Scattering of Plasma Sheet Electrons Leading to Diffuse Auroral Precipitation: 2. Evaluation for Whistler Mode Chorus Waves. *Journal of Geophysical Research: Space Physics*, 116(A4). doi:10.1029/2010JA016233.

Ni, B., Thorne, R. M., Zhang, X., Bortnik, J., Pu, Z., Xie, L., Hu, Z.-J., Han, D., Shi, R., Zhou, C., et al., 2016. Origins of the Earth's Diffuse Auroral Precipitation. *Space Science Reviews*, 200(1-4):205–259.

Northrop, T. G., 1963. Adiabatic Charged-Particle Motion. *Reviews of Geophysics*, 1(3): 283–304.

Ohtani, S., Singer, H. J., and Mukai, T., 2006. Effects of the Fast Plasma Sheet Flow on the Geosynchronous Magnetic Configuration: Geotail and GOES Coordinated Study. *Journal of Geophysical Research: Space Physics*, 111(A1). doi:10.1029/2005JA011383.

Ohtani, S., Miyoshi, Y., Singer, H. J., and Weygand, J. M., jan 2009. On the Loss of Relativistic Electrons at Geosynchronous Altitude: Its Dependence on Magnetic Configurations and External Conditions. *Journal of Geophysical Research: Space Physics*, 114 (A1). ISSN 01480227. doi:10.1029/2008JA013391.

Olson, W. P. and Pfitzer, K. A., 1977. Magnetospheric Magnetic Field Modeling Ann. Sci. Rep. *Contract F44620-75-C-0033, Air Force Off. of Sci. Res., McDonnell Douglas Astronautics Co., Huntington Beach, Calif.*

Orlova, K. and Shprits, Y., 2014. Model of Lifetimes of the Outer Radiation Belt Electrons in a Realistic Magnetic Field Using Realistic Chorus Wave Parameters. *Journal of Geophysical Research: Space Physics*, 119(2):770–780. doi:10.1002/2013JA019596.

Orlova, K., Spasojevic, M., and Shprits, Y., 2014. Activity-dependent Global Model of Electron Loss inside the Plasmasphere. *Geophysical Research Letters*, 41(11):3744–3751. doi:10.1002/2014GL060100.

Orlova, K., Shprits, Y., and Spasojevic, M., 2016. New Global Loss Model of Energetic and Relativistic Electrons Based on Van Allen Probes Measurements. *Journal of Geophysical Research: Space Physics*, 121(2):1308–1314. doi:10.1002/2015JA021878.

Ozeke, L. G., Mann, I. R., Murphy, K. R., I., J. R., and Milling, D. K., 2014. Analytic Expressions for ULF Wave Radiation Belt Radial Diffusion Coefficients. *Journal of Geophysical Research: Space Physics*, 119(3):1587–1605. doi:10.1002/2013JA019204.

Peck, E. D., Randall, C. E., Green, J. C., Rodriguez, J. V., and Rodger, C. J., 2015. POES MEPED Differential Flux Retrievals and Electron Channel Contamination Correction. *Journal of Geophysical Research: Space Physics*, 120(6):4596–4612. doi:10.1002/2014JA020817.

Pfitzer, K. A. and Winckler, J. R., 1968. Experimental Observation of a Large Addition to the Electron Inner Radiation Belt after a Solar Flare Event. *Journal of Geophysical Research*, 73(17):5792–5797. doi:10.1029/JA073i017p05792.

Pickett, J. S., Grison, B., Omura, Y., Engebretson, M. J., Dandouras, I., Masson, A., Adrian, M. L., Santolík, O., Décréau, P. M. E., Cornilleau-Wehrlin, N., et al., 2010. Cluster Observations of EMIC Triggered Emissions in Association with Pc1 Waves near Earth's Plasmapause. *Geophysical Research Letters*, 37(9). doi:10.1029/2010GL042648.

Polyanin, A. D., 2001. Handbook of Linear Partial Differential Equations for Engineers and Scientists.

Press, W. H., Teukolsky, S. A., Vetterling, W. T., and Flannery, B. P., 1992. Numerical Recipes in C++. *The art of scientific computing*, 2:1002.

Reagan, J. B., Meyerott, R. E., Gaines, E. E., Nightingale, R. W., Filbert, P. C., and Imhof, W. L., 1983. Space Charging Currents and Their Effects on Spacecraft Systems. *IEEE Transactions on Electrical Insulation*, (3):354–365. doi:10.1109/TEI.1983.298625.

Reeves, G. D., McAdams, K. L., Friedel, R. H. W., and O'Brien, T. P., 2003. Acceleration and Loss of Relativistic Electrons during Geomagnetic Storms. *Geophysical Research Letters*, 30(10). doi:10.1029/2002GL016513.

Reeves, G. D., Spence, H. E., Henderson, M. G., Morley, S. K., Friedel, R. H. W., Funsten, H. O., Baker, D. N., Kanekal, S. G., Blake, J. B., Fennell, J. F., et al., 2013. Electron Acceleration in the Heart of the Van Allen Radiation Belts. *Science*, 341(6149):991–994. doi:10.1126/science.1237743.

Reeves, G. D., Friedel, R. H. W., Larsen, B. A., Skoug, R. M., Funsten, H. O., Claudepierre, S. G., Fennell, J. F., Turner, D. L., Denton, M. H., Spence, H. E., et al., 2016. Energy-dependent Dynamics of kev to MeV Electrons in the Inner Zone, Outer Zone, and Slot Regions. *Journal of Geophysical Research: Space Physics*, 121(1):397–412. doi:10.1002/2015JA021569.

Rodger, C. J., Raita, T., Clilverd, M. A., Seppälä, A., Dietrich, S., Thomson, N. R., and Ulich, T., 2008. Observations of Relativistic Electron Precipitation from the Radiation Belts Driven by EMIC Waves. *Geophysical Research Letters*, 35(16):L16106. ISSN 0094-8276. doi:10.1029/2008GL034804.

Rodger, C. J., Hendry, A. T., Clilverd, M. A., Kletzing, C. A., Brundell, J. B., and Reeves, G. D., 2015. High-resolution in Situ Observations of Electron Precipitation-Causing EMIC Waves. *Geophysical Research Letters*, 42(22):9633–9641. ISSN 00948276. doi:10.1002/2015GL066581.

Roederer, J. G. *Dynamics of Geomagnetically Trapped Radiation*, volume 2. Springer Science & Business Media, 2012.

Rossi, B. B. and Olbert, S., 1970. Introduction to the Physics of Space.

Rostoker, G., Skone, S., and Baker, D. N., 1998. On the Origin of Relativistic Electrons in the Magnetosphere Associated with Some Geomagnetic Storms. *Geophysical research letters*, 25(19):3701–3704. doi:10.1029/98GL02801.

Rothwell, P. and McIlwain, C. E., 1960. Magnetic Storms and the Van Allen Radiation Belts – observations from Satellite 1958ε (Explorer IV). *Journal of Geophysical Research*, 65(3):799–806. doi:10.1029/JZ065i003p00799.

Rowland, D. E. and Wygant, J. R., 1998. Dependence of the Large-Scale, Inner Magnetospheric Electric Field on Geomagnetic Activity. *Journal of Geophysical Research: Space Physics*, 103(A7):14959–14964. doi:10.1029/97JA03524.

Runov, A., Angelopoulos, V., Sitnov, M. I., Sergeev, V. A., Bonnell, J., McFadden, J. P., Larson, D., Glassmeier, K.-H., and Auster, U., 2009. THEMIS Observations of an Earthward-Propagating Dipolarization Front. *Geophysical Research Letters*, 36(14). doi:10.1029/2009GL038980.

Runov, A., Angelopoulos, V., Zhou, X.-Z., Zhang, X.-J., Li, S., Plaschke, F., and Bonnell, J., 2011. A THEMIS Multicase Study of Dipolarization Fronts in the Magnetotail Plasma Sheet. *Journal of Geophysical Research: Space Physics*, 116(A5). doi:10.1029/2010JA016316.

Russell, C. T. and Thorne, R. M., 1970. Structure of the Inner Magnetosphere. *Cosmic Electrodyn.*, 1.

Russell, C. T., Holzer, R. E., and Smith, E. J., 1969. OGO 3 Observations of ELF Noise in the Magnetosphere: 1. Spatial Extent and Frequency of Occurrence. *Journal of Geophysical Research*, 74(3):755–777. doi:10.1029/JA074i003p00755.

Sarris, T. E., Li, X., Tsaggas, N., and Paschalidis, N., 2002. Modeling Energetic Particle Injections in Dynamic Pulse Fields with Varying Propagation Speeds. *Journal of Geophysical Research: Space Physics*, 107(A3):SMP–1. doi:10.1029/2001JA900166.

Schiller, Q., Li, X., Koller, J., Godinez, H., and Turner, D. L., 2012. A Parametric Study of the Source Rate for Outer Radiation Belt Electrons Using a Kalman Filter. *Journal of Geophysical Research: Space Physics*, 117(A9). doi:10.1029/2012JA017779.

Schulz, M. and Eviatar, A., 1969. Diffusion of Equatorial Particles in the Outer Radiation Zone. *Journal of Geophysical Research*, 74(9):2182–2192. doi:10.1029/JA074i009p02182.

Schulz, M. and Lanzerotti, L. J. *Particle Diffusion in the Radiation Belts*, volume 7. Springer Verlag, 1974.

Selesnick, R. S. and Albert, J. M., 2019. Variability of the Proton Radiation Belt. *Journal of Geophysical Research: Space Physics*, 124(7):5516–5527. doi:10.1029/2019JA026754.

Selesnick, R. S. and Blake, J. B., 2000. On the Source Location of Radiation Belt Relativistic Electrons. *Journal of Geophysical Research: Space Physics*, 105(A2):2607–2624. ISSN 01480227. doi:10.1029/1999JA900445.

Sergeev, V. A., Chernyaev, I. A., Dubyagin, S. V., Miyashita, Y., Angelopoulos, V., Boakes, P. D., Nakamura, R., and Henderson, M. G., 2012. Energetic Particle Injections to Geostationary Orbit: Relationship to Flow Bursts and Magnetospheric State. *Journal of Geophysical Research: Space Physics*, 117(A10). doi:10.1029/2012JA017773.

Shi, R., Summers, D., Ni, B., Fennell, J. F., Blake, J. B., Spence, H. E., and Reeves, G. D., 2016. Survey of Radiation Belt Energetic Electron Pitch Angle Distributions Based on the Van Allen Probes MagEIS Measurements. *Journal of Geophysical Research: Space Physics*, 121(2):1078–1090. doi:10.1002/2015JA021724.

Shprits, Y., Kondrashov, D., Chen, Y., Thorne, R., Ghil, M., Friedel, R., and Reeves, G., 2007. Reanalysis of Relativistic Radiation Belt Electron Fluxes Using CRRES Satellite Data, a Radial Diffusion Model, and a Kalman Filter. *Journal of Geophysical Research: Space Physics*, 112(A12). doi:10.1029/2007JA012579.

Shprits, Y., Subbotin, D., Ni, B., Horne, R., Baker, D., and Cruce, P., 2011. Profound Change of the Near-Earth Radiation Environment Caused by Solar Superstorms. *Space Weather*, 9(8):1–13. doi:10.1029/2011SW000662.

Shprits, Y., Kellerman, A., Kondrashov, D., and Subbotin, D., 2013a. Application of a New Data Operator-Splitting Data Assimilation Technique to the 3-D VERB Diffusion Code and CRRES Measurements. *Geophysical Research Letters*, 40(19):4998–5002. doi:10.1002/grl.50969.

Shprits, Y. Y., Thorne, R. M., Friedel, R., Reeves, G. D., Fennell, J., Baker, D. N., and Kanekal, S. G., 2006. Outward Radial Diffusion Driven by Losses at Magnetopause. *Journal of Geophysical Research: Space Physics*, 111(A11). doi:10.1029/2006JA011657.

Shprits, Y. Y., Elkington, S. R., Meredith, N. P., and Subbotin, D. A., 2008a. Review of Modeling of Losses and Sources of Relativistic Electrons in the Outer Radiation Belt I: Radial Transport. *Journal of Atmospheric and Solar-Terrestrial Physics*, 70(14): 1679–1693. doi:10.1016/j.jastp.2008.06.008.

Shprits, Y. Y., Subbotin, D. A., Meredith, N. P., and Elkington, S. R., 2008b. Review of Modeling of Losses and Sources of Relativistic Electrons in the Outer Radiation Belt II: Local Acceleration and Loss. *Journal of Atmospheric and Solar-Terrestrial Physics*, 70(14):1694–1713. doi:10.1016/j.jastp.2008.06.014.

Shprits, Y. Y., Subbotin, D., and Ni, B., 2009. Evolution of Electron Fluxes in the Outer Radiation Belt Computed with the VERB Code. *Journal of Geophysical Research: Space Physics*, 114(A11). doi:10.1029/2008JA013784.

Shprits, Y. Y., Subbotin, D., Drozdov, A., Usanova, M. E., Kellerman, A., Orlova, K., Baker, D. N., Turner, D. L., and Kim, K.-C., 2013b. Unusual Stable Trapping of the Ultrarelativistic Electrons in the Van Allen Radiation Belts. *Nature Physics*, 9(11): 699. doi:10.1038/nphys2760.

Shprits, Y. Y., Kellerman, A. C., Drozdov, A. Y., Spence, H. E., Reeves, G. D., and Baker, D. N., 2015. Combined Convective and Diffusive Simulations: VERB-4D Comparison with 17 March 2013 Van Allen Probes Observations. *Geophysical Research Letters*, 42(22):9600–9608. doi:10.1002/2015GL065230.

Shprits, Y. Y., Drozdov, A. Y., Spasojevic, M., Kellerman, A. C., Usanova, M. E., Engebretson, M. J., Agapitov, O. V., Zhelavskaya, I. S., Raita, T. J., Spence, H. E., Baker, D. N., Zhu, H., and Aseev, N. A., 2016. Wave-Induced Loss of Ultra-Relativistic Electrons in the Van Allen Radiation Belts. *Nature Communications*, 7: 12883. doi:10.1038/ncomms12883.

Shprits, Y. Y., Kellerman, A., Aseev, N., Drozdov, A. Y., and Michaelis, I., 2017. Multi-MeV Electron Loss in the Heart of the Radiation Belts. *Geophysical Research Letters*, 44(3):1204–1209. doi:10.1002/2016GL072258.

Shue, J.-H., Chao, J. K., Fu, H. C., Russell, C. T., Song, P., Khurana, K. K., and Singer, H. J., 1997. A New Functional Form to Study the Solar Wind Control of the Magnetopause Size and Shape. *Journal of Geophysical Research: Space Physics*, 102(A5): 9497–9511. doi:10.1029/97JA00196.

Smirnov, A. G., Kronberg, E. A., Latallerie, F., Daly, P. W., Aseev, N., Shprits, Y. Y., Kellerman, A., Kasahara, S., Turner, D., and Taylor, M. G. G. T., 2019. Electron Intensity Measurements by the Cluster/RAPID/IES Instrument in Earth's Radiation Belts and Ring Current. *Space Weather*, 17(4):553–566. doi:10.1029/2018SW001989.

Southwood, D. J. and Wolf, R. A., 1978. An Assessment of the Role of Precipitation in Magnetospheric Convection. *Journal of Geophysical Research: Space Physics*, 83(A11): 5227–5232. doi:10.1029/JA083iA11p05227.

Spasojevic, M. and Shprits, Y. Y., 2013. Chorus Functional Dependencies Derived from CRRES Data. *Geophysical Research Letters*, 40(15):3793–3797. doi:10.1002/grl.50755.

Spasojevic, M., Shprits, Y. Y., and Orlova, K., 2015. Global Empirical Models of Plasmaspheric Hiss Using Van Allen Probes. *Journal of Geophysical Research: Space Physics*, 120(12):10–370. doi:10.1002/2015JA021803.

Spence, H. E., Reeves, G. D., Baker, D. N., Blake, J. B., Bolton, M., Bourdarie, S., Chan, A. A., Claudepierre, S. G., Clemmons, J. H., Cravens, J. P., Elkington, S. R., Fennell, J. F., Friedel, R. H. W., Funsten, H. O., Goldstein, J., Green, J. C., Guthrie, A., Henderson, M. G., Horne, R. B., Hudson, M. K., Jahn, J. M., Jordanova, V. K., Kanekal, S. G., Klatt, B. W., Larsen, B. A., Li, X., MacDonald, E. A., Mann, I. R., Niehof, J., O'Brien, T. P., Onsager, T. G., Salvaggio, D., Skoug, R. M., Smith, S. S., Suther, L. L., Thomsen, M. F., and Thorne, R. M., nov 2013. Science Goals and Overview of the Radiation Belt Storm Probes (RBSP) Energetic Particle, Composition, and Thermal Plasma (ECT) Suite on NASA's Van Allen Probes Mission. *The Van Allen Probes mission*, 179(1-4):311–336. ISSN 00386308. doi:10.1007/978-1-4899-7433-4-10.

Stern, D. P., 1975. The Motion of a Proton in the Equatorial Magnetosphere. *Journal of Geophysical Research*, 80(4):595–599. doi:10.1029/JA080i004p00595.

Strang, G. *Computational Science and Engineering*, volume 791. Wellesley-Cambridge Press Wellesley, 2007.

Su, Y.-J., Selesnick, R. S., and Blake, J. B., 2016. Formation of the Inner Electron Radiation Belt by Enhanced Large-Scale Electric Fields. *Journal of Geophysical Research: Space Physics*, 121(9):8508–8522. doi:10.1002/2016JA022881.

Subbotin, D., Shprits, Y., and Ni, B., 2010. Three-dimensional VERB Radiation Belt Simulations Including Mixed Diffusion. *Journal of Geophysical Research: Space Physics*, 115(A3). doi:10.1029/2009JA015070.

Subbotin, D. A. and Shprits, Y. Y., 2009. Three-dimensional Modeling of the Radiation Belts Using the Versatile Electron Radiation Belt (VERB) Code. *Space Weather*, 7(10). doi:10.1029/2008SW000452.

Subbotin, D. A. and Shprits, Y. Y., 2012. Three-dimensional Radiation Belt Simulations in Terms of Adiabatic Invariants Using a Single Numerical Grid. *Journal of Geophysical Research: Space Physics*, 117(A5). doi:10.1029/2011JA017467.

Subbotin, D. A., Shprits, Y. Y., Gkioulidou, M., Lyons, L. R., Ni, B., Merkin, V. G., Toffoletto, F. R., Thorne, R. M., Horne, R. B., and Hudson, M. K., 2011a. Simulation of the Acceleration of Relativistic Electrons in the Inner Magnetosphere Using RCM-VERB Coupled Codes. *Journal of Geophysical Research: Space Physics*, 116(A8). doi:10.1029/2010JA016350.

Subbotin, D. A., Shprits, Y. Y., and Ni, B., 2011b. Long-term Radiation Belt Simulation with the VERB 3-D Code: Comparison with CRRES Observations. *Journal of Geophysical Research: Space Physics*, 116(A12). doi:10.1029/2011JA017019.

Summers, D. and Thorne, R. M., 2003. Relativistic Electron Pitch-Angle Scattering by Electromagnetic Ion Cyclotron Waves during Geomagnetic Storms. *Journal of Geophysical Research*, 108(A4):1143. ISSN 0148-0227. doi:10.1029/2002JA009489.

Summers, D., Thorne, R. M., and Xiao, F., 1998. Relativistic Theory of Wave-Particle Resonant Diffusion with Application to Electron Acceleration in the Magnetosphere. *Journal of Geophysical Research: Space Physics*, 103(A9):20487–20500. doi:10.1029/98JA01740.

Summers, D., Ni, B., Meredith, N. P., Horne, R. B., Thorne, R. M., Moldwin, M. B., and Anderson, R. R., 2008. Electron Scattering by Whistler-Mode ELF Hiss in Plasmaspheric Plumes. *Journal of Geophysical Research: Space Physics*, 113(A4). doi:10.1029/2007JA012678.

Sweby, P. K., 1984. High Resolution Schemes Using Flux Limiters for Hyperbolic Conservation Laws. *SIAM journal on numerical analysis*, 21(5):995–1011. doi:10.1137/0721062.

Thébault, E., Finlay, C. C., Beggan, C. D., Alken, P., Aubert, J., Barrois, O., Bertrand, F., Bondar, T., Boness, A., Brocco, L., et al., 2015. International Geomagnetic Reference

Field: the 12Th Generation. *Earth, Planets and Space*, 67(1):79. doi:10.1186/s40623-015-0228-9.

Thomsen, M. F., Henderson, M. G., and Jordanova, V. K., 2013. Statistical Properties of the Surface-Charging Environment at Geosynchronous Orbit. *Space Weather*, 11(5): 237–244. doi:10.1002/swe.20049.

Thorne, R. M., 2010. Radiation Belt Dynamics: The Importance of Wave-Particle Interactions. *Geophysical Research Letters*, 37(22). doi:10.1029/2010GL044990.

Thorne, R. M. and Kennel, C. F., 1971. Relativistic Electron Precipitation during Magnetic Storm Main Phase. *Journal of Geophysical research*, 76(19):4446–4453. doi:10.1029/JA076i019p04446.

Thorne, R. M., Smith, E. J., Burton, R. K., and Holzer, R. E., 1973. Plasmaspheric Hiss. *Journal of Geophysical Research*, 78(10):1581–1596. doi:10.1029/JA078i010p01581.

Thorne, R. M., O'Brien, T. P., Shprits, Y. Y., Summers, D., and Horne, R. B., 2005. Timescale for MeV Electron Microburst Loss during Geomagnetic Storms. *Journal of Geophysical Research: Space Physics*, 110(A9). doi:10.1029/2004JA010882.

Thorne, R. M., Shprits, Y. Y., Meredith, N. P., Horne, R. B., Li, W., and Lyons, L. R., 2007. Refilling of the Slot Region between the Inner and Outer Electron Radiation Belts during Geomagnetic Storms. *Journal of Geophysical Research: Space Physics*, 112 (A6). doi:10.1029/2006JA012176.

Thorne, R. M., Ni, B., Tao, X., Horne, R. B., and Meredith, N. P., 2010. Scattering by Chorus Waves As the Dominant Cause of Diffuse Auroral Precipitation. *Nature*, 467 (7318):943. doi:10.1038/nature09467.

Toffoletto, F., Sazykin, S., Spiro, R., and Wolf, R., 2003. Inner Magnetospheric Modeling with the Rice Convection Model. *Space Science Reviews*, 107(1-2):175–196. doi:10.1023/A:1025532008047.

Tsurutani, B. T. and Smith, E. J., 1974. Postmidnight Chorus: A Substorm Phenomenon. *Journal of Geophysical Research*, 79(1):118–127. doi:10.1029/JA079i001p00118.

Tsyganenko, N. A., 1989. A Magnetospheric Magnetic Field Model with a Warped Tail Current Sheet. *Planetary and Space Science*, 37(1):5–20. doi:10.1016/0032-0633(89)90066-4.

Tsyganenko, N. A., 1995. Modeling the Earth's Magnetospheric Magnetic Field Confined within a Realistic Magnetopause. *Journal of Geophysical Research: Space Physics*, 100(A4):5599–5612. doi:10.1029/94JA03193.

Tsyganenko, N. A., 2002. A Model of the near Magnetosphere with a Dawn-Dusk Asymmetry 1. Mathematical Structure. *Journal of Geophysical Research: Space Physics*, 107(A8):SMP–12. doi:10.1029/2001JA000219.

Tsyganenko, N. A. and Mukai, T., 2003. Tail Plasma Sheet Models Derived from Geotail Particle Data. *Journal of Geophysical Research: Space Physics*, 108(A3). doi:10.1029/2002JA009707.

Tsyganenko, N. A. and Sitnov, M. I., 2005. Modeling the Dynamics of the Inner Magnetosphere during Strong Geomagnetic Storms. *Journal of Geophysical Research: Space Physics*, 110(A3). doi:10.1029/2004JA010798.

Tsyganenko, N. A. and Sitnov, M. I., 2007. Magnetospheric Configurations from a High-Resolution Data-Based Magnetic Field Model. *Journal of Geophysical Research: Space Physics*, 112(A6). doi:10.1029/2007JA012260.

Tu, W., Cunningham, G. S., Chen, Y., Henderson, M. G., Camporeale, E., and Reeves, G. D., 2013. Modeling Radiation Belt Electron Dynamics during GEM Challenge Intervals with the DREAM3D Diffusion Model. *Journal of Geophysical Research: Space Physics*, 118(10):6197–6211. doi:10.1002/jgra.50560.

Turner, D. L. and Li, X., 2008. Quantitative Forecast of Relativistic Electron Flux at Geosynchronous Orbit Based on Low-Energy Electron Flux. *Space Weather*, 6(5):1–8. doi:10.1029/2007SW000354.

Turner, D. L., Shprits, Y., Hartinger, M., and Angelopoulos, V., 2012. Explaining Sudden Losses of Outer Radiation Belt Electrons during Geomagnetic Storms. *Nature Physics*, 8. doi:10.1038/nphys2185.

Turner, D. L., Claudepierre, S. G., Fennell, J. F., O'Brien, T. P., Blake, J. B., Lemon, C., Gkioulidou, M., Takahashi, K., Reeves, G. D., Thaller, S., et al., 2015. Energetic Electron Injections Deep into the Inner Magnetosphere Associated with Substorm Activity. *Geophysical Research Letters*, 42(7):2079–2087. doi:10.1002/2015GL063225.

Turner, D. L., Fennell, J. F., Blake, J. B., Clemmons, J. H., Mauk, B. H., Cohen, I. J., Jaynes, A. N., Craft, J. V., Wilder, F. D., Baker, D. N., Reeves, G. D., Gershman, D. J., Avanov, L. A., Dorelli, J. C., Giles, B. L., Pollock, C. J., Schmid, D., Nakamura, R., Strangeway, R. J., Russell, C. T., Artemyev, A. V., Runov, A., Angelopoulos, V., Spence, H. E., Torbert, R. B., and Burch, J. L., 2016. Energy Limits of Electron Acceleration in the Plasma Sheet during Substorms: A Case Study with the Magnetospheric Multiscale (MMS) Mission. *Geophysical Research Letters*, 43(15). doi:10.1002/2016GL069691.

Ukhorskiy, A. Y., Anderson, B. J., Takahashi, K., and Tsyganenko, N. A., 2006. Impact of ULF Oscillations in Solar Wind Dynamic Pressure on the Outer Radiation Belt Electrons. *Geophysical Research Letters*, 33(6). doi:10.1029/2005GL024380.

Ukhorskiy, A. Y., Shprits, Y. Y., Anderson, B. J., Takahashi, K., and Thorne, R. M., may 2010. Rapid Scattering of Radiation Belt Electrons by Storm-Time EMIC Waves. *Geophysical Research Letters*, 37(9). ISSN 00948276. doi:10.1029/2010GL042906.

Usanova, M. E., Mann, I. R., Rae, I. J., Kale, Z. C., Angelopoulos, V., Bonnell, J. W., Glassmeier, K.-H., Auster, H. U., and Singer, H. J., 2008. Multipoint Observations of Magnetospheric Compression-Related EMIC Pc1 Waves by THEMIS and CARISMA. *Geophysical Research Letters*, 35(17). doi:10.1029/2008GL034458.

Usanova, M. E., Drozdov, A., Orlova, K., Mann, I. R., Shprits, Y., Robertson, M. T., Turner, D. L., Milling, D. K., Kale, A., Baker, D. N., et al., 2014. Effect of EMIC Waves on Relativistic and Ultrarelativistic Electron Populations: Ground-based and Van Allen Probes Observations. *Geophysical Research Letters*, 41(5):1375–1381. doi:10.1002/2013GL059024.

Van Allen, J. A. and Frank, L. A., 1959. Radiation around the Earth to a Radial Distance of 107,400 Km. *Nature*, 183. doi:10.1038/183430a0.

Vernov, S. N., Gorchakov, E. V., Kuznetsov, S. N., Logachev, Y. I., Sosnovets, E. N., and Stolpovsky, V. G., 1969. Particle Fluxes in the Outer Geomagnetic Field. *Reviews of Geophysics*, 7(1-2):257–280. doi:10.1029/RG007i001p00257.

Volland, H., 1973. A Semiempirical Model of Large-Scale Magnetospheric Electric Fields. *Journal of Geophysical Research*, 78(1):171–180. doi:10.1029/JA078i001p00171.

Walt, M., 1994. Introduction to Geomagnetically Trapped Radiation. *Camb. Atmos. Space Sci. Ser., Vol. 10,*, 10.

Wang, D., Shprits, Y. Y., Zhelavskaya, I. S., Agapitov, O. V., Drozdov, A. Y., and Aseev, N. A., 2019. Analytical Chorus Wave Model Derived from Van Allen Probe Observations. *Journal of Geophysical Research: Space Physics*, 124(2):1063–1084. doi:10.1029/2018JA026183.

Weimer, D. R., 1996. A Flexible, IMF Dependent Model of High-Latitude Electric Potentials Having "Space Weather" Applications. *Geophysical Research Letters*, 23 (18):2549–2552. doi:10.1029/96GL02255.

Weimer, D. R., 2001. An Improved Model of Ionospheric Electric Potentials Including Substorm Perturbations and Application to the Geospace Environment Modeling

November 24, 1996, Event. *Journal of Geophysical Research: Space Physics*, 106(A1): 407–416. doi:10.1029/2000JA000604.

Weimer, D. R., 2005. Improved Ionospheric Electrodynamic Models and Application to Calculating Joule Heating Rates. *Journal of Geophysical Research: Space Physics*, 110 (A5). doi:10.1029/2004JA010884.

Williams, D. J. and Smith, A. M., 1965. Daytime Trapped Electron Intensities at High Latitudes at 1100 Kilometers. *Journal of Geophysical Research*, 70(3):541–556. doi:10.1029/JZ070i003p00541.

Wygant, J. R., Bonnell, J. W., Goetz, K., Ergun, R. E., Mozer, F. S., Bale, S. D., Ludlam, M., Turin, P., Harvey, P. R., Hochmann, R., et al. The Electric Field and Waves Instruments on the Radiation Belt Storm Probes Mission. In *The Van Allen Probes Mission*, pages 183–220. 2013. doi:10.1007/s11214-013-0013-7.

Xiao, F., Su, Z., Zheng, H., and Wang, S., 2009. Modeling of Outer Radiation Belt Electrons by Multidimensional Diffusion Process. *Journal of Geophysical Research: Space Physics*, 114(A3). doi:10.1029/2008JA013580.

Xiao, F., Su, Z., Zheng, H., and Wang, S., 2010. Three-dimensional Simulations of Outer Radiation Belt Electron Dynamics Including Cross-Diffusion Terms. *Journal of Geophysical Research: Space Physics*, 115(A5). doi:10.1029/2009JA014541.

Xiao, F., Yang, C., Su, Z., Zhou, Q., He, Z., He, Y., Baker, D. N., Spence, H. E., Funsten, H. O., and Blake, J. B., 2015. Wave-driven Butterfly Distribution of Van Allen Belt Relativistic Electrons. *Nature communications*, 6. doi:10.1038/ncomms9590.

Yu, Y., Koller, J., Jordanova, V. K., Zaharia, S. G., Friedel, R. W., Morley, S. K., Chen, Y., Baker, D., Reeves, G. D., and Spence, H. E., 2014. Application and Testing of the L* Neural Network with the Self-Consistent Magnetic Field Model of RAM-SCB. *Journal of Geophysical Research: Space Physics*, 119(3):1683–1692. doi:10.1002/2013JA019350.

Yu, Y., Jordanova, V. K., Ridley, A. J., Albert, J. M., Horne, R. B., and Jeffery, C. A., 2016. A New Ionospheric Electron Precipitation Module Coupled with RAM-SCB within the Geospace General Circulation Model. *Journal of Geophysical Research: Space Physics*, 121(9):8554–8575. doi:10.1002/2016JA022585.

Yu, Y., Jordanova, V. K., Ridley, A. J., Toth, G., and Heelis, R., 2017. Effects of Electric Field Methods on Modeling the Midlatitude Ionospheric Electrodynamics and Inner Magnetosphere Dynamics. *Journal of Geophysical Research: Space Physics*, 122(5): 5321–5338. doi:10.1002/2016JA023850.

Yu, Y., Rastätter, L., Jordanova, V. K., Zheng, Y., Engel, M., Fok, M.-C., and Kuznetsova, M. M., 2019. Initial Results from the GEM Challenge on the Spacecraft Surface Charging Environment. *Space Weather*, 17(2):299–312. doi:10.1029/2018SW002031.

Zalesak, S. T., 1987. Advances in Computer Methods for Partial Differential Dquations, VI, Eds. *IMACS, Rutgers University*.

Zhang, Y., Zhu, H., Zhang, L., He, Y., Gao, Z., Zhou, Q., Yang, C., and Xiao, F., 2014. Effect of Low Energy Electron Injection on Storm-Time Evolution of Radiation Belt Energetic Electrons: Three-Dimensional Modeling. *Astrophysics and Space Science*, 352(2):613–620. doi:10.1007/s10509-014-1984-x.

Zhao, H., Li, X., Baker, D. N., Claudepierre, S. G., Fennell, J. F., Blake, J. B., Larsen, B. A., Skoug, R. M., Funsten, H. O., Friedel, R. H. W., et al., 2016. Ring Current Electron Dynamics during Geomagnetic Storms Based on the Van Allen Probes Measurements. *Journal of Geophysical Research: Space Physics*, 121(4):3333–3346. doi:10.1002/2016JA022358.

Zhelavskaya, I. S., Shprits, Y. Y., and Spasojević, M., 2017. Empirical Modeling of the Plasmasphere Dynamics Using Neural Networks. *Journal of Geophysical Research: Space Physics*, 122(11). doi:10.1002/2017JA024406.